MICROSTRUCTURES AND PROPERTIES OF ALUMINIUM-MAGNESIUM ALLOYS WITH ADDITIONS OF MANGANESE, ZIRCONIUM AND SCANDIUM.

by

Arve Johansen

A thesis submitted to
The Norwegian University of Science and Technology (NTNU)
in partial fulfilment of the requirements for the degree of

Doktor Ingeniør

Trondheim
March 2000

ACKNOWLEDGEMENTS

The work presented in this thesis has been carried out at the Norwegian University of Technology and Science, Department of Materials Technology and Electrochemistry, in Trondheim from January 1997 to January 2000. My supervisor has been Professor Nils Ryum and I gratefully acknowledge his enthusiasm, encouragement and interest in the field of my work.

I would also like to thank the members of the steering committee, Dr. Øystein Bauger, Dr. Oddvin Reiso, Dr. Svein R. Skjervold, Dr. Ulf Tundal and Professor Otto Lohne, for the most inspiring discussions throughout the experimental work. Hydro Aluminium is also acknowledged for the financial support through the Aluminium in Ships research project.

During the three years of study I have learned to know a great number of persons at NTNU and SINTEF. I would like to thank all them for being friendly and helpful during my stay at the university. Especially, I am very grateful for all kinds of help in the laboratories provided by Mr. Pål Ulseth, Ms. Tone Anzjøn, Dr. Bjørn Rønning, Mr. Tore Jørgensen, Mr. Robert Flatval, Mr. Geir Åge Lyng, Mr. Tor Nilsen, Mr. Morten Raanes, Mr. Wilhelm Dall, Prof. Jan K. Solberg, Mr. Lars Lodgaard, Mr. Morten Skylstad and Mr. Bjørn Olsen and his staff at the workshop. My experimental work could not have been carried out properly without the help from all of these highly experienced persons. In addition, I would give a special thank to Ms. Ingrid Page for the help with the manuscript and Dr. Jürgen Hirsch for performing the texture measurements. A special thank also to the persons at the casting laboratory at the research centre in Hydro Aluminium at Sunndalsøra, Mr. Ivar Olav Rød and Mr. Alf Einar Gravem, who provided me with the experimental alloys.

Furthermore, I am very grateful for many interesting, fruitful and controversial discussions with Mr. Ronny Nilsen, Mr. Amund Slettan, Mr. Bjarne Salberg, Mr. Knut Iver Aastorp, Mr. Jo Fenstad, Dr. Børge Forbord, Dr. Øyvind Frigaard, Mr. Jostein Røyset and Dr. Tanja Pettersen.

Finally, I would like to thank Bente for her patience, encouragement and understanding during the work with this thesis. Her support made it easier to write this book.

Trondheim, 2000-03-03
Arve Johansen

TABLE OF CONTENTS

ABSTRACT

The present work reports on the effect of Mn-, Zr- and Sc-additions upon hot deformation properties, recrystallization properties and mechanical properties for different temper conditions of Al-Mg alloys.

It can be stated that the addition of Mn, Zr and Sc improves the recrystallization properties and the mechanical properties of Al-Mg alloys. It should be emphasised that the precipitation of the metastable cubic Al_3Zr and the stable cubic $Al_3(Sc,Zr)$ is favourable in an aluminium-magnesium matrix due to a close similarity of the lattice structures. The $Al_3(Sc,Zr)$-phase is similar to the equilibrium Al_3Sc-phase and has a high thermal stability and thus the coherency with the aluminium matrix is retained to very high temperatures. The present work has demonstrated the beneficial features of the $Al_3(Sc,Zr)$-phase upon recrystallization and strength. This also results in an increase in the deformation resistance and a reduction in the hot ductility. In particluar, manganese reduces hot ductility.

After casting most of the Zr and Sc remained in solid solution. The Mn was partly present in large primary constituent particles and partly in solid solution. Segregations of all three elements were detected. Decomposition of solid solutions of these elements resulted in the formation of dispersoids of the type Al_6Mn (orthorombic), Al_3Zr (cubic) and $Al_3(Sc,Zr)$ (cubic)

It was found that the flow stress increased in the presence of the dispersoids. As compared to the alloy without dispersoids, the presence of Al_6Mn and Al_3Zr or $Al_3(Sc,Zr)$ increased the flow stress by 20-100% depending on the temperature and strain rate. The effect of the particles decreases as the Zener-Hollomon parameter increases. Extrusion experiments also confirm these results. In addition, manganese reduces the hot ductility considerably.

Furthermore, the present work has demonstrated that the recrystallization properties of Al-Mg alloys may be affected considerably by introducing Mn, Zr and Sc. The recrystallization behaviour after hot deformation may be effectively determined by the Zener drag exhibited by the dispersoids on grain boundaries. Al_6Mn showed to be least effective while $Al_3(Sc,Zr)$ is extremely effective in retarding recrystallization.

After cold deformation, however, the recrystallization behaviour is different due to a higher amount of stored energy. In the alloy without dispersoids, recrystallization occurred by classical nucleation at microstructural

heterogeneities, while particle stimulated nucleation operates in the other alloys. Recrystallization of cold rolled material resulted in an extremely fine-grained microstructure. Once recrystallized, extensive grain growth occurs in alloys containing Al_6Mn and/or Al_3Zr. Contrary, alloys containing Al_6Mn and $Al_3(Sc,Zr)$ are very stable and the fine-grained structure seems to be very stable up to 550°C. This clearly proves that $Al_3(Sc,Zr)$ are thermally stable and efficiently pin grain boundaries up to very high temperatures.

In the last part of this thesis the mechanical properties of the investigated alloys were mechanically tested in several temper conditions. It was found that the presence of Al_6Mn and $Al_3(Sc,Zr)$ caused an increase in the flow stress of 36 MPa in the O-temper condition, probably due to the Orowan mechanism. The effect of Al_6Mn and Al_3Zr alone or in combination was less pronounced.

Furthermore, the retained deformation microstructure after extrusion was associated with the Zener drag forces exhibited by the dispersoids and resulted in considerable strengthening. For instance, the combination of Al_6Mn and $Al_3(Sc,Zr)$ increased the strength by approximately 100 MPa compared to the dispersoid free alloy. Again the effect of Al_6Mn and Al_3Zr is less pronounced due to the lower capacity in retarding recrystallization.

The capability of the dispersoids to retard recrystallization should be an opportunity to increase the strength of the heat-affected zone after fusion welding. This is an important aspect since strain hardened conditions are used commercially. However, it has been demonstrated that a complete utilisation of the strength increase in the base material is not achieved as long as the weld metal is the weakest part in the weldment. However, a yield strength of 160 MPa was achieved for the material containing both Al_6Mn and $Al_3(Sc,Zr)$, while somewhat lower values were obtained for the alloys with Al_6Mn and/or Al_3Zr.

PART I
GENERAL INTRODUCTION

1. INTRODUCTION

Binary aluminium-magnesium alloys are the basis for an important class of non-heat treatable alloys commonly referred to as the 5xxx-series alloys. These alloys are widely used for applications in the automotive industry, marine and offshore constructions and in materials subjected to cryogenic conditions. Examples of use are hull plates for ships, body plates for cars, helicopter decks, buildings, containers and tanks for storing or transportation of liquid gases etc.

1.1 CHEMICAL COMPOSITION

Aluminium sheets of the 5xxx-series alloys show a good combination of mechanical strength, formability and ductility and exhibit an excellent resistance to corrosion in corrosive environments. The properties of these alloys are determined by the presence of the different alloying elements. Chemical composition of the most important high strength 5xxx-alloys is shown in Table I-1 and in the following, the effect of each alloying element will be briefly reviewed, Altenpohl (1965) and Mondolfo (1976).

Magnesium is the main alloying element and provides considerable strengthening through a combination of solute hardening and strain hardening. Mg in solid solution increases the deformation resistance of aluminium considerably. Al-Mg alloys exhibit the best corrosion resistance of all aluminium alloys.

Manganese is a transition element added to improve strength and to control recrystallization. It forms large primary constituents during solidification and small secondary dispersoids during homogenisation. Another important feature is that it improves the corrosion properties by tying up the iron.

Silicon is present as an impurity element. At small contents of magnesium, the alloy becomes age-hardenable due to the formation of the Mg_2Si-phase. However, at high Mg-contents the solubility of Mg_2Si becomes very small and the hardening effect is negligible. Silicon is usually considered as an impurity element in 5xxx alloys.

Iron is also an impurity element and reduces the corrosion resistance considerably. The solid solubility of Fe in aluminium is very small and most of it is found in primary constituents as Al_3Fe. If Mn is present most Fe is tied up in phases like $Al_6(MnFe)$.

Titanium is frequently added as a grain refiner. It usually forms coarse intermetallic phases with aluminium and too large amounts may have detrimental effect on mechanical properties and ductility.

Zirconium has been introduced to some of the recent 5xxx-alloys. The purpose of its addition has been to replace Ti as a grain refiner and to increase the recrystallization temperature.

Zinc has not been a traditional alloying element in 5xxx-alloys. In new alloys it has been added in an attempt to increase the strength in the HAZ by forming hardenable precipitates and to increase the corrosion resistance after ageing. However, Zn seems to reduce the resistance against corrosion in the HAZ, especially after ageing, Dif et al. (1998).

Copper additions improves the mechanical properties but decrease the hot ductility (Ratchev et al. (1997)), the corrosion resistance and the weldability (Mondolfo (1976)).

Chromium is often added in combinations with manganese, and exhibits the a stronger effect than Mn. Especially the ability of increasing the recrystallization temperature and retaining the deformation structure after hot deformation are important features.

Table I-1 *Chemical composition windows of common 5xxx wrought alloys.*

Alloy	Al	Mg	Mn	Fe	Zn	Cu	Si	Zr	Cr	Ti
5083[1]	Bal	4.0-4.9	0.4-1.0	0-0.4	0-0.25	0-0.1	0-0.4	-	0.05-0.25	0-0.15
5383[1]	Bal	4.0-5.2	0.7-1.0	0-0.25	0-0.7	0-0.2	0-0.25	0-0.2	0-0.25	0-0.15
5059[1] (Alustar™)	Bal	5.0-6.0	0.8-1.1	0-0.5	0.4-1.5	0-0.3	0-0.5	0.05-0.25	0-0.3	0-0.2
1561[2]	Bal	5.5-6.5	0.8-1.1	0-0.2	0-0.2	-	0-0.2	0.02-0.1	-	

[1] Marthinussen (2000) and European Standard EN 573-3.

1.2 MECHANICAL PROPERTIES

Aluminium-magnesium alloys have been widely used for commercial wrought and casting alloys due to a good combination of chemical and mechanical properties. Wrought alloys contain approximately1 to 6 wt% Mg while cast alloys contain 6 to 10 wt% Mg. In general, both wrought and cast alloys are used in a solution heat-treated condition due to a rather weak response to precipitation hardening. The reason for this is the stability of the incoherent equilibrium phases formed upon ageing. GP-zones and other metastable phases are only stable at very low temperatures and are not able to produce a strengthening increment that can be exploited for commercial purposes.

The strength of Al-Mg alloys comes from a combination of solute hardening and strain hardening. Strength of plates and sheets is usually obtained from hot rolling followed by cold rolling. Extruded profiles also exhibit some strengthening due to a retained deformation microstructure after extrusion. The strongest wrought alloys have a magnesium content of 4-6 wt% and due to very high deformation resistance caused by the solute atoms, very high deformation forces are required for mechanical processing. The extrudability and the friction stir weldability are therefore rather low reducing the productivity drastically compared to 6xxx and 7xxx alloys. The low extrudability makes the rolling process a more favourable and cost effective production process.

Alloying with an increasing amount of magnesium result in an increase in yield strength and tensile strength, while the ductility is reduced. Increasing the manganese and/or the chromium content also increases the strength values. Strain hardened tempers usually exhibit anisotropic properties but annealing procedures have been developed in order to control texture and anisotropy, Hatch (1984) and Altenpohl (1965)

1.3 CORROSION PROPERTIES

5xxx-alloys have been widely used for applications that require good resistance against corrosion. Table I-2 shows the electrolytical potential for several alloys and compounds. Additions of Mg to aluminium reduce the galvanic potential only slightly but produce an oxide layer with a larger specific volume than the metal from which it forms and thus results in an impervious oxide film. Thus, due to the protective oxide film, Al-Mg alloys have a better corrosion resistance to salt water and mild alkali than pure aluminium. Increasing the amount of Mg above approximately 3-4 wt% increases the susceptibility to intergranular and stress corrosion. This is due to the formation of AlMg intermetallics at grain boundaries causing these areas to be anodic. Al-Mg alloys may therefore exhibit stress corrosion after ageing or after long-term storing/service due to precipitation of anodic phases. Especially, cold rolled sheets are susceptible due to precipitation on the very fine network of the dislocation substructure. A heat treatment procedure in order to dissolve the intermetallic phases removes most of the susceptibility to stress and intergranular corrosion, Mondolfo (1976). Manganese has a positive effect on the corrosion resistance. First of all, it forms compounds (Al_6Mn) with an electrolytic potential that does not differ significantly from the aluminium matrix inrespective whether the manganese is in solid solution or in compounds. Thus, aluminium-manganese alloys have good resistance against stress corrosion, intergranular corrosion and pitting corrosion. Iron and silicon compounds are strongly positive compared to the aluminium matrix and may cause severe pitting of the matrix. When manganese is present, Fe and Si can be absorbed into Mn-bearing compounds and thus reducing the potential differences and practically eliminating pitting, Mondolfo (1977).

Table I-2 *Electrolytic potential of several alloys and compunds in a NaCl-H_2O-solution against a 0.1 N Calomel electrode. After Mondolfo (1977).*

Alloy	E [V]	Compound	E [V]
Al (high purity)	-0.85	Mg_2Si	-1.50
Al-1%Si	-0.81	Al_3Mg_2	-1.07
Al-4%Cu	-0.69	$MgZn_2$	-1.04
Al-1%Zn (in sol.)	-0.96	Al_6Mn	-0.85
Al-4%Zn (in sol.)	-1.02	$Al_6(MnFe)$	-0.84
Al-4%Mg (in sol.)	-0.87	Al_3Ni	-0.73
Al-1%Mn (in sol.)	-0.85	Al_3Fe	-0.56
Al-1%Mg2Si (in sol.)	-0.83	Al_8Fe_2Si	-0.58
Al-1%MgZn2 (in sol.)	-1.07	Al_2Cu	-0.53
Al-4.5%Cu-1%Mg (in sol.)	-0.66		
Al-4.5%Cu-1%Mg (precipitated)	-0.80		

1.4 WELDABILITY

The weldability of Al-Mg alloys is usually very good. It means that they can be fusion welded without being too susceptible to hot cracking. Filler wires of approximately the same composition as the base material are used for welding of 5xxx-alloys. Consequently, welding of strain hardened sheets results in a lower strength in HAZ and in the weld metal compared to the base metal. In most cases the strength of a fully annealed condition are used as a design criterion due to the loss of strength in the heat affected zone after welding.

1.5 SCOPE OF WORK

Al-Mg alloys of the 5xxx-series are used as hull plates in small to medium size aluminium boats/ships due to exellent corrosion properties. The post-weld strength of these alloys is reduced compared to the base metal. This is due to a lower strength in the cast structure of the weld metal and lower strength in the recrystallized heat affected zone. The demand for weight savings in the transportation industry in order to build larger constructions and to achieve higher speeds requires both innovative designs and stronger aluminium alloys.

While high strength 5xxx alloys have been developed in Russia (1561), the traditional AA5083 alloy has served as the major hull plate material in the ship industry in Western Europe during the past 50 years and little work has been carried out to improve this alloy. However, recently two new alloys have been introduced, 5383 and 5059, with improved strength properties and with all other properties equal to or better than 5083. These two new alloys contain Zr and Zn as grain refiner and corrosion stabiliser, respectively, while the increased strength is mainly due to a higher magnesium content.

The objective of the present study is to extend the knowledge of 5xxx-series alloys and to find the effect of the dispersoid forming elements Mn, Zr and Sc on the hot deformation properties, mechanical properties and recrystallization properties. An increase in the strength of the base material by addition of new dispersoid forming alloying elements should also give an increased strength in the heat affected zone after welding.

2. PHASE RELATIONS IN AL-MG-X ALLOYS

In order to understand the mechanisms of precipitation, deformation, recrystallization and strengthening it is advantageous to review the equilibrium phase relationships of the governing alloy systems. The present study deals with Al-Mg-X alloys where X may be the elements Mn, Zr and Sc or combinations of these. In addition, Fe and Si will play a role as the major impurity elements. The following paragraphs will discuss the effect of these elements upon the formation of constitutional phases and solubility limits in the aluminium rich corner of the phase diagrams.

2.1 EQUILIBRIUM PHASE DIAGRAMS

2.1.1 The Al-Mg-system

The solid solubility of Mg in Al increases with temperature and reaches the maximum value of 17.4 wt% at the eutectic temperature of 450°C, Mondolfo (1976). The eutectic reaction is $L \rightarrow Al+Al_3Mg_2$ at 35% Mg, Figure I-1. The Al_3Mg_2-phase (β) exists over the composition range 34.8-37.1 wt% Mg, and thus the formula Al_8Mg_5 fits the composition of this phase better. However, both formulas are used in the literature and the former will be used in this thesis. The equilibrium β-Al_3Mg_2-phase has a fcc structure with the lattice parameter a=2.8239 nm and the space group Fd3m, Samson (1965).

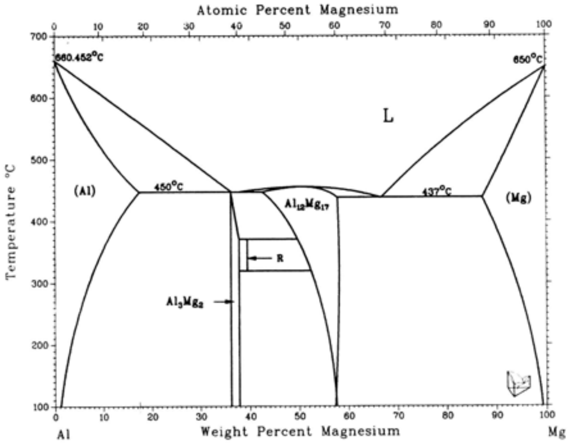

__Figure I-1__ The equilibrium phase diagram of the Al-Mg system.

2.1.2 The Al-Mg-Mn, Al-Mg-Fe, Al-Mg-Si and Al-Mn-Fe systems

2.1.2.1 Al-Mg-Mn

Besides the binary compounds, Al_3Mg_2 and Al_6Mn, a ternary compound exists is this system, i.e. $Al_{18}Mn_2Mg_3$. The ternary eutectic reaction is $L \rightarrow Al+Al_3Mg_2+Al_{18}Mn_2Mg_3$ at approximately 27 wt% Mg and 0.2 wt% Mn at 437°C. A ternary peritectic reaction, $L+Al_6Mn \rightarrow Al+Al_{18}Mn_2Mg_3$, occurs at 22 wt% Mg and <0.5 wt% Mn, Mondolfo (1976 and 1977), Figure I-2 a). Mg and Mn reduce each other's solid solubility considerably. At the eutectic temperature the maximum solubility is 12 wt% Mg and 0.5 wt% Mn compared to 17.4 wt% and 1.8 wt%, respectively, in the binary alloys, Mondolfo (1977).

2.1.2.2 Al-Mg-Fe

No ternary phases have been observed in the Al-Mg-Fe alloy system in the composition range 0-6 wt% Fe and 0-10 wt% Mg, Phillips (1959). The only constituents formed are those of the two binary systems, i.e. β-Al_3Mg_2 and Al_3Fe. A ternary eutectic reaction occurs at 0.15 wt% Fe and 33 wt% Mg: $L \rightarrow Al+Al_3Mg_2+Al_3Fe$, Mondolfo (1976), Figure I-2 b). The solid solubility of Mg decreases with the addition of Fe, being 14.1 wt% at the ternary eutectic temperature compared to 17.4 wt% in the binary alloy. Addition of Mg probably reduces the maximum solubility of Fe in Al from 0.05 wt% in the binary Al-Fe alloy, Mondolfo (1976).

2.1.2.3 Al-Mg-Si

In this system no ternary phases occur, thus only those compounds of the binary alloys are formed. Two ternary eutectic reactions are obseved: $L \rightarrow Al+Mg_2Si+Al_3Mg_2$ and $L \rightarrow Al+Mg_2Si+Si$. See Mondolfo (1976) for more details.

2.1.2.4 Al-Mn-Fe

Only binary compounds may exist in the aluminium rich corner of this system (Al, Al_3Fe, Al_6Mn and Al_4Mn), Mondolfo (1976). However, up to 50 % of the manganese in Al_6Mn can be replaced by Fe ($Al_6(MnFe)$). At Mn content >4 wt% the phase Al_4Mn may be formed but it is consumed in the peritectic reaction: $L+Al_3Fe+Al_4Mn \rightarrow Al_6(MnFe)$. The location of this reaction is 727° at 2.5 wt% Fe and 3.5 wt% Mn. At 754°C, 1.7 wt% Fe and

0.7 wt% Mn a terary eutectic reaction occurs: L→Al+Al_3Fe+$Al_6(MnFe)$, Figure I-2 e) and f). The solubility of Fe is very small (< 0.05 wt%) and will not be affected appreciably by Mn additions. The solubility of Mn decreases drastically in the presence of Fe, Mondolfo (1976, 1977).

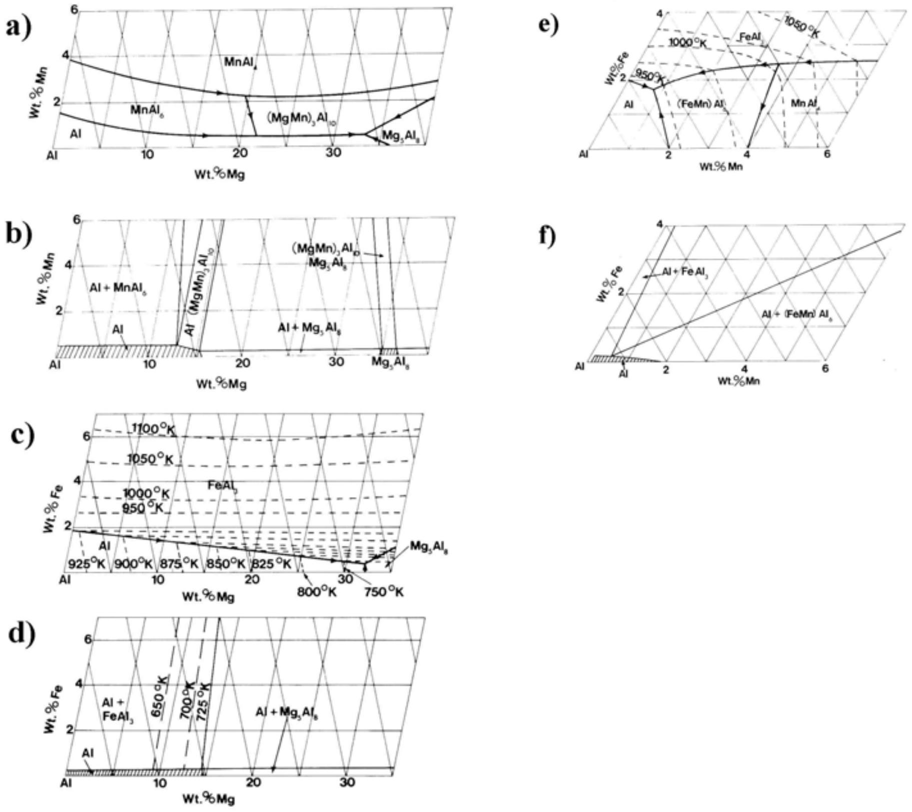

Figure I-2 Ternary phase diagrams. a) Al-Mg-Mn, liquidus, b) Al-Mg-Mn, phase distributions at 447°C, c) Al-Mg-Fe, liquidus, d) Al-Mg-Fe, phase distribution at 452°C, e) Al-Mn-Fe, liquidus and f) Al-Mn-Fe, phase distribution at 627°C. After Mondolfo (1976).

2.1.3 The Al-Mg-Mn-Fe, Al-Mg-Fe-Si and Al-Mg-Mn-Si systems

2.1.3.1 Al-Mg-Mn-Fe

The addition of Fe to Al-Mg-Mn produces no drastic changes and no new phases are formed other than those existing in the ternary systems, i.e. Al, Al_3Mg_2, Al_3Fe, Al_6Mn, $Al_6(MnFe)$ and $Al_{18}Mn_2Mg_3$, Figure I-3 a) and b).

The peritectic reaction: $L+Al_6(MnFe) \rightarrow Al+Al_{18}Mn_2Mg_3+Al_3Fe$ is followed by the eutectic reaction: $L \rightarrow Al+Al_{18}Mn_2Mg_3+Al_3Fe+Al_3Mg_2$. If the Fe and Mn are crystallized together into $Al_6(MnFe)$, then the peritectic reaction do not proceed to any extent and $Al_{18}Mn_2Mg_3$ can only be formed directly from the liquid, Barlock and Mondolfo (1975).

2.1.3.2 Al-Mg-Fe-Si

In the quaternary Al-Mg-Fe-Si alloy there are two ternary phases, Al_5SiFe and Al_8SiFe_2, and one quaternary phase, $Al_8Si_6Mg_3Fe$, Figure I-3 c) and d). The ternary phases does not appear in quinary alloys with Mn if Mn>Fe, Barlock and Mondolfo (1975). For low concentrations of Mg, Fe and Si the formation of the quaternary compound can be suppressed and the phases appearing in the solid state is formed according to the quaternary eutectic reaction, $L \rightarrow Al+Al_3Mg_2+Al_3Fe+Mg_2Si$.

2.1.3.3 Al-Mg-Mn-Si

No quaternary phase is formed in this system and all the phases can be derived from the binary and ternary systems, Barlock and Mondolfo (1975) and Mondolfo (1977). Phase diagrams and invariant reactions are shown in Figure I-3 g) and h) and Table I-3, respectively.

2.1.3.4 Al-Mn-Fe-Si

No quaternary phase is formed in this system. However, most of the Mn in $Al_{15}Si_2Mn_3$ can be replaced by Fe and the $Al_{15}Si_2(MnFe)_3$ is the phase found in most alloys. See phase diagrams and invariant reactions in Figure I-3 e) and f) and the invariant reactions are listed in Table I-3.

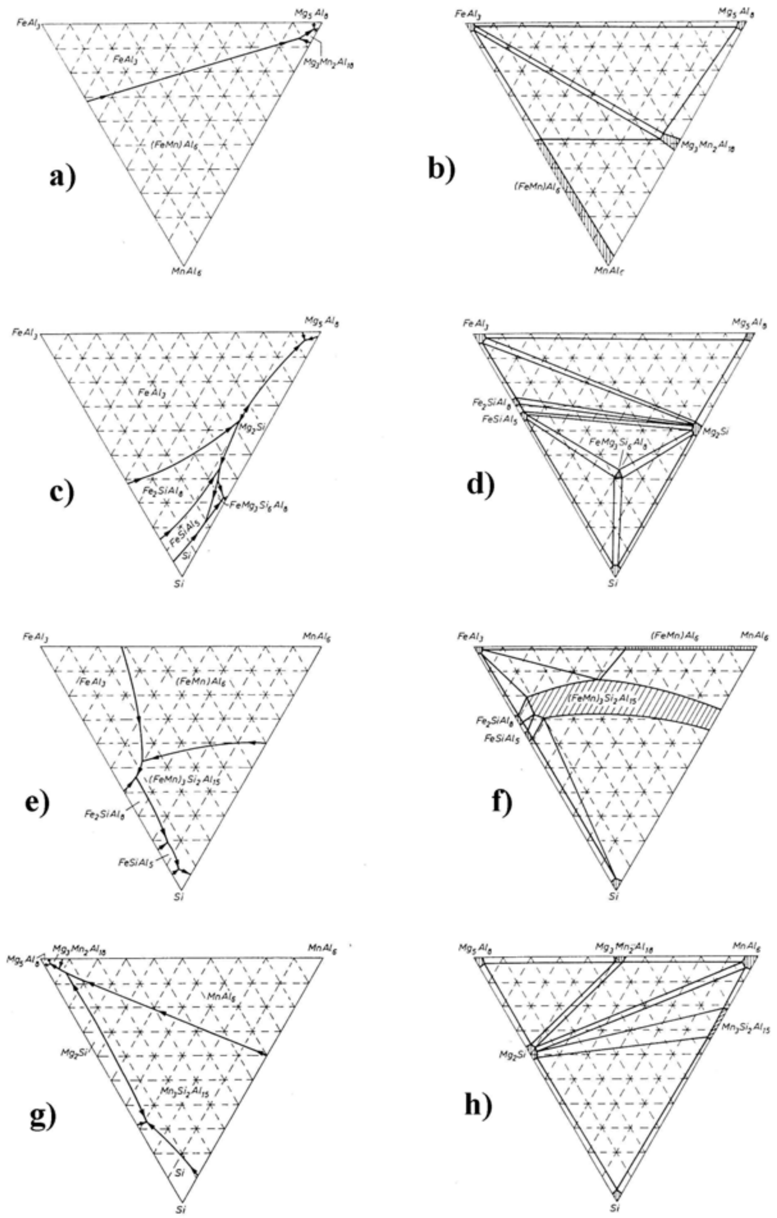

Figure I-3 *Quaternary phase diagrams after Barlock and Mondolfo (1975):*
Al-Mg-Mn-Fe a) liquidus and b) phase distribution in solid,
Al-Mg-Fe-Si c) liquidus and d) phase distribution in solid,
Al-Mn-Fe-Si e) liquidus and f) phase distribution in solid and
Al-Mg-Mn-Si g) liquidus and h) phase distribution in solid.

2.1.4 The Al-Mg-Mn-Fe-Si system

The Al-Mg-Mn-Fe-Si system is very important because it completely covers the commercial alloys in the 3xxx, 4xxx, 5xxx and 6xxx series. However, due to its complexity, few investigations have been made on this quinary system so a complete and accurate phase diagram is not available. The information available on invariant reactions is listed in Table I-3.

No quinary phase is formed and all phases found can be traced back to the pertinent binary, ternary and quaternary alloy systems. For more details on the occurrence and the nature of the different phases see Phragmen (1949) and Barlock and Mondolfo (1975).

Table I-3 *Binary, ternary, quaternary and quinary invariant reactions in the Al-Mg-Mn-Fe-Si system.*

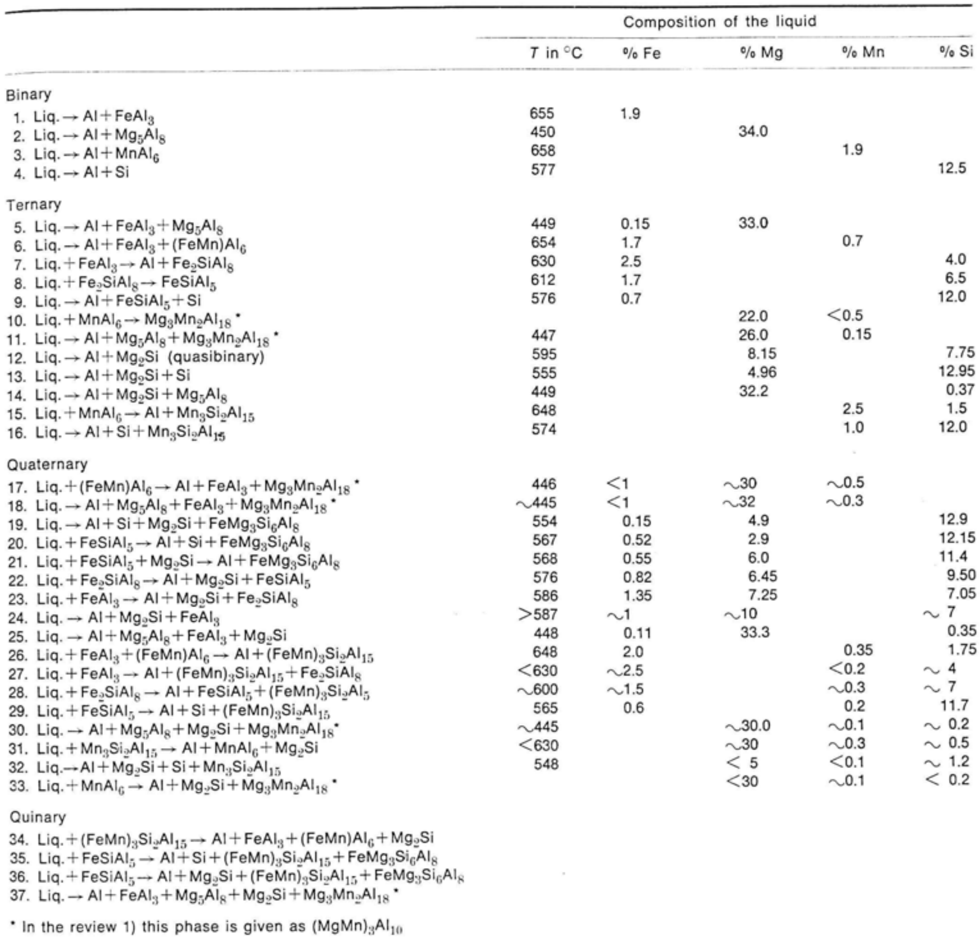

	Composition of the liquid				
	T in °C	% Fe	% Mg	% Mn	% Si
Binary					
1. Liq. → Al + $FeAl_3$	655	1.9			
2. Liq. → Al + Mg_5Al_8	450		34.0		
3. Liq. → Al + $MnAl_6$	658			1.9	
4. Liq. → Al + Si	577				12.5
Ternary					
5. Liq. → Al + $FeAl_3$ + Mg_5Al_8	449	0.15	33.0		
6. Liq. → Al + $FeAl_3$ + $(FeMn)Al_6$	654	1.7		0.7	
7. Liq. + $FeAl_3$ → Al + Fe_2SiAl_8	630	2.5			4.0
8. Liq. + Fe_2SiAl_8 → $FeSiAl_5$	612	1.7			6.5
9. Liq. → Al + $FeSiAl_5$ + Si	576	0.7			12.0
10. Liq. + $MnAl_6$ → $Mg_3Mn_2Al_{18}$ *			22.0	$<$0.5	
11. Liq. → Al + Mg_5Al_8 + $Mg_3Mn_2Al_{18}$ *	447		26.0	0.15	
12. Liq. → Al + Mg_2Si (quasibinary)	595		8.15		7.75
13. Liq. → Al + Mg_2Si + Si	555		4.96		12.95
14. Liq. → Al + Mg_2Si + Mg_5Al_8	449		32.2		0.37
15. Liq. + $MnAl_6$ → Al + $Mn_3Si_2Al_{15}$	648			2.5	1.5
16. Liq. → Al + Si + $Mn_3Si_2Al_{15}$	574			1.0	12.0
Quaternary					
17. Liq. + $(FeMn)Al_6$ → Al + $FeAl_3$ + $Mg_3Mn_2Al_{18}$ *	446	$<$1	$\sim$30	$\sim$0.5	
18. Liq. → Al + Mg_5Al_8 + $FeAl_3$ + $Mg_3Mn_2Al_{18}$ *	$\sim$445	$<$1	$\sim$32	$\sim$0.3	
19. Liq. → Al + Si + Mg_2Si + $FeMg_3Si_6Al_8$	554	0.15	4.9		12.9
20. Liq. + $FeSiAl_5$ → Al + Si + $FeMg_3Si_6Al_8$	567	0.52	2.9		12.15
21. Liq. + $FeSiAl_5$ + Mg_2Si → Al + $FeMg_3Si_6Al_8$	568	0.55	6.0		11.4
22. Liq. + Fe_2SiAl_8 → Al + Mg_2Si + $FeSiAl_5$	576	0.82	6.45		9.50
23. Liq. + $FeAl_3$ → Al + Mg_2Si + Fe_2SiAl_8	586	1.35	7.25		7.05
24. Liq. → Al + Mg_2Si + $FeAl_3$	$>$587	$\sim$1	$\sim$10		$\sim$ 7
25. Liq. → Al + Mg_5Al_8 + $FeAl_3$ + Mg_2Si	448	0.11	33.3		0.35
26. Liq. + $FeAl_3$ + $(FeMn)Al_6$ → Al + $(FeMn)_3Si_2Al_{15}$	648	2.0		0.35	1.75
27. Liq. + $FeAl_3$ → Al + $(FeMn)_3Si_2Al_{15}$ + Fe_2SiAl_8	$<$630	$\sim$2.5		$<$0.2	$\sim$ 4
28. Liq. + Fe_2SiAl_8 → Al + $FeSiAl_5$ + $(FeMn)_3Si_2Al_5$	$\sim$600	$\sim$1.5		$\sim$0.3	$\sim$ 7
29. Liq. + $FeSiAl_5$ → Al + Si + $(FeMn)_3Si_2Al_{15}$	565	0.6		0.2	11.7
30. Liq. → Al + Mg_5Al_8 + Mg_2Si + $Mg_3Mn_2Al_{18}$*	$\sim$445		$\sim$30.0	$\sim$0.1	$\sim$ 0.2
31. Liq. + $Mn_3Si_2Al_{15}$ → Al + $MnAl_6$ + Mg_2Si	$<$630		$\sim$30	$\sim$0.3	$\sim$ 0.5
32. Liq.→Al + Mg_2Si + Si + $Mn_3Si_2Al_{15}$	548		$<$ 5	$<$0.1	$\sim$ 1.2
33. Liq. + $MnAl_6$ → Al + Mg_2Si + $Mg_3Mn_2Al_{18}$ *			$<$30	$\sim$0.1	$<$ 0.2
Quinary					
34. Liq. + $(FeMn)_3Si_2Al_{15}$ → Al + $FeAl_3$ + $(FeMn)Al_6$ + Mg_2Si					
35. Liq. + $FeSiAl_5$ → Al + Si + $(FeMn)_3Si_2Al_{15}$ + $FeMg_3Si_6Al_8$					
36. Liq. + $FeSiAl_5$ → Al + Mg_2Si + $(FeMn)_3Si_2Al_{15}$ + $FeMg_3Si_6Al_8$					
37. Liq. → Al + $FeAl_3$ + Mg_5Al_8 + Mg_2Si + $Mg_3Mn_2Al_{18}$ *					

* In the review 1) this phase is given as $(MgMn)_3Al_{10}$

2.1.5 Alloying with Zirconium and Scandium

Up to now we have been dealing with alloy system with the maximum of five components. Due to difficulties in handling multicomponent systems and an even higher complexity by additions of Zr and Sc, a review of Zr and Sc containing alloys up to ternary systems will be given below.

2.1.5.1 Al-Zr and Al-Sc

Al and Zr form a peritectic diagram with the invariant peritectic reaction, $L + Al_3Zr \rightarrow Al$, at 663°C and 0.28 wt% Zr. The equilibrium Al_3Zr phase has a tetragonal $D0_{23}$ crystal lattice structure.

Al and Sc form a eutectic phase diagram with the eutectic reaction, $L \rightarrow Al + Al_3Sc$ at 655°C and 0.36 wt%. The equilibrium Al_3Sc phase has a cubic $L1_2$ crystal structure.

2.1.5.2 Al-Mg-Sc and Al-Mg-Zr

Several scientists have investigated the Al-Mg-Sc phase system in the aluminium rich corner and no ternary compounds have been found. This part of the phase diagram consists of a single-phase field of an aluminium-based solid solution, two two-phase fields, $Al + Al_3Mg_2$ and $Al + Al_3Sc$, and a three-phase field, $Al + Al_3Mg_2 + Al_3Sc$, Figure I-4 a). The invariant reaction that occurs in the concentration range 0.1 to 0.5 wt% Sc at 447°C is $L \rightarrow Al + Al_3Mg_2 + Al_3Sc$. The solubility of Mg is markedly decreased upon the addition of Sc. The mutual solid solubility of Mg and Sc in aluminium decreases considerably with temperature causing the possibility for solid solution decomposition and thereby a strong precipitation hardening and an increase of the recrystallization temperature for these alloys.

No ternary compounds have been determined in the aluminium corner of the Al-Mg-Zr phase system. A ternary eutectic is located at 450°C, $L \rightarrow Al + Al_3Mg_2 + Al_3Zr$, and thus only Al_3Mg_2 and Al_3Zr may exist in equilibrium with the aluminium solid solution, Mondolfo (1976), Petzow and Effenberg (1993). The solid solubility of Mg is not radically reduced by Zr, Mondolfo (1976).

2.1.5.3 Al-Mn-Sc and Al-Mn-Zr

No ternary phases have been found in the aluminium corner of the Al-Mn-Sc system. Thus, Al_3Sc and Al_6Mn from the binary systems are in equilibrium with the aluminium solid solution, Figure I-4 b). The invariant eutectic reaction, L→Al+Al_6Mn+Al_3Sc, occurs at 649°C, 1 wt% Sc and 1.5 wt% Mn and the solubility of Mn in Al_3Sc and of Sc in Al_6Mn is negligible. Mn seems to have no effect upon the solid solubility of Sc, while Sc decreases the solubility of Mn in aluminium. Toropova et al. (1998) claims that the solid solubility of Mn is reduced from 0.3 to 0.2 wt% at 500°C and from 1.0 to 0.55 wt% at 600°C in an Al-Mn-Sc alloy compared to a binary Al-Mn alloy.

No ternary compounds have been reported in the aluminium corner of the Al-Mn-Zr phase system, Mondolfo (1976) and Petzow and Effenberg (1993). It is thus assumed that only Al_6Mn and Al_3Zr can be in equilibrium with the aluminium solid solution.

2.1.5.4 Al-Sc-Zr

In this system no ternary compounds have been found in the aluminium corner and thus Al3Sc and Al3Zr are in equilibrium with aluminium solid solution. Figure I-4 c) shows the isothermal section of the Al-Sc-Zr system at 550°C and 600°C. Several investigators have shown that Zr and Sc can dissolve in Al_3Sc and Al_3Zr, respectively. Toropova (1998) reported that up to 40 at% Zr can dissolve in Al_3Sc and up to 20 at% Sc can dissolve in Al_3Zr without changing the lattice parameters considerably. The mutual solid solubility of Zr and Sc in aluminium is 0.06 and 0.03 wt% at 550°C and 0.09 and 0.06 wt% at 600°C, respectively.

2.1.5.5 Al-Mg-Zr-Sc

No other phases than those reported for the binary and ternary systems seem to exist in this quaternary system. It has been demonstrated that the same phase fields as for the Al-Mg-Sc system exist, Figure I-4 d), Toropova et al. (1998).

2.1.5.6 Other phase systems

Several authors have demonstrated that Zr and Sc form coarse secondary constituents with Si. In an Al-Si-Sc alloy Toropova et al. (1998) found that three intermediate phases were in equilibrium with the aluminium solid solution: Si, Al_3Sc and a new ternary V-phase (AlSiSc). Si has a negligible effect of the solubility of Sc whereas Sc markedly reduces the solubility of

Si in solid aluminium. The formation of coarse V-phase particles reduces the recrystallization resistance considerably, Toropova et al. (1998).

Few data exist on the Al-Si-Zr system, Mondolfo (1976). However, Reiso et al. (1981) found that coarse semicoherent (Al,Si)$_3$Zr-particles formed upon overageing of an Al-Mg-Si-Zr alloy, leading to poor recrystallization properties.

Limited information about the Al-Fe-Zr- and Al-Fe-Sc-phase diagrams seems to be available in the literature. However, the few existing data suggests that in the aluminium corner of these two systems, only Al$_3$Fe and Al$_3$Zr/Al$_3$Sc are in equilibrium with the aluminium solid solution, Mondolfo (1976), Petzow and Effenberg (1993).

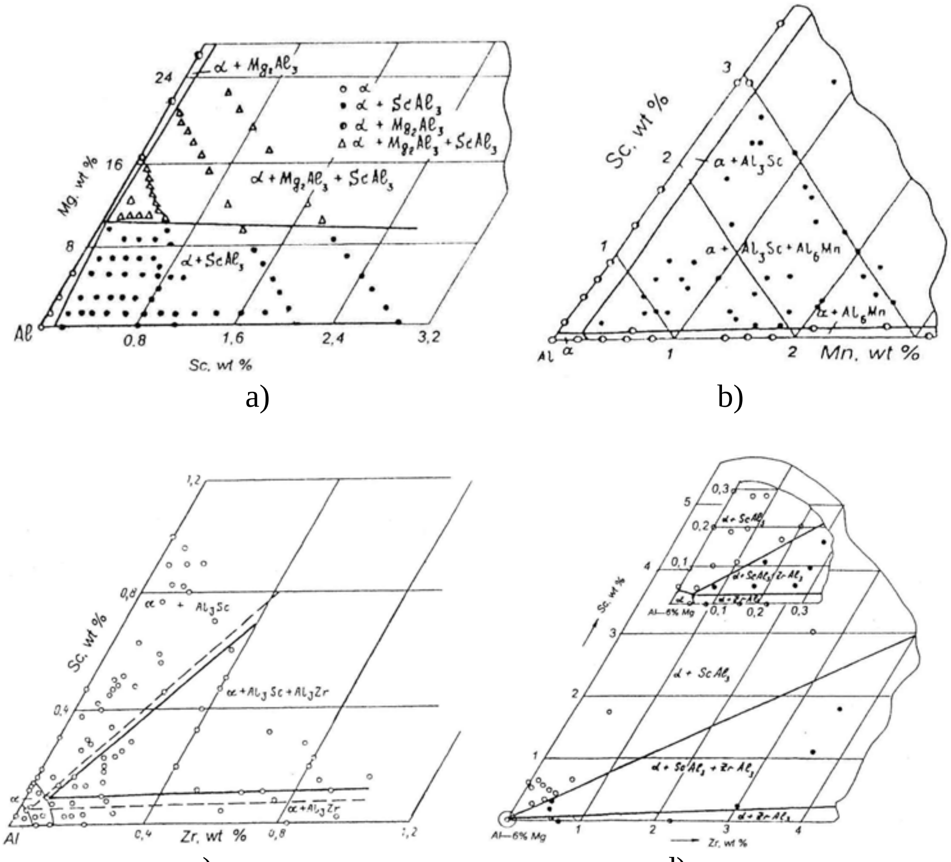

a)

b)

c)

d)

Figure I-4 *a) Isothermal section of a) the Al-Mg-Sc system at 430°C, b) the Al-Mn-Sc system at 500°C, c) the Al-Sc-Zr system at 550°C (dashed lines) and 600°C (solid lines) and d) the Al-Mg-Sc-Zr system at 500°C.*

2.2 SOLUBILITY OF ALLOYING ELEMENTS IN ALUMINIUM

As has been review in the previous paragraphs the equilibrium solubility of one alloying element can be strongly affected by the presence of another element. Usually, the mutual solid solubility of alloying elements in aluminium decreases. In multicomponent alloy systems the calculation of equilibrium concentrations becomes extremely complex and no attempts will be made here to describe this in more detail. However, Table I-4 shows an overview of how the solubility of the first alloying element (first column) is affected by the presence of a second alloying element (first row). The table is based on the information of the available phase equilibria in the Al-Mg-Mn-Fe-Si system and in addition the most important ternary systems of alloys containing Zr and Sc. It can be seen that in general the solubility is decreased or in some cases the solubility is unchanged.

Table I-4 *Solubility interactions between alloying elements in aluminium. The numbers in parentheses is a factor describing the amount of the solubility change.*

Al+	Mg	Mn	Fe	Si	Zr	Sc
Mg		↓ (0.7)	↓ (0.8)	↓ (?)	0	↓ (?)
Mn	↓ (0.3)		↓ (?)	↓ (?)	0	↓ (0.7)
Fe	↓ (?)	0		↓ (?)	0	↓ (?)
Si	↓ (?)	↓ (?)	?		↓ (?)	↓ (0.8)
Zr	↓ (?)	0	?	0		↓ (0.6)
Sc	↓ (?)	0	↓ (?)	0	↓ (0.3)	

For most elements the solubility increases with temperature. In binary alloys, this dependence is easily described by an Arrhenius relationship:

$$C_e = C_0 \cdot \exp\left(-\frac{Q}{RT}\right) \tag{I-1}$$

where C_0 and Q are constants, R is the universal gas constant and T is the absolute temperature.The solvus lines for binary Al-Mn-, Al-Fe-, Al-Zr- and Al-Sc-alloys are plotted in Figure I-5. Values for C_0 and Q are shown in Table I-5 together with solubility data collected from the literature.

Table I-5 *Solubility data of binary alloys.*

Element	**C_{max} [wt%]**	**T_{in} [°C]**	**C_0 (wt%)**	**Q (J/mole)**	**$C_{500°C}$ [wt%]**	**Reference**
Mg	17.4	450	318.3	17480	-	Mondolfo (1976)
Mn	1.82	660	2269.3 798.8	49598 48913	1.0 0.4	Phillips (1959) Mondolfo (1976)
Fe	0.052	655	17.3	44030	0.02	Phillips (1959)
Si	1.65	580	2228.7	50286	0.89	Mondolfo (1976)
Zr	0.28	660	2179.4 985.5	69503 63147	0.04 0.05	Phillips (1959) Wright and Willey (1960)
Sc	0.36	663	3573.3 836.4 884.3	72194 62643 60326	0.05 0.05 0.07	Drits et al. (1973) Berezina et al. (1987) Fujikawa et al. (1979)

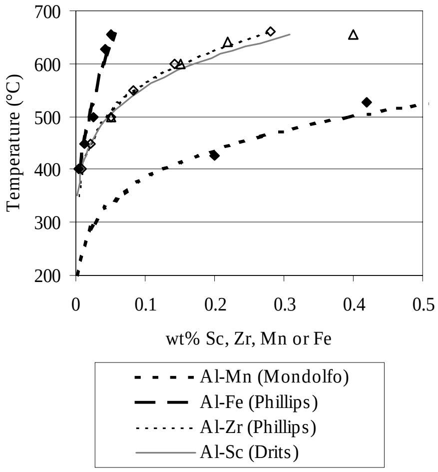

Figure I-5 *Solvus lines for binary alloys. Experimental points and lines calculated from Eq. I-1.*

2.3 NON-EQULIBRIUM CONDITIONS

Non-equilibrium conditions may be obtained if the solidification rate during casting or the quenching rate after high temperature annealing is sufficiently high. In both cases microstructures are formed which differ significantly from what may be predicted from the equilibrium phase diagrams. High solidification rates may suppress invariant reactions or the nucleation of equilibrium phases. This results in alloying elements in supersaturated solid solution in the aluminium matrix and possibility to control the microstructure by performing a proper heat treatment of the material. Commercial exploitation of these features (DC casting, twin roll casting) has been very important in the case of strength in age-hardenable alloys and the control of microstructure by dispersoids.

2.4 SUMMARY

Based on the study of the multicomponent aluminium phase equilibria it seems possible to produce microstructures of Al-Mg alloys with with improved mechanical properties by combined additions of manganese, zirconium and scandium. Several investigations have demonstrated that the commercial solidification rates obtained in modern DC casting of extrusion billets or rolling slabs are sufficient for these elements to be retained in solid solution in the aluminium matrix after casting, Toropova et al. (1998). In addition, the previous sections have shown that the elements Mg, Mn and Fe will not form any multicomponent phases with zirconium and scandium, except for Si which tends to form ternary phases with these elements. Based on the present review of the phase equilibria and experimental work reported in the literature it can be concluded that it is possible to produce Al-Mg alloys with dispersoids of Mn, Zr and Sc present as the binary compounds. Decomposition of solid solution of these elements can occur independently and is treated in more detail in Part II, Section 2.4.

3. DIFFUSION

Migration of atoms in solid state may be described by Fick's 2. law for diffusion:

$$\frac{\partial C}{\partial t} = D \cdot \nabla^2 C \tag{I-2}$$

where D is the diffusion coefficient. The diffusion coefficient depends on the direction (x-, y- and z-direction) of diffusion, the solute concentration and the temperature. However, it is usual to assume isotropic material and that D is independent of concentration. The diffusion coefficient may then be expressed in terms of an Arrhenius relationship as:

$$D = D_0 \cdot \exp\left(-\frac{Q}{RT}\right) \tag{I-3}$$

where D_0 is the diffusivity, Q is the activation energy for diffusion, R is the universal gas constant and T is the absolute temperature. Diffusion data of the most important elements in aluminium are collected from the literature and plotted in Figure I-6. The values of D_0 and Q are given in Table I-6.

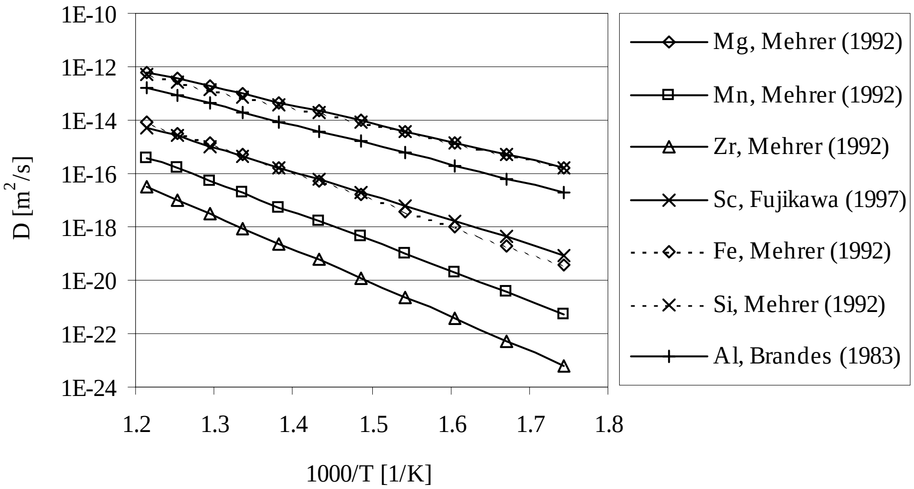

Figure I-6 *Diffusion coefficient as a function of the temperature.*

***Table I-6** Diffusion data for several elements in aluminium.*

Element	D_0 [m^2/s]	Q [kJ/mole]	$D_{500°C}$ [m^2/s]	References
Al*	$1.71 \cdot 10^{-4}$	142.3	$4.14 \cdot 10^{-14}$	Brandes (1983)
Mg	$1.24 \cdot 10^{-4}$	130.4	$1.91 \cdot 10^{-13}$	Mehrer (1992)
Mn	$1.04 \cdot 10^{-2}$	211.4	$5.39 \cdot 10^{-17}$	Mehrer (1992)
Zr	$7.28 \cdot 10^{-2}$ $6.80 \cdot 10^{-1}$	242.0 241.4	$3.03 \cdot 10^{-18}$ $3.31 \cdot 10^{-17}$	Mehrer (1992) Wagner (1961)
Sc	$5.31 \cdot 10^{-4}$	173.0	$1.08 \cdot 10^{-15}$	Fujikawa (1997)
Fe	$1.35 \cdot 10^{-2}$	192.6	$1.30 \cdot 10^{-15}$	Mehrer (1992)
Si	$3.50 \cdot 10^{-5}$	123.9	$1.48 \cdot 10^{-13}$	Mehrer (1992)

*Self diffusion

As can be seen from Table I-6 the diffusivity of Sc and Fe at 500°C is equal and approximately two orders of magnitudes lower than that of Mg and Si. Further, the diffusivity of Mn is more than one order of magnitude lower than that of Fe. According to Wagner (1961) the diffusivity of Zr equals that of Mn while the values of Mehrer (1992) is approximately 10 times lower. Brandes (1983) gives values of the self diffusion of aluminium that are close to the diffusivity of Mg and Si, Figure I-6.

4. PRECIPITATION

4.1 GROWTH OF PRECIPITATES

Decomposition of a supersaturated solid solution (α) is associated with the nucleation and growth of precipitates (β). Once nucleated, the growth of the precipitates may proceed by different mechanisms. The rate of the growth process strongly depends on the nature of the α/β-interface.

If the interface is incoherent, which means that it is a disordered phase boundary similar to a high angle grain boundary, growth is governed by several steps. First, solute atoms must be transported from the α-matrix to the α/β-interface by diffusion. Then, the atoms must jump across the interface and attach to, or rearrange into, the particle crystal lattice. The solute must also diffuse within the β-particle in order to make it homogeneous. The growth is diffusion controlled if diffusion of solute in α is slow. If the diffusion is fast, the growth rate is interface controlled, i.e. controlled by the rate at which the atoms jump across the interface. If the rate of the interface process and diffusion becomes comparable, the growth rate may be controlled by both diffusional and interface processes, Figure I-7

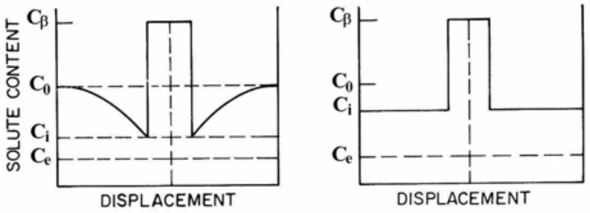

(a) Mixed (b) Interface Controlled

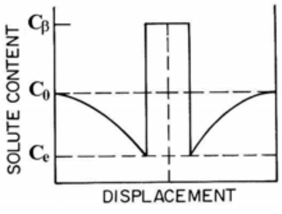

(c) Diffusion Controlled

Figure I-7 *Concentration profiles around a particle during a) mixed control, b) interface control and c) diffusion control, After Jena and Chaturvedi (1992).*

Fully coherent interfaces usually have considerably lower mobility than incoherent interfaces. If two phases with the same crystal structure are separated by a coherent interface, the interface may migrate by normal lattice diffusion. In this case there is no need for any interface reactions. Regarding semicoherent interfaces, the same situation arises provided that misfit dislocations can climb by vacancy creation or annihilation. A different situation arises if the two phases have different crystal lattice structures. It has been argued that growth of such an interface is difficult in the direction perpendicular to the surface because formation of high-energy interstitials is improbable, Figure I-8 a) and b). However, the growth rate may increase if the so-called ledge mechanism is operating, Figure I-8 c). If the interface contains several ledges, i.e. BC, DE, normal to the facets AB, CD, EF, atoms will be able to transfer more easily across the ledges than the facets, and the growth is then determined by the transverse migration of the ledges. It is thought that the rate at which the ledges migrate across the planar facets is controlled by how fast diffusion occur to and from the ledges. However, problems in nucleating new ledges may often lead to some degree of interface control when the interface advances perpendicular to itself.

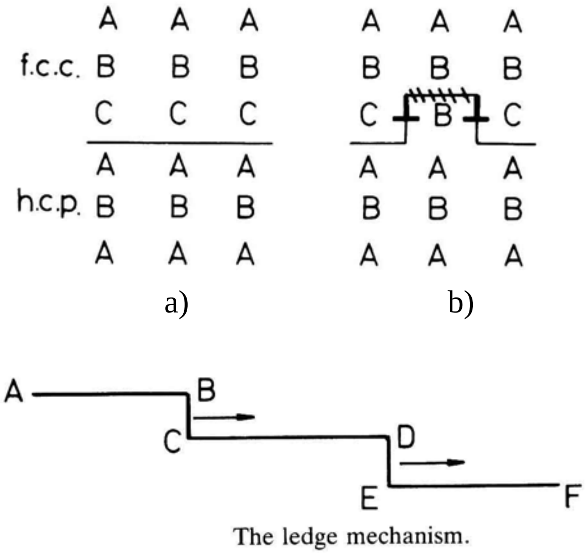

a) b)

c)

Figure I-8 *a) Formation of a high energy interstitial is difficult during migration of a coherent interface separating two phases with different lattice structures, b) Migration by the ledge mechanism. After Porter and Easterling (1992).*

Since diffusion is by far the most probable controlling factor in the growth of precipitates it will be discussed in more detail in the following. We consider radial growth of spherical or sylindrical particles of radius R and thickening of plates of thickness 2R, Figure I-9. In diffusion controlled growth the composition of the matrix at the interface attains the minimum possible concentration, C_e, which is the composition of α in equilibrium with β. C_β and C_m are the composition of the particle and the matrix away from the particle, respectively, Figure I-7 c).

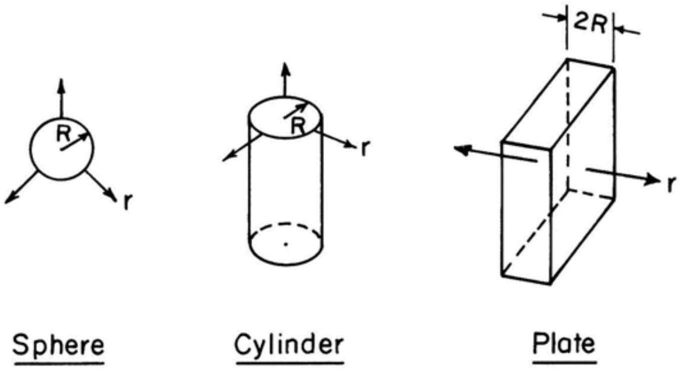

a) b) c)

Figure I-9 *Growth of spherical, cylindrical and plate-shaped particles. After Jena and Chaturvedi (1992).*

The concentration profile ahead of the growing particle is then described by $C = f(r)$ where r is the displacement along the growth direction. The mass balance of solute atoms per unit area across the interface must be fulfilled:

$$\left(C_\beta - C_e\right)\cdot\left(\frac{dr}{dt}\right)_{r=R} = D\cdot\left(\frac{\partial C}{\partial r}\right)_{r=R} \tag{I-4}$$

The kinetics of diffusion controlled growth of a particle is described by Equation I-1 which take the following form

$$\left(\frac{\partial C}{\partial t}\right) = D\cdot\left[\left(\frac{\partial^2 C}{\partial r^2}\right) + \frac{(j-1)}{r}\cdot\left(\frac{\partial C}{\partial r}\right)\right] \tag{I-5}$$

Here, j=3 for spherical particles, j=2 for cylidrical particles and j=1 for plate-shaped particles. The diffusion fields is expected to be symmetrical in such a way that the concentration is independent of the spherical coordinates θ and ϕ (j=3) or the cylindrical coordinates θ and z (j=2). Thus, the concentration is only dependent on the coordinate r in the diffusion field for all three geometries.

For a spherical particle, the boundary conditions are, see Figure I-7 c):

$$\begin{aligned} &C(r=R,t)=C_e \quad 0<t\leq\infty \\ &C(r,t=0)=C_0 \quad r\geq r_0 \\ &C(r=\infty)=C_0 \quad 0\leq t\leq\infty \end{aligned} \tag{I-6}$$

The stationary interface approximation (Whelan (1969)) leads to the following solution of Eqs. I-5 and I-6:

$$C(r,t)=C_0+\left(\frac{R(C_e-C_0)}{r}\right)\cdot\left(1-erf\left(\frac{r-R}{2\sqrt{Dt}}\right)\right) \tag{I-7}$$

Combining Eq. I-7 with the mass balance in Eq. I-4 and rearranging, we obtain the following expression for the growth rate of the spherical particle:

$$\frac{dR}{dt}=k\cdot\frac{D}{R}+k\cdot\sqrt{\frac{D}{\pi\cdot t}} \tag{I-8}$$

where

$$k=\frac{C_0-C_e}{C_\beta-C_e} \tag{I-9}$$

C_0, C_e and C_β is defined in Figure I-7 c). Integration of Eq. I-8 is not straightforward but it can be shown that this equation is satisfied by the following expression (Jena and Chaturvedi (1992)):

$$R=2\alpha\sqrt{Dt} \tag{I-10}$$

Here is α defined as:

$$\alpha = \frac{k}{2\sqrt{\pi}} + \sqrt{\frac{k}{2}\left(1 + \frac{k}{2\pi}\right)} \tag{I-11}$$

4.2 COARSENING OF PRECIPITATES

In precipitation-hardenable alloys the strength is directly related to the particle size of coherent precipitates that are formed. Another important feature of small particles is to retard recrystallization. It is therefore very desirable to inhibit further growth of particles after the initial formation in order to maintain high-temperature strength and recrystallization resistance. The modern theory of particle coarsening was first developed by Lifshiftz and Slyozov (1961) and Wagner (1961) (the LSW-model) and further developed by Ardell (1972) (the modified LSW-model (MLSW)).

After the formation and growth of second-phase particles the volume fraction approaches the volume fraction that one would predict from the phase diagram using the lever law. After this time, the growth does not stop, but proceeds by a process in which the larger particles grow at the expense of smaller ones. The driving force for this process is the reduction in the surface area of the particles in order to reduce the total energy of the system ($E_{surface}=A\gamma$).

By taking the size distribution of the particles into account and assuming that the particles are spherical and coherent and that the coarsening is diffusion controlled, the LSW-model arrives at the following coarsening equation:

$$\bar{r}^3 = \bar{r}_0^3 + \frac{8\gamma D C_e V_m^2 t}{9RT} \tag{I-12}$$

which gives the mean particle radius $\bar{r}$ at time t. $\bar{r}_0$ is the original mean particle radius at onset of coarsening, γ is the surface energy of the particle-matrix interface, D is the diffusion coefficient of solute in the matrix, C_e is the concentration of solute in the matrix in equilibrium with a particle of infinite size, V_m is the molar volume of the particle , R is the universal gas constant and T is the absolute temperature. Derivation of this equation can be found in Lifshiftz and Slyozov (1961) or Wagner (1961) and simplified treatment of the problem is given in Verhoven (1975).

Note that in order to predict the particle size after a given time at a certain temperature, values of the diffusion coefficient, the interfacial energy, and the equilibrium concentration has to be known. D is not necessarily simply equal to that for the diffusion of solute in the matrix because the growing particle may be subjected to certain diffusional effects, such as particle shape effects, volume effects and preferred diffusion paths. However, D can be replaced by an effective diffusion coefficient, D_{eff}, if such effects play a rule, Ardell (1972). Furthermore, values of γ are very often unknown, but reliable estimates can usually be obtained from Eq. I-12 if the other coefficients are accurately determined. Finally, the equilibrium concentration, C_e, is often also unknown, especially for multicomponent alloy systems and when dealing with metastable precipitates. In binary alloys C_e for equilibrium phases is easily determined from the binary phase diagrams, Ardell (1972).

5. DEFORMATION

5.1 OVERVIEW OF DEFORMATION MECHANISMS

During a material's lifetime it may undergo plastic deformation several times, either during processing of a product to a given shape or if the component is stressed during use. Thus, an ideal material should have a low resistance to forming and a high resistance to unwanted deformation during use.

Plastic deformation is carried out by the interaction between three main types of mechanisms: sliding of grain boundaries, diffusion of vacancies and the motion of lattice dislocations, Blum (1993). Grain boundary sliding is not sufficient for an overall shape change and needs support by additional processes in order to fulfill the requirements of grain compatibility. Diffusional flow of vacancies results in the socalled Nabarro-Herring creep (bulk diffusion) or Coble creep (grain boundary diffusion). Diffusional creep has a weak stress sensitivity and a strong dependence on grain size and thus its importance in metals is usually only when the grain size is small and the stress is low, Blum (1993) and Oikawa and Langdon (1985). However, a large amount of experimental data proves that dislocations are the most important carriers of plastic deformation, Blum (1993) and Oikawa and Langdon (1985). The dislocation motion can proceed by glide, cross slip and climb and the rate of plastic deformation is proportional to the density of the dislocation current, described by the basic Orowan equation:

$$\dot{\varepsilon} = \phi \cdot \rho_{mob} \cdot v_{mob} \cdot b \qquad \text{(I-13)}$$

where ϕ is a geometrical factor equal to the inverse of the Taylor factor for isotropic polycrystals, ρ_{mob} is the density of mobile dislocations, v_{mob} is the average velocity of the mobile dislocations and b is the Burgers vector.

5.2 MICROSTRUCTURAL DEVELOPMENT

In general, plastic deformation involves work hardening and dynamic recovery which may both be explained by a series of dislocation processes. While work hardening is predominant at low temperatures, dynamic recovery occurs at higher temperatures.

Work hardening is defined as a continuous increase in the flow stress as dislocations are being generated and stored at obstacles during straining of the material. A gradual refinement of the microstructure is usually observed and in general an inhomogeneously spatial distribution of dislocations develop. As the stress and strain increase, dislocations interact and may be accumulated into cell boundaries or subgrain boundaries. If the material is allowed to reach saturation the deformation may proceed under steady state condition, i.e. the rate at which dislocations generate is balanced by the rate at which they accumulate by dynamic recovery.

It should be emphasised that in the presence of solute atoms and small particles recovery rate is decreased (solute pinning and particle pinning) and the formation of a subgrain structure is effectively inhibited.

At low temperatures the material usually fractures before it saturates. However, increasing the temperature gives rise to thermal activation of dislocation migration and hence steady state deformation may occur at lower stresses. In high temperature deformation, the flow stress becomes more or less independent of the strain and dynamic recovery processes will then determine the operating mechanisms for the deformation process. Usually, hot working is performed in the temperature range $0.6T_m$ and up to temperatures close to the melting point or the solidus temperature (T_m=melting point). At these temperatures the deformation mechanisms are similar to those taking place in creep.

5.3 DYNAMIC RECOVERY AND DYNAMIC RECRYSTALLIZATION

Dislocations can move by various mechanisms such as cross slip, climb and glide. If these are dependent upon one another, the slowest mechanism is rate controlling and requires the highest activation energy. If the recovery rate is slow then the activation energy for the deformation is determined by the migration rate of the dislocations. This is the case for low stacking fault energy materials (e.q. Cu) in which cross slip is difficult. This may result in dynamic recrystallisation when a certain critical deformation condition is reached. Contrary, if the recovery rate is fast, then the activation energy for the deformation is determined by the rate at which the dislocations cross slip or climb. This is the case for high stacking fault energy materials (e.q. Al) in which high temperature deformation may proceed entirely by dynamic recovery. Depending on the influence upon cross slip, the activation energy for deformation is more or less equal to the activation energy for self diffusion.

The importance of the stacking fault energy is to determine the extent to which unit dislocations dissociate into partial dislocations. Such dissociation, which is promoted by a low value of SFE, hinders the climb and cross slip of dislocations. The two partial dislocations have to be contracted into an unextended form before cross slip may occur. The closer the partials are separated, the easier it is to contract them and as the distance between the two partials is inverse proportional to the energy of the stacking fault, cross slip becomes more easy with increasing stacking fault energies.

5.3.1 Pure metals

In a pure metal of a high stacking fault energy, such as aluminium, cross slip readily occurs and it is therefore assumed that the rate controlling reaction is thermal activation associated with the short range interactions between mobile dislocations and stored dislocations. In other words, this involves the dragging of joggs or climb of jogged dislocations, Nes (1997). This is what is observed at intermediate stresses during creep or the so-called power law creep regime, Figure I-10, Oikawa and Langdon (1985). With increasing stress the power law breaks down and an exponential relationship describes the creep rate. This indicates that a process of thermally activated glide takes over as a rate controlling process, Blum (1993).

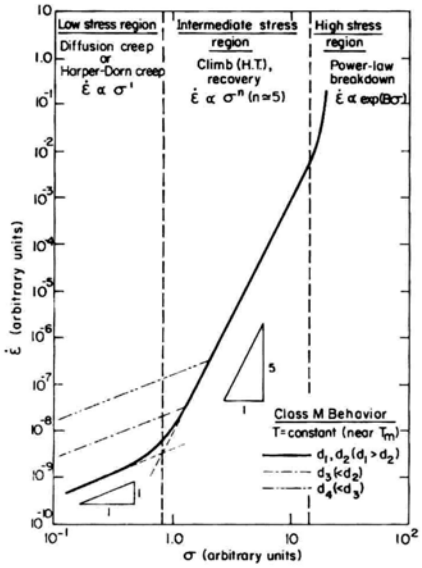

Figure I-10 *Creep rate versus stress for a pure metal. From Oikawa and Langdon (1985).*

5.3.2 The effect of solute atoms

Solute atoms are obstacles to dislocation motion and result in solute hardening. The solute atoms are regarded as immobile at low temperatures while their diffusive mobility increases drastically at high temperatures and are effectively attracted to dislocations. The dislocation glide velocity is reduced as they have to drag along with the solute atmospheres (solute pinning). Figure I-11 a) shows how the dislocation velocity varies with the effective stress in situations with and without solute pinning. The result of solute pinning of dislocation is a viscous glide regime at intermediate stresses, usually termed class A behaviour (A=Alloy), Figure I-11 b). At lower stress levels a transition to so-called class M behaviour (M=pure Metal) may occur because glide and climb are sequential processes and the slower mechanism is rate controlling. At higher stresses, the transition to class M behaviour is associated with dislocations breaking away from the solute atmospheres and thus making climb rate controlling again, Oikawa and Langdon (1985).

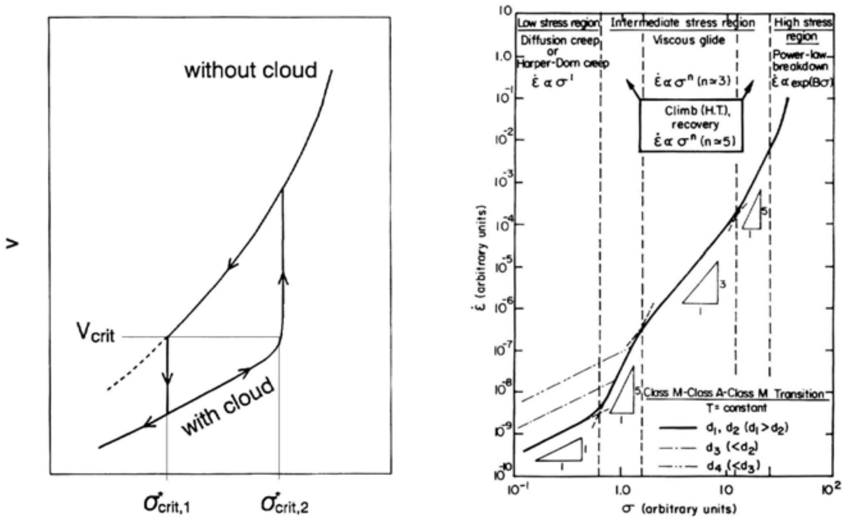

a) b)

Figure I-11 *a) Schematic description of dislocation velocity as a function of the effective stress with and without dragging of solute clouds. Blum (1993). b) Creep rate versus stress for a solid solution material. Oikawa and Langdon (1985).*

5.3.3 The effect of particles

In the presence of second phase particles, the creep rate may be reduced drastically, and in hot working the applied stress may be increased in order to give a certain plastic deformation of the material. The reason for this is the pinning effect of the particle obstacles and consequently the effective stress is decreased (σ-σ_o). The dislocations may pass the obstacles by cutting or climb. In the high stress regimes the particle strengthened material exhibits the same creep behaviour as the matrix without particles, i.e. deformation is controlled by climb of dislocations over the particles. However, at higher temperatures and lower stresses, a threshold stress is observed below which creep is suppressed. Such threshold stresses are often observed in materials with incoherent particles in which a strong interaction between dislocations and incoherent interfaces occurs. If the particles are coherent the threshold stress is reduced or may even be absent. Figure I-12 a) shows a schematic creep behaviour of a particle strengthened material and Figure I-12 b) shows the effect of Al_6Mn dispersoids in an Al-Mg alloy producing Orowan stresses.

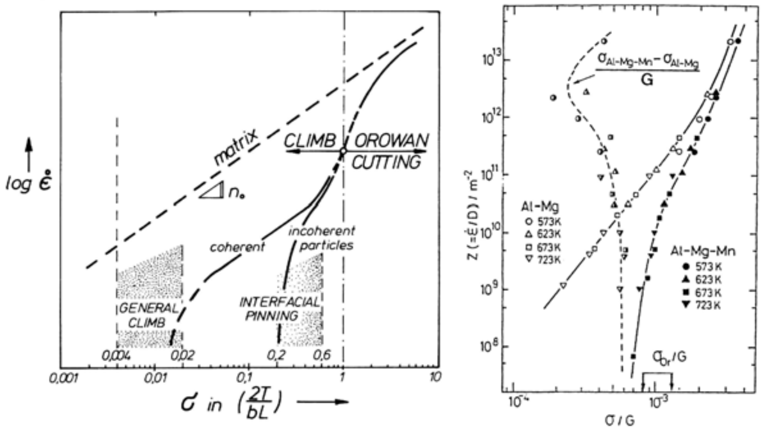

a) b)

Figure I-12 *a) Schematic creep behaviour in particle strengthened materials. . Oikawa and Langdon (1985). b) The effect of Al6Mn particles on the hot deformation behaviour of an Al-Mg alloy. Nakashima et al. (1990).*

6. RECOVERY AND RECRYSTALLIZATION

6.1 STORED ENERGY

During deformation a portion of the deformation work is stored as an internal energy in the material. The stored energy is associated with the energy of the dislocations present in the grain interior or/and in cell/subgrain boundaries. Thus, the stored energy, E_D, depends on the dislocation density, ρ, and the specific subgrain boundary energy, γ_s as (Humphreys and Hatherly (1996)):

$$E_D = E_{dis} \cdot \rho + A_s \cdot \gamma_s = \alpha_1 \cdot G \cdot b^2 \cdot \rho + \alpha_2 \cdot \frac{\gamma_s}{R} \qquad \text{(I-14)}$$

E_{dis} is the energy per unit length of dislocation line, G is the shear modulus, b is the Burgers vector, α_1 is a constant of the order of 0.5, A_s is the subgrain boundary area, R is the radius of the cell/subgrain and α_2 is a constant of the order of 1.5.

6.2 RECOVERY

Recovery and recrystallization are thermally activated processes of restoring the structure after deformation. Recovery is the term referring to the changes in the properties of a deformed material, which occur prior to recrystallization. Recovery and recrystallization are competitive processes as they both are driven by the stored energy of the deformed state. In contrast to recrystallization there is no clearly identifiable beginning or end of the recovery prosess. However, it is sometimes difficult to distinguish between the two phenomena.

Recovery involves primarily changes in the dislocation structure of the material and may consist of a series of micro-mechanisms, i.e. cell formation, dislocation annihilation, subgrain formation and subgrain growth (Humphreys and Hatherly (1996)). The extent by which these mechanisms occur during annealing of a specimen depends on a number of parameters, like material, purity, strain, deformation temperature and annealing temperature. Obviously, the recovery rate is determined by the speed of which the dislocations can move in the crystal lattice. The glide of dislocations are usually so fast that the rate controlling mechanisms are cross slip or climb. After the formation of a subgrain structure, the recovery may continue by subgrain growth.

One of the most important parameters determining the rate of recovery is the stacking fault energy, γ_{SFE}, which affects the extent to which dislocations dissociate. In metals of low stacking fault energy, like copper (γ_{SFE}=78mJ/m^2) climb is difficult, and little recovery occurs prior to recrystallization. However, in high stacking fault energy materials, like aluminium (γ_{SFE}=166mJ/m^2), climb is rapid and extensive recovery may occur. Examples of this behaviour is shown in Figure I-13.

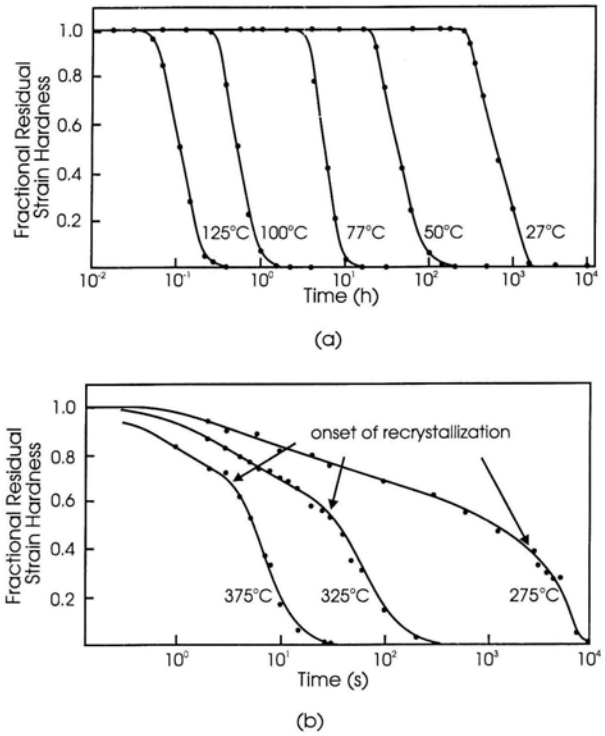

***Figure I-13** Recrystallization of copper (a) and recovery and recrystallization of aluminium (b). From Humphreys and Hatherly (1996).*

In alloys, solute elements may influence the recovery rate by changing the stacking fault energy of the material, by pinning dislocations (solute drag) or by affecting the concentration and mobility of vacancies. Hence, magnesium in solid solution tends to retard dynamic recovery.

6.3 RECRYSTALLIZATION

As opposed to recovery, which is relatively homogenous in terms of space and time, recrystallization can be divided into a nucleation and a growth event. A recrystallization nuclei is defined as “a crystallite of low internal energy growing into deformed material from which it is separated by a high angle grain boundary”, Humphreys and Hatherly (1996). For a nucleus to be viable, two requirements must be fulfilled: i) it must have a size advantage and ii) it must have a misorientation advantage. In order to be able to grow the nucleus must be larger than a critical size, δ_c, given by the Gibbs-Thomson relation:

$$\delta > \delta_c = \frac{4 \cdot \gamma_{GB}}{P_D} \tag{I-15}$$

γ_{GB} is the specific grain boundary energy and $P_D=E_D$ (Eq. I-15) is the driving pressure.

Only a very few subgrains or cells of the total amount will continue to grow into a new recrystallized grain. From numerous investigations it is clear that the nucleation of a new grain occurs in regions where a high angle grain boundary easily can form, i.e. at heterogeneities in the microstructure like grain boundaries, transition bands, shear bands or second phase particles (PSN). The topic of recrystallization nucleation will not be discussed further here.

The growth of recrystallized grains is much easier to quantify than the nucleation process and the kinetics of this process is usually analysed in terms of fraction recrystallized material. The kinetics of recrystallization will not be treated here. However, some general comments on the mobility of grain boundaries will be given below. It is generally accepted that a the growth rate, G, of a grain boundary, no matter if it is a low angle or a high angle grain boundary, can be expressed as:

$$G = M \cdot P = M \cdot (P_D - P_C) \tag{I-16}$$

where M is the mobility of the grain boundary and P is the net driving pressure. P_D is the driving pressure given by Eq.I-14 ($P_D=E_D$) and P_C is the retarding pressure due to the curvature of the new grain given by the Gibbs-Thompson relationship ($P_C=2\gamma_{GB}/R$). Hence, if the net pressure $P=P_D-P_C>0$

then growth occurs and recrystallization proceeds but if P<0 then further growth is suppressed.

Several factors affect the rate of recrystallization, for instance the feature of the deformed structure, the grain orientation, the original grain size, solute elements, deformation temperature and strain rate, the annealing conditions and the presence of particles. Only the latter effect, that of particles, will be commented here. For more details the reader is referred to literature dealing with these topics, for instance Humphreys and Hatherly (1996)

6.4 THE EFFECT OF LARGE SECOND PHASE PARTICLES

In commercial alloys second phase particles are always present and they affect the recrystallization in three ways: i) the stored energy may increase, ii) large particles may act as nucleation sites (PSN) and iii) small particles may exert a pinning effect on both small angle and high angle grain boundaries. The first two effects tend to promote recrystallization whereas the last tend to hinder recrystallization.

Some particularly important aspect can be stated concerning recrystallization in industrial alloys containing large second phase particles. Particle stimulated nucleation is a nucleation mechanism that is likely to occur in such alloys. The nucleation occurs in deformation zones formed around particles during deformation. These nucleation sites are well defined regions with a very high internal energy compared to the matrix and favourable orientation relationship for the growth of the new grain. The orientations of the recrystallization nuclei produced by PSN will be different from those produced by other recrystallization mechanisms. It is thus possible to control the recrystallization texture by controlling the amount of PSN. Finally, because the interaction of dislocations and particles is temperature dependent, PSN will only occur if the prior deformation is carried out below a critical temperature or strain rate.

The size criterion for a particle stimulated nuclei is the same as for classical nucleation, Eq. I-15. However, the size of the deformation zone, λ, is typically equal to the particle diameter, d_p, and PSN occurs if the particles have a diameter which is larger than a critical value, $d_{p,c}$:

$$d_p > d_{p,c} = \frac{4 \cdot \gamma_{GB}}{3 \cdot P_D} \qquad \text{(I-17)}$$

6.5 THE EFFECT OF SMALL SECOND PHASE PARTICLES

Small second phase particles will exert a restraining force on a moving grain boundary. This will have an effect both on a moving low angle boundary during recovery and on the movement of a high angle boundary during recrystallization and grain growth. The restraining pressure on a grain boundary, the so-called Zener drag (Smith (1948)), may be expressed as:

$$P_Z = \frac{3 \cdot \gamma_{GB} \cdot f}{2 \cdot r} \qquad \text{(I-18)}$$

Here, γ_{GB} is the grain boundary energy, r is the particle radius and f is the volume fraction of particles. However, it is assumed that the grain boundary is planar and rigid and that the particles are randomly distributed in the microstructure. Several authors (Nes et al. (1985), Hillert (1988) and Doherty et al. (1989)) have attempted more rigorous calculations of the Zener drag, but these more sophisticated calculations do not lead to relationships which differ significantly from Eq. I-18.

The presence of the Zener drag affects both the nucleation and growth of new recrystallized grains through a reduction in the net driving pressure. First, the critical size of the nucleus increases (Eq. I-15) and thereby making the nucleation more difficult. PSN is also suppressed by an increase in the critical particle size which is required for nucleation (Eq. I-17). Second, the growth rate of a growing grain is reduced (Eq. I-16). Thus, it is possible to control the grain size of commercial alloys by controlling the amount of PSN and dispersoids in thermo-mechanical processing of the material.

REFERENCES

Ardell, A.J. *The effect of volume fraction on particle coarsening: theoretical considerations,* Acta Met. vol. 20, January (1972), p. 61.

Altenpohl, D., Aluminium und Aluminiumlegierungen, Springer-Verlag, Berlin, 1965.

Barlock, J.G. and Mondolfo, L.F., *Structure of some aluminium-iron-magnesium-manganese-silicon alloys*, Z. Metallkunde, vol. 66, nr. 10 (1975), p.605.

Berezina, A.L., Volkov, V.A., Domashnikov, B.P. and Chuistov, K.V., Metallfizika, no. 5 (1987), pp. 43-47.

Blum, W., *High-temperature deformation and creep of crystalline solids*, in Materials Science and Technology, Plastic deformation and fracture of materials, eds. Cahn, R.W. , Haasen, P. and Kramer, E.J., VCH Publishers, Weinheim, Germany, 1993.

Brandes, E.A., Smithells Metals Reference Book, Butterworths, 1983.

Doherty, R.D., Li, K., Kashyap, K. Rollett, A.R. and Srolovitz, D.J., Proc. 10th Risø Symp., eds. Bilde-Sørensen et al., Risø, Denmark, 1989, p. 31.

Drits, M.E., Kadaner, E.S., Dobatkina, T.V. and Turkina, N.I., Izv. Akad. Nauk SSSR, Met. no.4, 1973, pp. 213-217.

Fujikawa, Sugaya, Takei, Hirano, *Solid solubility and residual resistivity of scandium in aluminium,* Journal of the Less-Common Metals, vol 63 (1979), pp. 87-97.

Hatch, J.E. (ed.), *Aluminium: Properties and physical metallurgy*, ASM, Metals Park, Ohio, 1984.

Hillert, M., Acta Met., vol. 36 (1988), p. 3177.

Humphreys, F.J. and Hatherly, M., Recrystallization and related annealing phenomena, Pergamon Press, Oxford, 1996.

Jena, A.K. and Chaturvedi, M.C., *Phase transformation in metals*, Prentice Hall, New Jersey, 1992.

Lifshiftz, I.M. and Slyozov, V.V., *The kinetics of precipitation from supersaturated solid solutions*, J. Phys. Chem. Solids, vol.19, nos.1/2 (1961), p.35.

Marthinussen, J.I., DNV specifications, private comunication, 2000.

Mehrer, H., *Diffusion in solid Metals and alloys*, ed. Neumann, G., vol. 26, Springer.Verlag, 1992, pp. 151.

Mondolfo, L.F. *Aluminium Alloys: Structure and properties*, Butterworths, London, 1976.

Mondolfo, L.F., *Manganese in aluminium alloys*, The Manganese Centre, 1977, ISBN 2901109-01-2.

Nakashima, H., Iwasaki, K., Goto, S. and Yoshinaga, H., *Combined effect of solution and dispersion hardenings at high temperatures*, Met. Trans. JIM, vol. 31, nr. 1 (1990), p. 35.

Nes, E., *Modelling work hardening and stress saturation in fcc metals*, Sintef report, STF24 S97525, Trondheim, 1997.

Nes, E., Ryum, N. and Hunderi, O., *On the Zener drag*, Acta Met., vol.33, no. 1 (1985), p. 11.

Oikawa, H. and Langdon, T.G., *The creep characteristics of pure metals and metallic solid solution alloys*, in Creep of Metals and Alloys, eds. Evans, R.W. and Wilshire, B., The Institute of Metals, Swansea, 1985.

Petzow, G. and Effenberg, G., *Ternary alloys, A comprehensive compendium of evaluated constitutional data and phase diagrams*, VCH Publishers, New York, 1993.

Phillips, H.W., *Annotated equilibrium diagrams of some aluminium alloys*, The Institute of Metals, London, 1959.

Phragmen, G., *On the phases occuring in alloys of aluminium with copper, magnesium, manganese, iron and silicon*, J. Inst. Metals, vol. 77 (1950), p.489.

Porter, D.A. and Easterling, K.E., *Phase transformations in metals and alloys*, Chapman and Hall, London, 1992.

Ratchev, P., Verlinden, B., Van Houtte, P. and De Smet, P., *Hot ductility of an Al-4wt%Mg-0.5wt%Cu alloy*, Mat. Sci. Eng., vol. A222 (1997), p. 189-196.

Reiso, O., Westengen, H. and Auran, L., *Effect of Si additions on precipitation and recrystallization in Al-0.18 wt%Zr alloys*, 7th International Light Metals Congress, Leoben/Vienna, 1981.

Samson, S., *The crystal structure of the phase* β Mg_2Al_3, *Acta. Cryst*., vol. 19, (1965), p. 401.

Smith, C.S., Trans. Met. Soc. AIME, vol. 175. (1948), p. 15.

Toropova, L.S., Eskin, D.G., Kharakterova, M.L. and Dobatkina, T.V., *Advanced aluminium alloys containing scandium, Structure and properties*, Gordon and Breach Science Publishers, Amsterdam, 1998.

Verhoven, J.D., *Fundamentals of physical metallurgy*, John Wiley & Sons, New York, 1975.

Wagner, C., *Theorie der Alterung von Niederschlagen durch Umlosen, Z. Elektrochemie*, vol. 65, nr. 7/8 (1961), p. 581.

Whelan, M.J., Mat.Sci.J., vol. 3 (1969), p. 95.

Wright and Willey, *Aluminium binary equilibrium diagrams*, Technical Paper No. 15, Alcoa Research Laboratories, 1960.

PART II

MICROSTRUCTURES OF CAST AND HEAT TREATED MATERIAL

1. INTRODUCTION

The physical and mechanical properties of the material is determined by the microstructure developed during casting and the further steps in the processing, such as heat treatment and deformation or thermomechanical treatment.

A cast structure may have a very heterogeneous microstructure with mechanical properties that can be crucial in subsequent deformation processes. Before extrusion, it is therefore usual to give the material a certain heat treatment in order to homogenize the microstructure. Heat treatment prior to hot rolling is also performed but this step is not as critical as it is for the extrusion process.

Usually the term ”homogenization” is used for the industrial heat treatment practice of extrusion ingots. For aluminium alloys containing transition elements this term will be rather deceptive. During heat treatment a range of different microstructural processes occurs, some of which could be termed homogenization while other could be termed heterogenization.

The main reason why heat treatment is carried out is to improve and control the mechanical properties such as strength, deformability, extrudability and ductility by:

- Removing residual stresses
- Homogenisation of segregations
- Dissolution of low melting primary constituents
- Spheriodising and coarsening of thermally stable primary constituents
- Precipitation of dispersoids

The present investigation has focused on the extrudability of Al-Mg alloys and hence the cast structure has been investigated with respect to primary constituents and segregations. Furthermore, the decomposition of Mg, Mn, Zr and Sc was studied during continuous heat treatment and under isothermal conditions in a range of different temperatures. Special attention was given to the identification of the type of dispersoids.

2 THEORY AND BACKGROUND

2.1 ELECTRICAL RESISTIVITY

Electrical resistivity measurements have been proven to be a useful method in order to get an easy, quick and exact estimate of the concentration of alloying elements in solid solution. Usually, the electrical resistivity depends both on temperature and solute concentration and may be expressed as, Altenpohl (1965):

$$\rho = \rho_p(T) + \rho_{res}(c_1, \ldots. c_n) \qquad \text{(II- 1)}$$

Here ρ is the measured resistivity, $\rho_p(T)$ is the temperature dependent resistivity of the pure metal matrix and $\rho_{res}(c_1, \ldots. c_n)$ is the residual resistivity caused by solute element numbers 1 to n. The dependence of temperature and concentration on resistivity as reported in the literature, seems both to be a linear type of relationship (Altenpohl (1965), Hatch (1984)) The change in resistivity with temperature of pure aluminium is aproximately 0.0115 μΩ·cm/°C in the range –160 to 300°C. The change in resistivity with temperature is essentially independent of chemical composition, Hatch (1984).

The effect of a solute element is stronger in solid solution than if it is present in second phase particles. If the electrical resistivity is measured at a constant temperature of 20°C then Eq. II-1 may be written as (Olafsson et al. (1996), Hatch (1983)):

$$\rho = \rho_{20^\circ C} + \sum_i \left(c_i' \cdot \rho_i^{ss} + c_i'' \cdot \rho_i^{oss} \right) \qquad \text{(II- 2)}$$

where $\rho_{20°C}$ is the resistivity of pure metal at 20°C, c'_i and c''_i are the concentration of element i in solid solution and out of solid solution, respectively, for elements i=1 to n and ρ_i^{ss} and ρ_i^{oss} are the charactheristic resistivities (resistivity increase per wt% solute) of element i in solid solution and out of solid solution, respectively. Values are given in Table II-1. Note that these values are only valid for pure binary alloys. The contributions from two or more elements are only additive if the elements form only binary intermetallic compounds, and individually go into solid solution. In this case, a change in resistivity of the alloy after heat treatment may be written as Eq.II-3:

$$\Delta\rho_{Alloy} = \sum_i \Delta\rho_i \tag{II- 3}$$

where $\Delta\rho_i=\rho-\rho_0$. Here $\Delta\rho_i$ is the change in resistivity due to element i, ρ and ρ_0 is the resistivity after and before heat treatment, respectively. If more than one of the alloying elements form a compound together with aluminium, then the resistivity may be reduced.

Table II-1 *Characteristic resistivities of some aluminium alloying elements in solid solution (ρ^{ss}) and out of solid solution (ρ^{oss}). After Hatch (1984).*

Element	Max. solubility in a binary alloy (wt%)	ρ^{ss} (μΩ·cm/wt%)	ρ^{oss} (μΩ·cm/wt%)
Magnesium	14.9	0.54	0.22
Manganese	1.82	2.94	0.34
Zirconium	0.28	1.74	0.044
Scandium$^{1)}$	0.35	2.05	-
Iron	0.052	2.56	0.058
Silicon	1.65	1.02	0.088
Titanium	1.0	2.88	0.12

$^{1)}$Jo and Fujikawa (1993).

2.4 DECOMPOSITION OF ELEMENTS IN SOLID SOLUTION

2.4.1 Magnesium

The precipitation behaviour of Al-Mg alloys has been extensively investigated and today it is well established that a decomposition results in a whole range of different precipitates depending on the applied ageing temperature. The precipitation sequence can be written (Nozato and Ishihara (1980), Nebti et al. (1995), Starink and Zahra (1998)):

$$\alpha_{ss} \rightarrow GP-zones \rightarrow \beta'' \rightarrow \beta' \rightarrow \beta \tag{II- 4}$$

α_{ss} is the aluminium matrix with magnesium in supersaturated solid solution with a cubic fcc structure. The lattice parameter of pure aluminium is a=0.405 nm, with an increasing value as the magnesium concentration increases.

GP-zones (Gunier-Preston zones) are solute-rich clusters with a thickness of only a few atomic planes. The clusters develop to thin plates elongated along [100]-directions (Sato et al. (1982), Osamura and Ogura (1984)).

β'' is an ordered $L1_2$-type structure with the composition Al_3Mg (Sato et al. (1982), Nebti et al. (1995))

β' is a semicoherent hexagonal intermediate phase with the chemical composition of approximately Al_3Mg_2. Its lattice parameters are a=1,002Å and c=1,636Å (Starink and Zahra (1998), Nebti et al. (1995)).

β is the equilibrium phase Al_3Mg_2 with a f.c.c. unit cell structure and the lattice parameter a=2,824Å (Samson (1965), Starink and Zahra (1998))

Several calorimetric studies have confirmed the precipitation sequence Eq. II-3 (Nozato and Ishihara (1980), Osamura and Ogura (1984), Nebti et al. (1995), Starink and Zahra (1998)). The different particles in the sequence are stable at different temperature intervals. Figure II-1 shows the temperature limits for the precipitates. The figure summarizes a number of results collected from the literature.

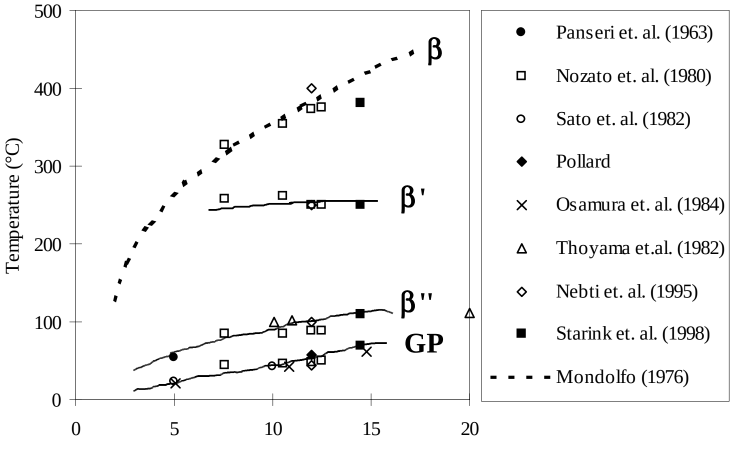

Figure II-1 *Solvus temperatures for the stable and the metastable phases in the Al-Mg phase system.*

2.4.2 Manganese

In aluminium-manganese alloys manganese decomposes directly to the equilibrium orthorombic Al_6Mn-phase with the lattice parameters a=0.75518 nm, b=0.64978 nm and c=0.88703 nm at temperatures above 550°C. Below 550°C the existence of a metastable bcc G-phase ($Al_{12}Mn$) and also a G'-phase is reported (see for instance Nagahama and Miki (1974, Chen and Morris (1984). However, the presence of iron and silicon may change the structure and/or the composition of the precipitated phase. The equilibrium Al_6Mn phase can dissolve up to 50% Mn but the structure does not change considerably. Depending upon the iron content, the lattice parameters will lie between that of Al_6Fe (a=0.7440 nm, b=0.6464 nm and c=0.8779) and that of Al_6Mn. If silicon is present, α-AlMnFeSi is the most probable phase to be formed. The α-phase is cubic with a lattice parameter a=1.268 nm. However, the Mn and Fe content can vary considerably and depends upon the overall concentration of the alloy (Dons (1984), Hanssen et al (1995)).

2.4.3 Zirconium and scandium

Zirconium decomposes according to the following precipitating sequence, Ryum (1969):

$$\alpha_{ss} \rightarrow \beta' - Al_3Zr \rightarrow \beta - Al_3Zr \qquad \text{II-5}$$

where α_{ss} denotes the aluminium matrix with Zr in supersaturated solid solution, β'-Al_3Zr is a metastable cubic phase with a Ll_2 structure and a lattice parameter of a=0.408 nm (Nes (1972)). The β- Al_3Zr is the tetragonal equilibrium phase with a $D0_{23}$ structure and lattice parameters a=0.401 nm and c=1.732 nm (Villars and Calvert (1985)). The $L1_2$-structure is fully coherent while the $D0_2$-structure is incoherent with the aluminium matrix. The Ll_2-structure is very stable, most likely due to a very low misfit (δ=0.74%) in the lattice parameters between the precipitate and the pure aluminium matrix and a correspondingly low surface energy. At high temperatures or long ageing times the metastable phase can be transformed and replaced by the equilibrium phase and thus the coherency is lost. The strength contribution from these particles will then decrease and the resistance against recrystallization is reduced.

In the case of scandium, this element decomposes directly to the equilibrium cubic Al_3Sc phase with a $L1_2$-type structure and a lattice parameter of a=0.410 nm (Villars and Calvert (1985), Toropova et al. (1998)). This $L1_2$-structure is fully coherent with a pure aluminium matrix, the misfit (δ) beeing approximately 1.2%. This facilitates homogeneous nucleation and slow growth of fine, uniformly distributed particles. In binary Al-Sc alloys, the decomposition seems to start at 250°C irrespective of Sc concentration and is completed at temperatures around 400°C after annealing for 1 to 2 hours. At temperatures above approximately 400°C the Al_3Sc-particles coarsen and tend to loose coherency. (Toropova et al. (1998))

The nucleation of the metastable Al_3Zr precipitates is strongly dependent on the purity of the alloy. The presence of impurities like iron, silicon, titanium etc. suppresses discontinuous precipitation and promotes homogeneous precipitation (Westengen et al. (1981), Sato et al. (1996). Furthermore, slow heating or low holding temperature also promotes homogeneous precipitation. Discontinuous precipitation occurs behind a moving grain boundary which enhances the grain boundary diffusion of solute atoms, and this is most likely to happen in a clean aluminium matrix at high temperatures. If the aluminium matrix contains solute atoms which can act as potent nucleation sites, homogeneous nucleation is favourable through lattice diffusion, and even more pronounced at small heating rates at which the condition for the formation of a nuclei is improved.

Thus, the similarity of crystal structure (lattice parameter) and the coherency between metastable Al_3Zr and equilibrium Al_3Sc are features that should govern a relatively homogenous nucleation of these particles. It has also been proven that Al_3Sc is very stable at higher temperatures while Al_3Zr tends to coarsen due to the transformation into the equilibrium incoherent thetragonal structure.

Furthermore, the lattice parameter of the aluminium matrix increases with an increasing concentration of magnesium atoms in solid solution resulting in an even lower misfit (δ) between the particles and the matrix. Drits et al. (1981) found that in an Al-6.5%Mg-0.3%Sc alloy the lattice misfit between the cubic Al_3Sc phase and the Al-Mg matrix is reduced to 0.56% (from 1.2%). This resulted in an increase in the stability of the particles and conservation of the coherency to higher temperatures. It also promotes homogeneous nucleation of precipitates. The corresponding lattice misfit for the cubic Al_3Zr-phase in a Al-6.5Mg alloy is reduced to 0.07% (from 0.74%) which is even lower than for the cubic Al_3Sc-phase. It can be concluded that Al-Mg alloys are particularly suitable for alloying with Zr and Sc.

3 EXPERIMENTAL PROCEDURE

3.1 ALLOY SELECTION AND DC-CASTING

The main goal of the present work was to identify the effect of additions of manganese, zirconium and scandium to Al-Mg alloys. It was therefore decided to use a chemical composition based on the traditional AA5083 alloy. This alloy has been used in a whole range of commercial applications for years and it has, more or less, become a reference for new commercialized alloys. Table II-2 gives the chemical analysis of the five alloys investigated in this work. The alloys will be designated as follows: 1) AlMg, 2) AlMgZr, 3) AlMgMn, 4) AlMgMnZr and 5) AlMgMnZrSc.

Table II-2 *Chemical analysis of investigated alloys.*

Element	AlMg	AlMgZr	AlMgMn	AlMgMnZr	AlMgMnZrSc
Al	bal	bal	bal	bal	bal
Mg	4.52	4.45	4.62	4.55	4.53
Mn	0.02	0.06	0.61	0.74	0.76
Zr	-	0.17	-	0.15	0.15
Sc	-	-	-	-	0.09
Fe	0.15	0.15	0.14	0.14	0.14
Si	0.02	0.02	0.03	0.03	0.03
Ti	0.03	0.02	0.03	0.03	0.03
Ni	0.01	0.02	0.01	0.02	0.02
Ga	0.01	0.01	0.01	0.01	0.01
Other	0.02	0.02	0.02	0.02	0.02
Each	<0.01	<0.01	<0.01	<0.01	<0.01

All five alloys contain approximately the same amount of magnesium as the main alloying element. As can be seen, the alloys are divided into two groups, one with and the other without manganese. One of the two alloys without manganese contains zirconium. One of the alloys with manganese also contains zirconium, while the last alloy contains both zirconium and scandium. It is also worth mentioning that the five alloys contain the same amount of impurity elements, most important iron and silicon. It was also decided to leave out chromium from this investigation although the AA5083 alloy contains between 0.05 and 0.25 wt% of this element. The reason for this was to reduce the number of parameters and the fact that the effect of this element has been well documented during the last decades.

The alloys were cast as extrusion ingots with a diameter of 95 mm and a length of approximately 180 cm. Four ingots of each alloy were cast using standard DC-casting conditions. The casting speed and the flow rate of cooling water ranged from 130-222 mm/min and 8-12 m^3/min, respectively. The casting temperature was approximately 700°C. An Al-5Ti-1B master alloy was used as a grain refiner and it was fed manually in the outlet of the casting furnace throughout the whole casting period.

3.2 HEAT TREATMENT

A series of heat treatment experiments were conducted in order to follow the homogenization of segregations, dissolution of constituents and, of special interests, the precipitation of dispersoids. Both isothermal and continuous heat treatments were carried out. The isothermal treatment was carried out in salt baths at temperatures ranging from 275°C to 550°C at intervals of 25°C. The specimens were quenched in water at 20°C after treatment. The temperature stability of the salt baths was estimated to be better than ±2°C. The continuous heat treatments were performed in a Heraeus K750 Tempering furnace with a temperature stability of approximately ±1°C. In these experiments, the holding temperature was preset to 550°C and three heating rates to this temperature were used: 10°C/h, 100°C/h and 4400°C/h. The highest heating rate was obtained by inserting the specimens directly into the furnace at 550°C. Specimens were quenched after reaching different temperatures during heat up and after different holding times at 550°C.

The specimens were cut out from the extrusion billets as shown in Figure II-2. For annealing times equal to or less than 1 hour specimen of dimensions 5x15x15 mm^3 were used while for longer annealing times specimens of dimensions 15x15x15 mm^3 were used.

Based on the results of this work it was decided to use the following heat treatment procedure for the material used to evaluate the hot deformation properties and the recrystallisation properties later in this thesis: heating rate: 100°C/h, holding temperature: 500°C, holding time: 12 h followed by water quenching.

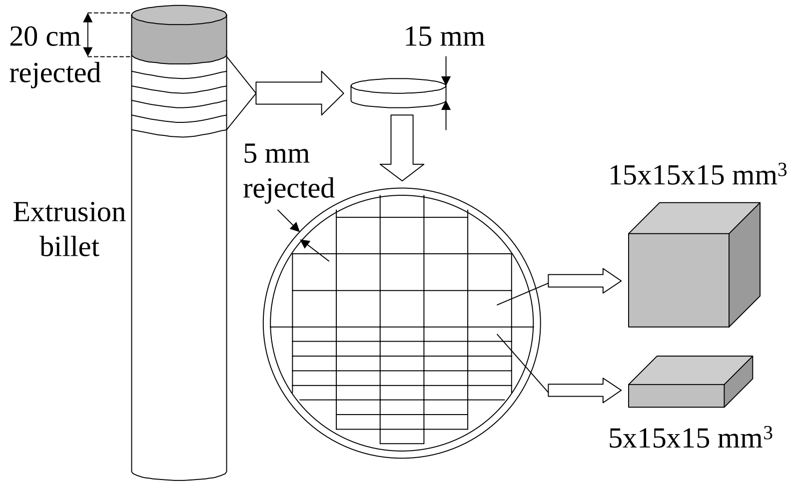

Figure II-2 *Specimens for heat treatment were cut out from the extrusion billets as shown in this figure.*

3.3 CONDUCTIVITY MEASUREMENTS

The microstrucural changes taking place during heat treatment was monitored by measureing the electrical conductivity of the material. The measurements were carried out on a Sigmatest D2.068 and were conducted both before and immediately after the heat treatments. Before measurements, the surface was ground on SiC paper to a surface finish of 1200 mesh in order to get a smooth surface and to remove the oxide layer and possible remaining salt. The conductivity values were converted to resistivity values.

According to the user manual, this instrument measures the conductivity with an absolute accuracy of ±1% of the measured value. Furthermore, the resistivity depends on the temperature at which the measurements are performed, Figure II-3. To reduce the effect of temperature variations on the conductivity measurements, all specimens were kept in a water bath of 20±1°C. The measurements were performed as quickly as possible after drying. Thus, the electrical resistivity values in this thesis is given with a maximum relative uncertainty better than approximately 2.3%, see Appendix A.

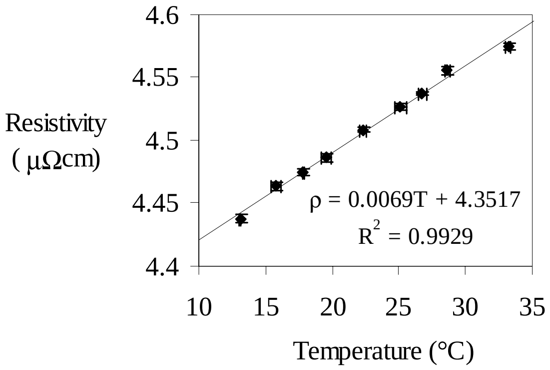

Figure II-3 *Electrical resistivity as a function of temperature in the AlMg alloy.*

3.4 MICROSTRUCTURAL INVESTIGATIONS

3.4.1 Specimens

The grain size and the secondary dendrite arm spacing (hereafter reffered to as SDAS) were measured at three locations along the billet for each alloy. The measurements were performed on the surface perpendicular to the casting direction at L=20, 75 and 150 cm and at r=24 mm (L=distance from the top of the billet and r=radius of the billet), see Figure II-4. Measurements along the radius were not performed.

The chemical composition was measured at a radius of approximately 24 mm on the disc shown in Figure II-4 by optical emmision spectrography. The measurements were carried out on a Baird instrument at Hydro Aluminium, Sunndalsøra. In the case of Sc, the ICP-method was used (Inductive Coupled Plasma) with a Jarrelach emmision spectrograph.

Estimation of grain size was performed by using the linear intercept method which involves counting a certain number, n, of grain boundary intercepts along a line. The distance, L, between the first and the last intercept was measured and then the grain size could be calculated as L/(n-1). Three measurements of 101 intercepts each were performed on each specimen. The measurements of the SDAS was done by counting the number of dendrite arms and measuring the distance over the dendrites. The SDAS could then be found easily. These measurements were carried out for 25 grains on each specimen.

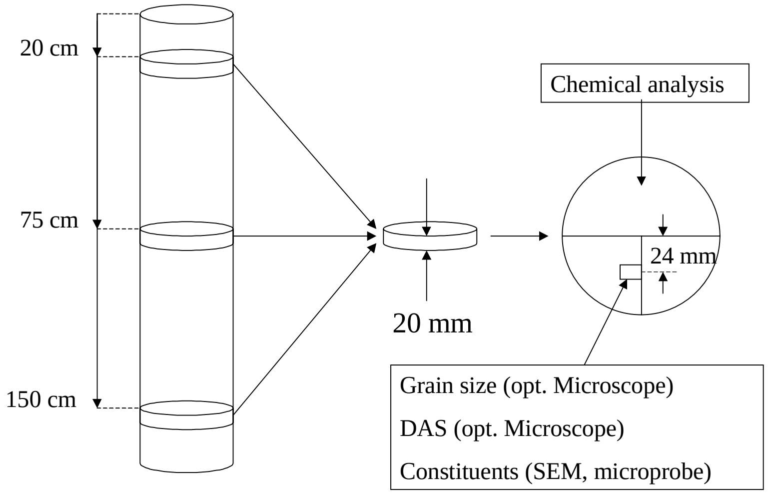

Figure II-4 *Position for measurement of grain size, SDAS and chemical composition in the extrusion billets.*

3.4.2 Optical microscopy

Investigation of the grain structure was performed in a Reichert MeF3A optical microscope using polarized light. The specimens were ground and polished to a surface finish of 1 μm and then anodized in a water solution of 5% HBF_4 at 20 V for 60 seconds.

Mn-rich particles were also observed by using polarized light but now the specimens were etched for 5 seconds at room temperature in a solution of 4 g $KMnO_4$ and 1 g NaOH dissolved in 100 ml destilled water. Mg-rich particles were observed after etching for 30 seconds in a 5% HF solution. Before etching all specimens were polished to 1 μm surface finish, as usual, and then polished for 5 seconds in a Struers OP-S suspension.

3.4.3 Electron microscopy

In order to get an overview of the primary constituents, an investigation in a scanning electron microscope and in an electron microprobe was performed. The electron microprobe was also used to detect concentration gradients of solute elements.

3.4.3.1 Scanning Electron Microscopy (SEM)

Specimens were analysed in a JEOL 840 interfaced with a LINK eXL EDS system which makes it possible to do qualitative x-ray analysis of the sample surface. The SEM was operating at an acceleration voltage of 15 kV giving an emision depth in aluminium of approximately 2.0 μm. Very small particles could then be analysed. The specimens were mechanically ground and polished to a final surface finish of 1 μm before examination.

3.4.3.2 Microprobe analysis

X-ray analysis were also carried out in a JXA 8900 R microprobe. An EDS-detector was used and both particles and segregations of the alloying elements were analysed. For both cases an acceleration voltage of 15 kV was used. Segregations were revealed by performing line scans over the dendrites. Several point analyses were performed along the line and the distance between each points was 2.5 μm. The following elements were scanned for: magnesium, manganese, iron, silicon, zirconium and scandium.

3.4.3.3 Transmission electron microscopy (TEM)

A TEM-study was performed in order to identify the dispersoids that precipitated during heat treatment of the cast material. Samples were studied in a Jeol JEM-2010 transmission electron microscope operating at an accelerating voltage of 200 kV. The microscope was interfaced with a LINK eXL EDS system which makes it possible to do qualitative x-ray analysis of the thin foil. Thin foils were prepared from the samples by mechanical grinding to a thickness of 50-100 μm. After grinding small circular specimens were punched out from the foils and polished electrolytically in a Struers Tenupol twin jet unit. The applied voltage was 20 V. The electrolyte was a 5% $HClO_4$-solution and the temperature of the electrolyte was kept at –20°C during polishing. The specimens were rinsed in methanol and ethanol after polishing

4 RESULTS AND DISCUSSION

4.1 DENDRITE ARM SPACING AND GRAIN SIZE

Figure II-5 shows the microstructure of the cast material. All alloys exhibit an equiaxed grain structure. The two alloys without zirconium have a grain size of approximately 50 µm while the three zirconium containing alloys have a grain size of approximately 80 µm. No systematic variations between the grain size along the billets was found, see Figure II-6a. The secondary dendrite arm spacing is in the range 13 – 15 µm and with no significant variation along the billets. As can be seen from Figure II-6b there is a slight reduction in SDAS when Mn, Zr and Sc are present in the alloys. However, it is difficult to say if these variations are significant taking into account the values of the standard deviation. Thus, it can be stated that the different alloys have different grain sizes but similar dendrite arm spacings. It is evident that the number of grain nuclei in the aluminium melt are dependent on the presence of titanium and zirconium in the alloy while the solidification rate is not effected by the alloy content.

The grain size of the material after heat treatment at 500°C for 12 hours affected the grain size only slightly, being approximately 50 µm for AlMg and AlMgMn and 85 µm for AlMgZr, AlMgMnZr and AlMgMnZrSc.

Since the additions of the Al-5Ti-1B master alloy was the same for all five alloys, it is clear that zirconium has a detrimental effect upon the grain refining efficiency of Ti and B, see Fig. II-6 a). This is in accordance with the findings in the literature. See for instance Jones and Pearson (1976) and Arjuna Rao et al. (1997). The poisoning effect of zirconium on the grain refining efficiency of Ti and B are still to be explained. Some results from the literature indicate that a change in the thermodynamic equilibriums could explain the phenomenon (Mondolfo (1983), McCartney (1989) or Tøndel (1994). However, it is beyond the scope of this thesis to discuss this in detail.

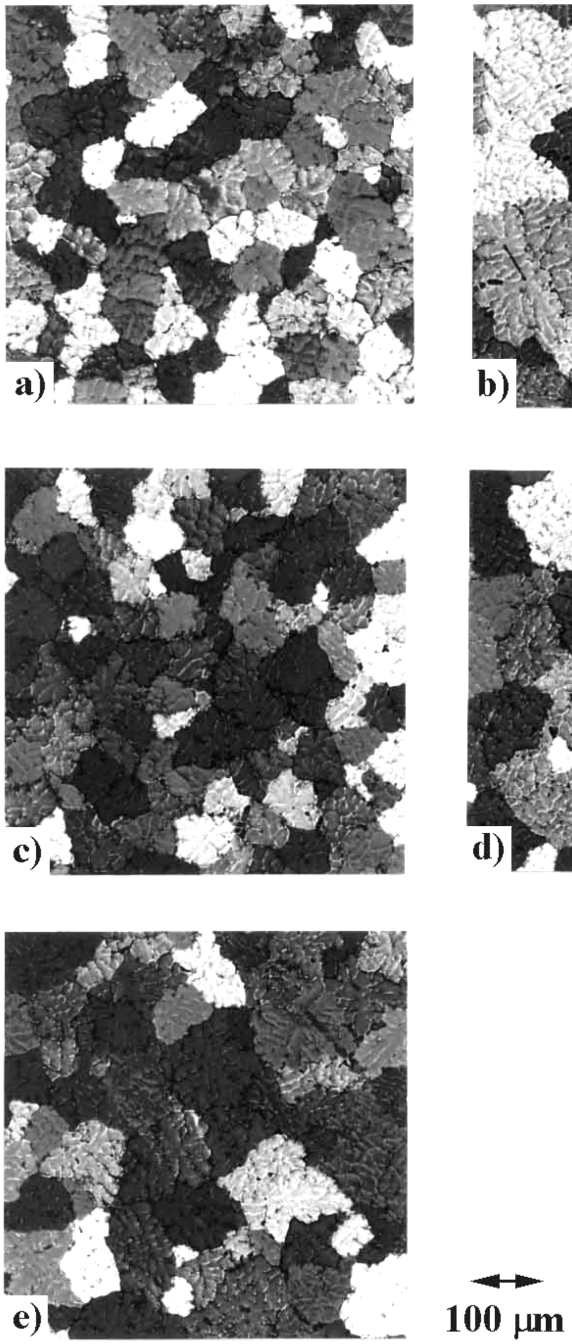

Figure II-5 *Grain structure in cast material, a) AlMg, b)AlMgZr, c) AlMgMn, d) AlMgMnZr and e) AlMgMnZrSc.*

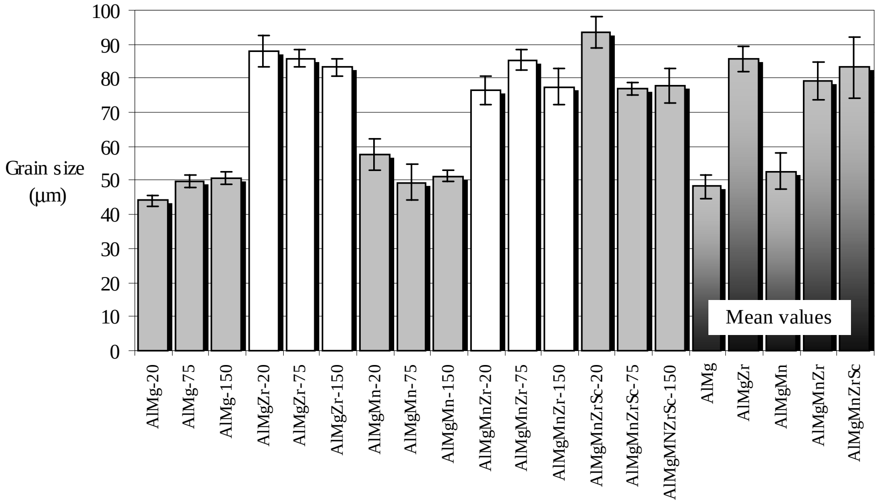

a)

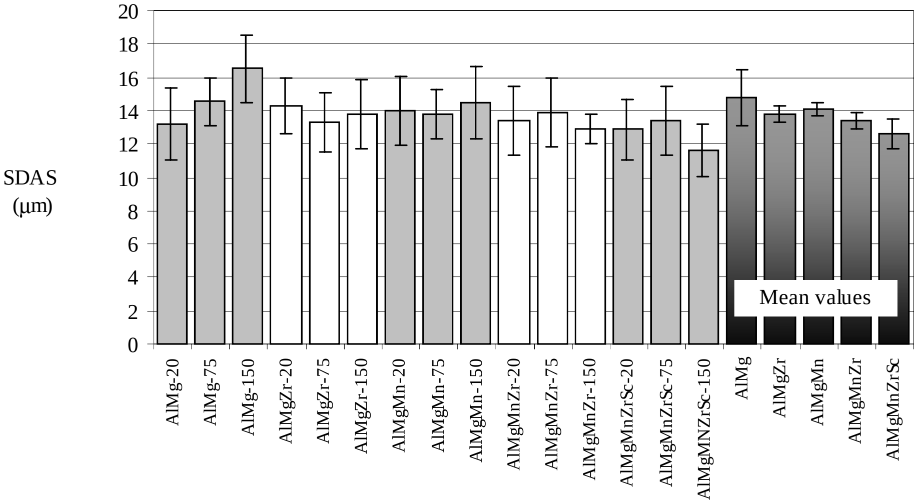

b)

Figure II-6 *a) Grain size and b) secondary dendrite arm spacing in the investigated alloys at different positions along the billets.*

4.2 SEGREGATIONS OF ALLOYING ELEMENTS

The concentration of magnesium and manganese across the dendritic grain structure in AlMgMn is shown in Figure II-7 a). A large variation in the magnesium concentration was observed. The minimum values are approximately 3 wt% while the maximum peak values are as high as 14 wt%. The variations in the manganese concentration were smaller, ranging between approximately 0.7 wt% and 0.2 wt%. It is important to observe that the segregation of magnesium and manganese are of opposite nature, i.e. the areas rich in magnesium are poor in manganese and vice versa. In Fig. II-7 b) the normalised concentration, C/C_0, for the elements Mg, Mn, Zr and Sc are plotted against the position relative to a dendrite boundary in alloy AlMgMnZrSc. Here C is the measured concentration of the element at a certain position and C_0 is the mean value of the measured concentrations in the heat treated specimen. The same observations were made in this alloy for magnesium and manganese as in alloy AlMgMn. In addition, a tendency for a lower Zr-concentration at the dendrite boundary compared to the interior of the dendrites was found. The concentration of scandium across the same boundary was surprisingly constant compared to that of zirconium. However, these observations are in accordance with the fact that zirconium and scandium are eutectic and peritectic elements in aluminium, respectively, (Massalski (1986), Phillips (1959)). Concentration gradients of iron and silicon could not be detected, due to the very low solubility of iron and the low content of silicon.

The concentration gradients after heat treatment (HR=100°C/h and 12 h at 500°C) was investigated and the normalised concentrations of Mg, Mn, Zr and Sc across a grain boundary are shown in Fig. II-7 c). It can be seen that magnesium segregations are completely levelled out after heat treatment while the elements Mn, Zr and Sc are still segregated. These results are more clearly illustrated in Fig. II-7 d) which shows the degree of segregation of the investigated elements after casting and after heat treatment. The degree of segregation is defined as the ratio between maximum and minimum concentrations, C_{max}/C_{min}.

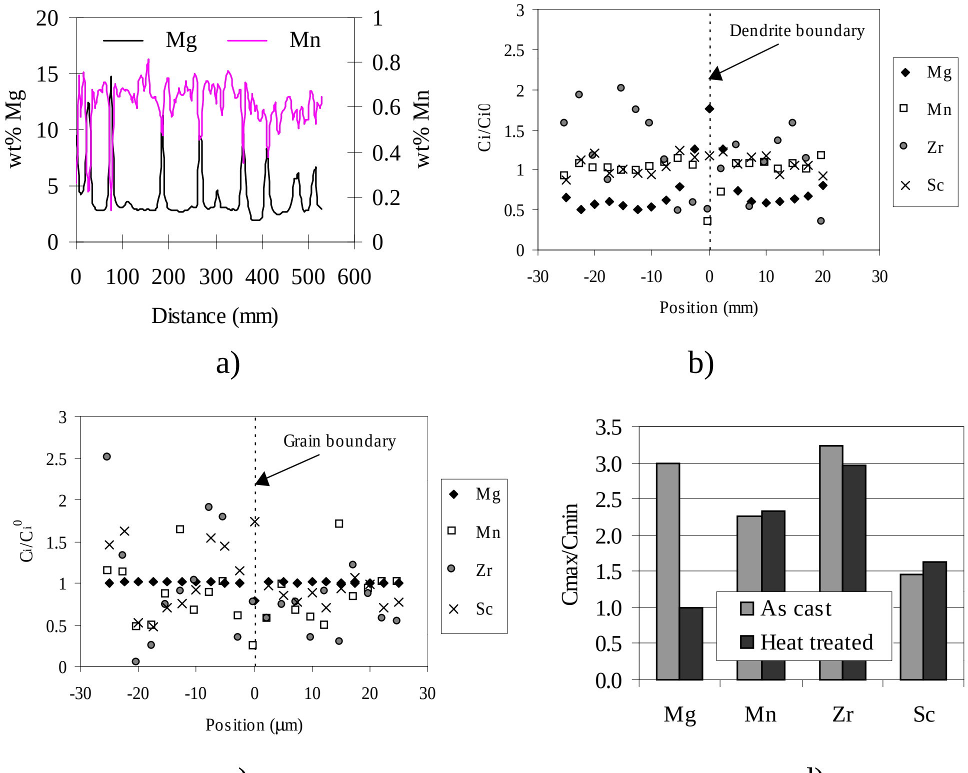

a) b)

c) d)

Figure II-7 *a) Microsegregations of Mg and Mn in AlMgMn, b) Microsegregations of Mg, Mn, Zr and Sc across a dendrite arm in AlMgMnZrSc, c) Microsegregations of Mg, Mn, Zr and Sc across a grain boundary in heat treated AlMgMnZrSc and d) Degree of segregations of Mg, Mn, Zr and Sc in cast and heat treated AlMgMnZrSc.*

The homogenisation of magnesium was investigated in more detail during isothermal heat treatment. The results are shown in Figure II-8. The difference between the maximum and the minimum concentration was measured after isothermal annealing at 400°C, 450°C, 500°C and 550°C. At the lowest temperature an annealing time of approximately 350 minutes is sufficient for complete removal of the segregations, while at the highest temperature it takes only 6 minutes.

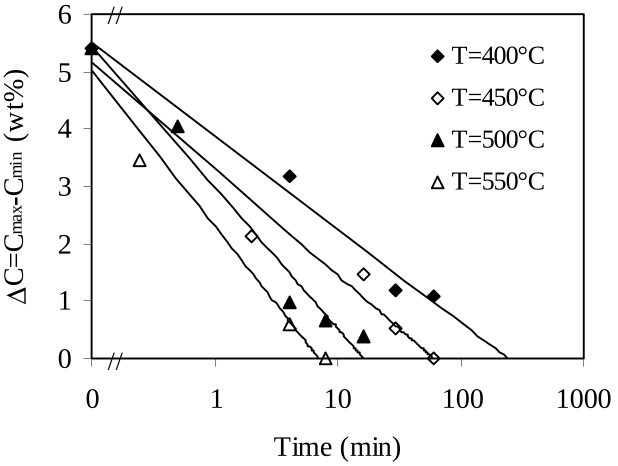

Figure II-8 *Decrease in Mg-concentration amplitudes across secondary dendrite arms.*

4.3 PRIMARY CONSTITUENTS

In a minor EDS-analysis (SEM and microprobe) of the cast microstructure four main types of constituents was found. These were AlMg-, AlMgSi-, AlFe- and AlMnFe-bearing particles. Determination of the exact stociometry was not performed. However, the first type is probably the equilibrium β-Al_3Mg_2 phase forming between dendrites in the late stage of solidification. The second type of particles, the AlMgSi-bearing ones, were observed rather seldom. These few particles could be the Mg_2Si-phase, which is commonly observed in Al-Mg-Si alloys where the silicon content is much higher. The third type of particles (AlFe) was only observed in the alloys without any additions of manganese. This phase could correspond to the equilibrium Al_3Fe-phase. In the alloys with additions of manganese the fourth type was observed. These AlMnFe-bearing constituents could be the equilibrium $Al_6(MnFe)$-phase. It seems that the iron is accumulated into this phase, rather than forming the separate iron-bearing AlFe-phase.

The homogenisation of magnesium segregations (Section 4.2) and the dissolution of primary β-Al_3Mg_2 were studied in the AlMg alloy, only. Figure II-9 shows the resistivity change after isothermal annealing of this alloy (single values in Appendix B, Table A-1). Annealing a binary Al-Mg alloy at a temperature within the single-phase area causes all Mg to go into solid solution. Since the same amount of Mg goes into solution at all temperatures in this area of the equilibrium phase diagram, it is expected that the resistivity reaches a constant value. Thus, the results in Figure II-9 are in accordance with the theory of dissolution of intermetallic particles. It should be noted that the other primary constituents (Al-Fe and Al-Mn-Fe) never disappeared during annealing at these temperatures. They were only spheroidized to some degree. The contribution to the resistivity increase is therefore attributed to the dissolution of primary low melting eutectics, presumably β-Al_3Mg_2 and a minor amount of Mg_2Si.

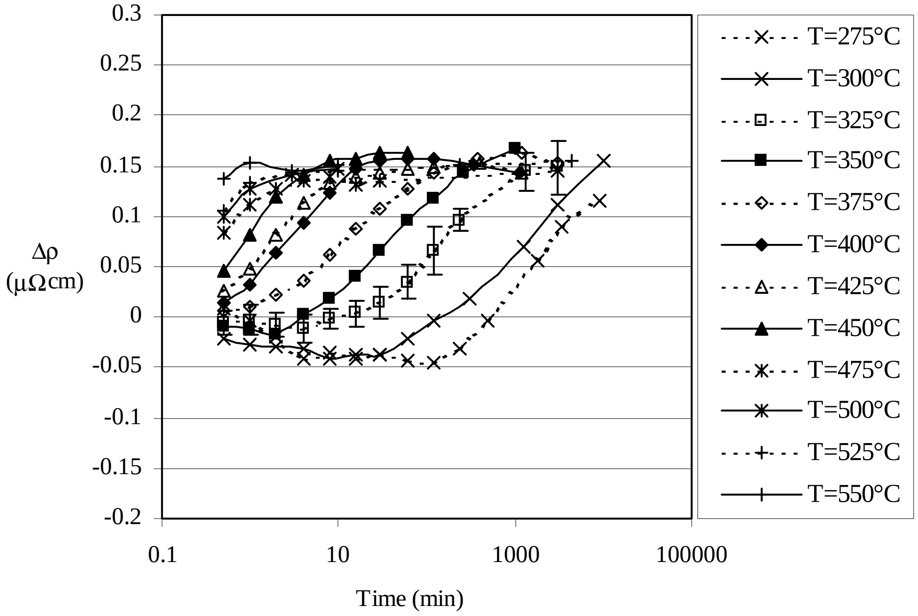

Figure II-9 *Electrical resistivity change in the AlMg alloy after isothermal heat treatment at various temperatures.*

The results from the resistivity measurements and the chemical analysis in the electron microprobe are summarised in Figure II-10. As can be seen the elimination of segregations takes longer time than the dissolution of the low melting eutectics. The reason for this is most likely due to the different diffusion distances for the two processes. As a magnesium atom has to move 7-8 μm in order to reach the centre of a dendrite, it only need to pass through the particle/matrix interface in order to reduce the size of the particle. It is therefore reasonable to assume that the dissolution process takes shorter time.

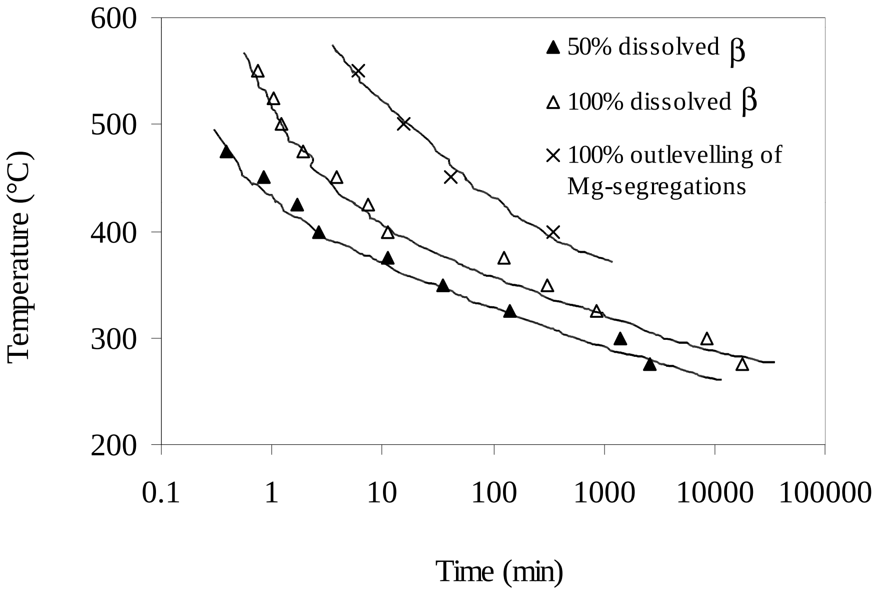

Figure II-10 *Time for outlevelling of segregations and for dissolution of low melting eutectics.*

4.5 DECOMPOSITION OF ELEMENTS IN SOLID SOLUTION

4.5.1 Magnesium

The non-age-hardenable aluminium-magnesium alloys usually exhibit some hardening response at Mg-contents above approximately 7-8 wt%. Coherent or semicoherent metastable Al-Mg precipitates probably cause the hardening effect. For alloys with lower magnesium content, no hardening effect after ageing is observed. Figure II-9 showed the annealing response of the AlMg alloy after isothermal heat treatment. The change in electrical resistivity has been plotted against the annealing time for various temperatures. It can be seen that there is a large dissimilarity of the response at low and high temperatures. Note that all temperatures are within the α-phase area in the binary Al-Mg phase system. After annealing, the resistivity is then expected to arrive at a constant level, which correspond to a situation where all magnesium is in solid solution in the aluminium matrix.

At low temperatures, however, the resistivity decreases and passes through a minimum value before it increases and approaches the constant value, see

Figure II-9. At high temperatures such a minimum value was not observed. Here the resistivity reaches the equilibrium value rather quickly and remains at that level after prolonged annealing. At intermediate temperatures there is a gradual increase to the equilibrium value. This transient annealing behaviour has not been reported for Al-Mg alloys earlier and an explanation for this phenomenon will be discussed in the following paragraphs.

It is evident that when annealing the cast material below the eutectic temperature, the material is partly in the single-phase area (α) and partly in the two-phase area ($\alpha+\beta$) at the starting time of the annealing process. Hence, there is a possibility to have precipitation of β-particles in the magnesium rich areas. This is most likely to take place at lower temperatures where the nucleation of β is more rapid than diffusion of magnesium. Figure II-11 shows that this precipitation takes place. After 10 minutes at 300°C a high number of small precipitates can be seen in the interdendritic areas. These areas correspond to high magnesium concentrations in the cast condition. After 700 hours most of the precipitates have gone back into solution.

This phenomenon can be treated as a diffusion problem and it is obvious that it can be divided into at least two concurrent diffusion processes. Firstly we have the nucleation of precipitates, which only requires short-range diffusion of magnesium atoms. Secondly, we have annealing out of the concentration gradients, which could be termed as a long-range diffusion process. The annealing out of concentration gradients depends on the applied temperature. At high temperatures diffusion of Mg is fast while at low temperatures the diffusion is slow. Hence, at high temperatures the annealing out of segregations could happen faster than the formation of stable precipitate nuclei. This is illustrated in a schematic manner in Figure II-12. Attempts have been made to solve this diffusion problem. This will be treated in detail in Part III of the thesis

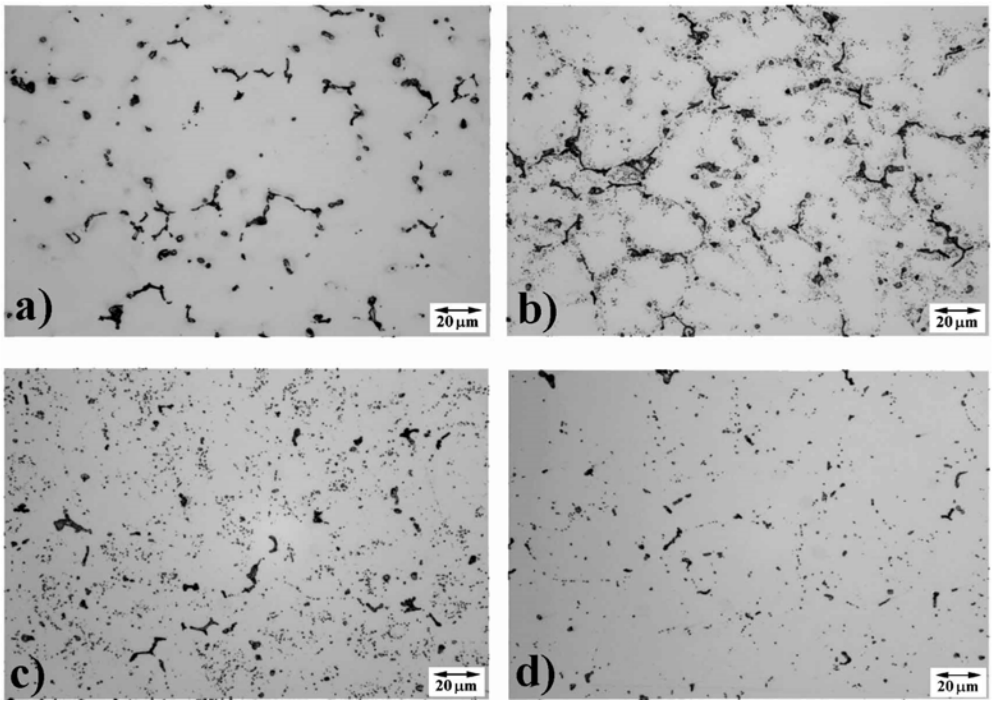

Figure II-11 *Optical micrographs showing precipitation of magnesium particles during isothermal annealing. a) As cast, b) 10 minutes at 300°C, c) 170 hours at 300°C and d) 700 hours at 300°C.*

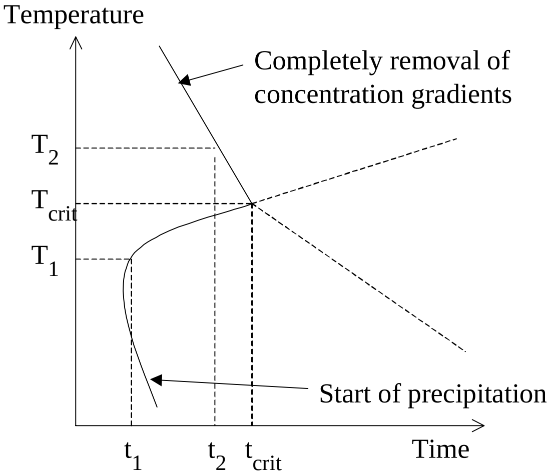

Figure II-12 *Interaction between local precipitation and homogenisation of segregations during isothermal annealing.*

4.5.2 Manganese

As described in Part I, the manganese in supersaturated solid solution will precipitate as dispersoids during thermomechanical treatment of the material. The size, density and distribution of precipitates depends on the applied heating rate, temperature, time and cooling rate.

The microstructures obtained after annealing at 300°C, 425°C and 525°C are shown in Figure III-13. At the lowest temperature very few precipitates are seen even after 50 hours at the annealing temperature. At an intermediate temperature the distribution of the particles follows a pattern which is similar to the dendritic structure. Going away from the dendrite boundary, the following observations can be made. First, a precipitate free zone in the interdendritic region is found. Next, a zone, which consists of a large number of very small particles, is observed (and could be called a precipitate rich zone). At last, the centre region of a dendrite is again free of precipitates. At high temperatures the particle size is larger, the density is lower and the particles seem to be more homogeneously distributed on a macroscopic scale. In addition, two different particle types are also observed, one with a regular shape and a low aspect ratio and the other with a platelike/needle shape and a high aspect ratio, see Figure II-13 e). Increasing the temperature and/or annealing time result in a coarsening of the particle structure. The only particles observed at short annealing times, are the regular ones, while the platelike particles seem to develop at prolonged annealing times.

Figure II-14 show some characteristic microstructures after heating to 550°C at a low and a high heating rate. A low heating rate of 10°C/h produced a fine distribution of small particles in the early stages of annealing. The precipitate free zones in the interdendritic areas are obvious. A high heating rate of 100°C/h caused a distribution of dispersoids in a pronounced dendritic pattern with the PFZ still present. After 12 hours at 550°C the microstructure contains a mixture of small regular shaped dispersoids and large platelike dispersoids. Thus, coarsening of the structure is evident after increasing the holding time and large particles have grown at the expense of small ones, which obviously have gone back into solution. The particle distribution seem to be homogeneous on a large scale and almost independent of the heating rate after 12 hours at 550°C, Figure II-14 c) and f), compared to the structure during heat up, Figure II-14 a) and d).

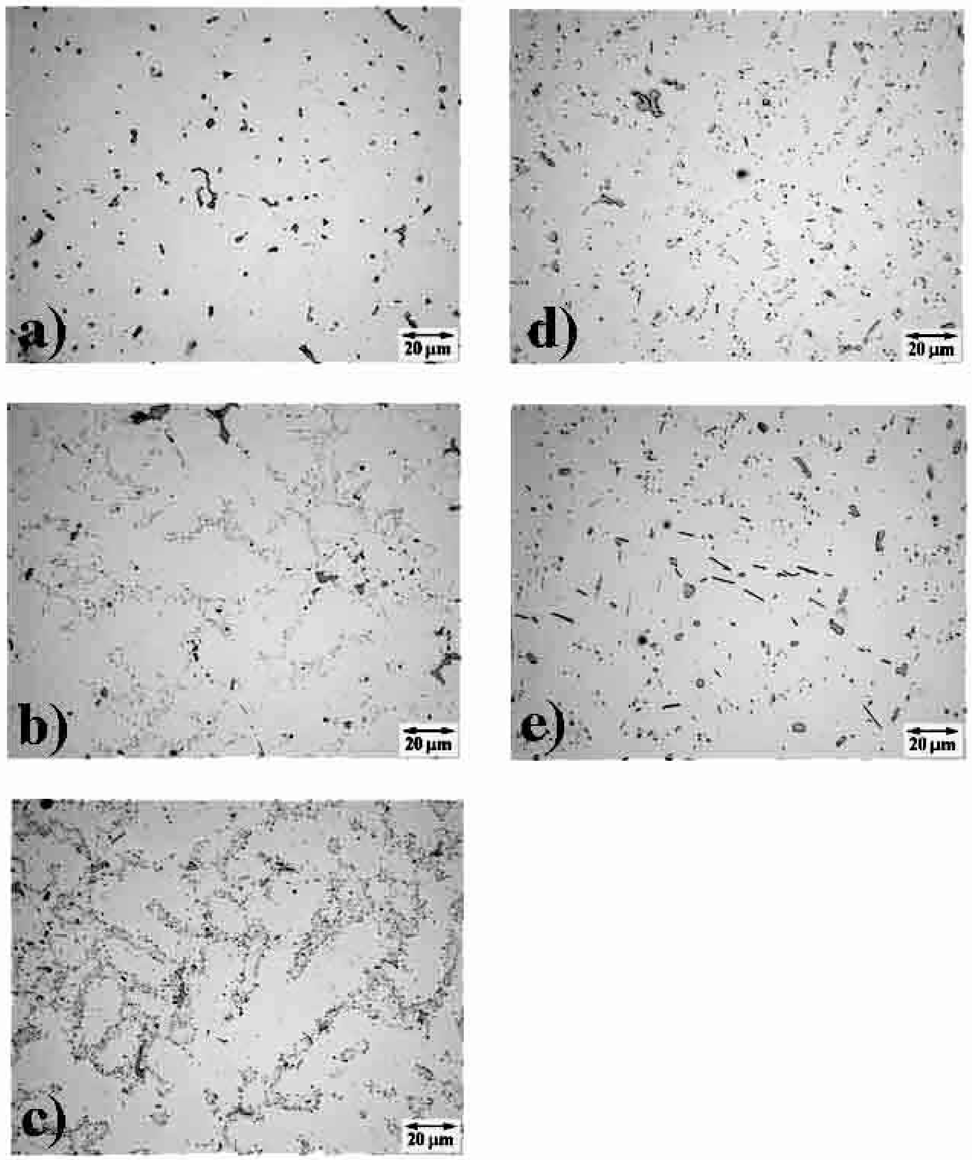

Figure II-13 *Optical micrographs showing manganese dispersoids after isothermal heat treatment at different temperatures and times. a) 50h at 300°C, b) 5h at 425°C, c) 50h at 425°C, d) 5h at 525°C and e) 50h at 525°C.*

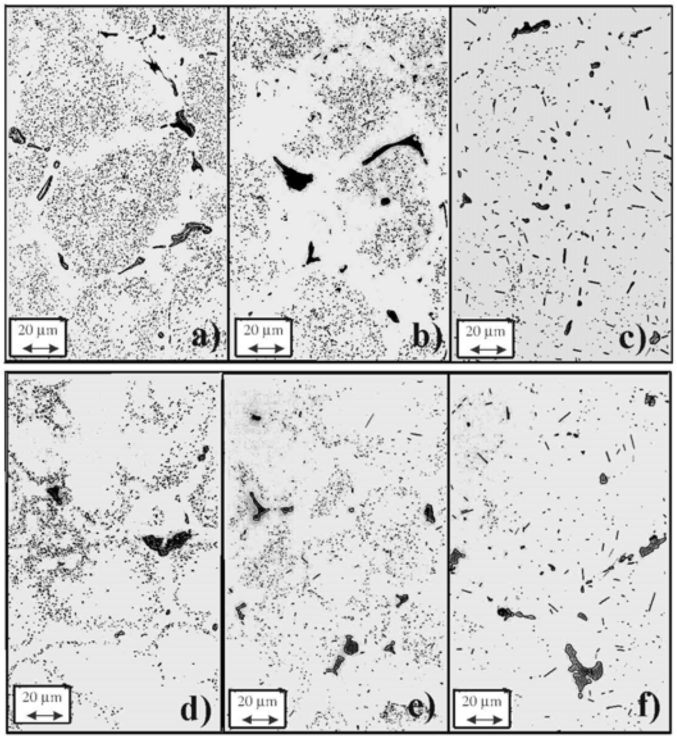

Figure II-14 *Optical micrographs showing manganese dispersoids after different stages of continuous heat treatment. a) Heated to 500°C, HR=10°C/h, b) 2h at 550°C, HR=10°C/h, c) 12h at 550°C, HR=10°C/h, d) Heated to 500°C, HR=100°C/h, e) 2h at 550°C, HR=100°C/h and f) 12h at 550°C, HR=100°C/h.*

The explanation for the coarsening of the particle structure with increasing temperatures or time is twofold. First, the solid solubility of manganese increases with temperature, bringing more solute in solid solution at higher temperatures and causing a lower volume fraction of particles. Second, the driving force for isothermal coarsening is the reduction in the total interfacial energy of the particles. The coarsening is a diffusional transformation process in which both dissolution of small particles and growth of larger particles are involved. However, this phenomenon will not be discussed further here, but the observations are consistent with those reported by other authors, see for instance Lee and Wu (1986), Sheppard and Raghunathan (1989) and Ratchev et al. (1995) for Al-Mg-Mn alloys and Goel at.al. (1974), Kattamis et al. (1989) and De Haan et al. (1996) for Al-Mn alloys.

The characteristic heterogeneous distribution of the particles and the presence of a precipitate free zone in the interdendritic region observed in Figure II-14 and II-15 was also observed by Sanders (1981), Lee and Wu (1986) and Sheppard and Raghunathan (1989) in Al-Mg alloys. The phenomenon has also been reported for Al-Mn alloys, see for instance Altenpohl (1965), Hatch (1984) and Sigli (1990). These observations will be discussed in the following.

The origin of the precipitate free zone is not fully understood. It is observed both in Al-Mn and in Al-Mg-Mn alloys, and different explanations for its formation have been published in the literature. Furrer and Hausch (1979) claim that depletion of manganese around primary particles take place by diffusion of manganese towards the particles during heat treatment. This process was coupled with the transformation of the $Al_6(Fe,Mn)$ phase into the α-$Al_{12}(Fe,Mn)_3Si$ phase. Sigli (1990), however, explained the depletion of manganese in the interdendritic region in a ternary Al-Mn-Fe alloy by means of interaction with iron during solidification. When the liquid solidifies, the material follows down the eutectic valley and the concentration of manganese in the liquid and in the solid aluminium matrix are forced to decrease, until the ternary eutectic is reached. Sanders (1981) proposed another theory. He found that manganese segregates opposite of magnesium as a result of reduced solubility with increasing magnesium concentration. The regions with the low manganese content will then make the PFZ after heat treatment. This theory was later supported by Lee and Wu (1986) and Sheppard and Raghunathan (1989) and could well be applied to the results of the present work.

Both manganese and magnesium are eutectic elements in aluminium and by considering binary alloys, it is found that the difference between the liquid and solid solute contents at the solidus temperature differs significantly, being 0.069 and 5.7 wt% for Al-0,7Mn and Al-4,5Mg, respectively (Phillips et al. (1959)). This suggests that practically no Mn segregations should be expected, in contrary to Mg. Thus, the observed Mn segregations are a result of the reduced Mn solid solubility in the presence of Mg. According to Mondolfo (1977) the maximum solid solubilities of Mn and Mg in binary alloys are 1.8wt% and 17.4 wt%, respectively. In a ternary Al-Mg-Mn alloy the solid solubilities are reduced to 0.5 wt% and 12 wt%, respectively. This explains the characteristic concentration gradients of Mn in an Al-Mg-Mn alloy system.

Upon heat treatment Mg diffuses towards the grain centres, increasing the Mg content here, while reducing it in the interdendritic regions. In addition Mn in supersaturated solid solution starts to precipitate.

When Mg have reached a uniform distribution, the concentration of Mn in the interdendritic regions is still low, and not leading to any precipitation. On the other hand, the grain interiors still have a high Mn concentration but a reduced solubility due to the increased Mg concentration. Thus, the supersaturation of Mn increases, leading to an increased driving force for precipitation in these areas. The resulting particle structure will be that of Figure II-14 a), a uniform distribution of Mn-dispersoids with PFZ's in the interdendritic areas. In this case the Mg segregations have levelled out before the Mn dispersoids started to precipitate. If the precipitation starts before the segregations have levelled out, i.e. in the case of using a very high heating rate to the holding temperature or a low temperature, then nucleation of dispersoids in the grain interior is suppressed and a particle structure like that seen in Figure II-14 d) develops.

Furthermore, it can be concluded that both the solubility and the initial concentration of Mn control the nucleation of Mn dispersoids. The solubility, and hence the supersaturation, may change during heat treatment due to the rapid diffusion of Mg, while the initial Mn concentration remains unaffected due to slow diffusion.

Selected area electron diffraction (SAD) and EDS-analysis were used in order to identify the dispersoids. SAD from some of the high aspect ratio particles showed that the dispersoids could be identified as the orthorhombic Al_6Mn-phase with lattice parameters a= 0.7498 nm, b=0.6495 nm and c=0.8837 nm, Figure II-15 a)-d). However, only a few SAD analyses were performed so it is not possible to conclude that the two particle morphologies have the same crystal structures. A more detailed EDS analysis shows that both types of particles contained mainly manganese, small amounts of iron and no silicon, Figure II-15 e) and f). These results suggest that the particles could be Al_6Mn but since some of the EDS-analyses gave a Mn-concentration between the Al_4Mn and Al_6Mn lines, some particles could also be the Al_4Mn phase.

Ratchev et.al (1995) performed a more detailed study of a 5182 Al-Mg-Mn alloy and found that the two types of particles had the same crystal structure but different orientation relationships with the aluminium matrix. The particles were identified as the orthorhombic $Al_6(MnFe)$ with the space group oC28 and lattice parameters a= 0.7498 nm, b=0.6495 nm and c=0.8837 nm. The low aspect ratio dispersoids had no orientation relationships, which means that these particles are incoherent with the matrix. On the other hand, the large plates had preferential growth planes and a semicoherent relationship to the matrix. The results of the present investigation are in accordance with the results of Ratchev et.al (1995).

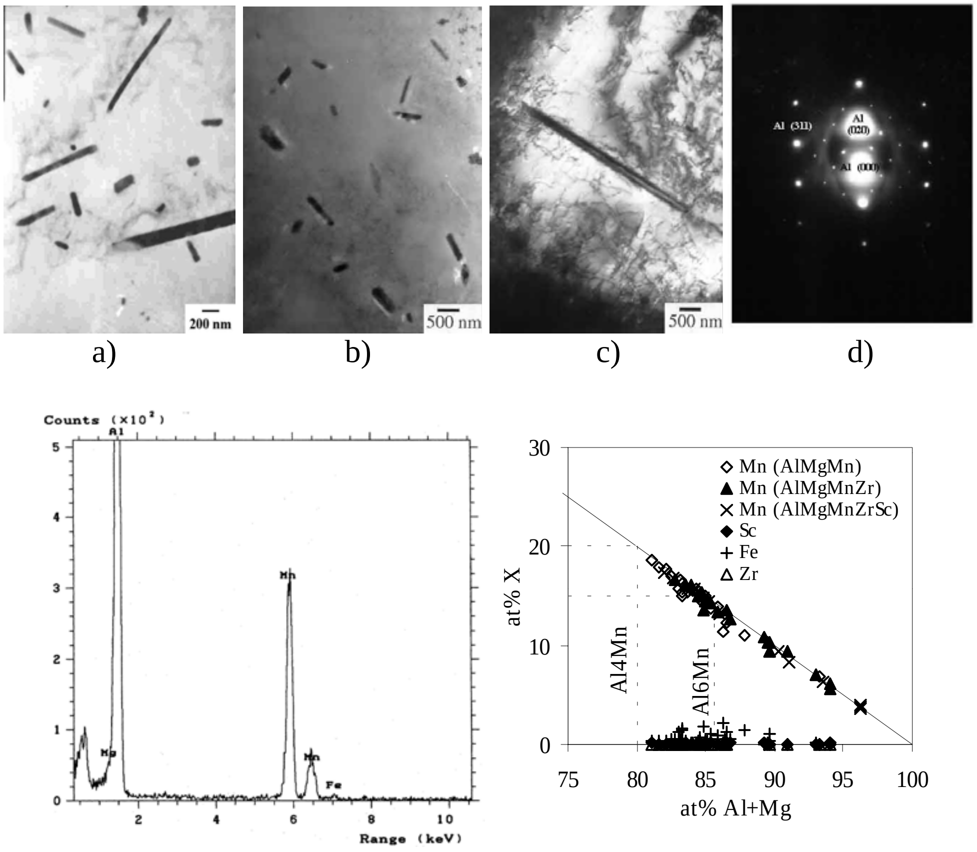

a) b) c) d)

e) f)

Figure II-15 a) Bright field TEM image showing small regular shaped and platelike Mn-dispersoids, b) Bright field TEM image showing small regular shaped Mn-dispersoids, c) Bright field TEM-image showing a large platelike Mn-dispersoid, d) SAD showing the (310)-matrix zone and superspots from the large platelike Mn-dispersoid shown in c), e) X-ray spectrum from a particle analysis and f) at% of alloying element versus at% Al+Mg.

4.5.3 Zirconium and scandium

Besides some coarse particles, most of the zirconium and scandium remained in solid solution after casting and precipitate as small dispersoids during heat treatment. The dispersoids of Zr and Sc were only investigated for the material which was heat treated at 500°C for 12 hours. In the alloys AlMgZr and AlMgMnZr the coherent metastable cubic β'-Al_3Zr phase with lattice parameter a=4.08Å was observed. The dispersoids were distributed heterogeneously in the matrix, some areas without dispersoids and others with a denser distribution. Very often dispersoids of this type was found in clusters of several particles. In the AlMgZr alloy only β'-Al_3Zr was observed, Figure II-16 a), while in alloy AlMgMnZr, both large Al_6Mn and β'-Al_3Zr was observed, Figure II-16 b) and c). The SAD pattern in Figure II-16 d) and the results from the EDS-analyses, Figure II-16 e) and f), show that these particles actually are the β'-Al_3Zr phase.

In the AlMgMnZrSc alloy the very small dispersoids corresponded to the coherent cubic Al_3Sc $L1_2$-structure with a lattice parameter of a=4.105Å. These dispersoids were much smaller than the β'-Al_3Zr and the density was also much higher, Figure 17 a)-c). From the EDS-analysis it was found that these particles contained both Sc and Zr, Figure 17 d) and e). According to Davydov et al. (1996) Sc atoms in the Al_3Sc phase can be replaced by Zr atoms without changing the lattice parameter noticeably when these elements are present in the alloy. The chemical formula of such a phase can be written $Al_3(Sc_x,Zr_{1-x})$ where x is a variable quantity. The value of x has been reported to vary from 0 to 0.7. In the present investigation Sc/Zr ratios ranged from 1.3 to approximately 6 with a mean value of 3.5. This gives x-values from 0.57 to 0.86 with a mean value of 0.73.

The size and density of the dispersoids are summarised in Table II-3. From these results and the above discussion it seems reasonable to assume that Al_6Mn and Al_3Zr or $Al_3(Sc,Zr)$ precipitates independent of each other in an Al-Mg matrix. Although no detailed analysis was made, the TEM-investigation suggests that the size and density of Al_3Zr in AlMgZr and AlMgMnZr is approximately the same. Further, the results (both TEM and metallography) also indicate that the size and density of Al_6Mn is approximately the same in AlMgMn, AlMgMnZr and AlMgMnZrSc. It is therefore obvious that the properties of these alloys are basically determined by the presence of an Al-matrix with Mg in solid solution and a certain amount of dispersoids.

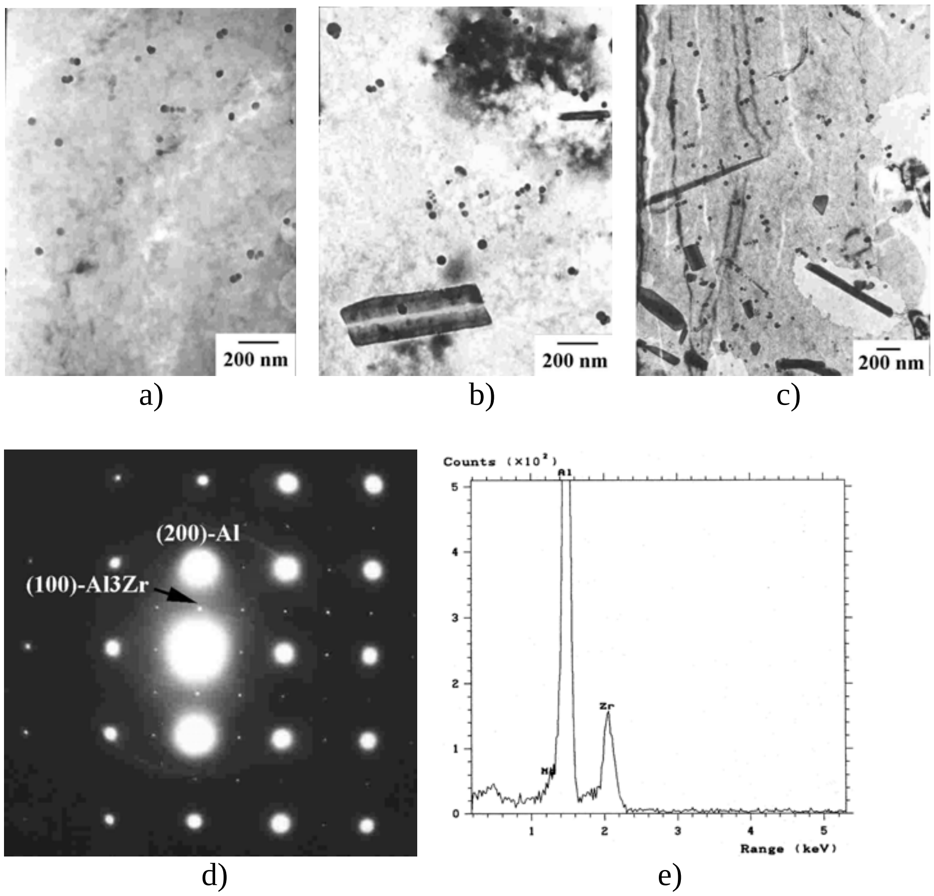

a) b) c)

d) e)

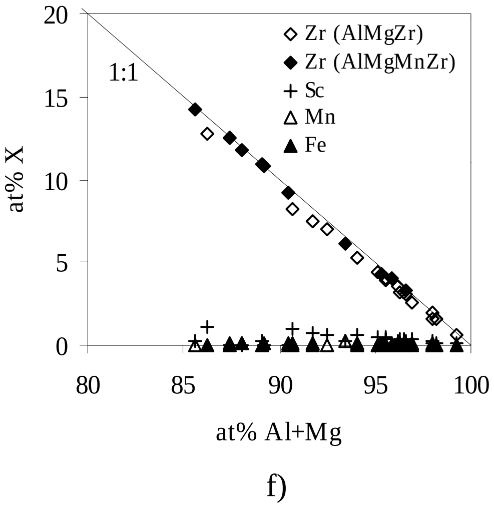

f)

Figure II-16 *a) TEM-image of β'-*Al_3Zr *in AlMgZr, b) and c) TEM-images of β'-*Al_3Zr *and Al6Mn in AlMgMnZr, d) SAD showing the (100)-zone of the metastable coherent cubic β'-*Al_3Zr *phase, e) X-ray spectrum from a β'-*Al_3Zr *particle and f) Composition plot of β'-*Al_3Zr *particles,*

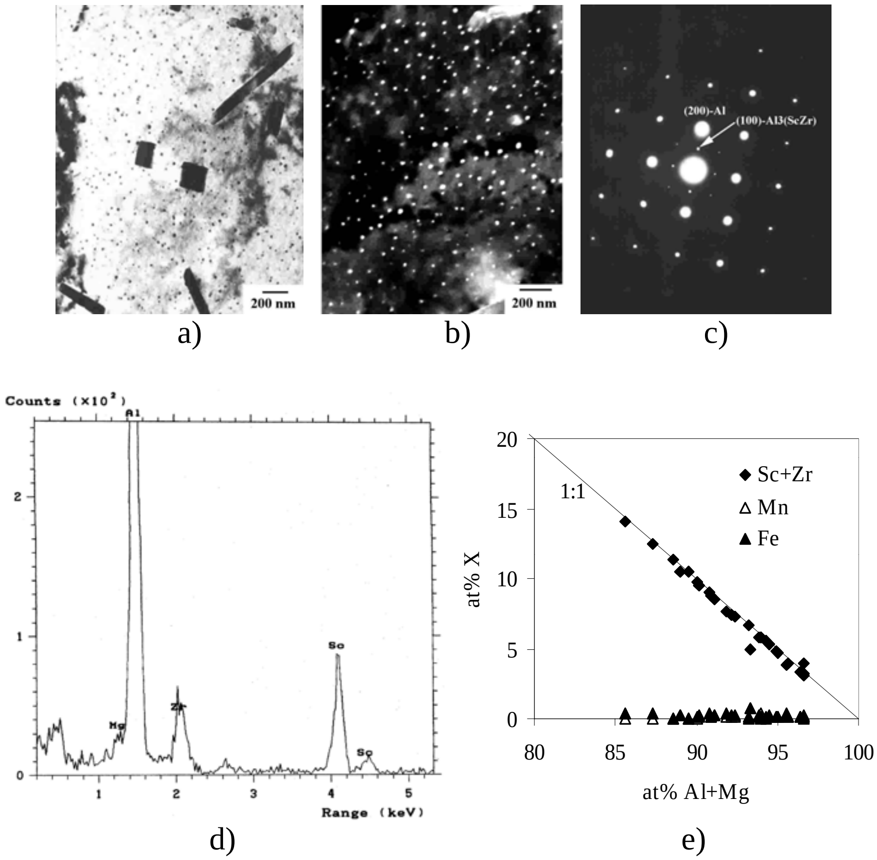

a) b) c)

d) e)

Figure 17 a) Bright field *TEM-image of Al_6Mn- and $Al_3(Sc_x,Zr_{1-x})$-dispersoids, b) Dark field TEM-image of $Al_3(Sc_x,Zr_{1-x})$-dispersoids, c) SAD showing the (100)-zone of the coherent cubic $Al_3(Sc_xZr_{1-x})$-phasec d) X-ray spectrum from a $Al_3(Sc_xZr_{1-x})$ particle, e) Composition plot of $Al_3(Sc_xZr_{1-x})$-particles.*

Table II-3 Density, size and interparticle distance of the dispersoids. D=diameter, $\overline{D}$ =mean diameter, *W=width and L=length.*

Alloy	Dispersoid	Density $(nm^{-3})x10^8$	Size range (nm)	$\overline{D}$ (nm)
AlMg	-	-	-	-
AlMgZr	Al_3Zr	4.4±0.8	D:30-80	49±10
AlMgMn	Al_6Mn	0.45±0.3	W:50-350 L:50-1700	118±63
AlMgMnZr	Al_3Zr	4.4±1.0	D:40-80	45±14
	Al_6Mn	0.48±0.2	W:50-350 L:50-1700	103±46
AlMgMnZrSc	$Al_3(Sc,Zr)$	46.4±10	D:10-30	22±5
	Al_6Mn	0.51±0.3	W:50-350 L:50-1700	99±25

4.6 KINETICS OF THE DECOMPOSITION OF MN, ZR AND SC FROM SOLID SOLUTION

Due to the very complex alloys studied in this work it was difficult to separate the contribution from the different elements. However, from the discussion above it can be stated that the decomposition of the solid solutions of Mn, Zr and Sc resulted in the formation of three different kinds of dispersoids, namely Al_6Mn, Al_3Zr and $Al_3(Sc,Zr)$.

The precipitation of these particles was investigated by means of electrical conductivity measurements after isothermal annealing. The resistivity is plotted against the annealing temperature in Figure II-18. Single values are tabulated in Appendix B. The contribution from the precipitation and redissolution of β-Al_3Mg_2 in alloy AlMg upon the electrical resistivity is subtracted, see Fig. II-9, i.e. it is assumed that Eq. II-3 is valid.

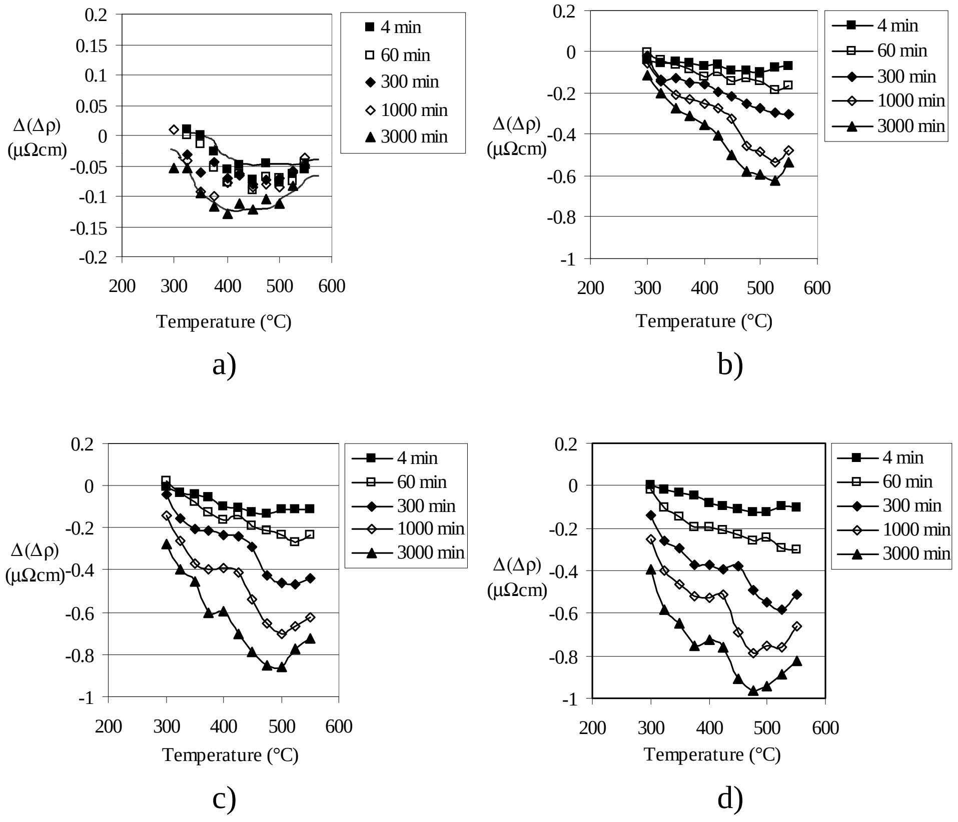

a) b) c) d)

Figure II-18 *Resistivity change as a function of annealing temperature for a) AlMgZr, b) AlMgMn, c) AlMgMnZr and d) AlMgMnZrSc.*

In AlMgZr the resistivity decreases and flattens out between –0.05 and –0.1 μΩcm at short annealing times. At the annealing times of 1000 min and 3000 min the resistivity reaches a minimum value at 400°C to 450°C before it increases again at higher temperatures. These results indicate that the decomposition of Al_3Zr occurs in the temperature range from 350°C to 450°C. At temperatures above 450°C the resistivity increases again which is most likely due to the increased solid solubility at higher temperatures and a corresponding coarsening of the precipitates.

In AlMgMn the resistivity decreases more pronounced and reaches a minimum value between 500°C and 525°C at the two longest annealing times (1000 and 3000 min). It is also evident from the resistivity curves that precipitation of Mn has occurred after annealing at very short times even at the lowest annealing temperatures. It is therefore concluded that the decomposition of manganese occurs in a temperature range from 300°C to 500°C.

The curves are even more depressed to lower resistivity values in AlMgMnZr and AlMgMnZrSc, which indicates that more elements go out from solid solution. The resistivity for these two alloys seems to pass trough a plateau at temperatures between 350°C and 450°C. This is even more pronounced in AlMgMnZrSc and it is attributed to the completion of the precipitation of Al_3Zr and $Al_3(Sc,Zr)$ in this temperature region.

The results are summarised in Figure II-19 a)-c), which shows resistivity curves for the decomposition of the individual alloying elements. It should be mentioned that any attempts to separate the contribution from scandium alone did not succeed. Thus, for the alloy containing scandium, the contribution from zirconium and scandium are added and treated as a single element. The curves in Figure II-19 d) are constructed on the basis of the resistivity curves (Figure II-19 a)-c)). Apparently, a homogenisation temperature of 500°C seems to be an optimum temperature to use in order to form dispersoids of the types Al_6Mn, Al_3Zr and $Al_3(Sc,Zr)$.

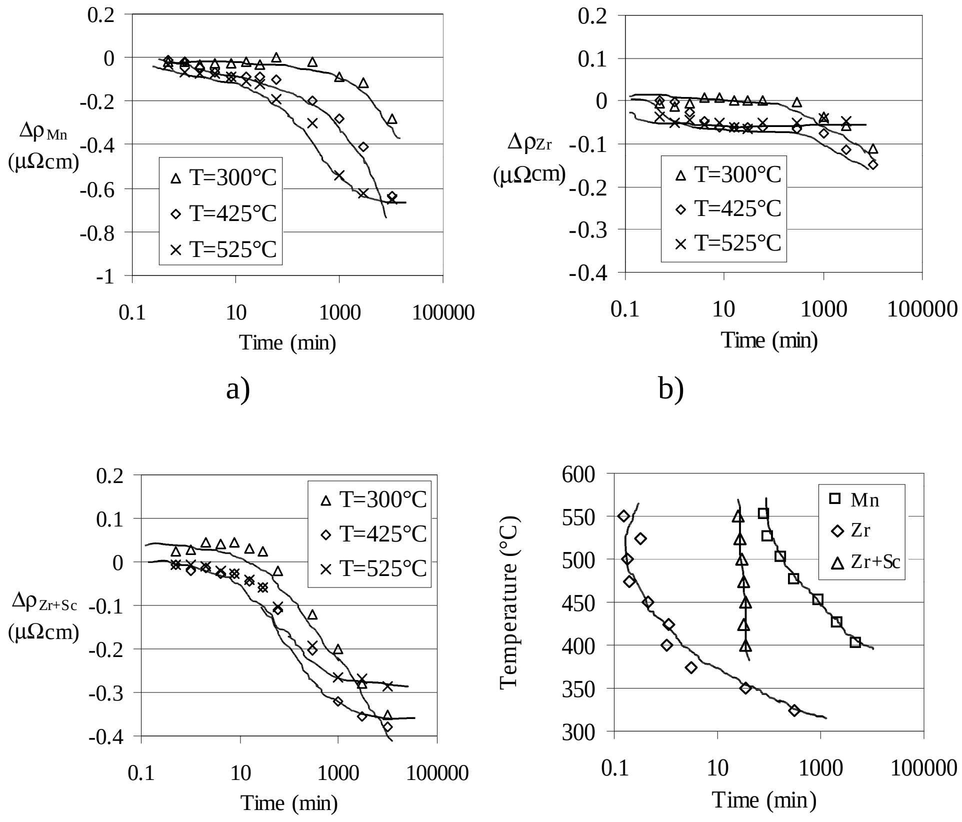

c)

d)

Figure II-19 *The effect of a) manganese, b) zirconium and c) zirconium + scandium on the electrical resistivity after isothermal annealing, d) isothermal transformation curves for the decomposition of Mn, Zr and Zr+Sc.*

5 CONCLUSIONS

- The grain size of the investigated alloys was the same before and after heat treatment, i.e. approximately 80 μm and 50 μm for alloys with and without additions of zirconium, respectively
- Magnesium, manganese, zirconium and scandium were all segregated in the cast material. Segregations of magnesium were completely removed after heat treating at 500°C for 12 hours. Segregations of Mn, Zr and Sc were still present after this heat treatment due to the diffusion coefficients.
- The cast structures contained primary constituents of the following type: AlMg, MgSi, AlFe and AlMnFe. Upon heat treatment, AlMg and MgSi dissolved while AlFe and AlMnFe were still present afterwards.
- Precipitation of β-Al_3Mg_2, cubic Al_3Zr, cubic $Al_3(Sc,Zr)$ and orthorhombic Al_6Mn have been observed in the investigated alloys.
- The precipitation of β-Al_3Mg_2 occurred at the early stages of annealing at low temperatures. The particles were redissolved after prolonged annealing times. This phenomenon is attributed to the presence of segregations and the correspondingly low diffusivity of Mg at the low temperatures at which this phenomenon occurs.
- The decomposition of manganese occurs in the temperature range 300°C to 500°C and starts by the formation of small regularly shaped precipitates identified as Al_6Mn. The nucleation of these particles depends on the superaturation of Mn in solid solution, the segregations of Mn and the applied heating rate and temperature. After prolonged heat treatment large platelike particles develops. These were also identified as Al_6Mn. The size of these dispersoids was large and the density was rather low.
- The precipitation of the metastable cubic Al_3Zr particles occurred in the temperature range 350°C to 450°C and resulted in a higher density than for Al_6Mn. In addition, the precipitates were much smaller. However, it seems that the precipitates are rather heterogeneously distributed in the structure, most likely reflecting the micro-segregations of Zr.
- The precipitation of the cubic $Al_3(Sc,Zr)$ dispersoids with a structure similar to that of the cubic $L1_2$-structure of Al_3Sc was observed. The small size and the fine dispersity of these particles indicate an extremely good lattice fit with the matrix promoting both nucleation and the thermal stability compared to Al_3Zr and Al_3Sc.

REFERENCES

Altenpohl, D., *Aluminium und Aluminiumlegierungen*, Springer-Verlag, Berlin, 1965.

Arjuna Rao, A., Murthy, B.S. and Chakraborty, M., *Role of zirconium and impurities in grain refinement of aluminium with Al-Ti-B*, Met. Sci. Tech., vol. 13, September (1997), p. 769.

Chen, L. and Morris, J.G., *The precipitation behaviour of strip cast 3004 aluminium alloy*, Scripta Met., vol. 18 (1984), p. 1365.

Davydov, V.G., Elagin, V.I., Zakharov, V.V. and Rostova, T.D., *Alloying aluminium alloys with scandium and zirconium additives*, Met. Sci. Heat Treat., vol. 38. no. 7-8 (1996), p. 347.

De Haan, P.C.M., Rijkom, J. and Söntgerath, J.A.H., *The precipitation behaviour of high-purity Al-Mn alloys*, Mat. Sci. Forum, vol. 217-222 (1996), p. 765.

Dons, A.L., *Variations in the composition of AlMnFeSi-particles in aluminium*, Scand. J. Met., vol. 13 (1984), p. 137.

Drits, M.E., Pavlenko, S.G., Toropova, L.S., Bykov, Y.G. and Ber, L.B., *Mechanism of the influence of scandium in increasing the strength and thermal stability of alloys of the Al-Mg system*, Sov. Phys. Dokl., vol. 26, March (1981), p.344.

Furrer, P. and Hausch, G., *Recrystallization behaviour of commercial Al-1%Mn alloy*, Met. Sci., March-April (1979), p. 155.

Goel, D.B., Roorkee, U.P. Furrer, P. and Warlimont, H., *Ausscheidungsverhalten von Aluminium-Mangan-(Kupfer, -Eisen-) Legierungen, Aluminium*, vol. 50, nr. 8 (1974), p. 511.

Hanssen, V., Andersson, B. Tibbals, J.E. and Gjønnes, J., *Metallurgical reactions in two industrially strip-cast aluminium-manganese alloys*, Met. Mat. Trans. B, vol. 26B, August (1995), p. 839.

Hatch, J.E., *Aluminium: Properties and physical metallurgy*, ASM, Metals Park, Ohio, 1984.

Jo, H.-H. and Fujikawa, S.-I., *Kinetics of precipitation in Al-Sc alloys and low temperature solid solubility of scandium in aluminium studied by electrical resistivity measurements,* Met. Sci. Eng., A171 (1993), p. 151.

Jones, G.P. and Pearson, J., *Factors affecting the grain-refinement of aluminium using titanium and boron additives,* Met. Trans. B., vol. 7B, June (1976), p. 223.

Kattamis, T.Z., Merchant, H.D., Skolianos, S. and Scharf, G., *Homogenization and coarsening in cast 3004 aluminium alloy,* Aluminium, vol. 65, nr. 4 (1989), p. 367.

Lee, S.-L. and Wu, S.-T., *Influence of soaking treatments on hot ductility of Al-4.85 Pct Mg alloys containing Mn,* Met. Trans. A, vol. 17A, May (1986), p. 833.

Massalski, T.B., *Binary alloy phase diagrams,* ASM, Metals Park, Ohio, vol. 1, 1986.

McCartney, D.G., *Grain refining of aluminium and its alloys using inoculants,* Int. Mat. Rew., vol. 34, no. 5 (1989), p. 247.

Mondolfo, L.F., *Manganese in aluminium alloys*, The Manganese Centre, 1977, ISBN 2901109-01-2.

Mondolfo, M.L., *Grain refinement in the casting of non-ferrous alloys*, eds. Abbaschian, G.J. and David, S.A., The Metallurgical Society of AIME, Warrendale, Pennsylvania, 1983, p. 3.

Nagahama, K. and Miki, I., *Precipitation during recrystallization in Al-Mn and Al-Cr alloys*, Trans. JIM, vol. 15 (1974), p. 185.

Nebti, S., Hamana, D. and Cizeron, G., *Calorimetric study of pre-precipitation and precipitation in Al-Mg alloy,* Acta. Met., vol. 43, no. 9 (1995), p. 3583.

Nes, E., *Precipitation of the metastable cubic Al3Zr-phase in supereutectic Al-Zr alloys,* Acta. Met., vol. 20, April (1972), p.499.

Nozato, R. and Ishihara, S., *Calorimetric study of precipitation process in Al-Mg*, Trans. JIM, vol. 21, no. 9 (1980), p. 580.

Olafsson, P., Sandström, R. and Karlsson, Å., *Electrical conductivity of aluminium alloys*, Mat. Sci. Forum, vol. 217-222 (1996), p. 981.

Osamura, K. and Ogura, T., *Metastable phases in the early stage of precipitation in Al-Mg alloys*, Met. Trans. A, vol. 15A, May (1984), p. 835.

Phillips, H.W., *Annotated equilibrium diagrams of some aluminium alloys*, The Institute of Metals, London, 1959.

Ratchev, P., Verlinden, B. and Van Houtte, P., *Effect of preheat temperature on the orientation relationship of (Mn,Fe)Al6 precipitates in an AA5182 aluminium-magnesium alloy*, Acta. Metall. Mater., vol. 42, no. 2 (1995), p.621.

Ryum, N., *Precipitation and recrystallization in an Al-0.5wt%Zr-alloy*, Acta Met., vol. 17, march (1969), p. 269.

Samson, S., *The crystal structure of the phase* β Mg_2Al_3, *Acta. Cryst*., vol. 19, (1965), p. 401.

Sanders, T.H., *Observation of nonuniform precipitation of Mn in an Al-Mg ingot*, Metallography, vol. 14 (1981), p. 177.

Sato, T., Kamio, A. and Lorimer, W., *Effect of Si and Ti additions on the nucleation and phase stability of the* $L1_2$*-type* Al_3Zr *phase in Al-Zr alloys*, Mat. Sci. Forum, vol. 217-222 (1996), p.895.

Sato, T., Kojima, Y. and Takahashi, T., *Modulated structures and GP zones in Al-Mg alloys*, Met. Trans. A, vol. 13A, August (1982), p. 1373.

Sheppard, T. and Raghunathan, N., *Modification of cast structures in Al-Mg alloys by thermal treatments*, Mat. Sci. Tech., vol. 5, March (1989), p. 268.

Sigli, C., *Origin of precipitate-free zones in Al-Mn-Fe alloys*, Proceedings of The 4th International Conference on Aluminium Alloys, ICAA 4, Trondheim, 1990.

Starink, M.J. and Zahra, A.-M., *β' and β precipitation in an Al-Mg alloy studied by DSC and TEM*, Acta Met., vol. 46, no. 10 (1998), p.3381.

Toropova, L.S., Eskin, D.G., Kharakterova, M.L. and Dobatkina, T.V., *Advanced aluminium alloys containing scandium, Structure and properties*, Gordon and Breach Science Publishers, Amsterdam, 1998.

Tøndel, P.A., *Grain refinement of hypoeutectic Al-Si foundary alloys*, Ph.D. Dissertation, Norwegian University of Science and Technology, 1994.

Villars, P. and Calvert, L.D., *Pearson's handbook of crystallographic data of intermetallic phases,* ASM, Metals Park, Ohio, vol. 2, 1985.

Westengen, H., Auran, L. and Reiso, O., *Effect of minor additions of transition elements on the recrystallization of some commercial aluminium alloys*, Aluminium, vol. 57, nr. 12 (1981), p. 797.

PART III
HOT TORSION EXPERIMENTS

1. INTRODUCTION

Commercial wrought alloys of the 5xxx-system are used both as extruded profiles and as rolled sheets or plates Due to the high extrusion pressure required to extrude these alloys, profiles are restricted to rather simple geometries and small quantities. Hot rolling is therefore the dominating process route for high strength 5xxx-alloys.

An important feature for both extrusion and hot rolling processes are the pressure needed to deform the material. The extrusion pressure and the rolling pressure can be easily calculated from the flow stress required for the deformation. Another important factor is the maximum amount of work which the material can withstand before failure is obtained. The metallurgical term for this feature is usually *hot ductility*.

The flow stress is dependent both on strain rate, temperature and chemical composition of the material while the hot ductility is more dependent on the microstructure, such as grain structure, primary constituents, inclusions etc.

In this part of the thesis the influence of Mn, Zr and Sc on the flow stress and the ductility during hot deformation has been investigated by use of the hot torsion test.

2. THEORETICAL BACKGROUND

2.1 CALCULATION OF σ-ε DATA FROM M-θ DATA

In the hot torsion test a circular cylindrical specimen is twisted with a given angular velocity,ω, at a given temperature, T. The quantities which are measured and recorded during testing are the torque, M, angle of twist, θ, and the temperature of the specimen. The torque-twist data is generally not useful because it depends on the specimen geometry. It is therefore desirable to convert the torque, twist angle and angular velocity to equivalent stress, strain and strain rate.

Considering a cylindrical bar of length *L* and a circular cross section of radius *r* subjected to a total twist angle θ, the shear strain, γ, and the shear strain rate, $\dot{\gamma}$, are given by Eq. III-1 and III-2:

$$\gamma = \frac{r}{L} \cdot \theta \tag{III- 1}$$

$$\dot{\gamma} = \frac{r}{L} \cdot \frac{d\theta}{dt} = \frac{r}{L} \cdot \omega \tag{III- 2}$$

The shear stress can be calculated by the method proposed by Fields and Backhofen (1957). Assuming that the ω/θ-ratio is constant the shear stress in the outer surface of the specimen can be expressed by Eq. III-3:

$$\tau_a = \frac{M}{2 \cdot \pi \cdot a^3} \left[3 + p + q \right] \tag{III- 3}$$

where *M* is the applied torque, *a* is the radius of the gauge section of the specimen and *p* and *q* are defined as follows:

$$p = \left(\frac{\partial \ln M}{\partial \ln \theta} \right)_{\omega} \tag{III- 4}$$

$$q = \left(\frac{\partial \ln M}{\partial \ln \omega} \right)_{\theta} \tag{III- 5}$$

For derivation of these expressions, see Nadai (1950) and Fields and Backhofen (1957) or the review of Rønning (1998).

By applying Eq. III-2 and III-3, the strain rate sensitivity can be defined according to Eq. III-6:

$$m = \frac{\partial \ln \tau}{\partial \ln \dot{\gamma}} = \frac{\partial \ln M}{\partial \ln \omega'} + \frac{\partial \ln(3 + p + q)}{\partial \ln \omega'} \qquad \text{(III- 6)}$$

Calculating the flow stress requires that the values of p and q are determined first. In the present investigation the peak torque has been used for further evaluation. The reason for this choice was the shape of the flow curves which in most cases showed an initial rise in the flow stress up to a peak value after which it declined. In this case, p=0 and only q has to be found. In Eq. III-3 the term q is very often replaced by the strain rate sensitivity, m. This substitution is only correct if q does not vary with the angular velocity which may be the case at low angular velocities. The value of q is usually in the range of 0.1-0.3 for temperatures above approximately $0.5T_m$ where T_m is the melting temperature. For high angular velocities q is no longer independent of the twist rate and hence q has to be adjusted accordingly, Rønning (1998).

Further, by employing the von Mises criterion for plastic flow, the shear stress, shear strain and shear strain rate can be converted to equivalent stress, strain and strain rates, Eqs. III-7, III-8 and III-9 (Bailey (1985)):

$$\sigma_a = \sqrt{3} \cdot \gamma_a \qquad \text{(III- 7)}$$

$$\varepsilon = \frac{\gamma}{\sqrt{3}} \qquad \text{(III- 8)}$$

$$\dot{\varepsilon} = \frac{\dot{\gamma}}{\sqrt{3}} \qquad \text{(III- 9)}$$

2.2 CONSTITUTIVE EQUATIONS

Constitutive equations describe the relationships between stress, strain, strain rate and temperature. Usually, at hot working temperatures, the flow stress saturates and reaches a steady state value. In these cases the strain is neglected. At hot working temperatures the deformation mechanisms are the same as for steady state creep which means that the same equations may be used in both cases. The most used equations are the power law, the exponential law and the hyperbolical sine law. In terms of the Zener-Hollomon parameter, Z, these equations are given as follows (Sellars and Tegart (1966)):

$$Z = A \cdot \sigma^{n} \qquad \text{(III- 10)}$$

$$Z = B \cdot \exp(\beta \cdot \sigma) \qquad \text{(III- 11)}$$

$$Z = C \cdot [\sinh(\alpha \cdot \sigma)]^{n'} \qquad \text{(III- 12)}$$

where A, B and C are constants while α, β, n and n’ are coefficieints that may vary with temperature. The Zener-Hollomon parameter, Z, is defines as (Zener and Hollomon (1944)):

$$Z = \dot{\varepsilon} \cdot \exp\left(\frac{Q}{R \cdot T}\right) \qquad \text{(III- 13)}$$

where $\dot{\varepsilon}$ is the equivalent strain rate, Q is the activation energy for hot deformation, R is the universal gas constant and T is the absolute temperature. The concept of the Zener-Hollomon parameter is that for a constant value of Z, the stress-strain curve could be obtained from different combinations of strain rate and temperature. Thus, for a constant level of stress the activation energy can be determined from the slope of a $\ln\dot{\varepsilon}$ -1/T plot as Q=slope·(-R).

Before one can apply these equations, all the coefficients need to be determined. One way of doing this is by the use of torque-twist data from the hot torsion test. The determination can be done either by graphical methods or by the use of a descrete least square approximation. It is then assumed that all coefficients are constants. It is important to note that the determined activation energy is also regarded as a curve fitting coefficient when the equations are fitted to the experimental data and that it has no physical meaning beyond this. Comparing data between alloys and conditions should be performed at constant Zener-Hollomon parameters. Thus the same activation energy has to be used. For this reason, the coefficients should be determined by fixing the activation energy to a certain value.

3. EXPERIMENTAL PROCEDURES

3.1 HOT TORSION EXPERIMENTS

3.1.1 The hot torsion machine

The hot torsion tests were carried out on a computer controlled torsion machine, Figure III-1. The specimens were mounted in two water-cooled grips and heated by use of an induction coil. The shaft was rotated by a hydraulic engine at a given angular velocity and the temperature was controlled by a Coreci temperature controller. The temperature in the specimens and the applied torque were measured by a calibrated K-type thermocouple and a calibrated load cell, respectively.

The input parameters were angular velocity, ω, total angle of twist, θ_{tot}, and temperature, T. The applied temperature scheme was programmed in the temperature controller and the other parameters were programmed in the computer. The output parameters, which were recorded by the computer, were the torque, angle of twist, time and temperature.

3.1.2 The hot torsion tests

The specimens used in this investigation had a gage length of 10 mm and a radius of the gage section of 5 mm. The specimen geometry is shown in Figure III-2. The specimens were machined from the extrusion billets with the centre axis of the specimens parallell to the centre axis of the billets. When the specimens were cut out from the billets, the periphery and the center of the cross section were avoided in order to use the most homogeneous parts of the cast billets.

Each alloy was tested at four temperatures (475, 500, 525 and 550°C) and four strain rates (0.003, 0.03, 0.3 and 1 s^{-1}) and all specimens were deformed to fracture. The alloys were tested in two conditions, as cast and heat treated. The material was heat treated at 500°C for 12 hours and water quenched afterwards. The heating rate to the holding temperature was 100°C/h.

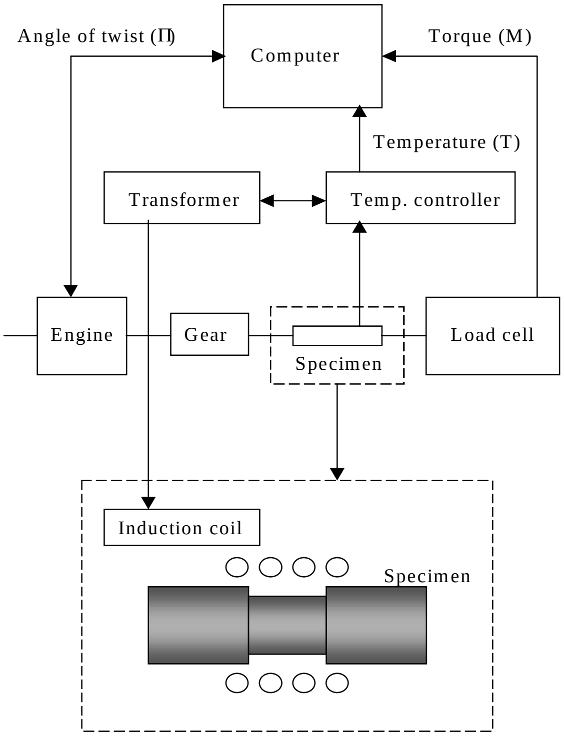

Figure III-1 *The experimental setup of the hot torsion machine.*

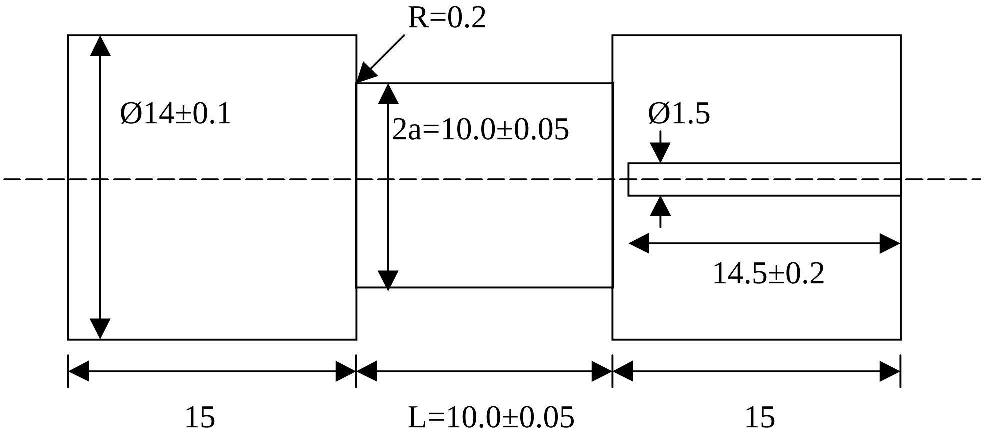

Figure III-2 *Geometry of the hot torsion specimens. Numbers in mm.*

After mounting, the specimens were subjected to the thermal programme listed in Table III-1. In order to avoid temperature overshoot the heating rate was lowered at the end of the heating cycle. In addition, the specimens were held at the deformation temperature for 180 seconds before deformation was started to minimize temperature gradients in the torsion specimen. All specimens were water-quenched immediately after deformation.

Table III-1 *Heating rates and times for a torsion test.*

Temperature interval (°C)	Heating rate (°C/s)	Time (s)
20-350	2	165
350-(T_{def}-20)	1	30, 80, 130, 180
(T_{def}-20)-T_{def}	0.5	40
T_{def}	0	180+time for def.

3.1.3 Temperature in the torsion specimens

At low strain rates and long duration times of the test, the temperature controller will maintain the temperature close to the setpoint value by balancing the relatively small heat generation rate by a correspondingly lower energy input from the induction heating system. However, at very high strain rates and short duration times, the temperature in the specimen will increase rapidly because the heat generation rate is much larger than the heat loss due to convection, radiation and conduction. Calculations of the temperature increase is very complex but usually convection and radiation to the surroundings can be neglected because their contributions are much lower than the conduction of heat to the watercooled shafts.

Neglecting heat loss due to radiation and convection, the real temperature in the torsion specimen is given by Eq. III-14:

$$T = T_{measured} + \Delta T_{pos} + k(\dot{\varepsilon}) \cdot \Delta T_{ad} \qquad \text{(III- 14)}$$

where $T_{measured}$ is the temperature measured 0.5 mm from the gauge section at the center axis, see Figure III-2, ΔT_{pos} is the difference between the temperature in the control position and the maximum temperature in the gauge section (outer fibre in the centre) before deformation, $k(\dot{\varepsilon})$ is a factor correcting for heat conduction and ΔT_{ad} is the temperature rise due to generation of heat during deformation. It can be assumed that $k(\dot{\varepsilon}) \approx 0$ at strain rates below 0.5 s^{-1} (Rønning (1998)), and other works have also shown that this assumption is valid at all testing conditions used in the present work, Zhou and Clode (1997).

4. RESULTS AND DISCUSSION

4.1 GENERAL OBSERVATIONS

In general, a decrease in the temperature is equivalent to an increase in the strain rate and results in an increased flow stress during deformation at elevated temperatures. These features are illustrated in Figure III-5 and Figure III-6 for cast and heat treated material, respectively. This is attributed to the high activation energy barrier for dislocation climb which is more seldom exceeded at lower temperatures. An increased strain rate simply increases the dislocation density, and thereby causes an increase in the flow stress.

In addition, by studying the flow curves in Figure III-5 and III-6 some other general observations can be made:

1. A small, but marked, decrease in the torque in the early stage of deformation can be observed. This can be clearly seen for the AlMg alloy, but is also observed for AlMgZr, AlMgMn and AlMgMnZr. It is observed both in cast and heat treated material, but it is more pronounced in the heat treated conditions for AlMgMn and AlMgMnZr.

2. The maximum torque increases with increasing alloy content, i.e. AlMg has the lowest torque whereas AlMgMnZrSc has the highest torque. The heat treated condition seems to have approximately the same maximum torque values. This will be discussed in more detail when evaluating the constitutive equations.

3. Further, a steady state torque is reached for the AlMg alloy whereas for the four other alloys the torque decreases gradually until fracture eventually occurs. This behaviour is observed both in the cast condition and in the heat treated condition. Thus, addition of Zr, Sc and especially Mn reduces the hot ductility of Al-Mg alloys.

4. The strain at fracture decreases as the alloy content increases, i.e. AlMg has the highest ductility whereas AlMgMnZrSc has the lowest ductility. The ductility is improved in the heat treated condition compared to the cast condition.

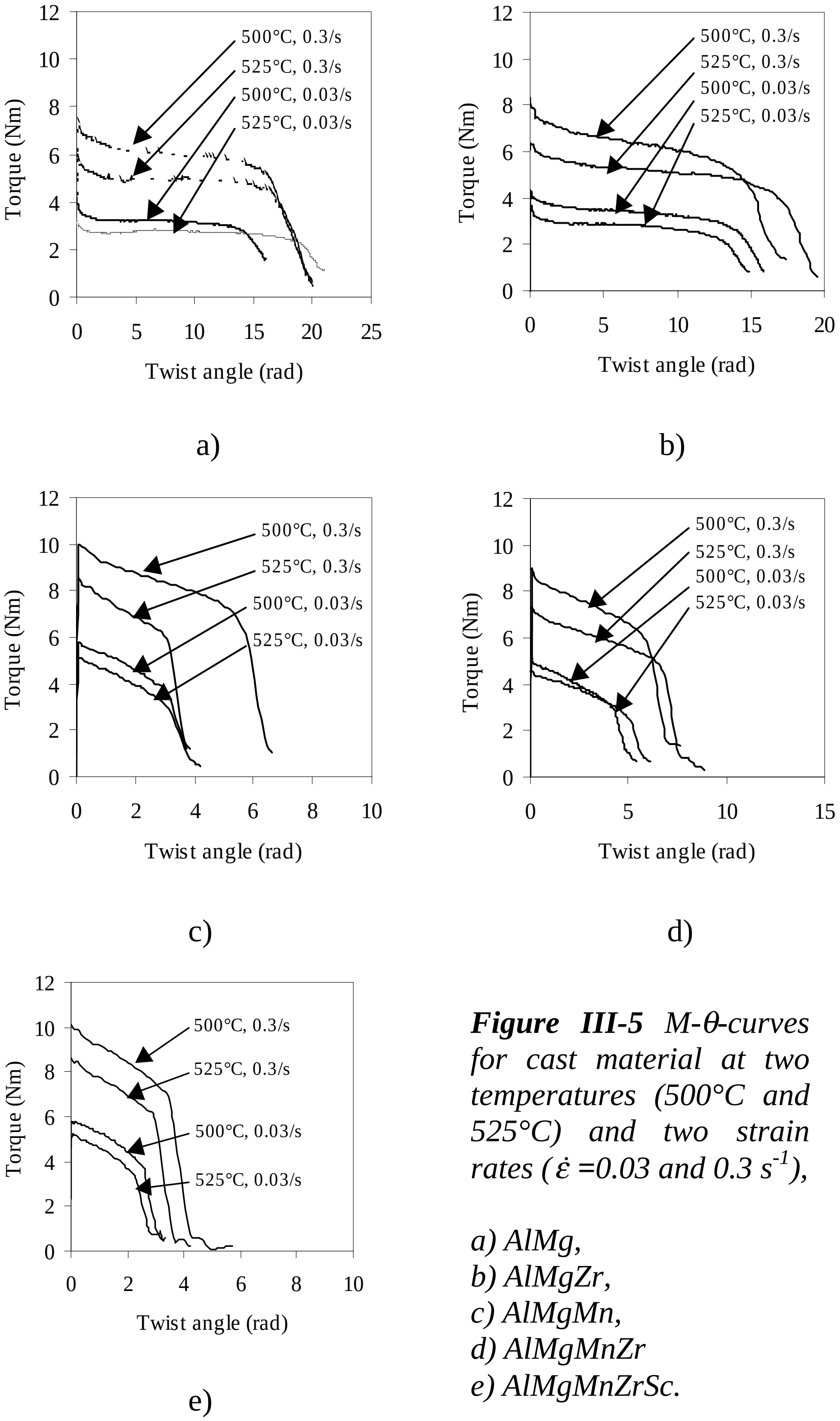

Figure III-5 *M-θ-curves for cast material at two temperatures (500°C and 525°C) and two strain rates ($\dot{\varepsilon}$ =0.03 and 0.3 s^{-1}),*

a) AlMg,
b) AlMgZr,
c) AlMgMn,
d) AlMgMnZr
e) AlMgMnZrSc.

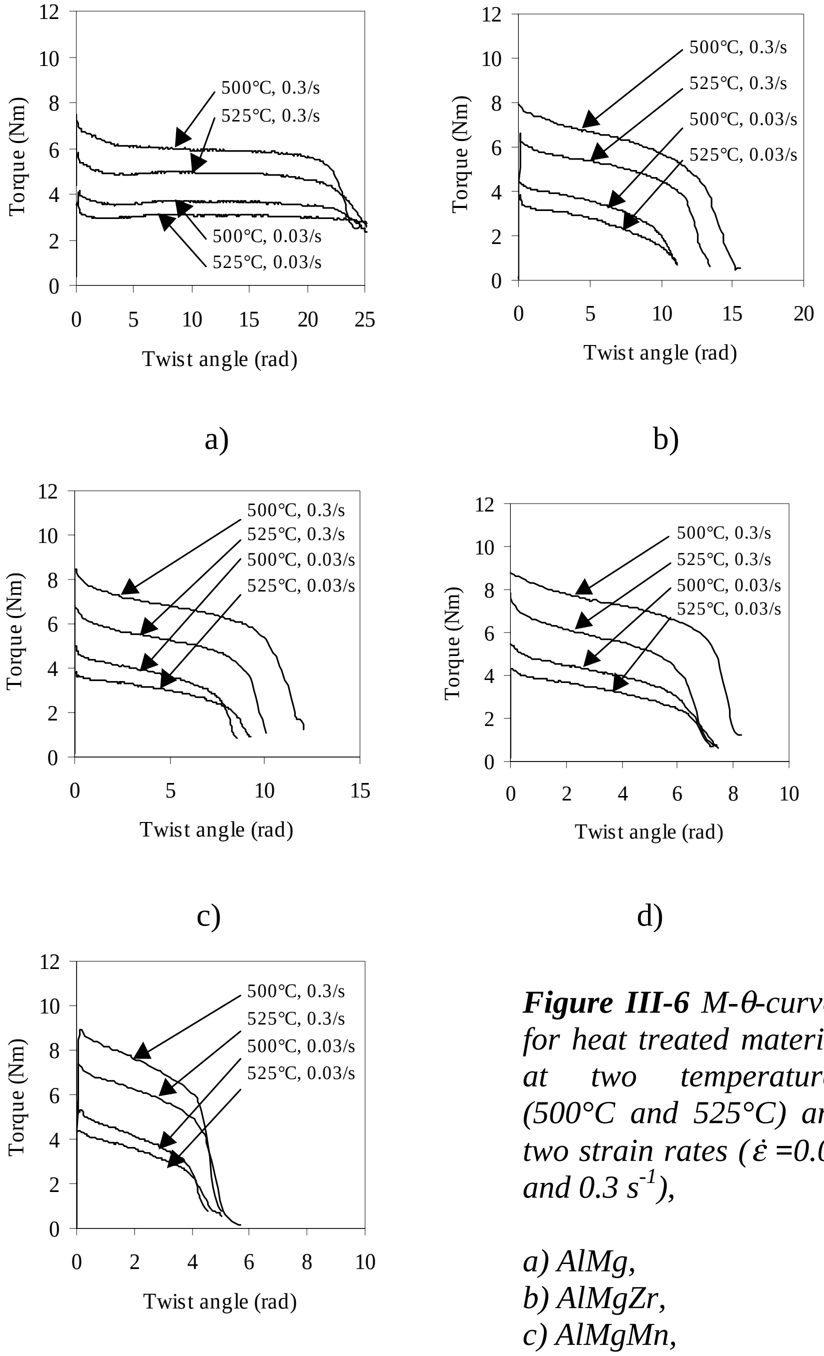

a) b)

c) d)

e)

Figure III-6 *M-θ-curves for heat treated material at two temperatures (500°C and 525°C) and two strain rates (*$\dot{\varepsilon}$ *=0.03 and 0.3* s^{-1}*),*

a) AlMg,
b) AlMgZr,
c) AlMgMn,
d) AlMgMnZr
e) AlMgMnZrSc.

4.2 FLOW STRESS PROPERTIES

4.2.1 Calculation of σ-ε data from M-θ data

Equation III-3 gives the relationship between the torque and the shear flow stress. Since the maximum values of the torque are being used, p=0, and only q has to be determined. This is done by plotting lnM versus lnω for constant strain rate and temperature. In order to correlate the measured torque to a given reference temperature, the relationship between torque and temperature was fitted to a power function, Eq. III-15, by use of the least square approximation method for each level of angular velocity. Values of the correlation factor, R^2, for the fitting of the coefficients a and b were better than 0.98

$$M = a \cdot T^{b} \qquad \text{III- 15}$$

Figure III-5 shows Eq.III-15 plotted together with the experimental data points for the AlMg alloy in the cast condition.

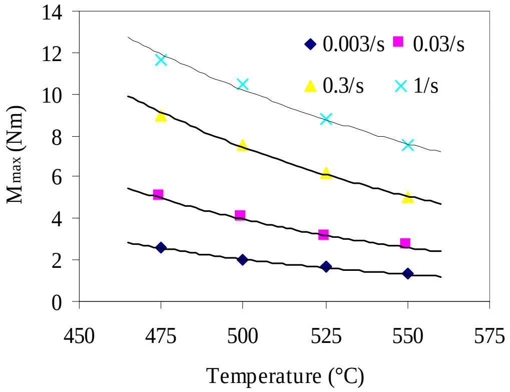

Figure III-5 *Maximum torque versus temperature for the AlMg alloy tested in the cast condition. Symbols indicates experimental values and lines are calculated from Eq. III-15.*

The torque was then recalculated (M’) by means of Eq. III-15 for the reference temperatures, i.e. the deformation temperatures, and these M’-values were used to construct lnM’-lnω-plots. In the range of the applied angular velocities good linear fits were obtained with a correlation factor better than 0.99 for all alloys. An example of a lnM'-lnω-plot is shown in Fig. III-6 for the cast condition of the AlMg alloy.

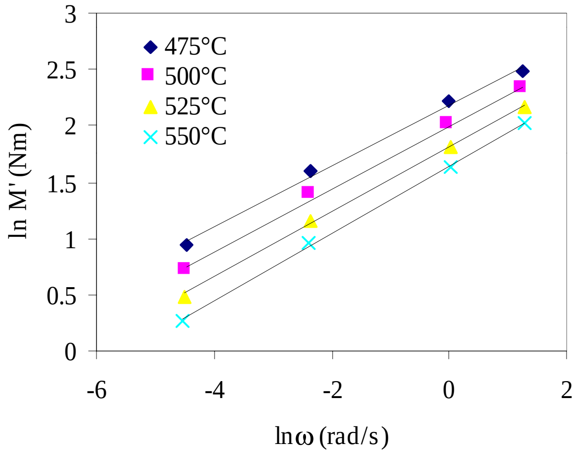

Figure III-6 *ln M' versus ln ω for alloy AlMg tested in the cast condition.*

As the results seem to correlate well in a linear relationship, the q-value is constant and can simply be determined as the slope of the lnM'-lnω-curves, see Eq. III-5. This was done by performing a least square approximation of the relationship lnM'=lnK+q·lnω. The resulting q-values are plotted as a function of temperature in Fig. III-7. The results are the mean value of two parallells with the error bar indicating two standard deviations. As can be seen, the q-values decrease with increasing alloy content, i.e. the additions of Mn, Zr and Sc decrease the value of q. The values of q also seems to be smaller in the heat treated material. However, even though this is not the case for AlMg it seems to be a general trend for the other alloys. It is also clear that the q-values increase slightly with temperature. For this reason another least square approximation was performed in order to obtain the coefficients c and d in the linear relationship in Eq. III-16:

$$q = c \cdot T + d \qquad \text{III- 16}$$

Equation III-16 was optimized for each alloy and for each of the two testing conditions (cast and heat treated). By combining Eqs. III-3, III-7 and III-16, the maximum equivalent flow stress can be calculated by use of the following expression:

$$\sigma_a = \frac{\sqrt{3} \cdot M_{\max}}{2 \cdot \pi \cdot a^3} \cdot \left[3 + c \cdot T + d\right] \tag{III- 17}$$

All the results from the torsion tests are tabulated in Appendix C.

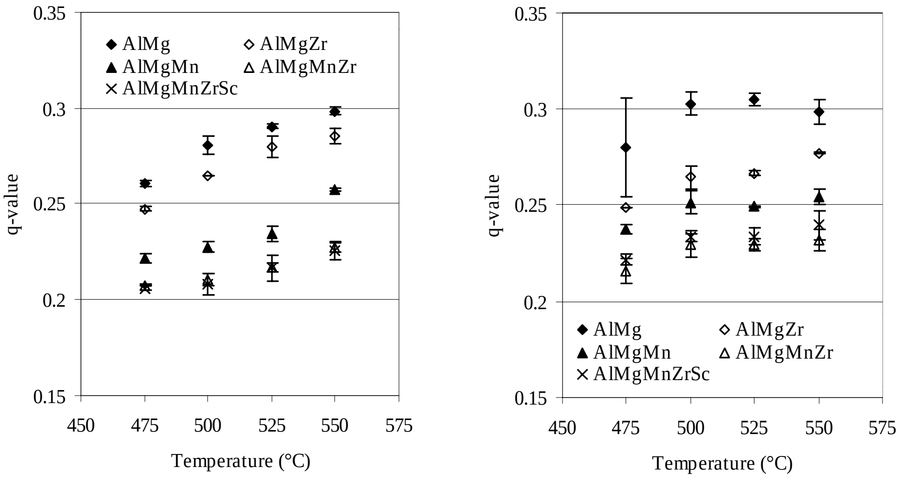

a)

b)

Figure III-7 *q-values as a function of temperature for all alloys. a) cast material and b) heat treated material.*

4.2.2 Coefficients in the constitutive equations

By fitting the constitutive equation to the experimental torison data it is possible to use the equations to evaluate the flow stress behaviour of the different alloys. Rønning (1998) calculated the coefficients in the constitutive equations for a range of different Al-Zn-Mg alloys. He used both graphical metods and the descrete least square approximation method (DLSA) and concluded that the latter method gave smaller error values. Thus, in the present investigation only the DLSA method was used and the application of this method is described in Appendix D.

The results of applying the DLSA method is given in Appendix E. The coefficients in the power law, exponential law and hyperbolical sine law are listed for all alloys. The error per datapoint, E_s/k, is also listed in the tables.

The three constitutive equations gave approximately the same value for the activation energy. However, the activation energy varied between the alloys, with an increase in the value with increasing alloy content, the values being in the range 136-161 kJ/mole, regardless of equation applied. It is worth mentioning that fitting all data of all alloys in one single approximation resulted in a value for Q of 143 kJ/mole. This is very close to the value of the activation energy for self diffusion in aluminium which is reported to be in the range 142-144 kJ/mole, Brown and Ashby (1980), Jena and Chaturvedi (1992), Brandes (1983). All the values obtained in the present investigation is within the range of values reported in the literature. According to Sellars and McGregor Tegart (1966) the activation energies for hot torsion are between 125 and 180 kJ/mole.

An important result is also the different error per datapoint which are very high for the exponential law, with values ranging between 0.20 and 0.30, Figure III-16. The power law gave an error per datapoint which was only 1/10 of the value of the exponential law. The reason for this is the relatively low stress level at which the tests were conducted. The exponential law is only valid at high stress levels while the power law is valid in the low stress regime. The hyperbolic sine law, which covers a wider stress regime (both low and high stresses), gave an even better fit to the experimental data with error values even lower than that of the power law, Figure IV-8.

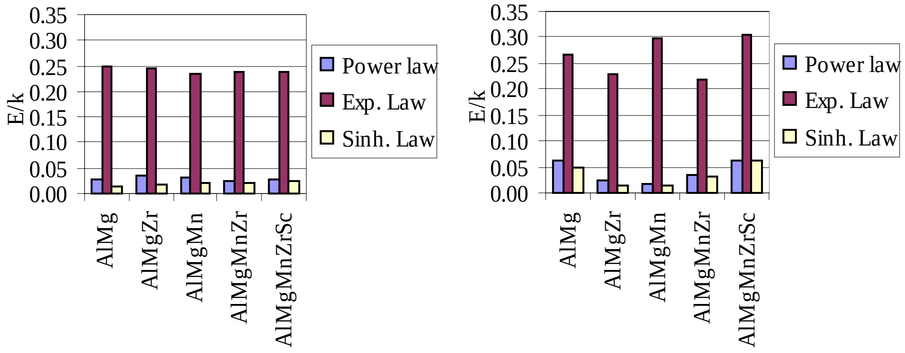

a) b)

Figure III-8 *Error per data point, E/k, for a) cast material and b) heat treated material.*

Thus, due to the low values of error per data point, the hyperbolic sine law is used in the further evaluation.

A new descrete least squares approximation was performed, but now with a constant value of the activation energy of 143 kJ/mole. The new values of the coefficients are listed in Tables III-3 and III-4.

Table III-3 *Coefficients in the hyperbolic sine law obtained with Q=143 kJ/mole. Cast material.*

	α	n'	ln C	E/k
AlMg-c	0.01692	3.107	20.784	0.01355
AlMgZr-c	0.01551	3.272	20.919	0.01995
AlMgMn-c	0.01174	3.816	21.742	0.02516
AlMgMnZr-c	0.00646	4.400	24.483	0.02573
AlMgMnZrSc-c	0.00778	4.308	23.519	0.03310

Table III-4 *Coefficients in the hyperbolic sine law obtained with Q=143 kJ/mole. Heat treated material.*

	α	n'	ln C	E/k
AlMg-h	0.01688	3.061	20.874	0.04906
AlMgZr-h	0.01511	3.398	21.034	0.01604
AlMgMn-h	0.00565	3.954	25.255	0.02052
AlMgMnZr-h	0.01158	4.071	21.924	0.02966
AlMgMnZrSc-h	0.003879	4.173	26.741	0.02290

In hot working, it is often desirable to express the flow stress as a function of the Zener-Hollomon parameter according to the hyperbolic sine law and Eq. III-12 then takes the following form:

$$\sigma = \frac{1}{\alpha} \cdot \operatorname{arcsin} h\left[\left(\frac{Z}{C}\right)^{\frac{1}{n'}}\right] \tag{III-18}$$

The experimental data and Eq. III-18 is plotted for the as cast material in Fig. III-9. The coefficients in Table III-3 were used and similar results were obtained for the heat treated material.

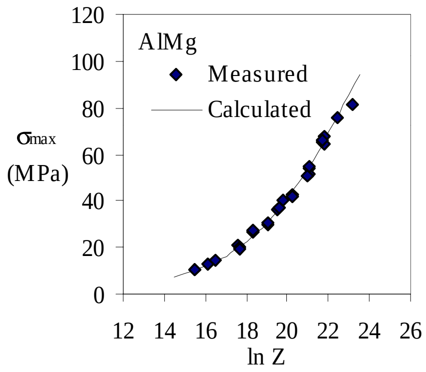

a)

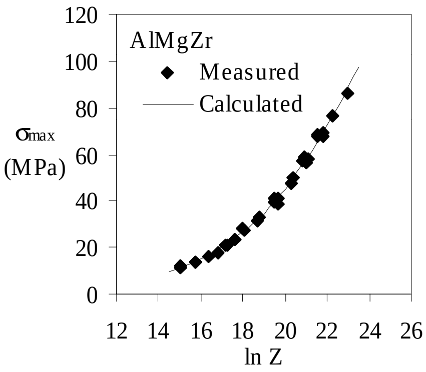

b)

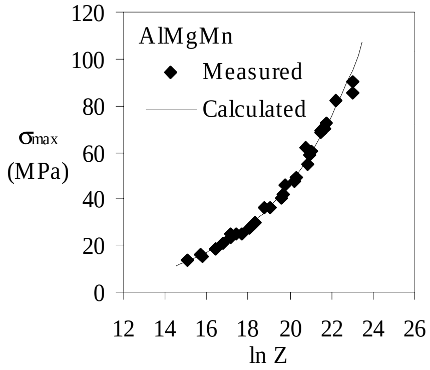

c)

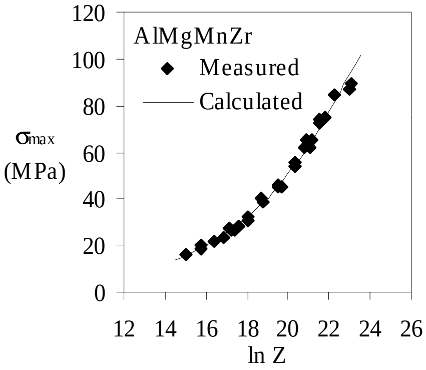

d)

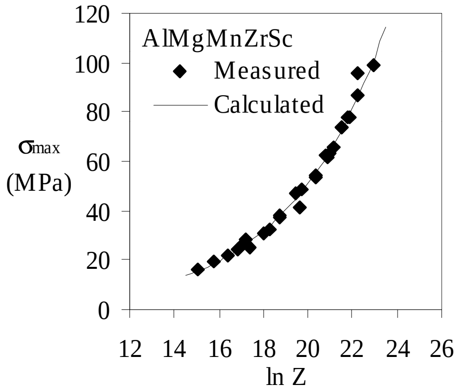

e)

Figure III-9 *Maximum equivalent flow stress as a function of the Zener-Hollomon parameter for heat treated material. Symbols are experimental data and lines are calculated by Eq. IV-18*

a) AlMg,
b) AlMgZr,
c) AlMgMn,
d) AlMgMnZr and
e) *AlMgMnZrSc.*

4.2.3 Effect of heat treatment on the flow stress

The flow stress is plotted as a function of the Zener-Hollomon parameter in Fig. III-18. The results show that the flow stress for the cast material and heat treated material of the AlMg and AlMgZr alloys is practically the same over the whole Z-range investigated. This can be explained by considering Fig. II-10, which shows that heat treatment of cast material at a temperature at 475°C and above, no more than approximately 3 minutes is necessary to dissolve all β-Al_3Mg_2. The torsion specimens were held at temperature for three minutes in addition to the heating period. This means that at the time when the deformation of the cast material starts, all magnesium will be in solid solution. Thus, it can be concluded that since all β-Al_3Mg_2 is dissolved in the two conditions, they will exhibit practically the same high temperature flow stress.

Considering the alloys containing Mn, Zr and Sc, it is shown that the flow stress is reduced somewhat when the material is heat treated, Fig. III-10 c)-e). This could be explained in terms of a reduction in the solid solution concentration, especially of manganese, due to precipitation of dispersoids during heat treatment, see Part II of the thesis. However, the difference is not very large and it is assumed that precipitation in the as cast specimens will take place during heating and also during deformation to some degree. However, this has not been investigated in any detail.

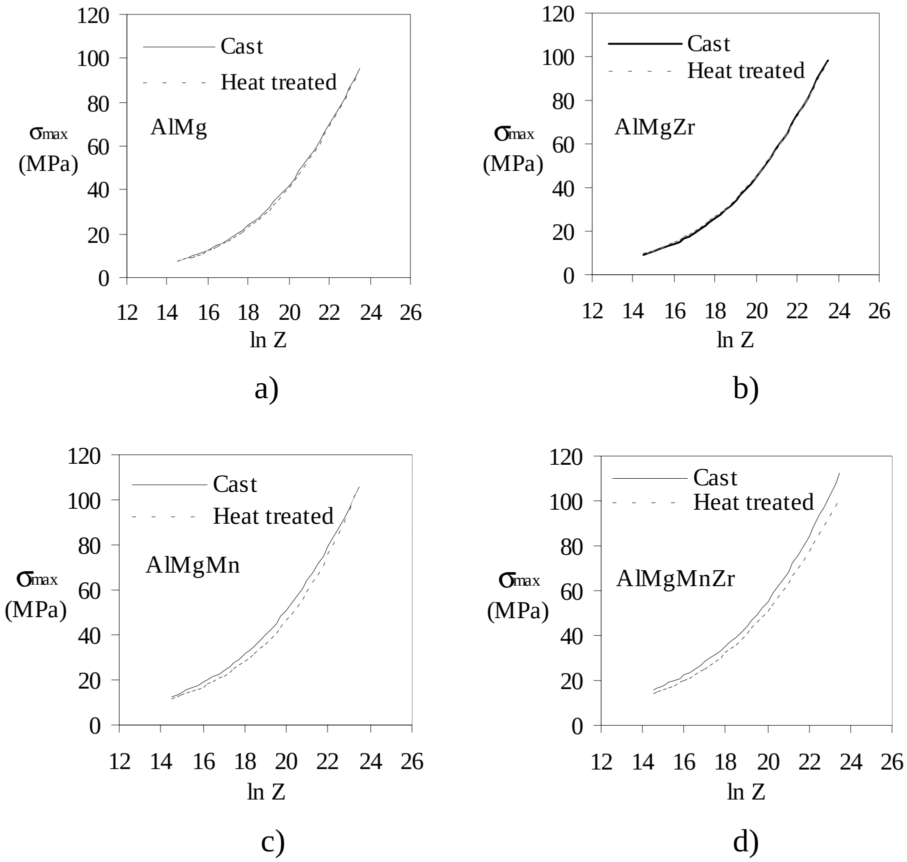

a)

b)

c)

d)

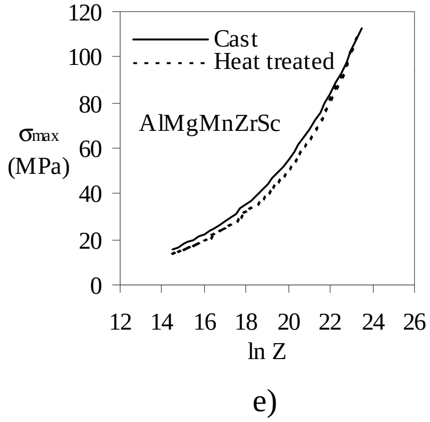

e)

Figure III-10 *Equivalent flow stress as afunction of Z for cast material and heat treated material.*

a) *AlMg,*
b) *AlMgZr,*
c) *AlMgMn,*
d) *AlMgMnZr and*
e) *AlMgMnZrSc.*

4.2.4 Effect of alloying elements on the flow stress

In order to assess the effect of additions of manganese, zirconium and scandium to the Al-4.5Mg alloy on the flow resistance, Eq. III-18 was evaluated by plotting the flow stress as a function of the Zener-Hollomon parameter, Fig. III-11.

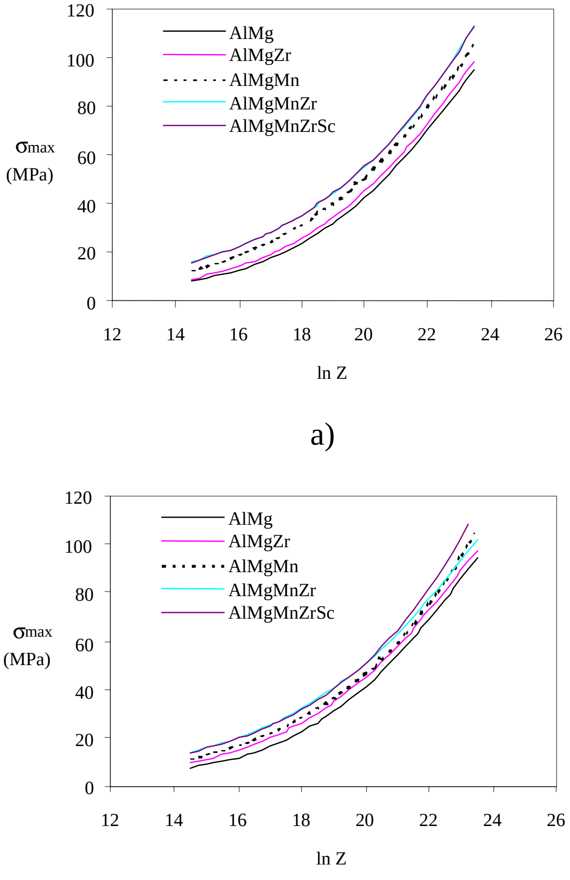

a)

b)

Figure III-11 *Eqiuvalent flow stress as a function of Z. a) cast material and b) heat treated material. Activation energy, Q, is 143 kJ/mole.*

The flow curves are shifted upwards to higher stresses as the content of alloying element increases. This means that additions of Mn, Zr and Sc, alone or in combinations, increases the flow stress of the alloys. Especially manganese increases the flow stress, while the effect of zirconium and scandium are smaller. It is shown that additions of manganese to Al, AlMgSi and AlZnMg-alloys increases the flow stress at hot working temperatures, see Castle and Lang (1977), Lang and Castle (1977) and Lang et al. (1981). The increase in the flow stress is due to hardening effects from solid solution and particles.

The relative change in flow stress is plotted as a function of the Zener-Hollomon parameter in Fig. III-12. The values for Mn, Zr, Mn+Zr and Mn+Zr+Sc are all calculated relative to the flow stress for the AlMg alloy while for Sc the values are calculated relative to the AlMgMnZr alloy. The effect of Mn, Zr and Sc strongly depends on the Zener-Hollomon parameter. At low values the increase in flow stress is large, while at high values the increase in flow stress is small. Nakashima et al. (1990) found that dispersed manganese dispersoids contributed to the athermal stress component and not to the thermal (effective stress) component. They explained this decreasing effect of manganese dispersoids with decreaseing Z-values by the fraction of dislocations interacting with the dispersoids. At low Z-values the dislocation density was low and the dislocation spacings become higher than the interparticle spacing. Thus, a large fraction of the dislocations interact with the dispersoids. At higher Z-values the dislocation density was higher and the dislocation spacing became smaller than the interparticle spacing. In this case a smaller fraction of the dislocation interacted with the dispersoids, thus reducing their effect upon the flow stress.

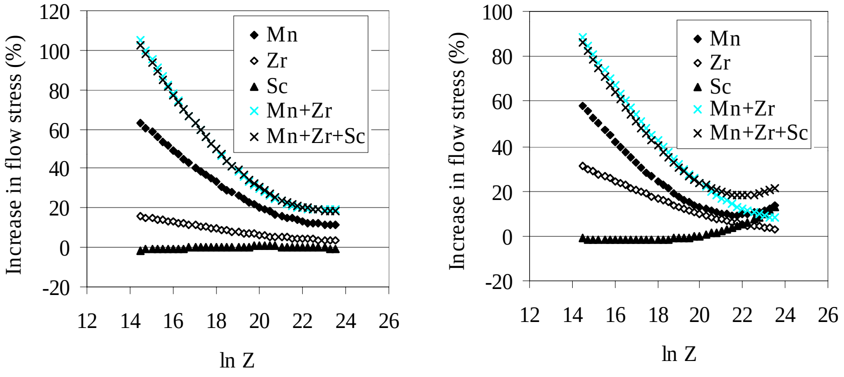

a) b)

Figure III-12 *Increase in flow stress due to Mn-, Zr- and Sc-additions to Al-4.5%Mg. a) Cast material, b) Heat treated material*

4.3 DECREASE IN TORQUE AT LOW TWIST ANGLES

The flow behaviour is different for the five alloys. In all tests the torque rises steeply, almost instantaneously, until a maximum value is reached. Then, for the AlMg alloy a decrease in torque follows in the early stage of deformation, before a steady state torque is reached. Finally, the torque decreases again until fracture occurs. The same observations are made for the cast condition of the AlMgZr alloy where a steady state is reached at the highest temperatures and the lowest strain rates. The decrease in torque in the early stage of deformation of the AlMg alloy can also be seen in the AlMgZr, AlMgMn and AlMgMnZr alloys, especially in the heat treated conditions, see Figure III-4 b), c) and d). However, no steady state plateau is observed for these alloys but the torque gradually decreases with an almost constant slope as the deformation proceeds until fracture occurs.

Several mechanisms have been proposed to explain a decrease in torque during torsion testing, (Pettersen (1999)):

i) Change in texture which causes a reduction in the average Taylor factor
ii) Increase in temperature during deformation
iii) Changes in the microstructure (cell or subgrain size)
iv) Deformation mechanisms, diffusional creep, grain boundary sliding or dynamic recovery and
v) Coarsening of particles (Nakashima et al. (1990)).

Except for an increase in the deformation temperature, little evidence of these mechanisms exists. Due to the nature of the flow behaviour observed, it is assumed that none of the abovementioned mechanisms i) to v) is responsible for the flow softening found in the present investigation. However, two other mechanisms are proposed to explain the observations:

vi) Dislocation and solute interactions causing a reduction in the frictional stress (Usui et al. (1986)) and
vii) Development of pores at second phase particles.

The transient decrease in torque at low strains in the AlMg alloy is ascribed to vi) while the continuous decrease in the torque in the other alloys is ascribed to vii). The latter mechanism is dealt with in the next section.

Observations of the transient decrease in torque similar to those in this work have been made by other investigators (Nakashima et al. (1990), Usui et al. (1986), Oliver and Nix (1982)) in Al-Mg alloys. It is believed that this could be related to the strong interactions between dislocations and solute magnesium atoms. An explanation for this theory is given in the following.

In terms of shear stresses, the deformation stress, τ, can be divided into two parts, a socalled quasi-athermal contribution, τ_{AT}, and a thermal contribution, τ_T, Eq. III-19, Nes (1997):

$$\tau = \tau_T + \tau_{AT} \qquad \text{III- 19}$$

The quasi-athermal contribution reflects the effects of strain rate and temperature on the microstructure and can be given by an expression of the type $\tau_{AT} = \alpha G b \sqrt{\rho}$. The thermal contribution is the flow stress contribution due to obstacle limited glide and is basically the frictional stress, τ_i, given by Eq. III-20:

$$\tau_T \equiv \tau_i = \frac{kT}{V_a} \cdot \operatorname{arcsin} h\left(\frac{\dot{\gamma} \cdot \exp(Q/kT)}{2\rho_m b^2 c \nu_D} \right) \qquad \text{III- 20}$$

Here, k is the Boltzmann constant, T is the absolute temperature, V_a is the activation volume, Q is the activation energy, $\dot{\gamma}$ is the shear strain rate, ρ_m is the density of mobile dislocations, b is the Burgers vector, c is a constant and ν_D is the Debye frequency.

Obstacle limited glide is the mechanisms involving interactions experienced by mobile dislocations and dislocation interactions with atoms in solid solution and dragging of jogged dislocations.

In Al-Mg alloys with a high solute content dislocations move by viscous glide (dragging of solute atmospheres) at intermediate stresses and hence the influence of the frictional stress is large (Oikawa and Langdon (1985)). During loading of the specimen, dislocations are generated and the density increases. However, it takes some time to obtain a steady state dislocation density and during this time it is assumed that the contribution from the athermal part is small. Considering Eq. III-20 and the Orowan equation, $\dot{\gamma} = \rho \cdot v \cdot b$, for a constant strain rate, the speed of the mobile dislocations has to be reduced if the dislocation density increases. The result is a decrease in the frictional stress and hence the total deformation stress decreases. This explains the apparent transient flow softening phenomenon at low strains in Al-Mg alloys.

4.4 DECREASE IN TORQUE AT HIGHER STRAINS - HOT DUCTILITY

4.4.1 Hot ductility and crack formation

The hot ductility is strongly dependent on whether the alloy contains manganese or not, Fig. III-13. In general, when Zr, Sc and/or Mn are added the ductility decreases, but manganese has the largest effect.

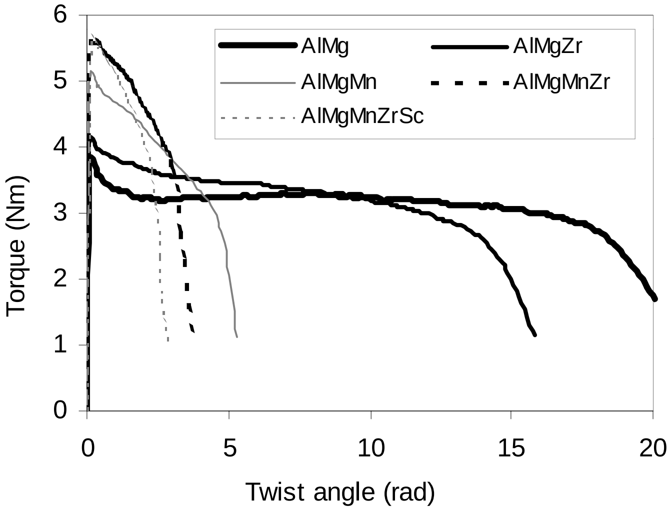

Figure III-13 *Flow curves for the alloys deformed in the cast condition at 500°C and 0.03 s^{-1}.*

The ductility can be improved by heat treatment. The ductility seems to increase with the thermal load and the flow curves become more or less similar to those of the alloys without manganese, Fig. III-14. As manganese has a major influence upon the hot ductility, the AlMgMn alloy was investigated in more detail. Samples of this alloy were continous heat treated to 500°C with a heating rate of 10°C/h and the resulting microstructure is shown in Fig. II-13 a), Part II. Some torsion tests were carried out in order to investigate the microstructures of the torsion specimens after deformation. Fig. III-15 show some microstructures of specimens deformed to different strains and it is evident that the continuous reduction in the flow stress is due to formation of pores. After a strain of ε=0.75 only some small pores can be seen in the surface regions of the specimen, Fig. III-15 a). At a strain of ε=1.5 large pores can be seen clearly in the surface regions. The micrographs in Fig. III-15 c) and d) show the microstructure of the sample deformed to ε=1.5 at a higher magnification. It can be seen that pores and cracks are always connected to primary constituents and precipitate free zones. It can be concluded that the drop in the flow stress during hot torsion testing is due to the formation of pores. The pores are nucleated at primary constituents and cracks grow along regions with a low density of dispersoids.

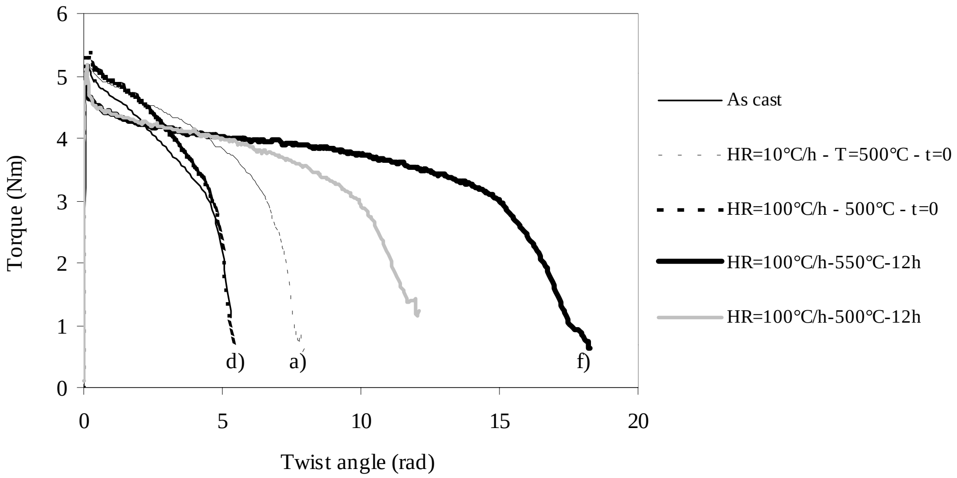

Figure III-14 *Flow curves for different conditions of AlMgMn deformed at 500°C and 0.03* s^{-1}. *a), d) and f) refers to the microstructures shown in Figure II-13, Part II.*

The results presented above can be explained as follows. The manganese is present in solid solution, in large primary constituents and in dispersoids. The primary constituents are very hard and may act as strain raisers during deformation. Thus, they constitute possible sites for void nucleation. As the deformation proceeds the voids can develop into cracks which finally results in a failure of the specimen.

As shown in Part II the microstructure can be manipulated by adjusting the heat treatment parameters (time, temperature). It was shown that a slow heating rate resulted in a very fine and homogeneous distribution of dispersoids inside the grains and precipitate free zones along interdendritic regions, Fig. II-14 a) The corresponding flow curve of this microstructure is shown in Fig. III-14 a). A more rapid heating followed by a long heating time at the temperature resulted in coarser dispersoids and a lower density, Fig. II-13 f). The corresponding flow curve is shown in Fig. III-14 f). An improvement of approximately 150% in ductility was obtained by changing the size and dispersity of the Mn-dispersoids.

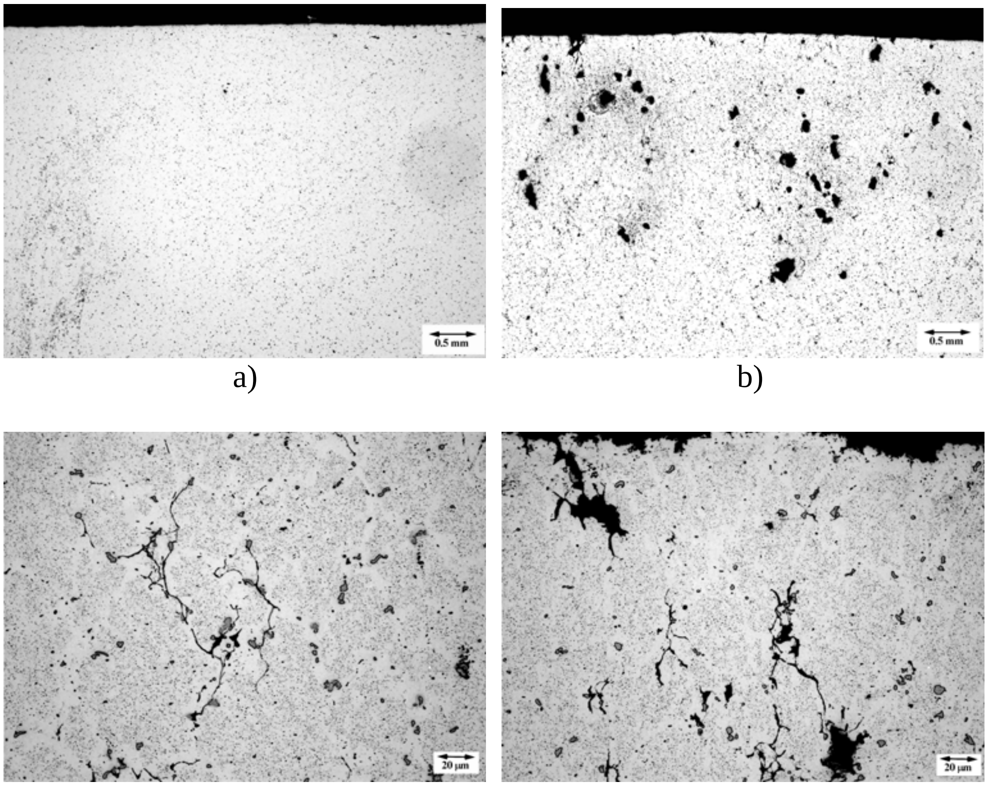

a) b)

c) d)

Figure III-15 *Micrographs showing pore formation in AlMgMn deformed in hot torsion,* $T_{def}=500°C$, $\dot{\varepsilon}=0.03\ s^{-1}$. *a)* $\varepsilon=0.75$ *(2.6 rad), surface region, b)* $\varepsilon=1.5$ *(5.2 rad), surface region, c)* $\varepsilon=1.5$, *r=3mm and c)* $\varepsilon=1.5$, *surface region*

The low ductility in the first case is most likely due to a combination of strain concentrations and void initiation in the precipitate free zones. These zones is the regions which initially have a low manganese concentration and where the primary constituents are located. The grain interior is filled up with small dispersoids, and gain strength from the particles. The precipitate free zones are soft regions with lower strength. As the material deforms the strain will be concentrated in the soft regions. Thus, the combination of the primary constituents as nucleation sites for voids and precipitate free zones with strain concentrations, makes these regions preferred regions for crack initiations and crack growth. The higher ductility in the latter case supports this theory. The rather homogeneous distribution of the dispersoids lowers the strain concentration and thereby the initiation of voids are suppressed.

5. CONCLUSIONS

- Two different types of flow softening were observed during torsion testing. In the purest alloy, AlMg, an initial transient decrease was observed before the torque reached a steady state torque. In the other alloys, a continuous decrease in torque until fracture eventually occurred was observed. Thus, additions of Zr, Sc and especially Mn affect the hot ductility.
- The hot ductility decreases as the content of alloying elements increases. Especially manganese reduces the ductility considerably. However, the ductility in the manganese containing alloys increases with an increase in the thermal load of the material due to a change in the size and distribution.
- The ductility is related to the formation of pores which initiates at primary constituents.
- The heat treated and the cast material exhibit more or less the same flow stress in AlMg and AlMgZr. However, the heat treated conditions of the Mn containing alloys have a slightly lower flow stress than the cast conditions. This is attributed to a lower content of Mn in solid solution in the heat treated conditions. Thus, the differences between cast and heat treated specimens are not appreciably large, probably due to precipitation of dispersoids during the heat-up period before deformation and during the deformation.
- The flow stress increases as the content of alloying element increases. The change in flow stress depends on the Zener-Hollomon parameter. At low Z-values the increase in flow stress is large while at high Z-values the increase in flow stress is lower.
- The amount of scandium (0.1wt%) does not influence the flow stress considerably. However in the heat treated material an increase in flow stress up to 10% was detected.
- 0.15 wt% zirconium increased the flow stress in the heat treated material from 30% to 5% at the highest and lowest Z-values, respectively.
- 0.7 wt% manganese increased the flow stress in the heat treated material from 60% to 10% at the highest and lowest Z-values, respectively.

REFERENCES

Bailey, J., *Fundamental aspects of torsional loading*, in Metals Handbook, vol. 8, ASM, Ohio, 1985.

Brandes, E.A., *Smithells Reference Book*, Butterworth, London, 1983.

Brown, A.M. and Ashby, M.F., *Correlations for diffusion const*ants, Acta Met., vol. 28 (1980), p. 1085.

Castle, A.F. and Lang, G., *Der Einfluss von Zusatzelementen und Warmebehandlungen auf das Warmunformverhalten binarer Aluminiumlegierungen beim Stangpressen*, Aluminium, vol. 53, nr. 9 (1977), p. 535.

Fields, D.S. and Backhofen, W.A., *Determination of strain-hardening characteristics by torsion testing*, Am. Soc. Test. Mater. Proc., vol. 57 (1957), p. 1259.

Jena, A.K. and Chaturvedi, M.C., *Phase transformations in materials*, Prentice Hall, New Jersey, 1992.

Lang, G. and Castle, A.F., *Influence of copper, manganese and chromium additions on the extrudability of AlMgSi-alloys*, Proceedings of Second International Aluminium Extrusion Technology Seminar, Aluminium Assoc., Washington D.C., 1977, p. 293.

Lang, G., Vitalis, L. and Lakner, J., *Einfluss von chrom, mangan und zirkonium auf die Warm- und Kaltumformbarkeit von AlZn4,5Mg1*, Aluminium, vol. 57, nr. 6 (1981), p. 423.

Lefstad, M., *Metallurgical speed limitations during the extrusion of AlMgSi-alloys*, Dr. Scient. dissertation, University of Trondheim, Deparment of Physics, 1993.

Nakashima, H., Iwasaki, K., Goto, S. and Yoshinaga, H., *Combined effect of solution and dispersion hardenings at high temperatures*, Met. Trans. JIM, vol. 31, nr. 1 (1990), p. 35.

Nadai, A., *Theory of flow and fracture of solids*, McGraw-Hill Book Company, USA, 1950.

Nes, E., *Modelling work hardening and stress saturation in fcc metals*, Sintef report nr. STF24 S97525, Sintef Materials Technology, October 1997.

Oikawa, H. and Langdon, T.G., *The creep characteristics of pure metals and metallic solid solution alloys*, in Creep of Metals and Alloys, eds. Evans, R.W. and Wilshire, B., The Institute of Metals, Swansea, 1985.

Oikawa and Langdon (1985) in Progress in Creep and Fracture, vol.3.

Oliver, W.C. and Nix, W.D., *High temperature deformation of oxide dispersion strengthened Al and Al-Mg solid solutions*, Acta Met., vol. 30 (1982), p. 1335.

Pettersen, T., *A study of the deformation and recrystallization microstructures and textures in AA6060 and AA6082 alloys*, Ph.D. Dissertation, The Norwegian University of Science and Technology (NTNU), 1999.

Rønning, B., *Constitutive relationships for AlZnMg, AlZnMgCr and AlZnMgZr alloys*, Ph.D. Dissertation, The Norwegian University of Science and Technology (NTNU), 1998.

Sellars and Tegart (1966)

Usui, E., Inaba, T. and Shinano, N., *Influence of Mn and Mg additions on hot deformation of aluminium and aluminium alloys*, Z. Metallkunde, vol. 77, nr. 3 (1986), p. 179.

Zhou, M. and Clode, M-P., *Modelling of high temperature viscoplastic floe of aluminium alloys by hot torsion testing*, Mat. Sci. Tech., vol. 13, October (1997), p. 818.

PART IV

EXTRUSION EXPERIMENTS

1. INTRODUCTION

In general, the high strength Al-Mg alloys are difficult to extrude due to their very high deformation resistance caused by the magnesium in solid solution. Therefore, these alloys are usually being hot rolled to plates and sheets. Extrusion of these alloys is very often restricted to profiles with a very simple geometry. The extrudability of different alloys is very often ranked after the force/pressure each alloy requires in order to be pressed through a certain die.

This part of the thesis gives a discussion of how Mn, Zr and Sc affect the force required for extruding these alloys.

2. THEORY AND BACKGROUND

2.1 RAM LOAD DURING EXTRUSION

Hot extrusion is a process in which a billet, enclosed in a container, is pushed through a shaped opening at an elevated temperature. As a result of the forming operation, the initial cross section area of the billet is reduced and a profile of solid or hollow cross section is produced.

The most important parameters in hot deformation processes are the material properties, the forming temperature, T_{def}, the ram speed, V_{ram}, and the reduction ratio, R. All of these factors will affect the ram load required to press the billet through the die. Figure IV-1 shows a typical variation of the ram load as a function of the ram displacement.

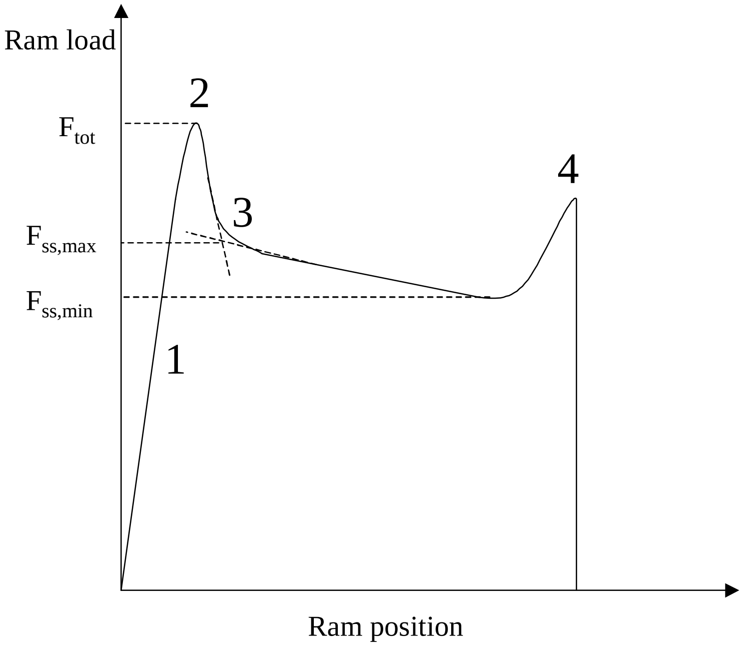

Figure IV-1 *Schematic ram load versus ram displacement during direct hot extrusion.*

Some quantities are defined in the figure: F_{tot} is the maximum load, $F_{ss,max}$ is the maximum steady state load and $F_{ss,min}$ is the minimum steady state load.

The curve can be divided into four stages. First the load increases rapidly as the billet fills the container (1). The load increases further to a peak value (2) before it drops to the maximum steady state load (3). Sheppard and Tutcher (1980) attributed this shape of the load curve to the formation of a deformation zone. They also investigated the microstructure of the billet in TEM and found that a subgrain structure develops and grows ”backwards” in the billet as the load passes through the peak. When the load drops and reaches the maximum steady state load (3) it was observed that a subgrain structure had developed through the entire billet. As the extrusion continues, the load decreases steadily due to reduced friction between the billet and the container wall. At the end, the load increases (4) again due to radial material flow in the remaining billet, Laue and Stenger (1976).

2.2 PREDICTION OF THE RAM LOAD

An exact calculation of the required extrusion load is difficult because of the influence of a whole range of different factors. In addition to the factors mentioned above (material properties, T, V_{ram} and R), the load also depends on (Lange (1985)): i) stress distribution and loading, ii) temperature distribution, iii) alloy chemistry and microstructure, iv) strain and strain rate gradients, v) conditions of friction between billet and container and vi) tool geometry and tool material.

However, simplified methods have been developed and, in general, the total load during extrusion is the sum of the load required to deform the material and the load required to overcome the friction forces. An estimate of the total load during direct extrusion can be expressed as (Corneliussen (1987)):

$$F_{tot} = F_{def} + F_{fric} \qquad \text{IV-1}$$

where

$$F_{def} = \frac{\sigma \cdot A_b \cdot \ln R}{\eta_f} \qquad \text{IV-2}$$

and

$$F_{fric} = \frac{\sigma \cdot \mu \cdot \pi \cdot d_b \cdot (l_b - 0.5 \cdot (d_b - d_p))}{\eta_f} \qquad \text{IV-3}$$

Here, σ is the flow stress of the material being deformed, A_b and d_b are the area and the diameter of the billet after upsetting in the container, d_p is the diameter of the profile, l_b is the initial length of the billet, $R=(d_0/d_1)^2$ is the reduction ratio, μ is the friction coefficient for the friction between the billet and the container wall (0.04-0.1) and η_f is the efficiency factor of deformation (0.2-0.6 for hot deformation), Corneliussen (1987).

From Eqs. IV-2 and IV-3 it can be stated that the extrusion load strongly depends on the flow stress of the material and hence it is of great interest to be able to predict the flow stress of the material during extrusion. The most used expression for the mean equivalent flow stress is the hyperbolical sine law

$$\bar{\sigma} = \frac{1}{\alpha} \cdot \operatorname{arcsin} h\left[\left(\frac{Z}{C}\right)^{\frac{1}{n'}}\right] \qquad \text{IV-4}$$

where the Zener-Hollomon parameter, Z, is defined as:

$$Z = \dot{\varepsilon} \cdot \exp\left(\frac{Q}{R \cdot T}\right) \qquad \text{IV-5}$$

$\dot{\varepsilon}$ is the mean equivalent strain rate for the extrusion process, Q is the activation energy, R is the universal gas constant and T is the absolute temperature.

However, as the flow stress is dependent on the temperature and the strain rate there is a problem related to the calculation of Z. Material volumes flowing through the extrusion die exhibit different temperature and strain rate histories. Dependent on the ram speed, the material volumes exhibit equivalent strain rates from 1-2 s^{-1} to several hundreds when it enters the deformation zone near the die. Gradients of temperature and strain rate is thus expected in the billet and also in the profile and this makes the calculateion of Z very complicated . Furu et. al. (1993) simulated the extrusion of flat profiles (4x78,5 mm^2) and found no temperature gradients across the profile thickness for ram speeds of 0.5 mm/s and 2 mm/s. Increasing the ram speed to 25 mm/s resulted in a temperature variation of 60°C through the profile thickness. The strain rate varied sharply across the thickness. However, as the ram speed varied from 0.5 mm/s to 25 mm/s, which means a factor of 50, the variation in the Zener-Hollomon parameter is less than a factor of 4. Thus, at ram speeds less than 2 mm/s temperature gradients can be neglected while strain rate gradients still has to be taken into account.

In computer simulations, finite-element techniques (Grasmo et.al. (1992)) and the so-called minimized upper-bound extrusion solution (Sheppard (1981)) may be used to calculate Z. However, simplified methods may be used to to determine the mean equivalent strain rate, $\dot{\bar{\varepsilon}}$. In this work the Feltham equation has been used (Feltham (1956)):

$$\dot{\bar{\varepsilon}} = \frac{6 \cdot V_{ram} \cdot d_b^2 \cdot \ln R \cdot \tan \omega}{d_b^3 - d_p^3} \qquad \text{IV-6}$$

where V_{ram} is the ram speed, d_b is the billet diameter after upsetting, d_p is the diameter of the profile, R is the reduction ratio and ω is the deformation zone angle. Adie and Alexander (1967) found that the deformation zone angle varied with the reduction ratio as

$$\omega = 54.1 + 3.45 \cdot \ln R \qquad \text{IV-7}$$

Equation IV-6 is the most commonly used equation for strain rate calculations and it has been demonstrated that this equation produce acceptable results, Sheppard and Tutcher (1980).

By the use of Eqs. IV-4 to IV-7 it should be possible to make simplified calculations of average values of equivalent strain rate and stress for different combinations of temperatures and ram speeds.

3. EXPERIMENTAL PROCEDURES

3.1 THE EXTRUSION PRESS

Extrusion billets of a diameter Ø93 mm were extruded in a 8 MN vertical laboratory extrusion press, Figure IV-2. The container temperature was kept constant at 430°C and the temperature of the ram tip before each press was in the range 100-200°C. A thermocouple was placed in the die and made it possible to measure the temperature of the profile surface during extrusion. The response time of the thermocouple is estimated to be approximately 2 seconds, Lefstad (1993). The die geometry was constructed so as to give a cross sectional area of the profiles of 20x25 mm^2 (reduction ratio, R=13.6). Some profiles of dimensions 5x70 mm^2 in cross section area (R=19.4) were also produced for welding purposes. The details of the die geometries are given in Appendix F. The temperature, ram speed and ram load was recorded during extrusion. The experimental setup and the measuring techniques are explained in detail by Lefstad (1993).

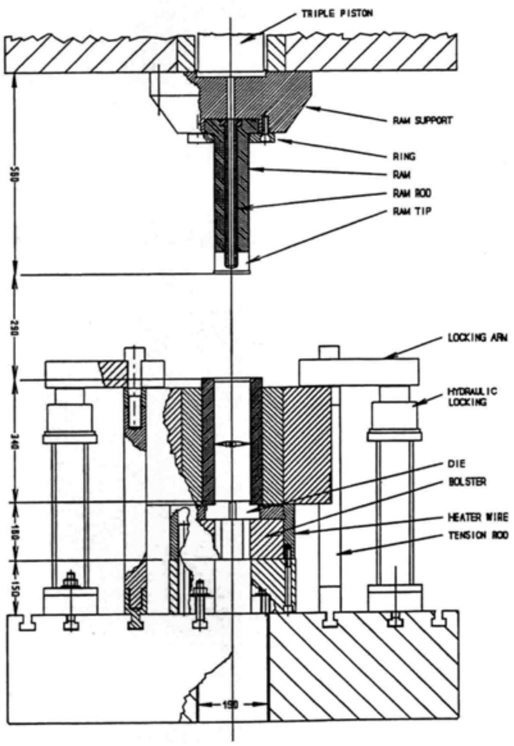

Figure IV-2 The extrusion press. Lefstad (1993).

3.2 THE EXPERIMENTS

The billets were cut into lengths of 150 mm, heat treated at 500°C for 12 hours with a heating rate of 100°C/h and then quenched in water at room-temperature. Before extrusion, the billets were heated to the extrusion temperature in an induction coil with a heating rate of approximately 1°C/s. Afterwards, the billets were quickly transferred to the container and then the extrusion was started. The billets were extruded at three temperatures (450, 475 and 500°C) with a ram speed of 1 mm/s. For the temperature of 475°C two other ram speeds were also applied (0.3 and 3 mm/s). For each testing condition two parallels were performed which means that (3+2)x2=10 billets of each alloy were extruded. The flat profiles (5x70 mm^2) were extruded at 475°C and a ram speed of 1 mm/s.

The water cooling system was arranged in such a way that the profiles entered the cooling zone approximately 100 cm below the outlet of the extrusion die. Due to the very low extrusion rates, the profiles were not effectively water-cooled before approximately 245, 74 and 25 seconds after they had left the outlet of the die when applying the ram speeds 0.3, 1 and 3 mm/s, respectively.

4. RESULTS AND DISCUSSION

4.1 RAM LOAD - RAM DISPLACEMENT CURVES

Examples of recorded load-displacement curves from the extrusion experiments is plotted in Figure IV-3. Temperature-displacement curves are included in the same plots. The load-curves are normalised such that the ram position at peak load is zero. The temperature curves are normalised accordingly and in addition the response time of the measuring system (2 seconds) is taken into account.

Some general considerations can be made by studying the figures. First of all, the ram load increases rapidly to a peak load before it decreases and reaches a minimum value towards the end of the extrusion. In the last part of the deformation, the load increases again before the press is stopped. The temperature rises steeply in the beginning of each press as the material starts to flow through the die and reaches a maximum at the peak load. The temperature then decreases towards the end of the press. This is probably due to the very low ram speeds used, which allow heat transfer into the container and the water-cooled end of the profile. The part of the profile which is cooled first, acts as a heat sink for the material that has not yet entered the cooling zone.

Figure IV-3 b) shows the effect of increasing the ram speed when keeping the billet temperature constant at 475°C. The ram force increases with the ram speed and the curves are approximately parallel. The temperature curves clearly illustrate the increased generation of deformation heat as the ram speed increases. Note that the maximum profile temperature at V_{ram}=0.3 mm/s is only 465°C which is well below the initial billet temperature (475°C). This is due to the temperature difference between the billet and the container (T_{cont}=430°C) which allows cooling of the billet at low ram speeds.

The effect of increasing the temperature at a constant ram speed of 1 mm/s is shown in Figure IV-3 c). Increased billet temperature results in a decrease in the peak load. However, at the end of the press, the load is the same for the three billet temperatures (450, 475 and 500°C). The reason for this can be seen from the temperature curves. At the start of the press the temperatures are at different levels while the temperature seems to converge with increasing displacement. Again, this could be explained by the water-cooling of the profiles.

An important result is the increase in the ram load with the increase in alloy content. Compared with AlMg, the peak load of AlMgMnZrSc increased approximately 22% at a billet temperature of 475°C and a ram speed of 1 mm/s, Figure IV-3 a). An corresponding temperature rise of approximately 10°C is also observed and is ascribed to a higher deformation heat generation as the alloy content is increased.

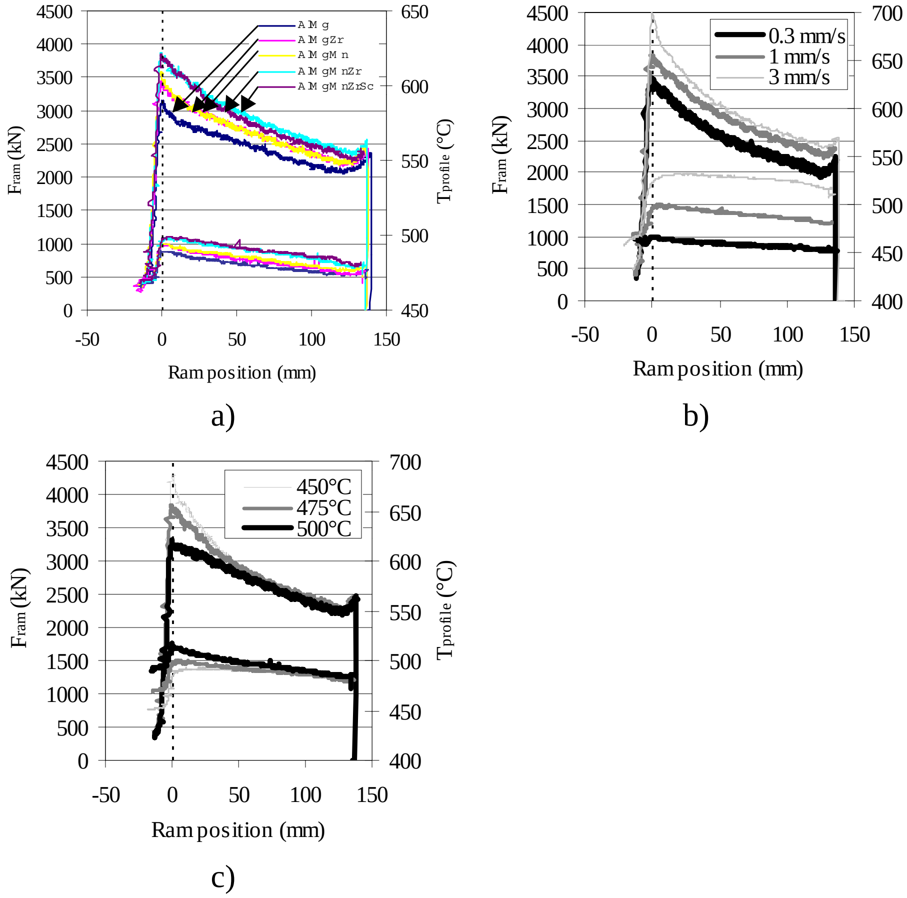

a)

b)

c)

Figure IV-3 *Recorded load-displacement curves. a)* T_{billet}*=475°C and* V_{st}*=1mm/s, b) effect of ram speed, alloy AlMgMnZrSc and c) effect of billet temperature, alloy AlMgMnZrSc.*

4.2 RAM LOAD AND FLOW STRESS

In order to analyse the extrusion data in more detail the flow stress of the material during extrusion was calculated by use of Eq. IV-4 and the coefficients in Table III-4. Zener-Hollomon parameters were calculated from Eqs. IV-5, IV-6 and IV-7 with an activation energy of 143 kJ/mole. Values of the flow stress were calculated at F_{tot}, $F_{ss,max}$ and $F_{ss,min}$ by using the corresponding temperatures in the Zener-Hollomon equation, Eq. IV-5. See Appendix G for single values. The results of these calculations are plotted in Figure IV-4 as the ram load versus flow stress.

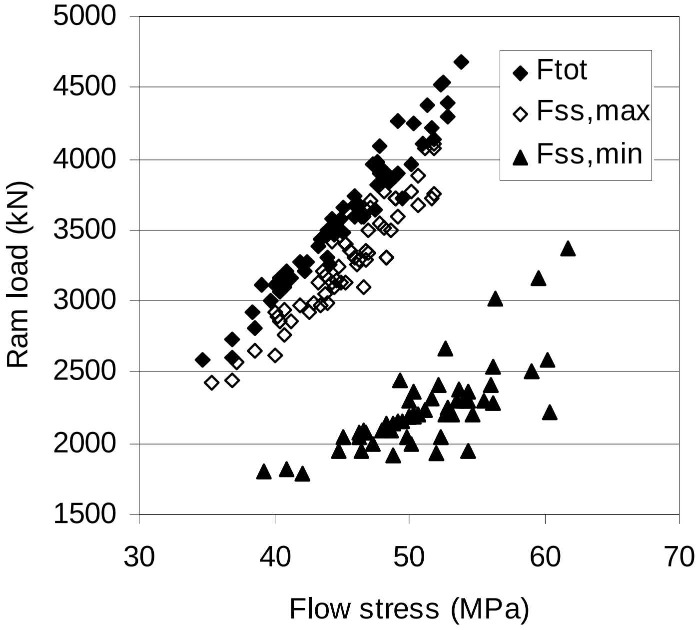

Figure IV-4 *Ram load versus flow stress.*

Linear relationships seem to be valid for F_{tot} and $F_{ss,max}$ while for $F_{ss,min}$ a large scatter was obtained. The limiting parameter for an industrial extrusion process is the available extrusion force. If the extrusion force of the material exceeds that of the available force then the material is not extrudable. From this consideration and from the results in the previous sections it was decided to use the peak load for further analysis.

The relationship between the ram load and the calculated flow stress was obtained by a least square approximation and can be expressed as Eq. IV-8:

$$F_{tot} = 105{,}2 \cdot \bar{\sigma} - 1167 \qquad \text{IV-8}$$

with an correlation factor $R^2=0.95$ and F_{tot} in kN and $\bar{\sigma}$ in MPa. Several attempts have been made to find correlations between the ram force and flow stress on one hand and the reduction ratio and the Zener-Hollomon parameter on the other hand. For instance, Sheppard and Tutcher (1980) found that the extrusion pressure could be related to R and Z as $p/\sigma = a + b \cdot \ln R + c \cdot \ln Z$ where p is the pressure. In this work only a few profiles with the reduction ratio of 20 was produced and the results from these experiments were not included in the calculations above. Consequently, results from only one profile geometry has been analysed and Eq. IV-8 gave the best relationship between the ram load and the flow stress. Eq. IV-8 was further used to calculate the ram load by using the results from the hot torsion test. This was done simply by combining Eqs. IV-4 and IV-8 and by using the coefficients in Table III-4. The calculated values of the peak ram load are plotted against the measured peak ram load, Figure IV-5. All data points fall on a straight 1:1 line with a correlation factor $R^2=0.95$, which demonstrates that the above equations can be used with good precision in the investigated Z-range.

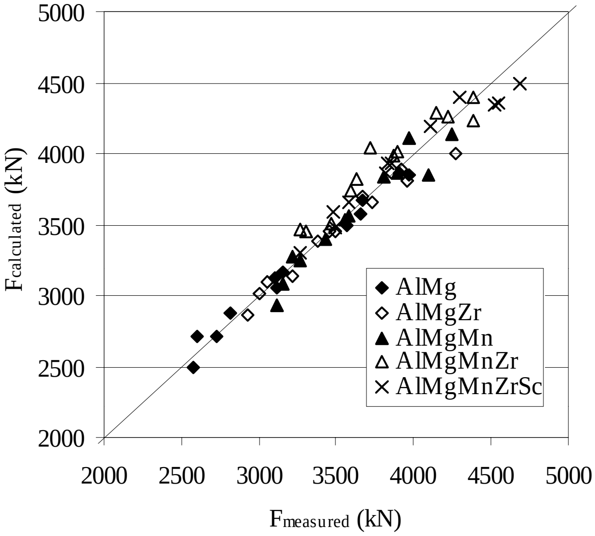

Figure IV-5 *Calculated ram load versus measured ram load.*

4.3 THE EFFECT OF MANGANESE, ZIRCONIUM AND SCANDIUM ON THE RAM LOAD.

As observed in the load-displacements curves in Section 4.1 the load increases with the addition of Mn, Zr and Sc. The peak load was calculated by use of Eqs. IV-4 to IV-8 and the results are shown in Figure IV-6 a). The values for the different alloys are almost parallel through the investigated range of Z-values. Relative to the AlMg alloy, the peak loads increase by approximately 420, 540, 1000 and 1000 kN for the alloys AlMgZr, AlMgMn, AlMgMnZr and AlMgMnZrSc, respectively. The contribution from the alloying elements on the ram load is plotted in Figure IV-6 b). As can be seen the load change decreases with Z for Zr and Mn while a very small change was observed for Sc. These observations are the same as those found in the results of the torsion testing, see Part III for further discussions.

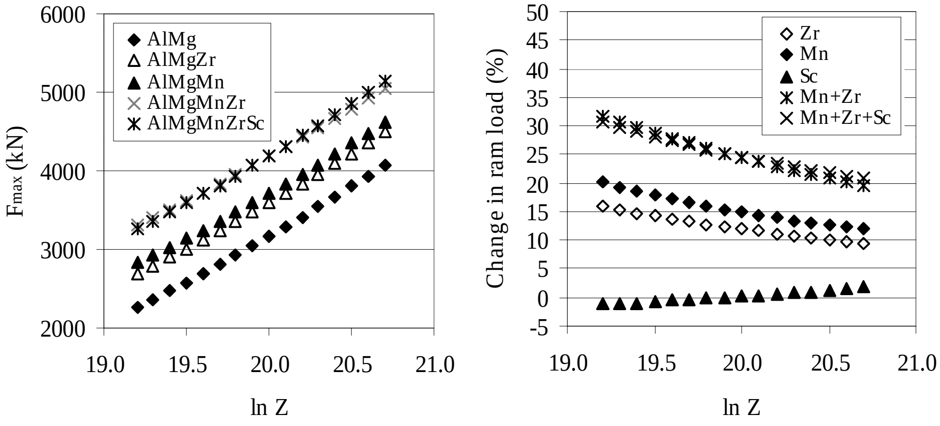

Figure IV-6 *a) F_{max} as a function of ln Z, calculated values and b) relative change in F_{max} as a function of ln Z.*

Thus, it may be concluded that Zr and Mn increases the extrusion force of the material, while the effect of Sc is very small. The increase in ram load is associated with the presence of dispersoids of the type Al6Mn, Al3Zr and Al3(Sc,Zr). These particles increase the flow stress of the material.

A combined addition of Mn, Zr and Sc increased the extrusion pressure by 20-30%.

5. CONCLUSIONS

- The break-through pressure increases with increasing ram speed and decreasing billet temperature
- The temperature in the material flowing through the tool increases with increasing ram speed due to increased friction forces between the flowing material and the die and container wall.
- The temperature in the flowing material decreases during extrusion due to the low ram speeds. Heat flow may occur into the container wall and into the extruded profile.
- The maximum ram load and the maximum and minimum steady state ram load are linearly proportional to the flow stress of the material.
- The hyperbolical sine law and the relationship between the ram load and the flow stress may be used to calculate the ram load. The coefficients in the hyperbolical sine law were derived from the torsion tests. Calculated ram loads correspond very well with measured ram loads.
- The addition of Mn, Zr and Sc results in an increase in the ram load. This increase is most likely due to the presence of dispersoids of type Al_6Mn, Al_3Zr and $Al_3(Sc,Zr)$.
- The effect of these dispersoids decreases with increasing Zener-Hollomon parameter.

REFERENCES

Aidie, J.F. and Alexander, J.M., *A graphical method of obtaining hodographs for upper-bound solutions to axi-symmetric problems,* Int. J. Mech. Sci., vol. 9 (1967), p. 349.

Corneliussen, R. G., *Plastiske bearbeidingsprosesser,* Universitetsforlaget, Oslo, 1987.

Feltham, P., *Extrusion of metals,* Met. Treat., November (1956), p. 440.

Furu, T., Sødahl, Ø., Nes, E., Hanssen, L. and Lohne, O., *The influence of the extrusion speed on texture in the surface layer of aluminium profiles investigated by the EBSP technique,* ICOTOM 10, 1993.

Grasmo, G., Holthe, K., Støren, S., Valberg, H., Flatval, R., Hanssen, L., Lefstad, M., Lohne, O., Welo, T., Ørsund, R. and Herberg, J., *Modelling of two-dimensional extrusion,* Proceedings from the International Aluminium Extrusion Technology Seminar, Chicago, 1992.

Lange, K., *Handbook of metal forming,* McGraw-Hill, New York, 1985.

Laue, K. and Stenger, H., *Extrusion: process, machinery, tooling,* ASM, Metals Park, Ohio, 1976.

Lefstad, M., *Metallurgical speed limitations during the extrusion of AlMgSi-alloys,* Dr. Scient. dissertation, University of Trondheim, Department of Physics, 1993.

Sheppard, T., *Temperature and speed effects in hot extrusion of aluminium alloys,* Met. Tech., April (1981), p. 130.

Sheppard, T. and Tutcher, M.G., *Development of duplex deformation substructure during extrusion of a commercial Al-5Mg-0.8Mn alloy,* Met. Sci., December (1980), p. 579.

PART V
RECRYSTALLISATION PROPERTIES

1. INTRODUCTION

One of the basic ideas of preparing Al-Mg alloys with the additions of dispersoid forming elements is to increase the resistance against recrystallization.

The recrystallization properties of Al-Mg alloys with the additions of Mn, Zr and Sc, have been investigated by means of metallography, hardness measurements and texture measurements. The following part of the thesis reports on the results from these investigations.

2. THEORY AND BACKGROUND

The theory of recovery and recrystallization was treated in Part 1 of this thesis and the reader is referred to that part for more general considerations. Here, a literature review of the effect of different alloying elements upon recrystallization properties will be given.

2.1 THE EFFECT OF SOLUTE DRAG AND ZENER DRAG ON THE RECRYSTALLIZATION RESISTANCE OF ALUMINIUM ALLOYS

Introduction of transition metals as alloying elements in aluminium alloys is based on the fact that these elements are effective in retarding recrystallization and thereby increasing the recrystallization temperature. The beneficial features that make most of the transition metals attractive for use as anti-recrystallization agents are (Toropova (1998)):

i) Incomplete 3d-shell with minimum electrons
ii) Large difference in atomic radius compared to aluminium
iii) Formation of supersaturated solid solutions with aluminium upon solidification, and
iv) Decomposition of these supersaturated solid solutions result in the formation of thermally stable fine precipitates.

Further, the ability of a specific alloying element to retard recrystallization usually depends on whether the element is in solid solution or if it is present in particles. In general, solutes forming large strain fields in the aluminium solid solution exhibit a high recrystallization resistance due to restrictions in the dislocation movement. If the element is present in form of a fine distribution of small particles the recrystallization is retarded due to pinning of subgrain boundaries and grain boundaries. However, if the particles are very coarse they will accelerate recrystallization by acting as nucleation sites for new grains.

2.1.1 Al-Mg

An increased recrystallization resistance is obtained when aluminium contains up to 1 wt% Mg in solid solution, Baxter et. al. (1998) and McQueen and Ryum (1985). This is believed to arise from a lower mobility of grain boundaries due to hindering of dislocation motion by solute drag.

However, at magnesium concentrations above 1 wt% it has been observed that the recrystallization resistance decreases with increasing concentration, Baxter et al. (1998) and Johansen (1998). This is ascribed to an increase in the stored energy, which compensates the effect of viscous drag of Mg atoms. Thus, the driving force for recrystallization is higher than the retarding solute dragging forces.

2.1.2 Al-Mn

The effect of Mn upon retarding recrystallization is generally higher in solid solution than when it is present in particles. Recrystallization resistance is therefore dependent on the applied heat treatment procedure during which the volume fraction of particles increases and the solid solution concentration decreases, as reported by Altenpohl (1965) and Firth and Williams (1969) for Al-Mn alloys. Westengen et al. (1981) found that Mn is most effective in solid solution both in binary Al-Mn alloys and in AlMgSi alloys of commercial purity.

Furrer and Hausch (1979) studied an Al-1%Mn alloy of commercial purity and found that recrystallization occurred by particle stimulated nucleation. If a fine particle dispersion is present, other nucleation sites is operating and the nucleation rate is reduced due to pinning of subgrain boundaries. An additional pinning effect originated from Mn in solid solution.

2.1.3 Al-Zr

Ryum (1969) studied a binary Al-0.5wt%Zr alloy and concluded that the Al_3Zr-dispersoids raised the recrystallization temperature considerable. This was caused by two effects: i) by altering the deformation mode resulting in a reduction in the lattice curvature and thereby retarding the recrystallization and ii) by pinning grain boundaries and subgrain boundaries. Westengen et. al. (1981) demonstrated that the recrystallization temperature of Al-0.17wt%Zr increased by 70°C and 180°C in as cast and heat treated material, respectively. Since most Zr is retained in solid solution in the as cast condition while small, dispersed Al_3Zr-dispersoids were formed in the heat treated condition, it is concluded that Zr-dispersoids are more effective in retarding recrystallization than Zr in solid solution. This was also observed for AlZnMg alloys.

2.1.4 Al-Sc, Al-Sc-Zr and Al-Sc-Mn

The effect of Sc in solid solution is almost absent, whereas Al_3Sc-dispersoids have a very strong effect in retarding recrystallization, Toropova et. al. (1998), see Part I, Section 2. They reported that in cold rolled sheets the temperature at which the recrystallization starts increases from 200°C (pure aluminium) to 340°C-380°C depending on the condition prior to cold rolling. They also show that the recrystallization temperature increases as the Zener-ratio (f/r) for Al_3Sc-particles increases. Riddle (1998) also found that Sc increases the recrystallization in Al-Sc alloys when Al_3Sc-particles are precipitated.

If Sc and Zr are simultaneously present in aluminium the recrystallization resistance is improved considerably compared to binary alloys (Al-Sc and Al-Zr). The reason for this is the ability of Zr to stabilize the supersaturated solid solution and to slow down the coarsening of the decomposition products. This has been demonstrated by several authors, for instance Davydov et al. (1996), Zakharov (1997) and Riddle (1998).

Mn-additions to binary Al-Sc alloys do not change the kinetics of the decomposition of the Al-Sc solid solution. It is claimed that this is connected with a relatively small effect that Mn has on the supersaturation of the solid solution of Sc in Al. In addition, the supersaturation of Mn and Sc decomposes independently and no combined phases of Sc and Mn are formed, see Part I, Section 2. Thus, it is expected that a decomposed alloy exhibits a high recrystallization resistance. If Mn-particles are large, this may reduce the resistance due to PSN.

2.1.5 Al-Mg-Mn, Al-Mg-Zr, Al-Mg-Sc and Al-Mg-Zr-Sc

The precipitation of Mn, Zr and Sc is not affected considerably in Al-Mg alloys, Part I, Section 2. Very few data on the effect of Mg on the decomposition of Mn in an Al-Mg alloy exists in the literature. However, since the solubility of Mn decreases with Mg concentration it is believed that the decomposition is accelerated and that the effect upon recrystallization is similar to that of binary Al-Mn alloys, Mondolfo (1976).

Some authors have found that the decomposition of Al_3Sc in an Al-Mg-matrix is more or less similar to that observed in binary Al-Sc alloys, Røyset and Ryum (1994), while other only find that the decomposition is suppressed to lower temperatures, Zakharov (1997). In fact, the lattice misfit between the coherent particles of the Al_3Zr- and Al_3Sc-phases and the Al-Mg matrix decreases with an increasing Mg-concentration. It is thus expected that the decomposition is easier and that the particles are more stable in an Al-Mg-matrix than in a pure Al-matrix. However, Riddle (1998) found that an Al-2Mg-0.12Zr alloy was recrystallized completely after 1 hour annealing at 400°C while Al-2Mg-0.12Zr-0.2Sc was unrecrystallized even after 1 hour at 550°C. Comparison of recrystallization data in Al-Mg- and Al-Mg-Sc-alloys show that the latter alloy system has an improved recrystallization resistance. It can be stated that: i) the temperature at which the recrystallization started increased from 300°C in an Al-4wt%Mg alloy to 575°C in a peak-aged Al-4wt%Mg-0.2wt%Sc alloy (25% cold deformed), Røyset and Ryum (1994), ii) the recrystallization temperature range extended by 200°C and iii) the fine Al_3Sc precipitates are preserved to higher temperatures at which the recrystallization starts.

2.2 PLASTIC DEFORMATION AND TEXTURE EVOLUTION

During deformation, preferred crystallographic textures develop; crystallographic texture is the non-random distribution of the crystallographic orientations of the crystallites in a polycrystalline material. The mechanism of plastic deformation of crystals is dislocation-induced slip. The process of slip does not produce lattice rotation by itself, but it is the accommodation of the new grain shape to the surrounding grains, which causes the change in orientation.

Plastic deformation is commonly described by the use of the Sachs model and the Taylor model, which are considered to be two extreme theories of plasticity.

In the Sachs model the external stress state is considered and it is assumed that all grains experience the same stress condition, σ_{ij}, and that slip only takes place on those slip systems for which the critical resolved shear stress, τ_c^s, is reached. The stress tensor is related to the critical resolved shear stress by $\sigma_{ij} \cdot m_{ij}^s = \tau_{ij}^s$ where s=1-12 denotes the slip systems and m_{ij}^s is the Schmid factor for slip system number s. However, compatibility at grain boundaries restricts the deformation of the grains in such a way that no stress equilibrium exists between differently oriented grains and the shape change, which is given by the shear strain for the active slip system, varies from grain to grain.

In the Taylor model the external strain state is considered. It is assumed that all grains experience the same strain condition, ε_{ij}, and that the five slip systems necessary for achieving a prescribed strain increment is selected from the criterion of minimum internal work, i.e. $\sum_s \tau_c^s \cdot \dot{\gamma}^s = \min$, where $\dot{\gamma}^s$ is the shear strain rate on the active slip system s. Several modifications of the Taylor theory have been developed, but it is beyond the scope of this thesis to discuss this any further.

The Sachs model has the disadvantage that different stresses and strains are associated with different grains, while the Taylor model avoids the latter difficulty. Still, this theory requires different stress states for differently oriented grains in order to achieve equal strains and thus the stress compatibility at grain boundaries is not fulfilled. However, the strain incompatibility in the Sachs model seems to be more severe than the stress incompatibility in the Taylor model. Both models can be improved by relaxing the restrictions on the strain or stress constraints. For a more detailed discussion, see literature referred to by Vatne (1995).

The predicted rolling textures by Taylor models of full and relaxed constraints are in good agreement with experimental results. The results show that during rolling of high stacking fault energy materials, most orientations are concentrated along two incomplete fibres at low degrees of rolling, Hirsch and Lücke (1988). The two fibres are the α-fibre, which runs from the goss (G) orientation {011}<100> to the brass (Bs) orientation {011}<211>, and the β-fibre, which runs from the copper (Cu) orientation {112}<111> over S orientation {123}<634> to Bs orientation {011}<211>, see Figure V-1. At an increasing degree of rolling, these fibre structures detoriate along the fibres, which were originally homogeneously occupied, and pronounced peak orientation forms, Hirsch and Lücke (1988). It should be emphasised that this description is valid only for a random initial texture, and that for different starting textures different rolling textures may be obtained. The effect of solid solution and particles has also been reported in the literature. Lücke and Engler (1992) reported that with increasing deformation of a supersaturated solid solution, the formation of small amounts of Cu-type shear bands was observed leading to an increase of the Bs orientation. In the presence of large non-shearable particles, more or less random distributed deformation zones around the particles give rise to a weakening and spreading of the rolling texture.

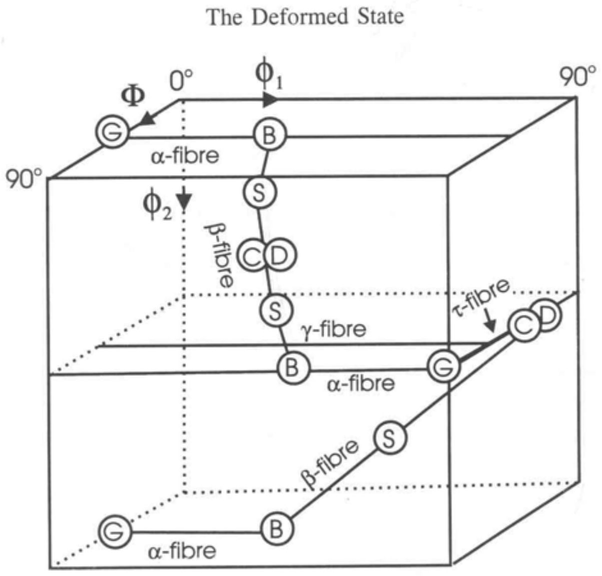

Figure V-1 *Different texture components that constitute the different fibres after deformation of fcc materials, Hirsch and Lucke (1988).*

2.3 RECRYSTALLIZATION TEXTURES

Recrystallization textures have been attributed to two main mechanisms, namely the oriented nucleation mechanism in which it is assumed that nuclei are formed with preferred orientations, or the oriented growth mechanism in which preferred growth from randomly oriented nuclei is assumed. Many observations have been made in support of both theories. The origin of recrystallization textures have been reviewed by several authors and will not be quoted here, for a more detailed overview see for instance the review of Vatne (1995). Instead, a summary of the most commonly observed recrystallization textures will be given below, Table V-1, see also Hirsch (1986).

The cube component {001}<100> is the dominant orientation in high purity Al when other recrystallization mechanisms are not active as in the presence of elements in solid solution or as precipitates. The volume fraction of the cube component is strongly dependent on: i) degree of deformation, ii) precipitation during softening, iii) deformation temperature, iv) volume fraction of the S component in the deformation texture, v) amount of particles which enhance PSN and vi) amount of shear banding, Engler et al. (1996) and Hirsch and Engler (1995).

An increased degree of the first four parameters leads to an increase in the volume fraction of the cube component while an increase in PSN and shear banding activity leads to a weakening in the cube most likely due to the introduction of new nucleation sites.

The R component {124}<211> is the main competitor to the cube component and it is very similar to the S component. It originates from the deformation texture either by an extended recovery process (preservation of the rolling texture) or by nucleation and growth processes, Hirsch and Engler (1995).

The P component {011}<122> is a result of nucleation of new grains at deformation inhomogeneties at second phase particles (deformation zones). In most cases where PSN plays a role it appears as a rather weak recrystallization texture, Hirsch and Engler (1995) and Engler et al. (1996).

The Q component {013}<231> originates by nucleation of recrystallization at deformation inhomogeneties such as shear bands. It is close to ND rotated cube orientations and it is usual in highly cold rolled and annealed material, which is prone to shear banding, for instance Al-Mg alloys, Hirsch and Engler (1995). A summary of the different features of recrystallization textures are given in Table VI-1, Lücke and Engler (1992).

***Table V-1** Euler angles, Miller indices and nucleation sites of the most important recrystallization texture components observed in commercial aluminium alloys after cold deformation and annealing.*

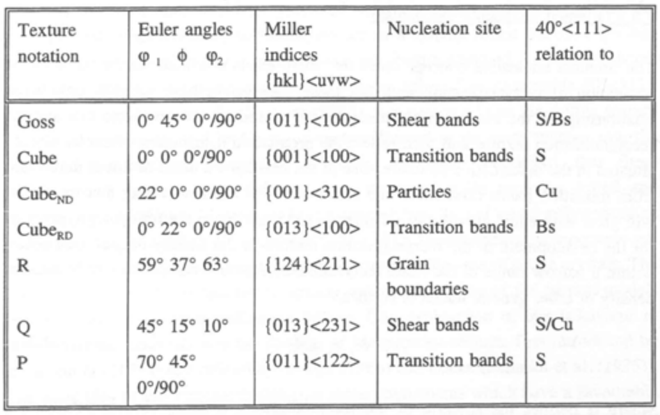

Texture notation	Euler angles φ_1 ϕ φ_2	Miller indices {hkl}<uvw>	Nucleation site	40°<111> relation to
Goss	0° 45° 0°/90°	{011}<100>	Shear bands	S/Bs
Cube	0° 0° 0°/90°	{001}<100>	Transition bands	S
Cube_{ND}	22° 0° 0°/90°	{001}<310>	Particles	Cu
Cube_{RD}	0° 22° 0°/90°	{013}<100>	Transition bands	Bs
R	59° 37° 63°	{124}<211>	Grain boundaries	S
Q	45° 15° 10°	{013}<231>	Shear bands	S/Cu
P	70° 45° 0°/90°	{011}<122>	Transition bands	S

3. EXPERIMENTAL TECNIQUES

3.1 COLD DEFORMATION

Slices of the extruded profiles were further cold rolled to different reductions in the cross sectional area ranging from 12.5% to 95%. The initial thickness of the profiles was 20 mm. Figure V-2 shows the hardness of the cold rolled material as a function of the equivalent strain. The equivalent strain can be calculated from $\varepsilon = (2 \cdot \ln R)/\sqrt{3}$ where $R = h_0/h_1$ and h_0 and h_1 are the initial and final profile thicknesses. The maximum reduction in the cross sectional area, which the material could withstand without breaking up, was approximately 75%. Hence, it was decided to perform further studies on the material cold rolled to a thickness reduction of 75%. This corresponds to an equivalent strain of 1.6.

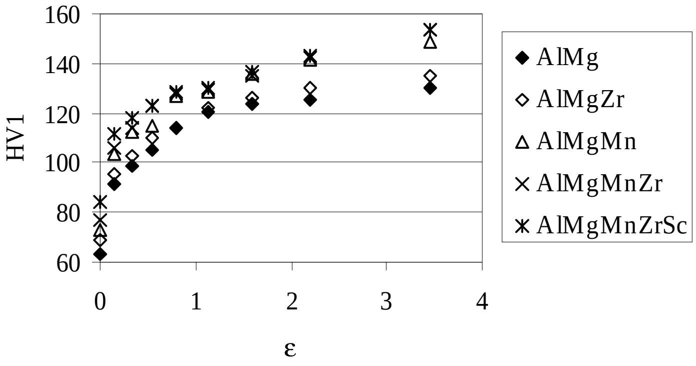

Figure V-2 *Hardness versus equivalent strain for the cold rolling of extruded profiles.*

3.2 HARDNESS MEASUREMENTS

The hardness measurements were performed on an Akashi AVK-C1 Hardness Tester equipped with the Leco Hardness Tester software. The applied load was 1 kg and the loading time was 15 seconds. The hardness tester was regularly calibrated against a hardness test standard with a hardness of 90±2 VHN.

3.3 MICROSTRUCTURAL INVESTIGATIONS

3.3.1 Metallography

The specimens for examining the grain structure were prepared according to the description in Part II, Section 3.4.2 in this thesis.

3.3.2 Texture measurements

The texture of a polycrystalline material is defined as the distribution of the orientations of its crystallites and can be described by pole figures and ODF's. A pole figure is a stereographich projection of the distribution of particular sets of crystal planes and hence it is a two-dimensional representation of the three-dimensional orientation space. A better way to describe the texture is by use of the **o**rientation **d**istribution **f**unction (ODF) which allows a complete description of the orientations in three dimensions.

In order to describe the orientations of the crystals in an ODF figure, three angles are required; these are the three Euler angles. In order to define the Euler angles a coordinate system, K_A, in the sample is defined. The axes of K_A are usually chosen to coincide with the rolling direction, normal direction and transverse direction. A second coordinate system, K_B, is defined for each crystals in the specimen and fixed with respect to the crystal axes. For a cubic crystal structure, K_B usually coincides with the directions [100], [010] and [001] in the crystals. Now the Euler angles are defined as the angles, which describes a rotation, $g=\{\varphi_1,\phi,\varphi_2\}$, from K_A to K_B. This can be expressed as:

$$K_B = g \cdot K_A \qquad \text{(V-1)}$$

In other words, $g=\{\varphi_1,\phi,\varphi_2\}$ is found by successively rotating K_B around the crystal axes until the axis coincides with that of K_A. As each crystallite represents an orientation, g, the texture of the material is the sum of all these orientations. The definition of the texture is then given by a continuous orientation distribution function, f(g), that represents the volume fraction of the orientation g:

$$f(g) = f(\varphi_1,\phi,\varphi_2) = \frac{dV(g)/V}{dg} \qquad \text{(V-2)}$$

where V is the total volume of the specimen and dV(g) is the sum of all volume elements which possess the orientation g within the element of orientation dg (from g to g+dg).

Due to the difficulties in measuring in the physical space, the ODF is calculated from measured pole figures. The calculations can be performed by use of the series expansion method developed by Bunge (1969). In the present work the ODF's were calculated on the basis of four incomplete pole figures ({111}, (200), {220} and {311}) and "ghost" corrected according to the method described by Lücke et al. (1981).

The texture measurements were performed on specimens from the centre of the cold rolled profiles in the rolling plane. Before measurements, the specimens were ground to 1200 mesh on SiC paper and then etched for 10 minutes in a 15% NaOH-solution and 20 seconds in a 25% HNO_3-solution and finally rinsed in water.

4. EXPERIMENTAL RESULTS

4.1 MICROSTRUCTURE OF EXTRUDED PROFILES

Regardless of deformation temperature and ram speed, profiles of AlMg were always recrystallized while those of AlMgMnZrSc displayed a fibrous grain structure at all deformation conditions. The fibrous grain structure is probably a non-recrystallised structure or a heavily recovered structure. The other three alloys were partly recrystallized. AlMgZr consisted of a recrystallized surface layer and a few recrystallized grains in the centre. AlMgMn also had a recrystallized surface layer but thicker than that of AlMgZr. In addition, AlMgMn had very coarse recrystallised grains in the centre elongated in the extrusion direction. AlMgMnZr displayed an even thinner recrystallized surface layer than AlMgZr and AlMgMn. Figure V-3 shows the microstructures of the extruded profiles.

In general, it is observed that the grain structure is much finer towards the profile surface independent of an equiaxed or a fibrous grain structure. AlMg has a larger grain size in the centre of the profile compared to the surface regions, Figure V-3 a) and b). AlMgMnZrSc also had a very coarse fibre structure in the centre compared to the surface, Figure V-3 i) and f). The other alloys with a recrystallized surface layer also display a finer structure towards the surface within the layer, Figure V-3 c), e) and g)

The effect of changing the ram speed and the billet temperature upon the thickness of the recrystallized layer is shown in Figure V-4. The thickness increases with the ram speed while it seems to be almost independent of the billet temperature.

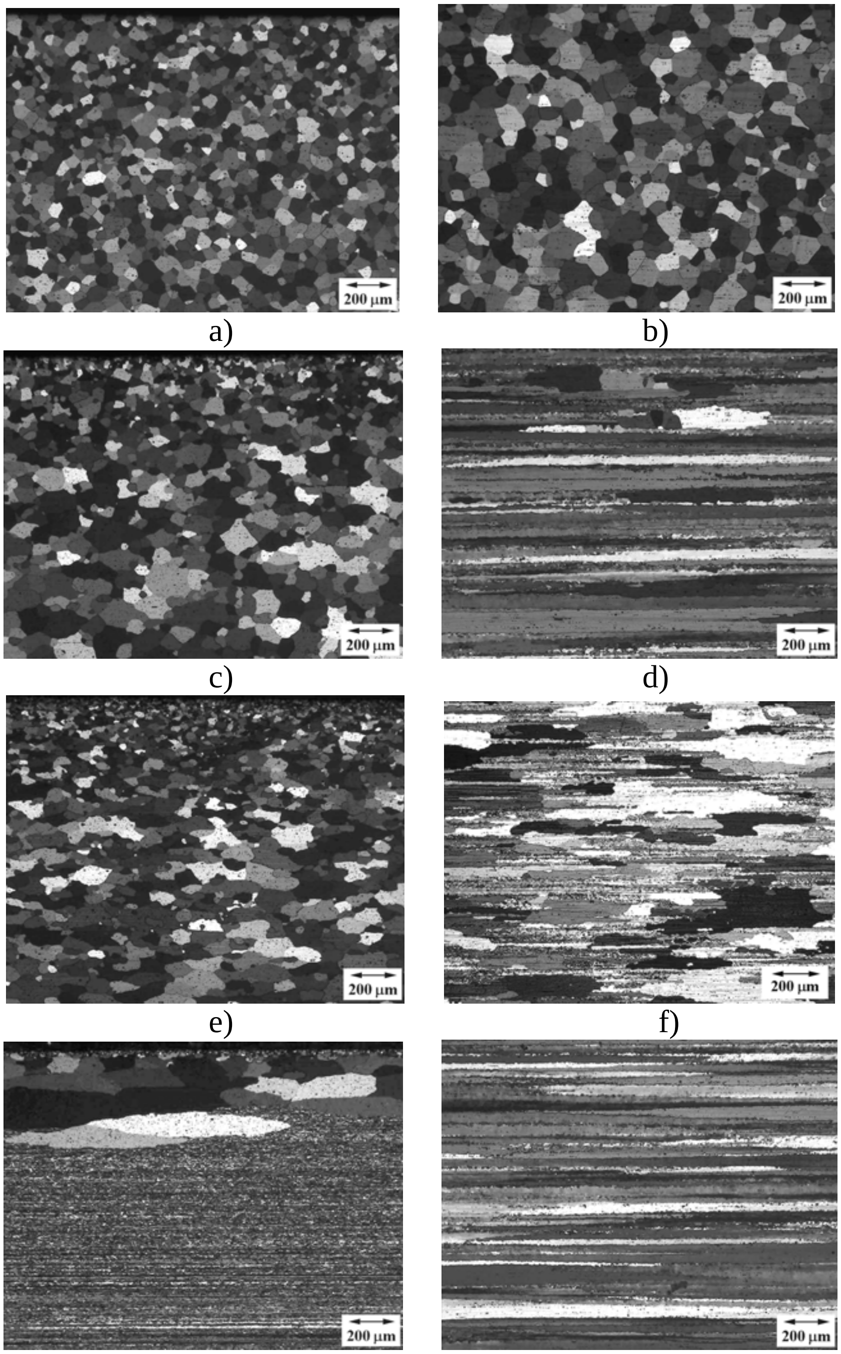

a) b)

c) d)

e) f)

g) h)

Figure V-3 *Continues on next page.*

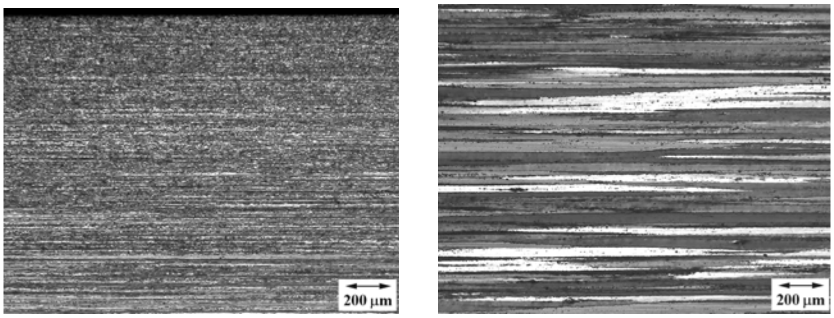

i) j)

Figure V-3 *Grain structure of extruded profiles a) AlMg surface, b) AlMg centre, c) AlMgZr surface, d) AlMgZr centre, e) AlMgMn surface, f) AlMgMn centre, g) AlMgMnZr surface, h) AlMgMnZr centre, i) AlMgMnZrSc surface and j) AlMgMnZrSc centre.*

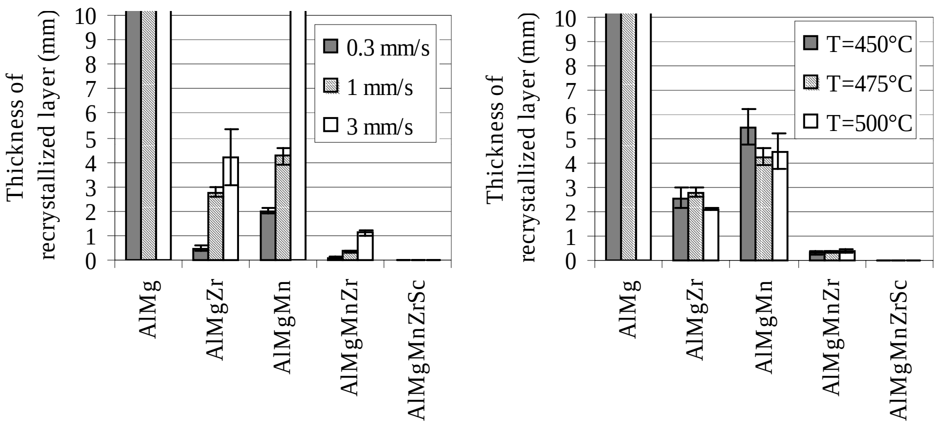

a) b)

Figure V-4 *Thickness of recrystallized layer, a) effect of ram speed and b) effect of billet temperature.*

4.2 ANNEALING OF EXTRUDED MATERIAL

An important feature of the material is the stability of the microstructure after hot deformation. The softening of the material due to recovery and recrystallization is important not only for the weldability of the material, but also the mechanical properties of the material are important for a whole range of applications. Thus, annealing of the extruded material was performed to check the stability of the extruded microstructures.

Softening curves for the isothermal annealing at 350°C, 450°C, 550°C and 570°C are presented in Figure V-5. Softening is observed in all alloys.

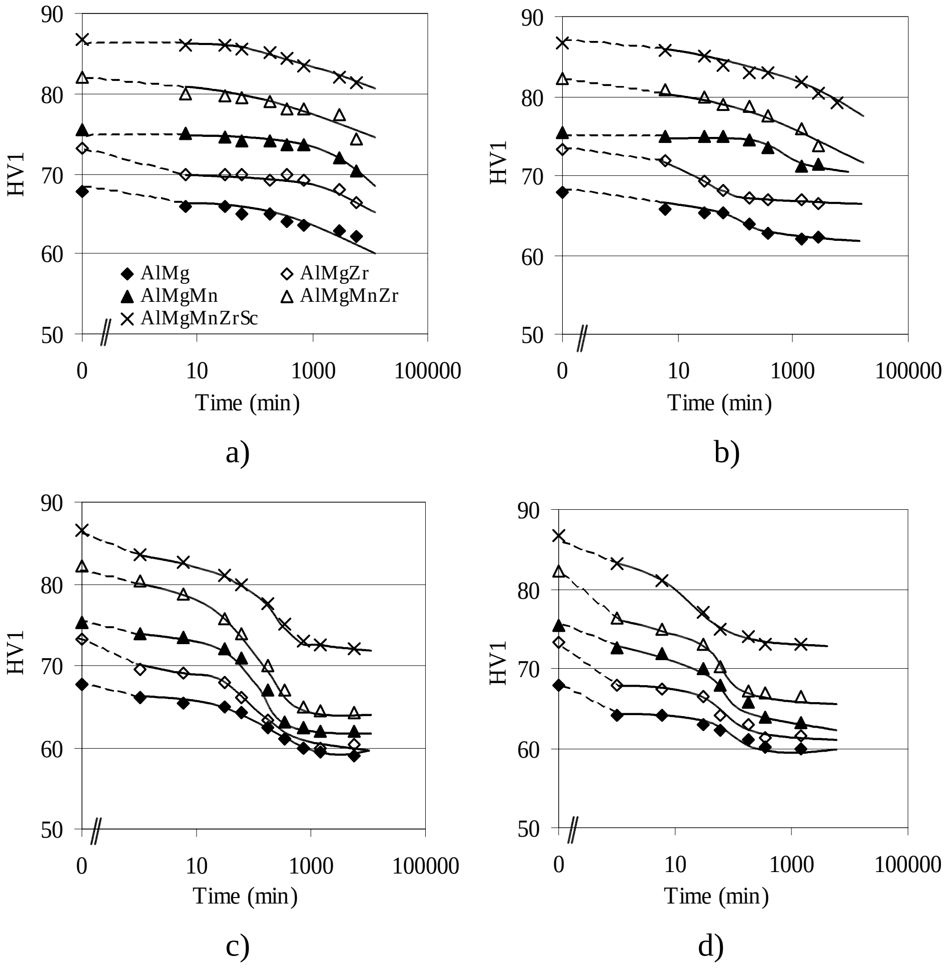

a) b)

c) d)

Figure V-5 *Hardness versus annealing time. a) T=350°C, b) T=450°C, c) T=550°C, d) T=570°C.*

Only a slight decrease in hardness is observed up to 95 hours at 350°C. The hardness curves for the different alloys are almost parallel. The same observation was made at 450°C, but the softening is somewhat more pronounced at this temperature. However, at 550°C and 570°C the softening has occurred more extensively and after only 1 minute the hardness has decreased to a lower level compared to the as extruded hardness. The hardness decrease from 1 minute to 30 minutes is moderate for all alloys, but from approximately 30 minutes the hardness decreases more rapidly followed by a more or less constant hardness level at prolonged annealing times.

It is interesting to see that the hardness in AlMgZr, AlMgMn and AlMgMnZr tends to approach the saturation level of AlMg. However, a small difference is still present in the completely softened condition, probably reflecting the effect of solid solution hardening and/or particle hardening. The hardness of AlMgMnZrSc saturates at a considerably higher level, Figure V-5 c) and d).

The observations made above can be explained by considering the microstructures of the different alloys and annealing conditions. Figure V-6 shows the microstructure of the alloys after annealing for 12 h at 450°C, 12 h at 550°C and 6 h at 570°C. The softening in AlMg is most likely due to grain growth. The grain size after 6 hours at 570°C is obviously larger than the as extruded grain size, Figures V-6 b) and V-6 c). The softening of AlMgZr, AlMgMn and AlMgMnZr is due to the development of a recrystallized grain structure, Figure V-6 d)-f), g)-i) and j)-l). However, the softening of AlMgMnZrSc needs a closer examination. From Figure V-6 o) it seems that this alloy preserves the fibrous grain structure even after 6 hours at 570°C. A higher magnification reveals that this alloy is also recrystallized. Figure V-7 a) and b) shows the fibrous structure 1 mm and 10 mm from the profile surface, respectively. The microstructure after 6 hours annealing at 570°C, Figure V-7 c) and d) show that extensive coarsening of the fibrous structure has occurred, demonstrating that recrystallization have taken place.

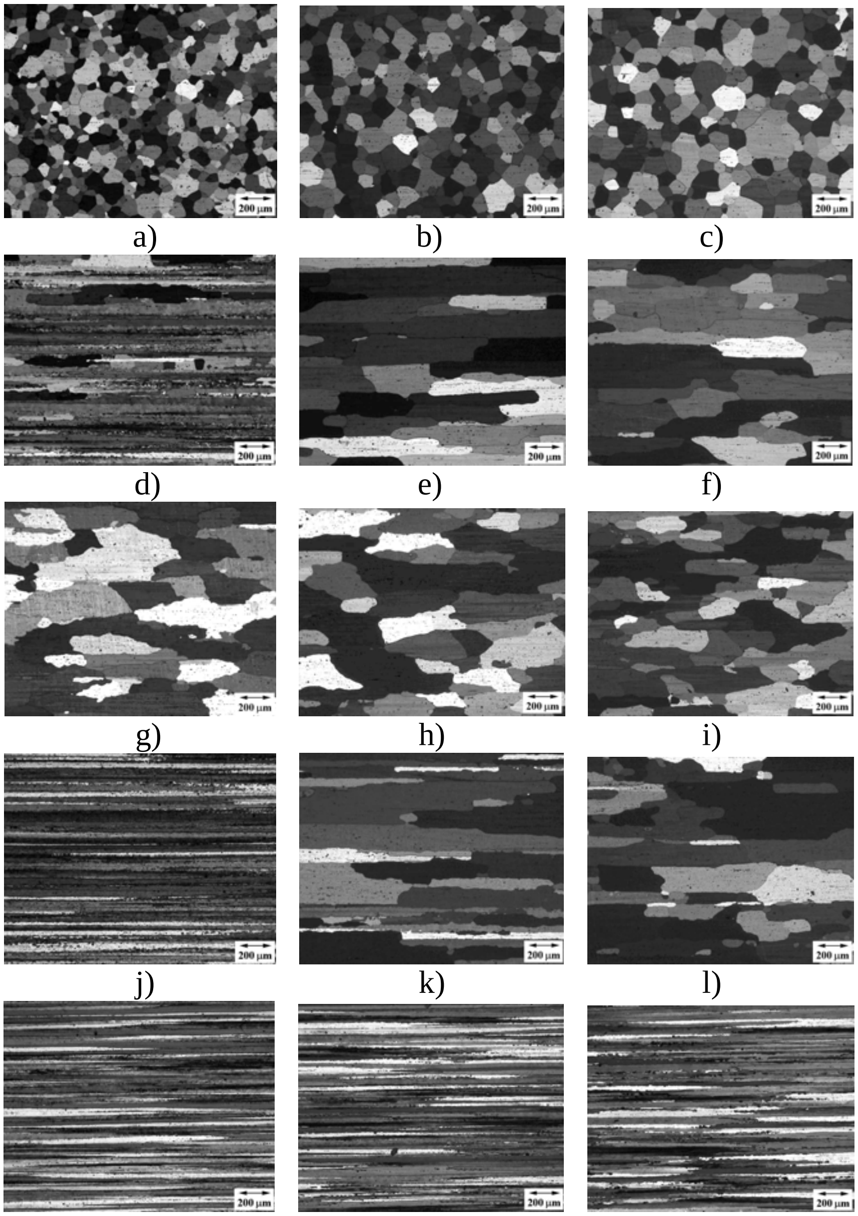

a) b) c) d) e) f) g) h) i) j) k) l) m) n) o)

Figure V-6 *Microstructure of annealed material.*
AlMg: a) 450°C-12h, b) 550°C-12h, c) 570°C-6h
AlMgZr: d) 450°C-12h, e) 550°C-12h, f) 570°C-6h
AlMgMn: g) 450°C-12h, h) 550°C-12h, i) 570°C-6h
AlMgMnZr: j) 450°C-12h, k) 550°C-12h, l) 570°C-6h
AlMgMnZrSc: m) 450°C-12h, n) 550°C-12h, o) 570°C-6h.

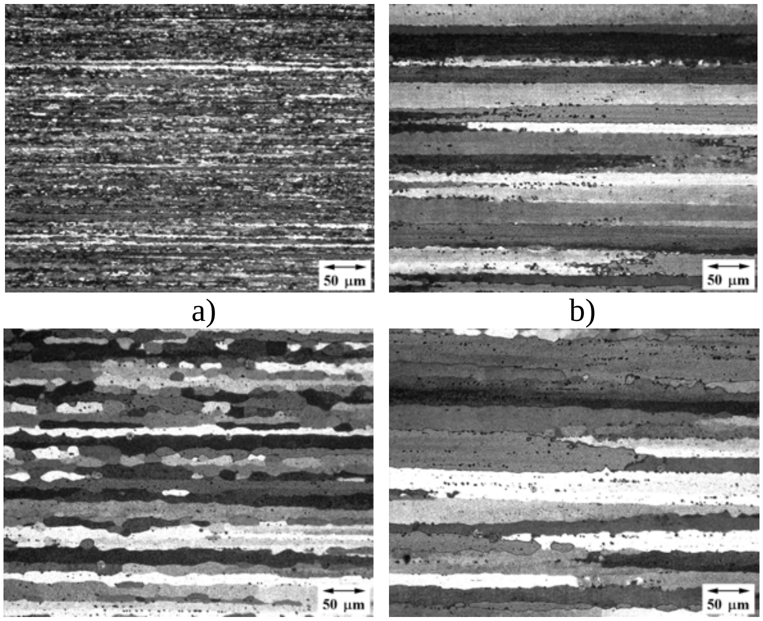

a) b)

c) d)

Figure V-7 *Microstructures of AlMgMnZrSc.*
a) As extruded, 1 mm from surface,
b) As extruded, 10 mm from surface,
c) Annealed 6h-570°C, 1 mm from surface,
d) Annealed 6h-570°C, 10 mm from surface.

4.3 COLD DEFORMATION AND BACK-ANNEALING

After extrusion the profiles were cold rolled to 75% reduction in thickness and isothermally annealed at temperatures from 200°C to 550°C. In the following subchapters the softening behaviour of the different alloys is presented in terms of hardness measurements, metallography and texture measurements.

4.3.1 Microstructure and texture of cold rolled material

Cold rolling produced a fibrous grain structure with the thickness of the fibres depending upon the initial grain structure in the extruded profiles. AlMg, which was fully recrystallized, and AlMgMn, which was partly recrystallized after extrusion, exhibit a coarser fibre structure after rolling than the other alloys. Shear banding was observed in all alloys after cold rolling. Figure V-8 shows examples of the cold rolled microstructure and the corresponding texture, presented as ODF figures.

In AlMg and AlMgMn most orientations are concentrated along a strong α fibre and a corresponding β fibre. The α fibre runs from {110}<001>-G orientation at $\phi=45^\circ$, $\varphi_2=90^\circ$, $\varphi_1=0^\circ$ to {110}<112>-B orientation at $\phi=45^\circ$, $\varphi_2=90^\circ$, $\varphi_1=35^\circ$, while the β fibre extends from {110}<112>-B orientation at $\phi=45^\circ$, $\varphi_2=90^\circ$, $\varphi_1=35^\circ$ through {123}<634>-S orientation at $\phi=37^\circ$, $\varphi_2=63^\circ$, $\varphi_1=59^\circ$ to {112}<111>-C orientation at $\phi=35^\circ$, $\varphi_2=45^\circ$, $\varphi_1=90^\circ$.

In AlMgZr, AlMgMn and AlMgMnZrSc the texture components in the α- and β-fibres are much sharper. The texture exhibits a pronounced S peak near (011)<211> B orientation at $\phi=45^\circ$, $\varphi_2=90^\circ$, $\varphi_1=40^\circ$. The β fibre deviates from the usual position in the form of a double fibre starting from a G/B position at $\phi=45^\circ$, $\varphi_2=90^\circ$, $\varphi_1=10\text{-}20^\circ$.

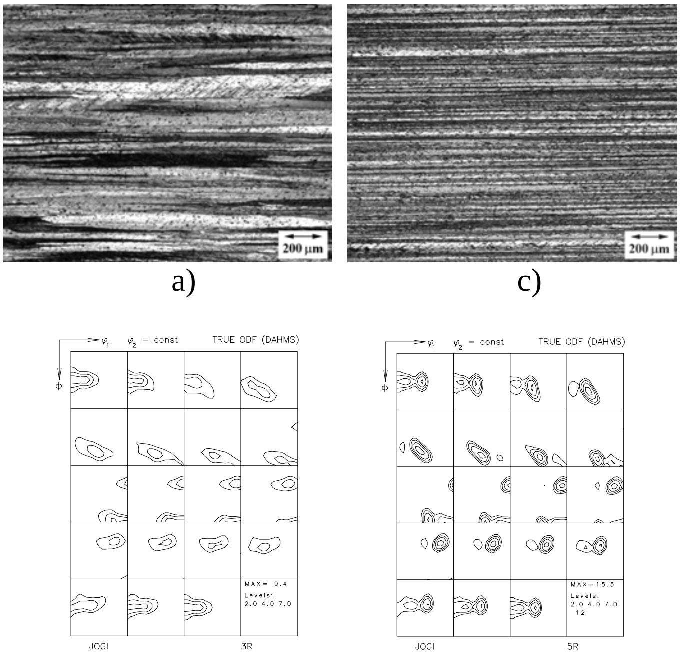

a) c)

b) d)

Figure V-8 *a) micrograph of cold rolled AlMgMn, b) corresponding ODF-plot, c) micrograph of cold rolled AlMgMnZrSc and d) corresponding ODF-plot.*

4.3.2 Microstructure and hardness of back-annealed material

The five different alloys showed different response to the back-annealing treatment. In Figure V-12 the softening curves are presented as hardness versus annealing time. The hardness decreases continuously until a constant level is reached. This constant level is regarded as a fully annealed condition and the hardness values are approximately 70, 75, 80, 83 and 90 VHN for AlMg, AlMgZr, AlMgMn, AlMgMnZr and AlMgMnZrSc, respectively.

In AlMg and AlMgZr the fibrous grain structure developed during cold rolling, is retained even after 3 hours annealing at 250°C, Figure V-9 a). The hardness decreased by at least 25% from the rolled condition and evidently extensive recovery has taken place, Figure V-12 a) and b). After 3 hours at 275°C the hardness has reached the values of the fully annealed conditions. After 3 hours at 350°C these two alloys seem to be completely recrystallized with an extremely fine grained structure as a result, Figure V-9 b). The effect of further increasing the annealing temperature is a coarsening of the grain structure and reducing the time for start and end of recrystallization. At 550°C the fully annealed condition is reached within the first minute of annealing, i.e. recrystallization is completed very fast and upon prolonged annealing, grain growth occurs, Figure V-9 d). The microstructural development illustrated in Figure V-9 for AlMgZr was also observed for AlMg.

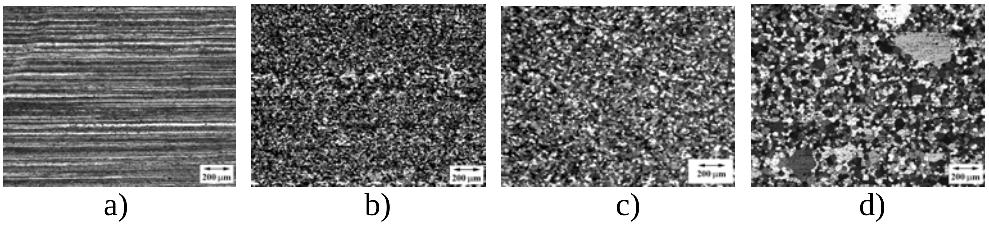

a) b) c) d)

Figure V-9 *Microstructure of AlMg at different annealing conditions. a) 3 hours at 250°C, b) 3 hours at 350°C, c) 3 hours at 450°C and d) 3 hours at 550°C.*

AlMgMn and AlMgMnZr recrystallize much faster than AlMg and AlMgZr, most probably due to the manganese content. From the hardness curves in Figure V-12 c) and d) it can be seen that complete recrystallization has occurred after only 10 minutes at 275°C. This is also the case after 3 hours at

250°C, Figure V-10 a). The coarsening of the grain structure at increased annealing temperature is also evident from Figure V-9.

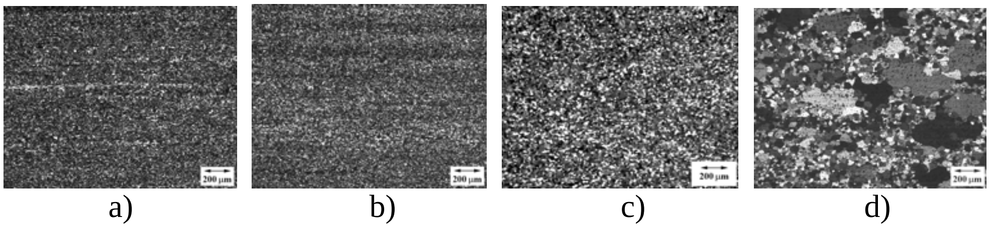

a) b) c) d)

Figure V-10 *Microstructure of AlMgMn at different annealing conditions. a) 3 hours at 250°C, b) 3 hours at 350°C, c) 3 hours at 450°C and d) 3 hours at 550°C.*

Among the five alloys, AlMgMnZrSc has the most stable microstructure, as can be seen from the hardness curves in Figure V-12 e). While a constant hardness level for the fully annealed conditions were obtained for the other alloys, different hardness levels occurred for AlMgMnZrSc. However, higher levels were obtained at all temperatures, except after annealing at 550°C where the hardness decreased to 80 VHN which is the same as for AlMgMnZr. An extremely fine-grained structure is retained even after 3 hours at 550°C, Figure V-11 d). From these micrographs and the hardness curves it can be stated that recrystallization is effectively suppressed in this alloy.

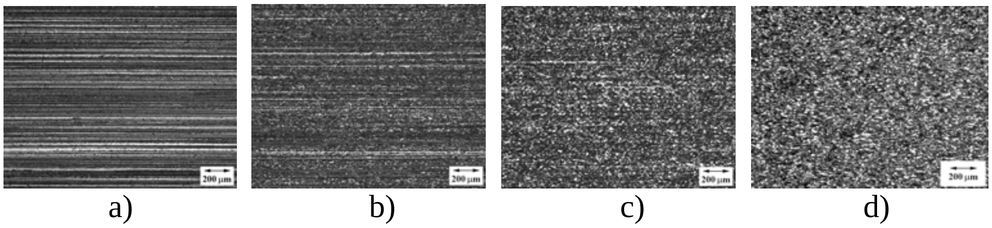

a) b) c) d)

Figure V-11 *Microstructure of AlMgMnZrSc at different annealing conditions. a) 3 hours at 250°C, b) 3 hours at 350°C, c) 3 hours at 450°C and d) 3 hours at 550°C.*

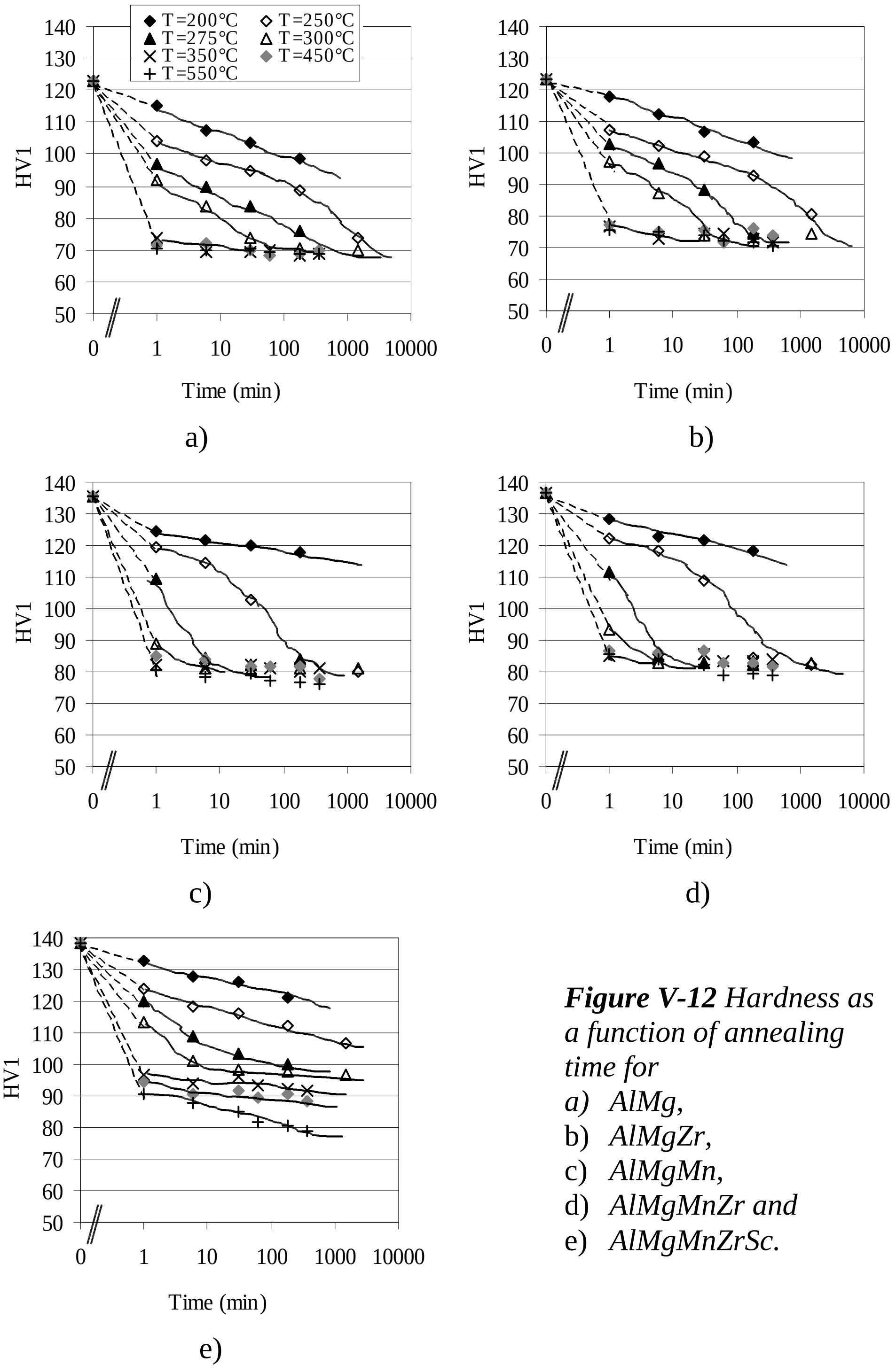

a)

b)

c)

d)

e)

Figure V-12 *Hardness as a function of annealing time for*

a) AlMg,
b) *AlMgZr,*
c) *AlMgMn,*
d) *AlMgMnZr and*
e) *AlMgMnZrSc.*

4.3.3 Texture of back-annealed material

From the results in the previous section it was found that the alloys exhibited different softening behaviour. The texture was measured after annealing at 550°C for 180 minutes.

In the back-annealed material the α- and β- fibres are totally absent. Compared to the Zr/Mn/Sc containing alloys, a completely different texture is observed in AlMg in which a whole range of texture components developed during annealing. The dominating component is the (124)<211> R orientation (ϕ=31°, φ_2=60°, φ_1=63°). Minor peaks in (011)<122> P orientation (ϕ=45°, φ_2=0/90°, φ_1=70°), (001)<210> ND rotated cube orientation (ϕ=0°, φ_2=0/90°, φ_1=0°) and some peaks near (011)<100> G orientation (near ϕ=45°, φ_2=0/90°, φ_1=0°) were also observed, see Figure V-13 a). The R-texture is typical for alloys in which nucleation at existing grain boundaries occur while the ND-rotated cube is typical for PSN-induced recrystallisation, Hirsch and Engler (1995).

In the other alloys mainly the cube texture and some other minor components were observed.

AlMgZr displayed only a (001)<210> ND rotated cube orientation (ϕ=0°, φ_2=0/90°, φ_1=20°), Figure V-13 b), which is typical for particle containing alloys (PSN) and inhibition of recrystallization due to solute atoms (solute drag).

AlMgMn shows a texture very similar to that of AlMgZr. However, the ND rotated cube component is weaker and in addition a weak (001)<100> RD rotated G component is observed (near ϕ=45°, φ_2=0/90°, φ_1=0°), Figure V-13 c). This type of texture is similar to that observed for the cold rolled 3104 alloy, Engler et al. (1996).

In AlMgMnZr a (001)<100> cube component and a weak (013)<231> Q orientation was observed. The occurrence of the cube component is an example of classical recrystallization nucleation while the Q orientaion indicates some nucleation on shear bands, Figure V-13 d). However, the weak texture peaks do not correspond to the coarse grain structure.

AlMgMnZrSc displays a weak ND rotated cube component and a weak (011)<122> P orientation (ϕ=45°, φ_2=0/90°, φ_1=50°). This texture can be interpreted as retained shear and some PSN texture, Figure V-13 d).

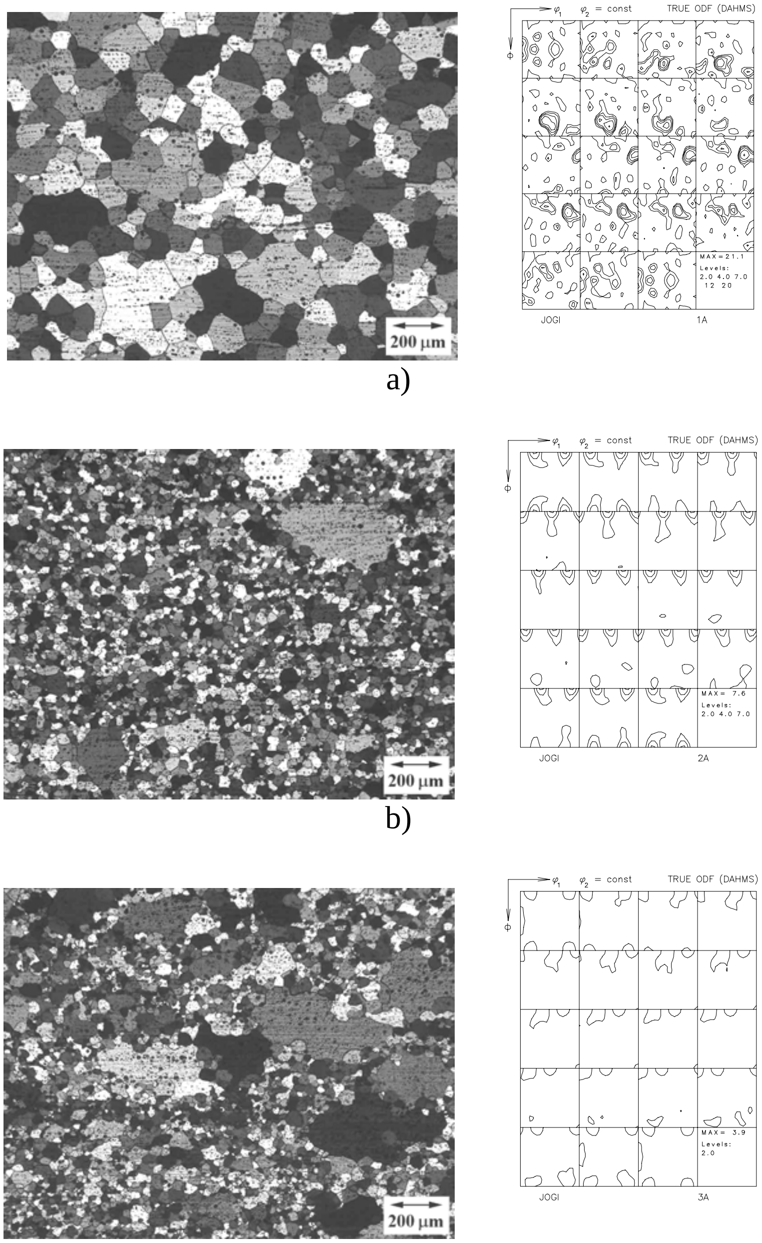

a)

b)

c)

Figure V-13 *Continues on next page.*

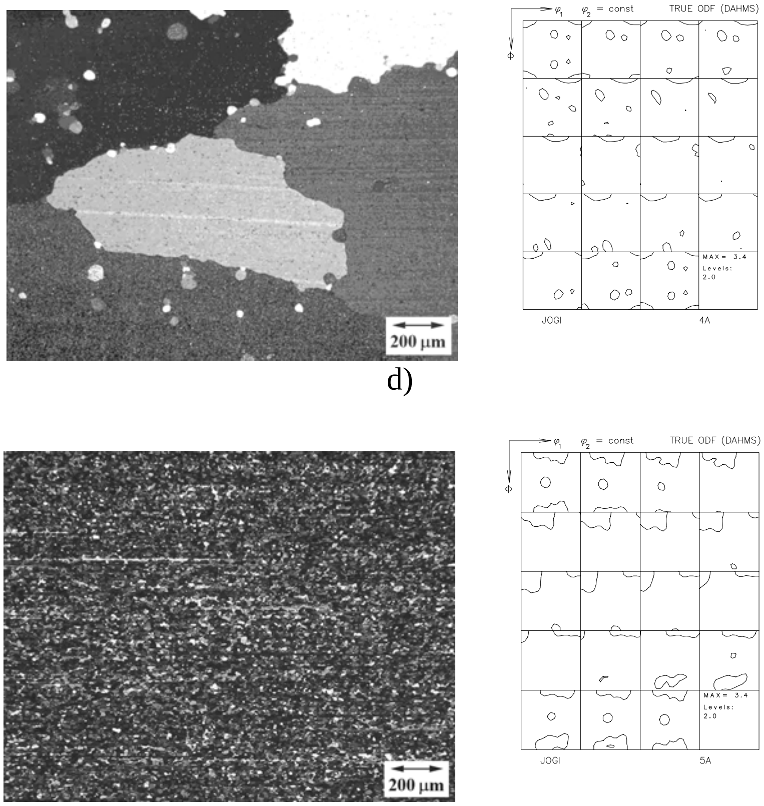

d)

e)

Figure V-13 *Microstructure and corresponding ODFs for material annealed at 550°C for 180 minutes. a) AlMg, b) AlMgZr, c) AlMgMn, d) AlMgMnZr and e) AlMgMnZrSc.*

5. DISCUSSION

5.1 ESTIMATION OF THE ZENER DRAG

Dispersoids are most effective at retarding recrystallization when they are small, well dispersed and coherent, Eqs. I-15 to I-18.

As was discussed in Part II of this thesis, the investigated alloys display a whole range of different particle microstructures. It was demonstrated how the additions of Mn, Zr and Sc precipitated and formed dispersoids during heat treatment of the cast material. The results are summarised in Table II-3 in terms of type, size and density of the dispersoids. From these results the volume fraction (f), the interparticle spacing (λ) and the Zener drag ratio (f/r) of the dispersoids have been estimated and will be used in the further discussion, Table VI-1. Note that the Al_6Mn-dispersoids were not spherical but appeared as thin plates. Thus, an equivalent radius gives the size of these particles.

Table V-1 *Estimation of volume fraction of dispersoids (f), the interparticle spacing (λ), the inverse of the interparticle distance (1/λ) and the Zener drag ratio (f/r).*

Alloy	Dispersoid	$\bar{r}$ (nm)	f	λ (nm)	$1/\lambda \cdot 10^4$ (nm^{-1})	$f/r \cdot 10^5$ (nm^{-1})
AlMg	None	-	0	-	-	0
AlMgZr	Al_3Zr	25	0.0029	674	14.8	11.5
AlMgMn	Al_6Mn	59	0.0039	1372	7.3	6.6
AlMgMnZr	Al_3Zr	23	0.0022	703	14.2	9.8
	Al_6Mn	52	0.0028	1415	7.1	5.4
	Total*	-	-	-	-	15.2
AlMgMnZrSc	$Al_3(Sc,Zr)$	11	0.0026	313	31.9	23.5
	Al_6Mn	50	0.0027	1400	7.1	5.3
	Total*	-	-	-	-	28.8

$^*(f/r)_{total} = f_{Al3Zr/Al3(Sc,Zr)}/\bar{r}_{Al3Zr/Al3(ScZr)} + f_{Al6Mn}/\bar{r}_{Al6Mn}$

However, before we move on to discuss the recrystallization properties some comments on the accuracy of the calculations will be made. The volume fraction, f, and the interparticle distance, λ, were simply calculated from the following equations:

$$f = \frac{(4/3) \cdot \pi \cdot \bar{r}^3 \cdot N_p}{A \cdot t_{foil}} \qquad \text{(V-3)}$$

$$\lambda = \sqrt{\frac{2\pi \bar{r}^2}{3f}} \qquad \text{(V-4)}$$

where $\bar{r}$ is the mean particle radius, N_p is the number of particles and t_{foil} is the thin foil thickness. Measuring all these quantities is associated with errors. First of all, the thickness of the investigated thin foils was not measured at all, but assumed to be constant and equal to 300 nm in the regions close to the edge of the hole. Next, the measured size of the particles and the number of particles is associated with an error due to i) small particles may not be resolved by the TEM, ii) small particles may be invisible because their images are overlapped by those of larger particles and iii) truncation errors in which the presence of particles with the centres lying outside of the foil, Schlesier and Nembach (1989). Finally, due to inhomogeneous distribution of particles, errors in the measured number of particles is highly relevant. It is important to bear in mind that the results from the present TEM-investigation are only estimates but can be used in comparative studies between the different alloys without larger errors.

It is assumed that the Zener drag from two different particle types are additive. For instance, the total Zener drag in a matrix containing a volume fraction, f_1 of particles with a radius, r_1, and a volume fraction, f_2, of particles with a radius, r_2, may be expressed as: $P_Z^{tot} \propto f_1/r_1 + f_2/r_2$. Thus, assuming that the two particle types have the same interfacial energy, the total Zener drag ratio was estimated for AlMgMnZr and AlMgMnZrSc, Table V-1.

5.2 RECRYSTALLIZATION OF HOT AND COLD DEFORMED MATERIAL

5.2.1 Recrystallisation after extrusion

Since the Zener drag is proportional to the f/r-ratio, $P_Z \propto f/r$ (Eq. VI-5), the f/r-values give a direct measure of the drag forces retarding both nucleation and growth of recrystallization. This Zener ratio (f/r) and the interparticle spacing will provide important information in the evaluation of recrystallization resistance of the material. Thus, from Table V-1 it can be stated that Al_6Mn is least effective, Al_3Zr is more effective while $Al_3(Sc,Zr)$ is most effective in suppressing recrystallization.

It is also possible to rank the alloys with respect to increasing Zener drag: AlMg (0), AlMgMn (6.6), AlMgZr (11.5), AlMgMnZr (15.2) and AlMgMnZrSc (28.8), Table V-1. The results from the microstructural investigation of the extruded profiles show that the degree of recrystallization decreases with the introduction of Mn, Zr and Sc. If it is assumed that the particles survive the extrusion process, i.e. that the volume fraction and size of particles are approximately the same before and after extrusion, it can be concluded that the different microstructures originate from the different values of the Zener drag forces. The stability of the particles at elevated temperatures will be discussed in a following paragraph.

5.2.2 Recrystallization after back annealing of extruded profiles

As demonstrated, the as extruded microstructures ranged from a fully recrystallized equiaxed grain structure (AlMg) to a non-recrystallized fibre grain structure (AlMgMnZrSc). It is believed that these grain structures are formed by dynamic recovery and subsequent static recovery (AlMgMnZrSc) or static recrystallization (AlMg). These processes continue upon back annealing.

The results from the microstructural investigations of the back annealed extruded material also suggests that the stability of the microstructure is determined by the Zener pinning forces. Softening behaviour was observed in all alloys. Except for AlMg in which grain growth is evident, recrystallization is accompanied by a decrease in hardness in the other alloys. Thus, the stability of the hot deformed microstructures is most likely determined by the thermal stability of the dispersoids.

5.2.3 Recrystallization after cold rolling

During cold rolling a considerable amount of energy was introduced to the material. The stored energy is associated with an overall high density of dislocations and at some locations the density may be even higher, for instance in deformation zones, shear bands, transition bands, subgrain boundaries etc. These deformation inhomogeneties are exellent nucleation sites for recrystallization. Thus, cold deformed material provides a higher amount of stored energy and a higher density of nucleation sites as compared to the hot deformed material.

It is therefore not unexpected that the recrystallization behaviour of cold rolled profiles is quite different from that observed after extrusion. The results showed, first of all, that all five alloys recrystallized and produced an extremely fine-grained microstructure after a certain annealing time. The formation of the fine-grained structure is interpreted by a high nucleation rate, which is a result of a high number of available nucleation sites. Once formed, the small grains coarsen by grain growth.

The effect of the dispersoids and primary constituents on the recrystallization properties is rather different from the hot deformed material. The behaviour of AlMg and AlMgZr is very similar, only a minor increase in the hardness level were observed for AlMgZr compared to AlMg. The same observation was made for the two Mn-containing alloys (AlMgMn and AlMgMnZr). This suggests that the Al_3Zr-dispersoids have a minor capacity of retarding recrystallization in Al-Mg alloys. This is consistent with the results of Riddle (1998) who found that Zr had no effect in a binary Al-0.12Zr alloy and that an Al-2Mg-0.12Zr recrystallized completely after 1 hour at least above 400°C. However, these results are opposed to that of Ryum (1969) who found that the recrystallization temperature of an Al-0.5Zr alloy increased considerably. Thus, the present work indicates that the driving force for recrystallization in cold rolled material exceeds that of the retarding Zener drag forces from the Al_3Zr-particles.

Dispersoids and primary constituents of the Al_6Mn-type accelerate recrystallization considerably. This can be stated by comparing the softening curves of AlMg/AlMgMn and AlMgZr/AlMgMnZr in Figure V-12. The average size of the Al_6Mn-dispersoids is approximately 50 nm (equivalent radius) with the length of the Al_6Mn-plates ranging from 50 nm to 1700 nm and the thickness ranging from 20 nm to 200 nm, Table II-3. Furthermore, the primary $Al_6(Mn,Fe)$-constituents were considerably larger and in the order of 10 μm to 20 μm. It is therefore most likely that the primary constituents and probably also the largest dispersoids promote nucleation of recrystallization significantly through the PSN mechanism.

These results are in accordance with results reported in the litterature which states that Mn is most effective in retarding recrystallization when it is in solid solution, Altenpohl (1965), Firth and Williams (1969) and Westengen et al. (1981). To avoid PSN, the dispersoids must be extremely small (r<1μm) and finly dispersed. This can be obtained only by a proper heat treatment procedure at lower temperatures, shorter times or by adjusting the heating rate or cooling rate, Furrer and Hausch (1979), de Haan et al. (1996) and Ratchev et al. (1995).

The results of AlMgMnZrSc clearly illustrates the effect of $Al_3(Sc,Zr)$-dispersoids in retarding recrystallization. It was found that the alloy softened and that the microstructure consisted of an extremely fine-grained microstructure even after 6 hours annealing at 550°C. The softening curves do not show any clear onset of recrystallization and it could be possible that only recovery occurs in this alloy and that the small grained structure is a stable subgrain-structure. Another possibility is that PSN also occurs in this alloy but further grain growth is effectively restricted by the dispersoids. Anyway, the excellent ability of the combination of Zr and Sc additions in retarding recrystallization of Al-Mg-Mn alloys has been demonstrated.

5.2.4 Textures observed after deformation and after back-annealing

It was demonstrated that two different rolling textures occurred. In the fully or partially recrystallized extruded profiles a clear α- and β-fibre texture developed during cold rolling. However, in the alloys with a retained fibrous grain structure after extrusion, the fibre texture deteriorated and the homogeneously occupied fibres were replaced by pronounced maxima around Bs-, S- and Cu-orientations, Table V-2. This difference in cold rolled textures is most likely due to differences in the starting texture, which unfortunately was not measured. The results are in accordance with the texture development observed in CuZn alloys by Hirsch and Lücke (1988). They found that at a low degree of deformation, a homogeneous distribution of orientations in the α- and β-fibres developed. An increasing degree of deformation resulted in a systematic change of the orientations of the β-fibre. The change was in the form of a sharpening of the individual texture components.

Table V-2 shows an overview of all texture components observed in cold rolled and back-annealed material. The recrystallization texture in AlMg comprised a whole range of different components with the R-component as the dominating one. This suggests that nucleation of recrystallization is governed by nucleation at grain boundaries. However, the other components also show that other mechanisms play a role (PSN, shear band, transition band). The presence of the Al_3Zr-particles in AlMgZr strongly affected the recrystallization texture by suppressing the R-component completely and increasing the intensity of the ND rotated component. This can be interpreted as a change in the operating nucleation mechanism from GB-nucleation to PSN. The ND-rotated cube component was also observed in AlMgMn and AlMgMnZrSc Furthermore, a P-component could be observed in AlMgMnZrSc. These results strongly indicate that recrystallization can be characterised by the PSN-mechanism and they are in accordance with the work of Engler et al. (1996).

Surprisingly, the normal cube component was observed in AlMgMnZr, but this can not be explained in terms of a change in nucleation mechanism. Since a ND rotated cube was observed in all the other alloys it should also be expected to appear in this alloy. However, abnormal grain growth appeared in this specimen which could explain the unexpected result.

In addition to the cube components minor peaks in G-, Q- and P-orientations could be found. These are attributed to additional operating nucleation mechanism, i.e. nucleation on shear bands (G and Q) and transition bands (P).

Table V-2 *Overview of the different texture components observed after cold rolling and after back-annealing of cold rolled material.*

Alloy	Deformation texture	Recrystallization texture
AlMg	α-fibre β-fibre	R, P G, Cube_{ND}
AlMgZr	Fibres with peaks in the following orientations: Bs, S, Cu and a peak near G-orientation	Cube_{ND}
AlMgMn	α-fibre β-fibre	Cube_{ND} G
AlMgMnZr	Fibres with peaks in the following orientations: Bs, S, Cu and a peak near G-orientation	Cube Q
AlMgMnZrSc	α-fibre, and peaks in the following orientations: Bs, S, Cu.	Cube_{ND} P

6. CONCLUSIONS

- The dispersoids of type Al_6Mn, Al_3Zr and $Al_3(Sc,Zr)$ affect recrystallization after extrusion considerably, but in different ways.
- AlMg without any dispersoids was completely recrystallized after extrusion.
- Al_6Mn has a minor effect in retarding recrystallization after hot deformation. The Zener-drag from these particles is rather low. The AlMgMn alloy displayed a partly fibrous grain structure with some recrystallized grains elongated in the extrusion direction.
- Al_3Zr exhibits higher Zener drag on grain boundaries and is much more efficient than Al_6Mn in retarding recrystallization after hot deformation. AlMgZr and AlMgMnZr were both unrecrystallized after extrusion. However, a thin recrystallized surface layer occurred being thinner for AlMgMnZr.
- $Al_3(Sc,Zr)$ showed a remarkable ability to retard recrystallization. These particles are extremely small and well dispersed compared to Al_3Zr and Al_6Mn and thus exhibit a very high Zener drag on moving grain boundaries. AlMgMnZrSc was completely unrecrystallized after extrusion.
- Further annealing resulted in a completely recrystallized structure in AlMgZr, AlMgMn and AlMgMnZr while AlMgMnZrSc was much more stable even up to the solidus temperature (570°C). This is probably due to coarsening of Al_6Mn and Al_3Zr while $Al_3(Sc,Zr)$ is very stable at high temperatures.
- The recrystallization behaviour after cold rolling is different from that observed after extrusion. Texture measurements show that nucleation on deformation heterogeneties play a crucial role in recrystallization mechanisms.
- PSN was observed in all alloys. Especially in the Mn-containing alloys this mechanism is important due to the presence of large constituent Mn-bearing particles.
- The effect of Al_3Zr and Al_6Mn in retarding recrystallization after cold rolling was almost totally absent, while the effect of $Al_3(Sc,Zr)$ was still considerable.
- All alloys seem to recrystallize rapidly and an extremely fine grain structure is evident. After prolonged annealing, considerable grain growth occurred in all alloys except in the AlMgMnZrSc-alloy containing $Al_3(Sc,Zr)$. The fine-grained structure in this alloy was stable up to at least 550°C.

REFERENCES

Altenpohl, D., *Aluminium und Aluminiumlegierungen*, Springer-Verlag, Berlin, 1965.

Baxter, G.J., Zhu, Q. and Sellars, C.M., *Effect of magnesium content on hot deformation and subsequent recrystallization behaviour of Aluminium-Magnesium alloys*, Proceedings from The 6th Int. Conf. on Aluminium Alloys, ICAA6, Toyahashi, Japan, 1998, vol. 2, p. 1233.

Bunge, H.J., *Matematische Methoden der Texturanalyse*, Akademie, Berlin, 1969.

Davydov, V.G., Elagin, V.I., Zakharov, V.V. and Rostove, T.D., *Alloying aluminium alloys with scandium and zirconium additives*, Met. Sci. Heat Treat., vol. 38, nr. 7-8 (1996), p. 347.

De Haan, P.C.M., Van Rijkom, J. and Söntgerath, J.A.H., *The precipitation behaviour of high-purity Al-Mn alloys*, Mat. Sci. Forum, vol. 217-222 (1996), p. 765.

Engler, O., Mulders, B. and Hirsch, J., *Influence of deformation temperature and strain rate on the recrystallization nucleation in Al-Mn1-Mg1*, Z. Metallkunde, vol. 87 (1996), p. 454.

Firth, M. and Williams, W.M., *The homogenization heat treatment of aluminium-manganese ingot*, Can. Met. Quarterly, vol. 8, nr. 4 (1969), p.331.

Furrer, P. and Hausch, G., *Recrystallization behaviour of commercial Al-1%Mn alloy*, Met. Sci., March-April (1979), p. 155.

Hirsch, J., *Recrystallization of fcc metals as investigated by ODF analysis*, Proceedings of the 7th Risø Int. Symp. on Metallurgy and Mat. Sci., Risø, 1986.

Hirsch, J. and Engler, O., *Texture, local orientation and microstructure in industrial Al- alloys*, Proceedings of the 16th Risø Int. Symp. on Mat. Sci., Risø, 1995.

Hirsch, J. and Lücke, K., *Mechanism of deformation and development of rolling textures in polycrystalline f.c.c. matals*, Acta Met., vol. 36, no. 11 (1988), p. 2863.

Johansen, A., *Aluminium in Ships. Tensile testing of 5xxx-alloys*, Sintef report nr. STF24 F98524, Sintef Material Technology, 1998.

Lücke, K. and Engler, O., *Recrystallization textures in non heat-treatable and heat-treatable aluminium alloys*, Proceedings from The 3rd Int. Conf. on Aluminium Alloys, ICAA3, Trondheim, 1992.

Lücke, K., Pospiech, K.H. and Virnich, K.H. and Jura, J., Acta Met., vol. 29 (1981), p. 167.

McQueen, H.J. and Ryum, N., *Hot working and subsequeunt static recrystallization of Al and Al-Mg-alloys*, Scand. J. Met., vol. 14 (1985), p. 183.

Mondolfo, L.F. *Aluminium Alloys: Structure and properties*, Butterworths, London, 1976.

Ratchev, P., Verlinden, B. and Van Houtte, P., *Effect of preheat temperature on the orientation relationship of (Mn,Fe)Al6 precipitates in an AA 5182 Aluminium-Magnesium alloy,* Acta Met., vol. 43, no. 2 (1995), p. 621.

Riddle, Y., *Control of recrystallization in Al-Mg alloys using Sc and Zr*, M.Sc. thesis, Georgia Institute of Technology, 1998.

Ryum, N., *Precipitation and recrystallization in an Al-0,5wt%Zr-alloy*, Acta Met., vol. 17, March (1969), p. 269.

Røyset, J. and Ryum, N., *Precipitation and recrystallization of an Al-Mg-Sc-alloy*, Proceedings from The 4th Int. Conf. on Aluminium Alloys, ICAA4, Trondheim, 1994.

Schlesier, C. and Nembach, E., *Precise transmission electron microscopy determination of the size and volume fraction of precipitates, as exemplified by Nimonic PE16*, Mat. Sci Eng., vol. A119 (1989), p. 199.

Toropova, L.S., Eskin, D.G., Kharakterova, M.L. and Dobatkina, T.V., *Advanced aluminium alloys containing scandium, Structure and properties*, Gordon and Breach Science Publishers, Amsterdam, 1998.

Vatne, H.E.,, Ph.D. Dissertation, The Norwegian University of Science and Technology, Trondheim, 1995.

Westengen, H., Auran, L. and Reiso, O., *Effect of minor additions of transition elements on the recrystallization of some commercial aluminium alloys*, Aluminium, vol. 57, nr. 12 (1981), p. 797.

Zakharov, V.V., *Stability of the solid solution of scandium in aluminium*, Met. Sci. Heat Treat., vol. 39, nr. 1-2 (1997), p. 61.

PART VI
MECHANICAL PROPERTIES

1. INTRODUCTION

Al-Mg wrought alloys in the 5xxx-series exhibit the highest strength properties of alloys based on solid solution hardening and strain hardening. It is possible to increase the strength up to values comparable to those of the 6xxx- and 7xxx-series alloys by cold deformation (H1-tempers), but the high-temperature stability of such microstructures are very low and in practice stabilising annealing of strain hardened sheets/plates have to be performed (H3-tempers).

Al-Mg alloys have exellent weldability. However, the loss of strength in the weldment has been of great concern and restricts the use of these alloys to low load bearing parts in most types of constructions. The loss of strength is basically caused by recrystallization of the base material in the heat affected zone and a lower strength of the cast structure in the weld metal.

In the present part the results from welding trials and tensile testing are reported. The effect of the dispersoids on the strength and ductility of heat treated material, extruded material, cold rolled material and welded joints have been emphasised.

2. THEORETICAL BACKGROUND

2.1 STRENGTHENING MECHANISMS IN NON AGE HARDENABLE ALLOYS

2.1.1 Solid solution and strain hardening

The basic mechanism for increasing the strength of a metal by addition of atoms in solid solution is to impede movement of dislocations through the crystal lattice. In real situations, an increase in the flow stress is usually not caused by one single mechanism alone. The near coupling between solution hardening and strain hardening always appears through solute-dislocation interactions and dislocation-dislocation interactions. Solution hardening has traditionally been treated as a contribution to the friction stress, which shifts the whole stress-strain curve to higher stresses. In this case, the contribution from solution hardening upon the total glide resistance is expressed as:

$$\tau = \tau_f(c) + \tau_d(\rho) \tag{VI-1}$$

where τ_f expresses the contribution from solute-dislocation interaction and τ_f the contribution from the dislocation-dislocation interactions. This means that the contribution from solution hardening and strain hardening is additive. This behaviour is observed for a range of Ag alloys, Cu-Au, Cu-Ni and Th-C, Kocks (1985). However, in many cases the superposition of solution hardening and strain hardening has been found to be proportional related causing the stress-strain curves to diverge at larger strain. This can be expressed as follows:

$$\tau = \tau_f(c) + [1 + k(c)] \cdot \tau_d(\rho) \tag{VI-2}$$

where the term $k \cdot \tau_d$ amounts to the interaction between solution and strain hardening. Classical examples of alloys with such behaviour are Al-Mg, Cu-Al and Ni-Mo, Kocks (1985)

2.1.2 Strengthening from dispersoids

There are in principle two distinct ways that particles can retard moving dislocations, i) particles may be cut by the dislocation and ii) particles can resist cutting and thereby force the dislocation to bypass, for instance by climb and cross slip.

Important parameters that determine the efficiency of the strength increment due to particles are the volume fraction and the size, which determine the interparticle spacing. A high density of small particles is much more efficient than a lower density of larger particles because a higher number of particle-dislocation interactions operate at the same time. Furthermore, whether a particle is cut or not depends not only on the particle size but also on its lattice structure, orientation relationship to the matrix and the particle strength. The following strengthening mechanisms can operate (Ardell (1985), Dieter (1988), Reppich (1983)):

- **Coherency strains** may origin from the lattice mismatch between the particle and the matrix causing restrictions in dislocation movements in the resulting strain fields.
- **Stacking fault energy (SFE):** if the particle and matrix have significant differences in the SFE and the particle can form extended dislocation then a hardening contribution origins from local variation in the fault widths when the dislocation enters the particle
- **Ordered structures** form anti phase boundaries when they are sheared giving rise to a hardening increment.
- **Modulus strengthening** may occur if the particle and the matrix have different shear modulus. This is due to the fact that the dislocation energy will change when it passes through a phase with a different shear modulus.
- **Formation of new surface** occurs when a particle is sheared and results in an increase in the surface energy, which must be supplied by the external stress.
- **Lattice friction stresses** contribute to a hardening increment due to different strengths of the particle and matrix.

Theoretical expressions have been developed for each of the mechanisms mentioned above, Ardell (1985) or Dieter (1988).

For age hardenable alloys, the strength increases with particle size and eventually decreases in overaged conditions. The decrease in strength has been associated with the loss of coherency between particle and matrix lattices and the possibility for dislocations to move around particles instead of cutting them. It should also be emphasised that the size of the particles could play a role for the change in the operating hardening mechanism.

If the particles are not shearable, then the dislocations are forced to bypass the particle and leaving a dislocation loop around it. This mechanism is acknowledged as the socalled Orowan mechanism. From dislocation theory it can be derived that the shear stress required bowing a dislocation to a radius R between two obstacles is approximately equal to Gb/2R (G=shear modulus and b=burger vector). If the obstacles are two hard particles then the maximum radius of the bowed dislocation becomes R=λ/2 (λ=interparticle spacing) and the corresponding stress required to force the dislocation between the two obstacles, the socalled Orowan stress, will be (Dieter (1988)):

$$\tau_O = \frac{Gb}{\lambda} \tag{VI-3}$$

The Orowan equation is the first reliable mathematical formulation of the dispersion strengthening and it is still the basis for the understanding of the effect of strengthening by non-deformable particles, Ardell (1985). A number of versions of this equation have been developed in order to correct for i) the interparticle mean free path in the glide plane, λ_p, ii) interaction between dislocation segments on either side of the particle. The most widely used version is the Orowan-Ashby equation, which takes the following form (Ashby (1966), Dieter (1988)):

$$\Delta\sigma = \frac{0.13 \cdot G \cdot b}{\lambda} \cdot \ln\left(\frac{r}{b}\right) \tag{VI-4}$$

where G is the shear modulus (27.5 GPa), b is the burgers vector (0.286 nm), r is the particle radius and λ is the mean free particle spacing in the slip plane given by (Dieter (1988)):

$$\lambda = \sqrt{\frac{2 \cdot \pi \cdot r^2}{3 \cdot f}} \tag{VI-5}$$

2.2 PROPERTIES OF COMMERCIAL 5XXX-ALLOYS

The new alloys AA5383 and AA5059 were developed in order to meet the requirements for alloys with improved strength without changing other properties such as fatigue strength, corrosion resistance and weldability. Strength and ductility values for these two alloys and for AA5083 are listed in Table VI-1. See Table I-1, Part I, for chemical composition.

Increased strength in AA5383 and AA5059 is mainly achieved by a higher level of Mg in solid solution. A higher susceptibility to intergranular and stress corrosion is compensated by introducing zinc. The zinc content reduces the electrochemical potential in the microstructure and thus reduces the corrosion susceptibility. A higher level of Mn also gives rise to a higher strength, mainly as dispersoid strengthening. A small amount of Zr is also introduced, mainly to help off with grain refinement, Sampath et al. (1998).

Table VI-1 *Yield strength, tensile strength and elongation for AA5083, AA5383 and AA5059. From Marthinussen (2000) and the European Standard EN 573.*

Alloy	Temper	$R_{p0.2}$ (MPa)	R_m (MPa)	A_5 (%)
AA5083	O/H111	125	275	14
	H321/H116	215	305	10
	H321/H116-welded[1]	125	275	-
AA5383	O/H111	145	290	17
	H321/H116	220	305	10
	H321/H116-welded[1]	140	290	-
AA5059	O/H111	160	330	24
	H321/H116	260	360	10
	H321/H116-welded[1]	160	300	-
	Extruded-H112-L[2]	225	350	12
	Extruded-H112-LT[3]	200	330	10
	Extruded+welded[1]	160	295	-

[1]Welded with 5183 filler wire, [2]L=longitudinal direction, [3]LT=longitudinal transverse direction.

3. EXPERIMENTAL

3.1 WELDING OF EXTRUDED PROFILES

Flat profiles with a cross sectional area of 5x70 mm^2 were extruded in the laboratory press. The billet temperature was 475°C and the ram speed was 1 mm/s, see Part IV for details.

The profiles were cut to 80 cm lengths and machined to a groove geometry for butt welding. The groove angle was 60° with a root face of 1 mm and a root gap of 2 mm, see Figure VI-1. The filler material was a SAFRA 66 filler wire with a diameter Ø1.2mm. The MIG-welding was performed at the welding laboratory at SINTEF Materials Technology on an ESAB ARISTO 500 welding facility. Other welding parameters are given in Appendix J.

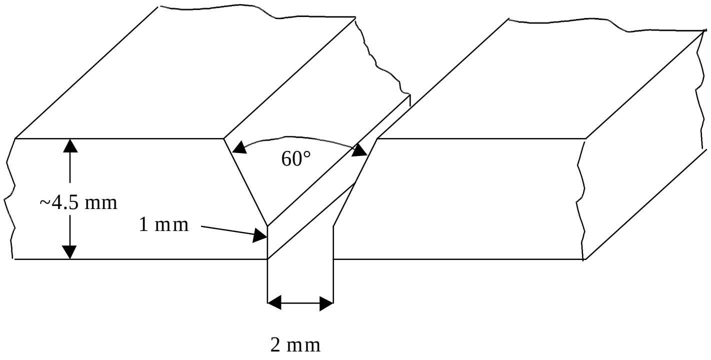

***Figure VI-1** Groove geometry for butt welding of extruded profiles.*

3.2 TENSILE TESTING

Tensile testing was performed in order to obtain strength and ductility data for the material investigated in this work. The testing procedures are described below and from the registered stress-strain curves the following parameters were calculated: yield stress ($R_{p0.2}$), tensile strength (R_m), elongation at maximum stress (A_m) and the fracture elongation (A_f). The results are based upon testing of at least 3 parallels.

3.2.1 Tensile testing of heat treated, extruded and cold rolled material

Tensile specimens were machined from the heat treated extrusion billets, the extruded profiles and the cold rolled profiles according to the dimensions shown in Appendix K.

The specimens from the heat treated extrusion billets were cut with the longitudinal centre axis parallel to the centre axis of the billet and at a billet radius of r/2≈23mm. The specimens for both as extruded material (20x25 mm^2) and cold rolled material were cut out from the centre of the extruded profiles and the cold rolled profiles, respectively, which means that the tensile specimens were machined from both sides.

The tensile testing was performed in a MTS 880 testing facility interfaced with a 790.90 TestStar II control system. A constant cross head velocity of 0.035 mm/s was applied, giving an engineering strain rate, $\dot{e}$, of 0.001 s^{-1}. The applied extensometer had a gauge section of 25 mm. The testing procedures are according to the international standard *ISO 6892 Metallic materials- Tensile testing at ambient temperature.*

3.2.2 Tensile testing of welded profiles

Cross weld tensile specimens were machined from the welded profiles. The specimens were flushed on both sides in order to remove the weld bead and the dimensions of the specimens are shown in Appendix K.

The tensile testing was performed in an INSTRON type 1126 testing machine. The cross head velocity was 5 mm/min and the specimens were fixed to the testing machine by means of pin-fork connectors. An INSTRON extensometer with a gauge length of 50 mm was applied. The extensometer was positioned symmetrical to the weld. The testing procedures are according to the international standard *ISO 6892 Metallic materials- Tensile testing at ambient temperature.*

3.3 HARDNESS MEASUREMENTS

The hardness measurements were carried out as described in Part VI, Section 3.2 in this thesis.

4. RESULTS AND DISCUSSION

4.1 STRENGTH AND DUCTILITY OF TENSILE TESTED MATERIAL

In the condition of the heat-treated material an increase in both yield strength and tensile strength was observed with the additions of Mn, Zr and Sc. The increase in the strength is also accompanied with a corresponding decrease in the ductility, Figure VI-2 a) and Table VI-2 a).

The yield strength in AlMgZr, AlMgMn, AlMgMnZr and AlMgMnZrSc has increased to 104, 117, 124 and 137 MPa, respectively, from 101 MPa in AlMg while the fracture elongation has decreased to 27, 20, 14 and 17% respectively, compared to 30% for AlMg.

The solute effect of magnesium atoms is most likely the main strengthening mechanism of AlMg. The solid solubility of Zr and Sc is very small so it is believed that the contribution from these elements is entirely from particles (dispersoids). However, the solubility of manganese is much higher and it is expected that the aluminium matrix will contain some manganese in solid solution. Thus, strength contribution from both solid solution and small particles (dispersoids) is expected to occur from manganese.

As opposed to the material tested in an undeformed condition, the strength and the ductility of extruded profiles will depend on the amount of recovery and recrystallization that occur during and after the extrusion process. A fully recrystallized microstructure is expected to have strength and ductility equal to that of a homogenized condition before deformation while the preservation of a deformed microstructure is expected to arrive at a higher strength and lower ductility compared to the homogenized condition.

The results in Figure VI-2 b) and Table VI-2 b) clearly illustrate the effect of recrystallization upon the mechanical properties. In Part V it was shown that AlMg was recrystallised and AlMgMn was partly recrystallised after extrusion. The strength and elongation for these two alloys are quite close to those of the heat treated condition. The properties for AlMgZr, AlMgMnZr and AlMgMnZrSc are changed to higher strength and lower ductility. In these three alloys the yield strength increases to 152, 176 and 200 MPa, respectively, from 96 MPa in AlMg. The fracture elongation is reduced by 50% to 70%.

The cold rolled profiles exhibit yield strengths in the range of 312 to 398 MPa and elongations from 5% to 7.5%. The strength increases and the elongation decreases slightly with increasing alloy content, Figure VI-2 c) and Table VI-2 c).

In the welded samples it was observed that the cross weld yield strength was higher than that of the heat treated conditions but lower than that of the extruded conditions, Figure VI-2 and Table VI-2. With increasing alloy content, the yield strength and the tensile strength increases while the elongation decreases. The yield strength is 107, 121, 123, 155 and 161 MPa for alloy AlMg, AlMgZr, AlMgMn, AlMgMnZr and AlMgMnZrSc, respectively, and the corresponding fracture elongation is 25, 21, 21, 14 and 12%.

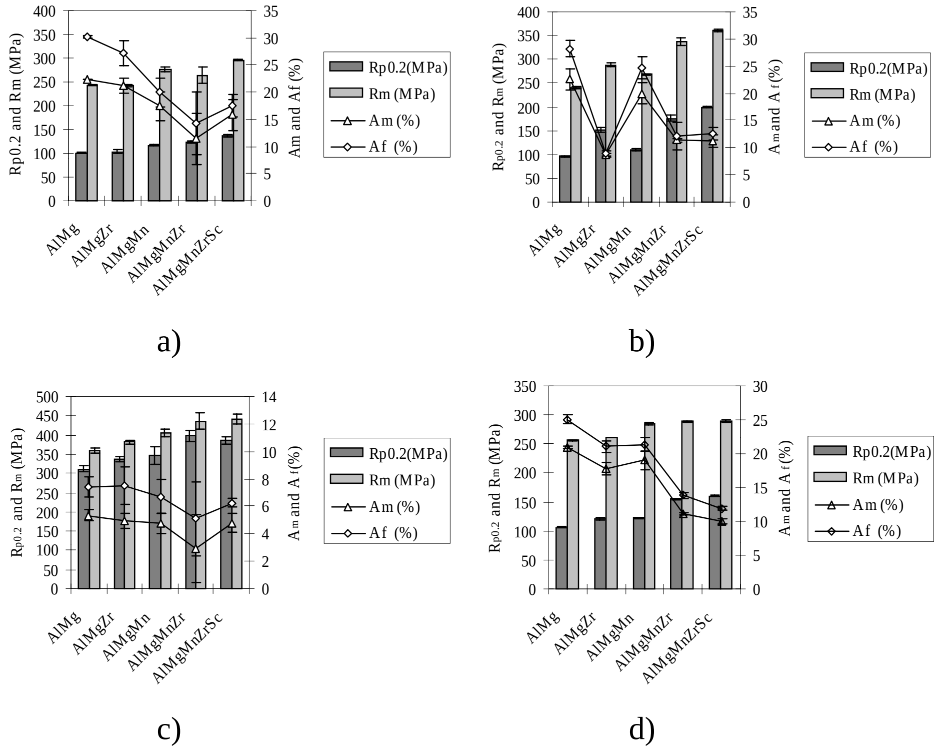

a) b)

c) d)

Figure VI-2 *Yield strength ($R_{p0.2}$), tensile strength (R_m), elongation at maximum stress (A_m) and at fracture (A_f) for a) heat treated material, b) extruded profiles, c) extruded and cold rolled profiles and e) extruded and welded profiles.*

Table VI-2 *Summay of average values for tensile testing of different conditions of AlMg, AlMgZr, AlMgMn, AlMgMnZr and AlMgMnZrSc.*

a) Heat treated material

Alloy	$R_{p0.2}$(MPa)	R_m (MPa)	A_m (%)	A_f (%)
AlMg	100.5	242.7	22.3	30.2
AlMgZr	103.9	242.3	21.3	27.1
AlMgMn	117.0	276.2	17.4	20.0
AlMgMnZr	124.0	263.4	11.4	14.3
AlMgMnZrSc	136.9	295.7	15.8	17.4

b) Extruded profiles

Alloy	$R_{p0.2}$(MPa)	R_m (MPa)	A_m (%)	A_f (%)
AlMg	95.7	240.2	22.6	28.2
AlMgZr	152.2	288.6	8.7	8.8
AlMgMn	110.7	268.5	20.0	24.7
AlMgMnZr	176.4	337.9	11.4	12.1
AlMgMnZrSc	199.5	361.6	11.2	12.6

c) Extruded and cold rolled profiles

Alloy	$R_{p0.2}$(MPa)	R_m (MPa)	A_m (%)	Af (%)
AlMg	311.9	358.7	5.3	7.4
AlMgZr	337.2	381.5	5.0	7.5
AlMgMn	345.2	404.3	4.8	6.7
AlMgMnZr	397.8	435.8	2.9	5.1
AlMgMnZrSc	386.3	440.6	4.8	6.2

d) Welded profiles

Alloy	$R_{p0.2}$(MPa)	R_m (MPa)	A_m (%)	A_f (%)
AlMg	106.8	256.5	21.0	25.0
AlMgZr	120.8	261.0	17.8	21.1
AlMgMn	122.5	285.0	19.0	21.4
AlMgMnZr	154.8	288.8	11.2	13.8
AlMgMnZrSc	160.8	289.5	10.0	11.9

A summary of single values, average values and standard deviations for the tensile tests are found in the tables in Appendix L.

The strength and ductility in the O-temper have been compared with the three commercial alloys AA5083, AA5383 and AA5059, Figure VI-3 a). Values from Table I-1 is compared with the AlMgMnZrSc alloy from the present investigation. It is obvious that alloying an Al-Mg alloy with a combination of the elements Mn, Zr and Sc gives both a higher strength and an improved ductility compared to 5083. It must be emphasised that the strength increase is obtained simply by changing the chromium with a combination of Zr and Sc. In addition, AlMgMnZrSc has a lower content of iron and silicon than is usual in AA5083.

Further, it can be seen that AlMgMnZrSc has a lower yield strength, a slightly higher tensile strength but the same ductility as compared to AA5383, Figure VI-3 a). The improved properties in AA5383 (compared to AA5083) are obtained by increasing the level of Mg, Mn, Zn and Zr and by reducing the level of the impurity elements Fe and Si. The AA5059 alloy has improved mechanical properties compared to all other alloys due to an increase in the level for all alloying elements, especially Mg, Mn and Zr.

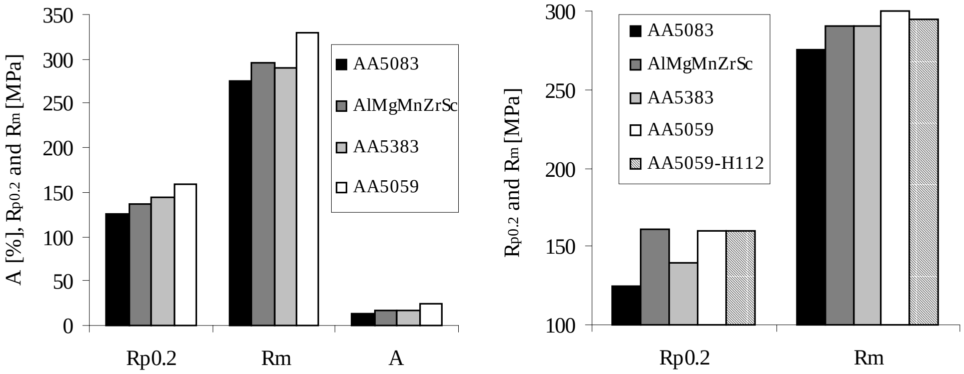

Figure VI-3 *Mechanical properties for AlMgMnZrSc and the commercial alloys AA5083, AA5383 and AA5059 in a) O-temper condition and b) H321+welded condition (5183 filler wire). (Note that AlMgMnZrSc and AA5059-H112 is in the extruded temper condition before welding and that AlMgMnZrSc was welded with the SAFRA filler wire.)*

In the welded condition, however, the mechanical properties for the AlMgMnZrSc is better than those for AA5083 and AA5383 and equal to those for AA5059 when welded with the SAFRA filler wire. This proves that a combined addition of Zr and Sc results in mechanical properties comparable to the strongest commercial Al-Mg alloys available

4.2 STRENGTHENING FROM DISPERSOIDS

The addition of manganese, zirconium and scandium to an Al-Mg alloy results in an increase in the yield strength, Figure VI-2 a). The strength increase is associated with the presence of the particles formed during heat treatment. Strengthening from second phase particles occurs due to a number of different contributions primarily determined by the differences in properties in the matrix and the second phase particles. Small and/or soft particles are cut and deformed by dislocations and strengthening occurs due to several mechanisms. If the particles are difficult to cut the strength increment can be explained by the Orowan mechanism.

Applying Eqs. VI-4 and 5 together with the data of the particle structure, Table VI-1, it is possible to calculate the Orowan stresses originating from the particles and comparing these values with the experimental values obtained from the tensile testing. The results are shown in Table VI-3. It can be seen that the calculated values for the Al_6Mn-dispersoids are underestimated by 14-16 MPa, while the calculated value for Al_3Sc-dispersoids is underestimated by 8 MPa. The calculated values of Al3Zr is overestimated in AlMgZr and underestimated in AlMgMnZr.

Table VI-3 *Experimental and estimated strength increment due to the different types of dispersoids in heat treated material.*

Alloy	Dispersoid type	$\Delta\sigma_{experimental}$ (MPa)	$\Delta\sigma_{calculated}$ (MPa)
AlMgZr	Al_3Zr	3	7
AlMgMn	Al_6Mn	16	4
AlMgMnZr	Al_6Mn	20	4
	Al_3Zr	7	6
	Total	27	10
AlMgMnZrSc	Al_6Mn	~16	4
	$Al_3(Sc,Zr)$	20	12
	Total	36	16

The deviation between the calculated and the experimental values for Al_6Mn can be explained in several ways. First of all, the contribution from the primary constituents is not taken into account. These particles will contribute to the strength increment in the same way as the dispersoids. Second, manganese in solid solution will give rise to strengthening. In a pure binary Al-Mn alloy the effect of manganese on the yield strength is 30.3 MPa/wt%

(Hatch (1984)) and this effect is probably not affected by additions of other alloying elements. Finally, the shape of the particles can influence the hardening effect. Kelly (1972) showed that, for a given volume fraction of particles with the shape of rods or plates, the Orowan stresses are considerably higher compared to spherical particles at the same volume fraction. The stress increment can be increased by a factor of two for particles with high aspect ratios.

The calculated strength increment for Al_3Zr and $Al_3(Sc,Zr)$ is in accordance with the experimental values taking into account the difficulties in determining accurate values for the volume fractions. Since the Al_3Zr-particles were unevenly distributed in the microstructure it is very difficult to obtain accurate results. The estimated particle density for Al_3Zr is most likely larger than the real value because only areas rather rich in particles were considered. Thus, a higher volume fraction of particles results in a lower value of the interparticle distance, Eq. VI-5, giving rise to the overestimation of the Orowan stress, Eq. VI-4. In the case of $Al_3(Sc, Zr)$ the particles were very small and the possibility of not resolving all particles in the TEM leads to a smaller volume fraction of precipitates and thus a lower calculated Orowan stress.

Rather limited data is available in the literature on the strengthening mechansims acting when the aluminium matrix contain particles of Al_6Mn, Al_3Zr and Al_3Sc. Parker et al. (1995) made some calculations on hardening of Al_3Sc-particles and concluded that the strengthening effect could be accounted for by the theories of the cutting mechanism. Strength increment contribution from the formation of an antiphase boundary and coherency strain agreed well with experimental data indicating that the precipitates were coherent and had an ordered structure. It should be mentioned that the size of the precipitates were extremely small, only approximately 3 nm. In a work of Torma et al. (1989) it was concluded that the hardening in a peak aged (1 hour at 310°C) Al-0.19at%Sc occurred by the Orowan mechanism. In this case the size of the precipitates were approximately 6 nm. Torma et al. (1989) also claim that in an under-aged condition, where extremely small precipitates are present, the cutting mechanism is operating. Drits et. al. (ref. [4] in Torma et al. (1989)) claim that the mechanisms of work hardening depend on the size of the precipitates formed during ageing. It was found that the cutting mechanism operated when the particle size was lower that 6.8 nm while for larger particles the Orowan mechanism operated. This is also consistent with Eq. VI-4 from which it should be recognized that for small particle diameters the Orowan mechanism will cease to be operative because the stress in the particle due to the Orowan loop will exceed the theoretical shear stress of the particle, Embury (1985).

In the present work similar calculations to those of Parker et al. (1995) gave unreasonable high values for the strength increment for Al_3Zr and $Al_3(Sc,Zr)$. Thus, considering the particles size (r=23 nm for Al_3Zr and r=11 nm for $Al_3(Sc,Zr)$) the results are in accordance with the findings in the literature and it can be concluded that the operating strengthening mechanism for the Al_3Zr- and $Al_3(Sc,Zr)$-dispersoids is the Orowan mechanism. It is assumed that this is also the case for the Al_6Mn-dispersoids.

4.3 DEFORMATION STRENGTHENING

Considerable strengthening was observed in the cold rolled material. This is due to energy storing in the microstructure during deformation. The energy increase is associated with an overall increase in the dislocation density and the formation of subgrain boundaries, Eq. I-14.

In the case of hot extrusion it was found that considerable strengthening was obtained in the alloys which displayed a fibrous structure after deformation ($\Delta\sigma$=48-63 MPa, Table VI-1). The microstructural evolution during extrusion was not investigated in this work, but it is believed that deformation in Al-Mg alloys is controlled by dynamic recovery processes. The presence of dispersoids retard recovery and hence a higher amount of energy may be stored in the structure, even if the material is slowly cooled from the deformation temperature after extrusion. The results clearly illustrate the effectiveness of the Al_6Mn, Al_3Zr and $Al_3(ScZr)$ in increasing the stored energy after hot working by preserving a stable deformation substructure. This is either due to retarding dynamic recovery or static recovery and recrystallization.

4.4 MICROSTRUCTURES AND HARDNESS PROFILES ACROSS THE WELDMENTS

The hardness profiles across the weldments show that the strength is determined primarily by the strength of the weakest part of the welded joint. In the completely recrystallized AlMg alloy, the hardness is approximately 8 VHN lower than that of the weld metal, Table VI-4. This means that the base metal is the weakest part and as a result the fracture was observed to be located outside the fusion zone, i.e. in the base material, after tensile testing. The same was observed for the welded AlMgZr-profile in which only a few recrystallized grains were observed and hence a fibrous structure was partly preserved after extrusion. However, the preservation of the fibre structure is not sufficient to increase the hardness above that of the weld metal. Consequently, the fracture was located outside the weld zone in this case as well. For AlMgMn, AlMgMnZr and AlMgMnZrSc the fractures after tensile testing were all located in the weld metal. As can be seen from Figure VI-4 the hardness profile across the weld in AlMgMn is more or less flat. The location of the fracture in the WM in this alloy is probably due to a high amount of coarse primary constituents formed during solidification of the weld pool. In AlMgMnZr and AlMgMnZrSc alloys the hardness in the base metal was higher than in the weld metal. Thus, the weld metal is the weakest part for these three alloys, Table VI-4.

Table VI-4 *Vickers hardness of base metal (BM) and weld metal (WM), hardness difference (┘HV) between BM and WM and location of fracture.*

Alloy	BM	WM	ΔHV	Fracture
AlMg	71	79	-8	BM
AlMgZr	74	79	-5	BM
AlMgMn	81	81	0	WM
AlMgMnZr	85	80	5	WM
AlMgMnZrSc	90	83	7	WM

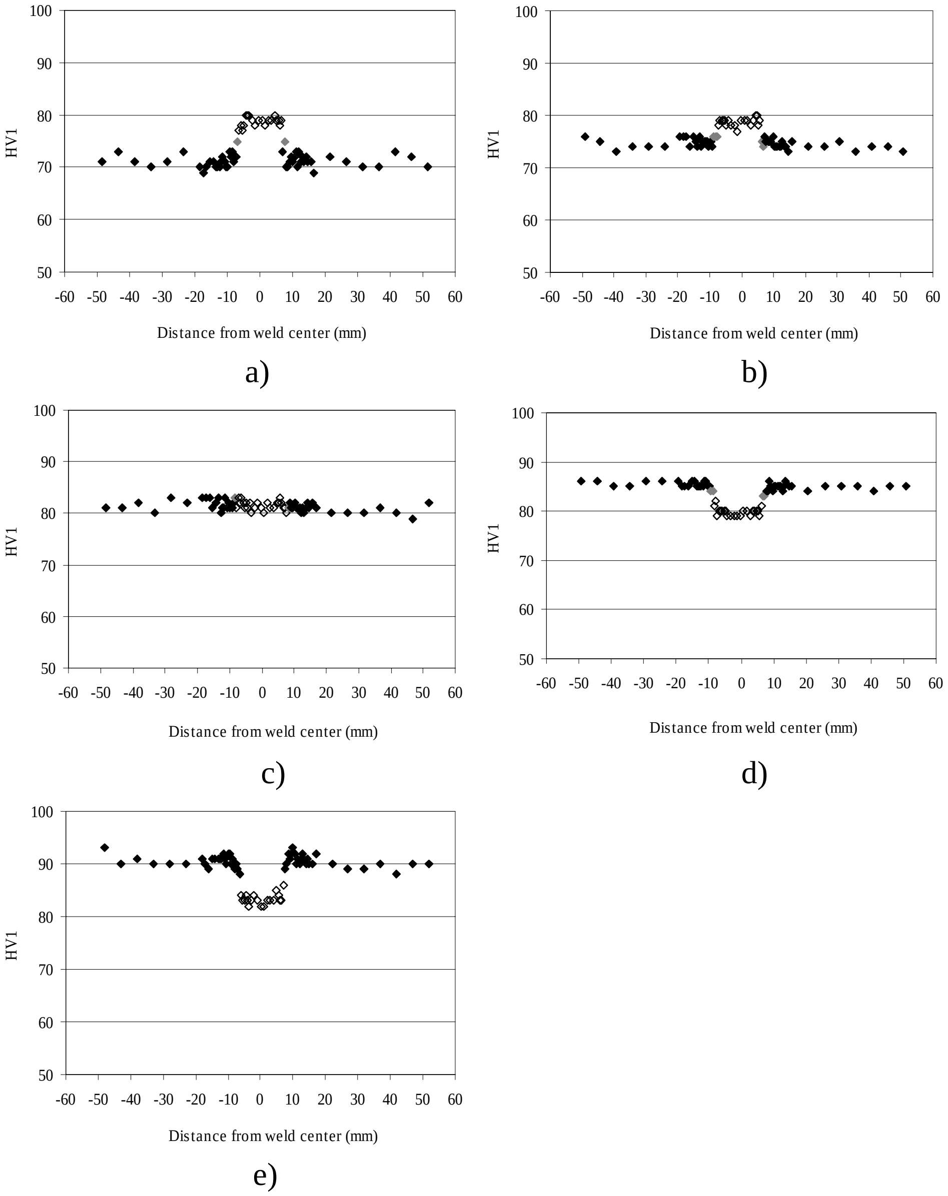

Figure VI-4 *Hardness profiles across the weldments. a) AlMg, b) AlMgZr, c) AlMgMn, d) AlMgMnZr and e) AlMgMnZrSc. Filled symbols: BM, open symbols: WM and grey symbols: probably BM (difficult to decide).*

Micrographs of the weldments of the five alloys are shown in Figure VI-5. A metallographical identification of the heat-affected zone was more or less impossible. However, from the hardness profiles in Figure VI-4 a minor hardness gradient from the base metal and towards the weld metal can be recognised. This is especially evident for AlMgMnZrSc. However, under any circumstances the WM is the weakest part in this alloy and an increase in the WM strength could possibly increase the overall strength in an AlMgMnZrSc/SAFRA weldment.

Based on the results from the back-annealing experiments of cold rolled material, it is expected that welding of a strain hardened material would give rise to a more pronounced HAZ than observed in the weldments of the extruded material.

A small increase in hardness (4 VHN) was observed in the WM in the AlMgMnZrSc/SAFRA weldment compared to AlMg/SAFRA, Table VI-4. It has been observed elsewhere that the chemistry of the WM can be changed by a mixing of the filler material and the base material, and thus changing the properties of the WM. The properties of the weld metal are usually determined by the cast structure, which develop during solidification of the weld pool. Thus, it can be concluded that alloying the base metal with Mn, Zr and Sc also gives rise to an increase of the weld metal strength.

A grain size effect in the weld metal, which is similar to that found for the cast extrusion billets, Part II, was also observed. It was found that the grain size of the weld metal is much smaller for the alloys without Zr, i.e. AlMg and AlMgMn, Figure VI-4. In cast structures Zr results in grain refinement. However, the grain refinement ability of Zr is absent when Ti and Zr are present simultaneously. The results are unexpected since the filler wire also contains 0.1 wt% Zr.

As a final comment it should be emphasised that the post weld strength is determined by the weakest part of the weldment. The results in the present investigation indicate that the weakest part is the weld metal. Utilisation of the strength increase in Al-Mg alloys by a combined addition of Mn, Zr and Sc as dispersoid forming elements can only be obtained by the use of a filler material with a considerably higher strength than SAFRA 66. Thus, development of new high strength filler wires is desirable. Another interesting topic for further consideration is the possibility of welding these alloys by use of the friction stir method.

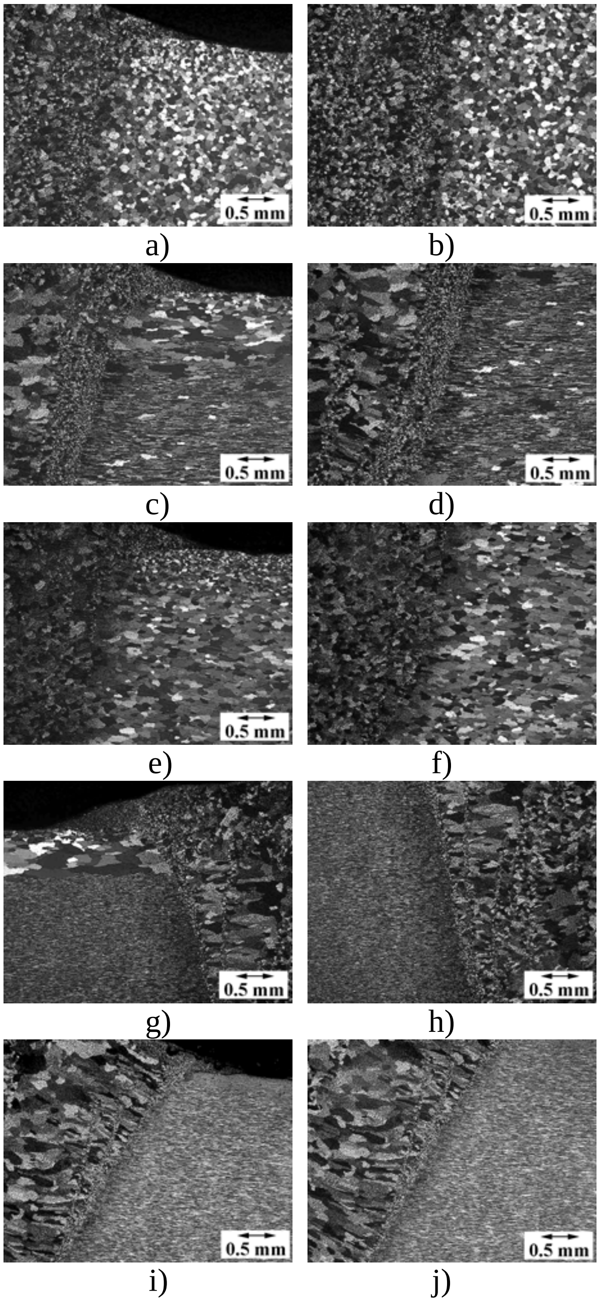

Figure VI-5 Micrographs of the fusion zone of welded profiles. a) AlMg, surface, b) AlMg, centre, c) AlMgZr, surface, d) AlMgZr, centre, e) AlMgMn, surface, f) AlMgMn, centre, g) AlMgMnZr, surface, h) AlMgMnZr, centre, i) AlMgMnZrSc, surface and j) AlMgMnZrSc, centre.

5. CONCLUSIONS

- Al-Mg can be strengthened considerably in the O-temper by addition of Mn, Zr and Sc. The strengthening is due to dispersoids of the type Al_6Mn, Al_3Zr and $Al_3(Sc,Zr)$ most likely through the Orowan mechanism.
- Strengthening after hot deformation was even more pronounced, especially the effect of the $Al_3(Sc,Zr)$-dispersoids. This strengthening is due to the retained deformation structure and is directly coupled with the Zener drag from the dispersoids.
- Identification of the HAZ in an optical microscope was difficult, but some softening towards the fusion line was revealed by hardness measurements in AlMgMnZrSc.
- Increasing the strength of the model alloys moves the position of the weakest part after welding from the base metal (AlMg and AlMgZr) to the weld metal (AlMgMn, AlMgMnZr and AlMgMnZrSc).
- Thus, it can be concluded that since the weld metal is the weakest part, the strength increase due to alloying with Mn, Zr and Sc may not be fully utilised after welding with SAFRA 66.

REFERENCES

Ardell, A.J., *Precipitation hardening*, Met. Trans. A, vol. 16A, December (1985), p. 2131.

Ashby, M.F., *Results and consequences of a recalculation of the Frank-Read and the Orowan stress*, Acta Met., vol. 14, May (1966), p. 679.

Dieter, G.E., *Mechanical Metallurgy*, McGraw-Hill Book Company, Singapore, 1988.

Embury, J.D., *Plastic flow in dispersion hardened materials*, Met. Trans. A, vol. 16A, December (1985), p. 2191.

Hatch, J.E., *Aluminium: Properties and physical metallurgy*, ASM, Metals Park, Ohio, 1984.

Kelly, P.M., *The effect of particle shape on dispersion hardening*, Scripta Met., vol. 6 (1972), p. 647.

Kocks, U.F., *Kinetics of solution hardening*, Met. Trans. A, vol. 16A, December (1985), p. 2109.

Marthinussen, J.I., DNV specifications, private comunication, 2000.

Parker, B.A., Zhou, Z.F. and Nolle, P., *The effect of small additions of scandium on the properties of aluminium alloys*, J. Mat. Sci., vol. 30 (1995), p. 452.

Reppich, B., *Particle strengthening, in Material Science and Technology*, eds. Cahn, R.W., Haasen, P. and Kramer, E.J., VCH Publishers, Weinheim, Germany, vol. 6 (1993), p. 311.

Sampath, D., Moldenhauer, S., Schipper, H.R. and Schrijvers, A.J., *Development of advanced ship building materials*, Preceedings of The 6th Int. Conf. on Aluminium Alloys, ICAA6, Toyahashi, Japan, 1998.

Torma, T., Kovacs-Csetenyi, E., Turmezey, T., Ungar, T. and Kovacs, I., *Hardening mechanisms in Al-Sc alloys*, J. Mat. Sci., vol. 24 (1989), p. 3924.

PART VII

CONCLUDING REMARKS
AND PERSPECTIVE FOR FURTHER WORK

1. CONCLUDING REMARKS

The present work has demonstrated a unique possibility of alloying Al-Mg alloys with a combination of the transition elements Mn, Zr and Sc.

After casting, most of the Zr and Sc remained in solid solution. The Mn was partly present in large primary constituent particles and partly in solid solution. However, large solid solution segregations were observed affecting the density and distribution of the dispersoids formed during heat treatment.

The decomposition of solid solutions of these elements resulted in the formation of dispersoids of the type:
- Al_6Mn with an orthorhombic lattice structure. This phase precipitated independently of the other elements in solid solution.
- Al_3Zr with a cubic lattice structure. This phase also precipitated independent of the other elements in solid solution.
- $Al_3(Sc,Zr)$ with a cubic lattice structure. This phase precipitated when Sc and Zr are present simultaneously in solid solution and independently of other elements. The mean value of the Sc/Zr-ratio was 3.5.

Large segregations of Mg occurred in the cast structure. Isothermal heat treatments at high temperatures in the single-phase area in the phase diagram allow rapid homogenisation of Mg-segregations and dissolution of low melting primary constituents (Al_3Mg_2). However, heat treatment at low temperatures in the single-phase area where diffusion rates of Mg is low, resulted in precipitation of Al_3Mg_2 in the Mg rich parts of the segregations. After long-term annealing the precipitates redissolved.

Manganese segregated opposite of what is expected from a eutectic element and showed a very low concentration in the interdendritic regions with a high content of magnesium. The Mn-segregations probably occurs due to a decreased solubility of Mn in the presence of Mg. As a consequence, during heat up or in the very early stages of the heat treatment a very high density of small dispersoids form inside the dendrites while Mn-precipitate free zones will form in the interdendritic regions. After prolonged heat treatment the PFZ's are not so pronounced due to particle growth and coarsening.

The low content of Zr and Sc made it difficult to analyse the segregations of these elements in detail. However, it seems that segregations of Zr are larger than those of Sc. Al_3Zr particles were distributed rather heterogeneously as compared to the $Al_3(ScZr)$-particles.

Due to the high magnesium content, which reduces the solubility of all the other elements, it may be assumed that all Mn, Zr and Sc are present in the dispersoids.

The effect of Mn, Zr and Sc upon the hot deformation properties is ascribed to the precipitated dispersoids. It was found that the particles increased the flow stress during hot deformation considerably. As compared to the alloy without dispersoids, the presence of Al_6Mn and Al_3Zr or $Al_3(Sc,Zr)$ increased the flow stress by 20-100% depending on the temperature and strain rate. The effect of the particles decreases as the Zener-Hollomon parameter increases. Extrusion experiments also confirm the hot torsion result. The ram load increased by 20-30% in the range of Z-values investigated. However, it is interesting to note that the effect of Al_3Zr and $Al_3(Sc,Zr)$ do not differ significantly and thus it can be concluded that Sc has a minor effect upon the flow stress and the ram load.

The hot ductility is reduced considerably with the presence of Zr, Sc and especially Mn. Microstructural observations suggest that the poor effect of Mn is related to the presence of primary constituents and dispersoid free zones in interdendritic regions. It was found that pores nucleate at the constituents and grow along the zones free of precipitates. It is assumed that this is due to strain localisation. The hot ductility may be improved by heat treatment. Increasing the thermal load results in a lower density and a more even distribution of dispersoids thus reducing the amount of strain localisation.

Furthermore, the present work has demonstrated that the recrystallization properties of Al-Mg alloys may be affected considerably by introducing Mn, Zr and Sc. The recrystallization behaviour after hot deformation may be effectively determined by the Zener drag exhibited by the dispersoids on grain boundaries. Al_6Mn showed to be least effective while $Al_3(Sc,Zr)$ is extremely effective in retarding recrystallization.

After cold deformation, however, the recrystallization behaviour is different due to a higher amount of stored energy. In the alloy without dispersoids, recrystallization occurred by classical nucleation at microstructural heterogeneties. Texture measurements showed that recrystallization is nucleated preferentially at grain boundaries but also minor nucleation at transition bands and shear bands could be possible. A minor texture component also indicated some particle stimulated nucleation. On the other hand, when dispersoids are present, the particle stimulated nucleation mechanism is dominating. Thus, the most favourable nucleation sites in the presence of dispersoids are within deformation zones at large primary constituents. Other nucleation mechanisms seem to be suppressed.

Recrystallization of cold rolled material resulted in an extremely fine-grained microstructure. Once recrystallised, extensive grain growth occurs in alloys containing Al_6Mn and/or Al_3Zr. Contrary, alloys containing Al_6Mn and $Al_3(Sc,Zr)$ are very stable and the fine-grained structure seems to be very stable up to 550°C. This clearly proves that $Al_3(Sc,Zr)$ are thermally stable and efficient in pinning grain boundaries up to very high temperatures.

In the last part of this thesis the mechanical properties of the investigated alloys were tested in several temper conditions by means of tensile testing. It was found that the presence of Al_6Mn and $Al_3(Sc,Zr)$ caused an increase in the flow stress of 36 MPa in the O-temper condition. The effect of Al_6Mn and Al_3Zr alone or in combination was less pronounced. The strengthening mechanism of the dispersoids is most likely dislocations bypassing the particles by the Orowan mechanism.

The retained deformation microstructure associated with the Zener drag forces exhibited by the dispersoids resulted in considerable strengthening. For instance, the combination of Al_6Mn and $Al_3(Sc,Zr)$ increased the strength by approximately 100 MPa compared to the dispersoid free alloy. Again the effect of Al_6Mn and Al_3Zr is less pronounced due to the lower capacity in retarding recrystallization.

The capability of the dispersoids to retard recrystallization should be an opportunity to increase the strength of the heat-affected zone after fusion welding. This is an important aspect since strain hardened conditions are used commercially. However, it has been demonstrated that utilisation of the strength increase in the base material is not achieved as long as the weld metal is the weakest part in the weldment. However, a yield strength of 160 MPa was achieved for the material containing both Al_6Mn and $Al_3(Sc,Zr)$, while somewhat lower values were obtained for the alloys with Al_6Mn and/or Al_3Zr. This is at the same level as the strongest commercial alloy (AA5059)

Thus, as a final conclusion it can be stated that the additions of Mn, Zr and Sc improves the recrystallization properties and the mechanical properties of Al-Mg alloys. It should be emphasised that the precipitation of the metastable cubic Al_3Zr and the stable cubic $Al_3(Sc,Zr)$ is favourable in an aluminium-magnesium matrix due to a close similarity of the lattice structures. The $Al_3(Sc,Zr)$-phase is similar to the equilibrium Al_3Sc-phase and has a high thermal stability and thus the coherency with the aluminium matrix is retained to very high temperatures. The present work has demonstrated the beneficial features of the $Al_3(Sc,Zr)$-phase upon recrystallization and strength. However, this also results in an increase in the deformation resistance and especially the features of manganese reduce the hot ductility.

2. PERSPECTIVE FOR FURTHER WORK

The present work has been concerned with several topics and a thorough and profound treatment of each has been difficult. However, this thesis serves as a basis for the understanding of the features of the dispersoids formed by the elements Mn, Zr and Sc in Al-Mg alloys and as a basis for further development. Thus, based on the results presented in this thesis, a list of the topics which is believed to have the highest potential for further development is given below.

- Heat treatment: The size and density of Al_6Mn-dispersoids is important for the recrystallization properties. In order to obtain particle structures with improved recrystallization properties more effort should be put into studying this topic. Lower temperature and shorter time would give a finer structure of the Al_6Mn-dispersoids.

- In order to understand the different features (size, distribution, coherency, coarsening) of the dispersoids Al_3Sc, Al_3Zr and $Al_3(Sc,Zr)$ upon recrystallization a broader investigation should be carried out.

- Characterisation of deformed microstructures was not performed at all in this work and should be done in order to improve the understanding of the effect of the different dispersoids.

- Considerable strengthening from Zr- and Sc-additions in Al-Mg alloys may be obtained after hot/cold working. However, utilisation of this strength increase is not obtained after fusion welding. Thus, further development of a high strength filler alloy is desirable.

- Friction stir welding should be considered. Even though this process may be not being suitable commercially, it could be of importance for special applications that requires extremely strong weldments.

APPENDICES

Appendix A

ACCURACY OF RESISTIVITY MEASUREMENTS

The resistivity, ρ, may be expressed by a function of the temperature, T, as:

$$\rho = a \cdot T + b \qquad \text{A-1}$$

where a and b are regression coefficients. In order to estimate the uncertainty, the following function u has to be considered:

$$u = a \cdot T + b - \rho \qquad \text{A-2}$$

The total differential of u is:

$$du = \frac{\partial u}{\partial T} dT + \frac{\partial u}{\partial \rho} d\rho \qquad \text{A-3}$$

and the maximum absolute uncertainty, $|\Delta u|$, may be estimated from the following expression:

$$|\Delta u| = \left| \frac{\partial u}{\partial T} \Delta T \right| + \left| \frac{\partial u}{\partial \rho} \Delta \rho \right| \qquad \text{A-4}$$

$\partial u / \partial T$ and $\partial u / \partial \rho$ is found from Eq. A-2 and thus the maximum relative uncertainty becomes:

$$\frac{|\Delta u|}{u} = \frac{|a \cdot \Delta T| + |\Delta \rho|}{u} \qquad \text{A-5}$$

Now the uncertainty can be estimated from the conditions under which the measurements were conducted. The temperature was 20±1°C, giving ΔT=2°C. Further, the conductivity of Al-4.5Mg at 20°C is 22,27±1% MS/m. The uncertainty of this measurement is 22,27±0.22 MS/m which corresponds to the resistivity being in the range 4.45 to 4.54 μΩcm. This gives Δρ=0.09 μΩcm.

Thus, applying Eqs. A-1 and A-5 to the results of Figure II-3 (a=0.0069 μΩcm/°C) gives a total relative uncertainty of the resistivity measurement of Al-4.5Mg at 20°C of 2.3%.

Appendix B

CHANGE IN RESISTIVITY DURING ISOTHERMAL ANNEALING.

Table A-1 *AlMg*

	T=275°C		T=300°C		T=325°C		T=350°C		T=375°C		T=400°C	
Time (min)	Δρ	St.dev.	Δρ	St.dev.	Δρ	St.dev.	Δρ	St.dev.	Δρ	St.dev.	Δρ	St.dev.
0.5	0.0076	0.0092	-0.0205	0.0104	-0.0053	0.0122	-0.0093	0.0221	0.0062	0.0058	0.0146	0.0010
1	-0.0027	0.0200	-0.0267	0.0131	-0.0031	0.0145	-0.0116	0.0062	0.0099	0.0104	0.0326	0.0060
2	-0.0187	0.0199	-0.0285	0.0197	-0.0076	0.0122	-0.0165	0.0082	0.0213	0.0069	0.0640	0.0040
4	-0.0410	0.0153	-0.0320	0.0273	-0.0112	0.0137	0.0028	0.0050	0.0367	0.0090	0.0938	0.0140
8	-0.0358	0.0097	-0.0407	0.0206	-0.0017	0.0095	0.0184	0.0089	0.0616	0.0121	0.1239	0.0115
16	-0.0405	0.0160	-0.0375	0.0223	0.0043	0.0129	0.0395	0.0115	0.0871	0.0075	0.1464	0.0091
30	-0.0376	0.0094	-0.0377	0.0208	0.0143	0.0152	0.0662	0.0065	0.1075	0.0131	0.1555	0.0074
60	-0.0436	0.0088	-0.0224	0.0127	0.0351	0.0168	0.0964	0.0109	0.1280	0.0139	0.1571	0.0075
120	-0.0444	0.0128	-0.0031	0.0107	0.0660	0.0240	0.1171	0.0081	0.1439	0.0228	0.1575	0.0126
300	-0.0321	0.0160	0.0174	0.0028	0.0964	0.0103	0.1438	0.0053	0.1574	0.0196	0.1521	0.0131
480	-0.0040	0.0144			*	*	*	*	*	*	*	*
1000	0.0258	0.0280	0.0702	0.0093	*	*	*	*	*	*	*	*
3000	0.0625	0.0242	0.1121	0.0127	0.1443	0.0191	0.1670	0.0133	0.1634	0.0298	0.1429	0.0140
10000	0.1155	0.0305	0.1545	0.0102	0.1485	0.0266	*	*	0.1522	0.0287	*	*

	T=425°C		T=450°C		T=475°C		T=500°C		T=525°C		T=550°C	
Time (min)	Δρ	St.dev.	Δρ	St.dev.	Δρ	St.dev.	Δρ	St.dev.	Δρ	St.dev.	Δρ	St.dev.
0.5	0.0254	0.0186	0.0451	0.0161	0.0844	0.0133	0.1005	0.0086	0.1056	0.0044	0.1380	0.0070
1	0.0490	0.0284	0.0821	0.0253	0.1118	0.0131	0.1278	0.0128	0.1343	0.0091	0.1534	0.0058
2	0.0816	0.0185	0.1186	0.0096	0.1281	0.0074	0.1411	0.0221	0.1424	0.0052	0.1454	0.0162
4	0.1133	0.0275	0.1404	0.0152	0.1356	0.0108	0.1479	0.0097	0.1448	0.0016	0.1520	0.0109
8	0.1337	0.0156	0.1545	0.0137	0.1394	0.0087	*	*	0.1519	0.0021	*	*
16	0.1394	0.0338	0.1580	0.0102	0.1308	0.0104	*	*	*	*	*	*
30	0.1432	0.0170	0.1623	0.0092	0.1356	0.0037	*	*	*	*	*	*
60	0.1468	0.0174	0.1631	0.0103	*	*	*	*	*	*	*	*
120	0.1489	0.0045	*	*	*	*	*	*	*	*	*	*
300	0.1528	0.0113	*	*	*	*	*	*	*	*	*	*
480	*	*	*	*	*	*	*	*	*	*	*	*
1000	*	*	*	*	*	*	*	*	*	*	*	*
3000	0.1442	0.0040	*	*	*	*	*	*	*	*	*	*
10000	*	*	*	*	0.1459	0.0102	*	*	0.1552	0.0095	*	*

Table A-2 *AlMgZr*

	T=300°C		T=325°C		T=350°C		T=375°C		T=400°C		T=425°C	
Time (min)	Δρ	St.dev.	Δρ	St.dev.	Δρ	St.dev.	Δρ	St.dev.	Δρ	St.dev.	Δρ	St.dev.
0.5	-0.0168	0.0088	-0.0117	0.0085	-0.0159	0.0038	-0.0124	0.0015	0.0013	0.0043	0.0266	0.0056
1	-0.0261	0.0094	-0.0157	0.0127	-0.0192	0.0025	-0.0077	0.0024	0.0112	0.0016	0.0452	0.0009
2	-0.0170	0.0049	-0.0117	0.0071	-0.0104	0.0038	0.0021	0.0024	0.0235	0.0055	0.0539	0.0044
4	-0.0074	0.0016	-0.0023	0.0067	0.0030	0.0031	0.0102	0.0029	0.0372	0.0047	0.0640	0.0049
8	-0.0036	0.0098	0.0058	0.0137	0.0170	0.0101	0.0269	0.0058	0.0566	0.0047	0.0706	0.0060
16	-0.0056	0.0078	0.0068	0.0047	0.0246	0.0021	0.0419	0.0048	0.0670	0.0096	0.0776	0.0087
30	-0.0023	0.0039	0.0145	0.0067	0.0567	0.0147	0.0551	0.0082	0.0802	0.0079	0.0818	0.0088
60	0.0211	0.0125	0.0360	0.0120	0.0807	0.0106	0.0753	0.0027	0.0793	0.0235	0.0842	0.0114
300	0.0485	0.0104	0.0983	0.0008	0.0887	0.0142	0.1055	0.0175	0.0812	0.0084	0.0866	0.0250
1000	0.0800	0.0019	0.1031	0.0045	0.0751	0.0217	0.0645	0.0179	0.0647	0.0104	0.0784	0.0205
3000	0.0573	0.0198	0.0954	0.0071	0.0557	0.0073	0.0341	0.0201	0.0217	0.0034	0.0383	0.0043
10000	0.0433	0.0010	0.0440	0.0067	0.0345	0.0104	0.0161	0.1372	0.0187	0.0146	0.0054	0.0012

	T=450°C		T=475°C		T=500°C		T=525°C		T=550°C	
Time (min)	Δρ	St.dev.	Δρ	St.dev.	Δρ	St.dev.	Δρ	St.dev.	Δρ	St.dev.
0.5	0.0424	0.0054	0.0576	0.0063	0.0648	0.0067	0.0858	0.0091	0.1017	0.0142
1	0.0538	0.0035	0.0693	0.0115	0.0701	0.0081	0.0842	0.0128	0.1025	0.0127
2	0.0624	0.0035	0.0826	0.0132	0.0688	0.0110	0.0839	0.0138	0.1011	0.0135
4	0.0661	0.0023	0.0897	0.0107	0.0688	0.0114	0.0825	0.0175	0.0963	0.0132
8	0.0687	0.0017	0.0936	0.0167	0.0669	0.0153	0.0847	0.0185	0.1009	0.0147
16	0.0694	0.0079	0.0860	0.0159	0.0661	0.0179	0.0777	0.0211	0.0904	0.0145
30	0.0660	0.0074	0.0808	0.0050	0.0683	0.0113	0.0757	0.0133	0.0869	0.0157
60	0.0732	0.0108	0.0783	0.0128	0.0784	0.0113	0.0756	0.0203	0.1032	0.0137
300	0.0686	0.0063	0.0769	0.0168	0.0799	0.0083	0.0915	0.0059	0.1003	0.0074
1000	0.0653	0.0225	0.0687	0.0231	0.0643	0.0094	0.0897	0.0050	0.1129	0.0155
3000	0.0281	0.0327	0.0450	0.0285	0.0373	0.0209	0.0676	0.0056	0.1036	0.0275
10000	-0.0086	0.0213	-0.0163	0.0162						

Table A-3 *AlMgMn*

	T=300°C		T=325°C		T=350°C		T=375°C		T=400°C		T=425°C	
Time (min)	Δρ	St.dev.	Δρ	St.dev.	Δρ	St.dev.	Δρ	St.dev.	Δρ	St.dev.	Δρ	St.dev.
0.5	-0.0473	0.0022	-0.0391	0.0065	-0.0305	0.0115	-0.0264	0.0110	0.0065	0.0011	0.0143	0.0023
1	-0.0533	0.0043	-0.0471	0.0013	-0.0370	0.0141	-0.0204	0.0058	0.0032	0.0043	0.0269	0.0037
2	-0.0756	0.0037	-0.0692	0.0098	-0.0451	0.0167	-0.0330	0.0089	0.0148	0.0059	0.0381	0.0062
4	-0.0736	0.0043	-0.0657	0.0109	-0.0471	0.0085	-0.0204	0.0024	0.0242	0.0037	0.0479	0.0106
8	-0.0811	0.0023	-0.0642	0.0032	-0.0431	0.0101	-0.0163	0.0073	0.0260	0.0075	0.0490	0.0152
16	-0.0771	0.0031	-0.0642	0.0072	-0.0320	0.0046	0.0061	0.0067	0.0333	0.0087	0.0537	0.0116
30	-0.0706	0.0065	-0.0552	0.0098	-0.0203	0.0081	0.0102	0.0179	0.0289	0.0120	0.0581	0.0261
60	-0.0226	0.0013	-0.0070	0.0155	0.0328	0.0272	0.0425	0.0188	0.0340	0.0010	0.0480	0.0141
300	-0.0033	0.0098	-0.0033	0.0056	0.0248	0.0204	-0.0004	0.0359	-0.0050	0.0454	-0.0430	0.0061
1000	0.0152	0.0109	-0.0003	0.0022	-0.0408	0.0364	-0.0676	0.0036	-0.1104	0.0506	-0.1286	0.0654
3000	0.0029	0.0032	-0.0524	0.0104	-0.1195	0.0109	-0.1594	0.0130	-0.2000	0.0390	-0.2542	0.0358
10000	-0.1266	0.0072	-0.2177	0.0332	-0.3434	0.0034	-0.3707	0.0251	-0.3792	0.0211	-0.4822	0.0120

	T=450°C		T=475°C		T=500°C		T=525°C		T=550°C	
Time (min)	Δρ	St.dev.	Δρ	St.dev.	Δρ	St.dev.	Δρ	St.dev.	Δρ	St.dev.
0.5	0.0285	0.0076	0.0402	0.0075	0.0410	0.0062	0.0702	0.0138	0.0913	0.0067
1	0.0402	0.0017	0.0464	0.0119	0.0498	0.0054	0.0687	0.0155	0.0917	0.0084
2	0.0460	0.0040	0.0533	0.0113	0.0491	0.0091	0.0665	0.0198	0.0835	0.0109
4	0.0464	0.0052	0.0471	0.0129	0.0517	0.0122	0.0702	0.0223	0.0812	0.0188
8	0.0431	0.0081	0.0419	0.0184	0.0421	0.0181	0.0609	0.0289	0.0711	0.0158
16	0.0361	0.0092	0.0380	0.0172	0.0337	0.0254	0.0462	0.0384	0.0481	0.0192
30	0.0285	0.0098	0.0169	0.0185	0.0131	0.0454	0.0272	0.0228	0.0176	0.0231
60	0.0178	0.0412	0.0191	0.0385	0.0095	0.0506	-0.0387	0.0124	-0.0125	0.0193
300	-0.0627	0.0143	-0.0997	0.0283	-0.1196	0.0390	-0.1462	0.0143	-0.1511	0.0395
1000	-0.1700	0.0544	-0.3082	0.0847	-0.3304	0.0106	-0.3852	0.0104	-0.3233	0.0370
3000	-0.3500	0.0251	-0.4266	0.0477	-0.4400	0.0032	-0.4706	0.0120	-0.3863	0.0422
10000	-0.6739	0.0124	-0.5769	0.0235	-0.5300	0.0345	-0.4983	0.0250	-0.3869	0.0330

Table A-4 *AlMgMnZr*

	T=300°C		T=325°C		T=350°C		T=375°C		T=400°C		T=425°C	
Time (min)	Δρ	St.dev.	Δρ	St.dev.	Δρ	St.dev.	Δρ	St.dev.	Δρ	St.dev.	Δρ	St.dev.
0.5	-0.0286	0.0007	-0.0334	0.0044	-0.0290	0.0055	-0.0165	0.0063	0.0008	0.0224	0.0061	0.0037
1	-0.0290	0.0055	-0.0339	0.0092	-0.0290	0.0089	-0.0253	0.0026	-0.0089	0.0046	0.0028	0.0050
2	-0.0394	0.0019	-0.0474	0.0063	-0.0414	0.0025	-0.0185	0.0031	-0.0028	0.0105	0.0076	0.0060
4	-0.0385	0.0023	-0.0446	0.0064	-0.0359	0.0094	-0.0193	0.0088	-0.0016	0.0081	0.0088	0.0163
8	-0.0441	0.0031	-0.0418	0.0044	-0.0354	0.0017	-0.0081	0.0088	0.0032	0.0085	0.0064	0.0212
16	-0.0485	0.0020	-0.0550	0.0053	-0.0323	0.0119	-0.0113	0.0133	-0.0145	0.0137	-0.0077	0.0151
30	-0.0473	0.0073	-0.0494	0.0097	-0.0318	0.0092	-0.0006	0.0077	-0.0101	0.0182	0.0068	0.0260
60	0.0024	0.0008	-0.0012	0.0134	0.0183	0.0125	0.0000	0.0044	-0.0077	0.0266	0.0044	0.0223
300	-0.0236	0.0119	-0.0225	0.0007	-0.0576	0.0001	-0.0643	0.0194	-0.1349	0.0027	-0.0894	0.0374
1000	-0.0730	0.0157	-0.1192	0.0164	-0.2144	0.0606	-0.2799	0.0681	-0.2466	0.0379	-0.2637	0.0881
3000	-0.1635	0.0358	-0.2485	0.0366	-0.4952	0.0214	-0.5131	0.0587	-0.4479	0.0489	-0.5520	0.0868
10000	-0.2298	0.0210	-0.5761	0.0369	-0.7591	0.0064	-0.7690	0.0991	-0.6761	0.0272	-0.7728	0.0909

	T=450°C		T=475°C		T=500°C		T=525°C		T=550°C	
Time (min)	Δρ	St.dev.	Δρ	St.dev.	Δρ	St.dev.	Δρ	St.dev.	Δρ	St.dev.
0.5	0.0202	0.0110	0.0163	0.0074	0.0349	0.0103	0.0466	0.0122	0.0604	0.0187
1	0.0101	0.0176	0.0249	0.0047	0.0369	0.0132	0.0416	0.0129	0.0559	0.0203
2	0.0226	0.0066	0.0134	0.0056	0.0402	0.0165	0.0379	0.0116	0.0604	0.0172
4	0.0166	0.0070	0.0012	0.0012	0.0324	0.0219	0.0297	0.0122	0.0390	0.0274
8	0.0141	0.0091	-0.0130	0.0031	0.0165	0.0192	0.0045	0.0186	0.0153	0.0310
16	-0.0028	0.0101	-0.0359	0.0110	-0.0033	0.0237	-0.0286	0.0194	-0.0210	0.0402
30	0.0036	0.0111	-0.0694	0.0080	-0.0342	0.0239	-0.0637	0.0218	-0.0545	0.0493
60	-0.0245	0.0031	-0.0627	0.0480	-0.0809	0.0178	-0.1189	0.0239	-0.0818	0.0654
300	-0.1403	0.0020	-0.2721	0.0032	-0.3075	0.0164	-0.3149	0.0069	-0.2868	0.0596
1000	-0.3856	0.0717	-0.5760	0.0484	-0.5494	0.0465	-0.5147	0.0450	-0.4713	0.0175
3000	-0.6403	0.0403	-0.7771	0.0241	-0.7064	0.0125	-0.6256	0.0310	-0.5720	0.0204
10000	-0.8513	0.0651	-0.8088	0.0380	-0.7450	0.0424	-0.6708	0.0214	-0.6226	0.0565

Table A-5 *AlMgMnZrSc*

	T=300℃		T=325℃		T=350℃		T=375℃		T=400℃		T=425℃	
Time (min)	Δρ	St.dev.	Δρ	St.dev.	Δρ	St.dev.	Δρ	St.dev.	Δρ	St.dev.	Δρ	St.dev.
0.5	-0.0241	0.0089	-0.0249	0.0050	-0.0237	0.0094	-0.0050	0.0033	0.0021	0.0064	0.0066	0.0063
1	-0.0266	0.0095	-0.0229	0.0076	-0.0295	0.0083	-0.0206	0.0083	-0.0050	0.0090	0.0079	0.0031
2	-0.0299	0.0034	-0.0287	0.0038	-0.0233	0.0032	-0.0107	0.0038	0.0033	0.0038	0.0246	0.0113
4	-0.0324	0.0079	-0.0319	0.0093	-0.0274	0.0109	-0.0132	0.0020	0.0094	0.0079	0.0191	0.0120
8	-0.0369	0.0155	-0.0324	0.0033	-0.0328	0.0015	-0.0041	0.0019	0.0137	0.0094	0.0199	0.0108
16	-0.0447	0.0103	-0.0365	0.0073	-0.0340	0.0063	-0.0083	0.0026	0.0050	0.0131	0.0083	0.0093
30	-0.0452	0.0129	-0.0558	0.0089	-0.0435	0.0066	-0.0112	0.0126	0.0046	0.0225	0.0008	0.0199
60	-0.0421	0.0138	-0.0702	0.0025	-0.0510	0.0030	-0.0672	0.0082	-0.0359	0.0244	-0.0630	0.0153
300	-0.1226	0.0000	-0.1306	0.0028	-0.1457	0.0134	-0.2200	0.0051	-0.2180	0.0058	-0.2449	0.0098
1000	-0.1841	0.0011	-0.2532	0.0331	-0.4049	0.0329	-0.5361	0.0089	-0.3841	0.0485	-0.3694	0.0609
3000	-0.2775	0.0328	-0.4322	0.0232	-0.7420	0.0480	-0.8486	0.0865	-0.5735	0.0120	-0.6103	0.0081
10000	-0.4799	0.0632	-0.8433	0.0119	-1.1213	0.0106	-1.1505	0.0534	-0.9059	0.0333	-0.8983	0.0066

	T=450℃		T=475℃		T=500℃		T=525℃		T=550℃	
Time (min)	Δρ	St.dev.	Δρ	St.dev.	Δρ	St.dev.	Δρ	St.dev.	Δρ	St.dev.
0.5	0.0266	0.0112	0.0264	0.0132	0.0393	0.0058	0.0642	0.0085	0.0729	0.0025
1	0.0287	0.0139	0.0260	0.0073	0.0367	0.0100	0.0629	0.0115	0.0627	0.0081
2	0.0350	0.0144	0.0226	0.0115	0.0329	0.0157	0.0570	0.0076	0.0559	0.0045
4	0.0275	0.0107	0.0109	0.0171	0.0208	0.0190	0.0511	0.0084	0.0466	0.0058
8	0.0212	0.0168	0.0000	0.0057	0.0058	0.0224	0.0336	0.0173	0.0192	0.0026
16	0.0041	0.0256	-0.0258	0.0202	-0.0149	0.0296	0.0041	0.0261	-0.0062	0.0022
30	-0.0088	0.0326	-0.0636	0.0334	-0.0525	0.0340	-0.0300	0.0334	-0.0528	0.0062
60	-0.0663	0.0172	-0.1095	0.0258	-0.0957	0.0222	-0.1414	0.0120	-0.1511	0.0319
300	-0.2314	0.0458	-0.3404	0.0134	-0.3139	0.0225	-0.4315	0.0094	-0.3607	0.0406
1000	-0.5366	0.0380	-0.6352	0.0807	-0.5743	0.0414	-0.6070	0.0151	-0.5131	0.0416
3000	-0.7591	0.0344	-0.8181	0.0242	-0.7930	0.0372	-0.7382	0.0127	-0.6736	0.0141
10000	-1.0076	0.0206	-0.9710	0.0232	-0.8804	0.0119	-0.7834	0.0404	-0.7156	0.0150

Appendix C

HOT TORSION DATA

Table A-6 *AlMg, cast.*

Lognr.	$T_{def.}$	ω	M_{max}	σ
	°C	rad/s	Nm	MPa
13057	550	0.0256	1.61	11.7
13065	525	0.0264	2.21	16.0
13066	500	0.0254	2.65	19.1
13067	475	0.0255	3.22	23.2
13103	550	0.0106	1.30	9.5
13124	525	0.0112	1.64	11.9
13142	500	0.0113	2.00	14.5
13158	475	0.0114	2.59	18.6
13187	550	0.0910	2.65	19.3
13200	525	0.0932	3.09	22.4
13209	500	0.0941	4.00	28.9
13218	475	0.0942	4.99	35.9
13231	550	1.0170	5.00	36.4
13239	525	1.0106	6.19	44.9
13244	500	1.0012	7.58	54.8
13249	475	1.0025	8.97	64.6
13326	550	3.6191	7.51	54.7
13339	525	3.5975	8.83	63.8
13350	500	3.5198	10.49	75.5
13357	475	3.4941	11.69	83.8
13773	550	0.0125	1.39	10.1
13767	525	0.0126	1.75	12.7
13760	500	0.0130	2.25	16.2
13752	475	0.0106	2.58	18.6
13742	550	0.1006	2.67	19.4
13731	525	0.1020	3.30	23.9
13724	500	0.1030	4.19	30.2
13717	475	0.1034	5.34	38.4
13706	550	1.0079	5.01	36.5
13698	525	1.0182	5.98	43.4
13691	500	1.0657	7.51	54.3
13684	475	1.0502	9.51	68.5
13675	550	3.4297	7.84	57.1
13665	525	3.5407	9.14	66.3
13655	500	3.9468	10.50	75.9
13650	475	3.5001	11.99	86.3

Table A-7 *AlMg, heat treated.*

Lognr.	T_{def}.	ω	M_{max}	σ
	°C	rad/s	Nm	MPa
14502	550	0.0155	1.49	10.8
14499	525	0.0155	1.77	12.9
14495	500	0.0158	1.67	12.2
14489	475	0.0151	2.87	20.8
14480	550	0.1415	2.76	20.1
14478	525	0.1402	3.66	26.6
14476	500	0.1405	4.14	30.1
14474	475	0.1064	5.02	36.4
14465	550	0.9359	5.06	36.9
14463	525	0.9484	5.84	42.5
14461	500	1.0227	7.42	53.9
14459	475	1.0276	9.30	67.4
14453	550	4.1051	7.12	51.9
14451	525	4.0974	9.01	65.6
14447	475	4.0189	11.27	81.7
14503	550	0.0155	1.49	10.9
14501	525	0.0155	1.81	13.1
14497	500	0.0107	2.03	14.8
14481	550	0.1409	2.68	19.5
14479	525	0.1413	3.75	27.3
14477	500	0.1409	4.20	30.5
14475	475	0.1391	5.51	39.9
14466	550	0.9317	4.54	33.1
14464	525	0.9436	5.76	41.9
14462	500	0.9395	6.94	50.4
14460	475	1.0238	8.94	64.8
14454	550	4.0960	7.50	54.6
14452	525	4.1008	9.09	66.2
14450	500	4.0822	10.43	75.8
13675	550	3.4297	7.84	57.1
13665	525	3.5407	9.14	66.3
13655	500	3.9468	10.50	75.9
13650	475	3.5001	11.99	86.3

Table A-8 *AlMgZr, cast.*

Lognr.	T_{def}.	ω	M_{max}	σ
	°C	rad/s	Nm	MPa
13107	550	0.0111	1.48	10.7
13126	525	0.0112	1.83	13.2
13147	500	0.0113	2.40	17.3
13166	475	0.0118	3.00	21.5
13189	550	0.0919	2.72	19.7
13202	525	0.0951	3.47	25.1
13212	500	0.0954	4.33	31.2
13221	475	0.0943	5.27	37.8
13232	550	1.0145	5.24	38.0
13240	525	1.0122	7.01	50.6
13245	500	1.0015	7.89	56.8
13250	475	1.0006	9.35	67.0
13328	550	3.5612	8.10	58.7
13342	525	3.6281	9.49	68.6
13351	500	3.5278	11.06	79.6
13358	475	3.5056	12.09	86.7
13774	550	0.0125	1.56	11.3
13768	525	0.0126	2.02	14.6
13763	500	0.0129	2.54	18.3
13753	475	0.0107	2.86	20.5
13743	550	0.1015	2.93	21.2
13732	525	0.1025	3.68	26.6
13726	500	0.1031	4.34	31.3
13718	475	0.1033	5.72	41.0
13707	550	1.0303	5.26	38.1
13699	525	1.0248	6.39	46.1
13692	500	1.0740	8.30	59.7
13685	475	1.0370	10.11	72.5
13676	550	3.4273	7.85	56.9
13666	525	3.5771	9.48	68.5
13658	500	3.4937	11.04	79.4
13651	475	3.5203	12.00	86.0

Table A-9 *AlMgZr, heat treated.*

Lognr.	T_{def}.	ω	M_{max}	σ
	°C	rad/s	Nm	MPa
14058	550	0.0100	1.61	11.6
14052	525	0.0102	1.91	13.8
14045	500	0.0099	2.30	16.5
14036	475	0.0111	2.94	21.1
14029	550	0.1346	3.20	23.2
14023	525	0.1041	3.83	27.6
14016	500	0.1063	4.59	33.0
14009	475	0.1052	5.72	41.0
13995	550	1.0326	5.38	38.9
13989	525	1.0279	6.60	47.6
13951	500	1.0460	7.89	56.7
13944	475	1.1067	9.65	69.2
13982	550	3.1724	7.93	57.3
13975	525	3.3815	9.41	67.8
13960	475	3.4419	11.97	85.8
14125	550	0.0103	1.64	11.8
14117	525	0.0109	1.91	13.8
14110	500	0.0153	2.52	18.1
14104	475	0.0105	2.88	20.7
14189	550	0.1261	3.26	23.5
14186	525	0.1009	3.96	28.5
14182	500	0.1017	4.38	31.5
14178	475	0.1045	5.51	39.5
14172	550	1.0547	5.69	41.1
14168	525	1.0538	6.97	50.3
14163	500	1.1143	8.04	57.8
14159	475	1.0679	9.48	67.9
14151	550	3.4583	8.18	59.1
14146	525	3.3827	9.49	68.4
14141	500	3.3896	10.67	76.7

Table A-10 *AlMgMn, cast.*

Lognr.	T_{def}.	ω	M_{max}	σ
	°C	rad/s	Nm	MPa
13109	550	0.0113	2.00	14.3
13131	525	0.0116	2.75	19.7
13150	500	0.0111	3.16	22.5
13173	475	0.0113	3.63	25.8
13192	550	0.0983	3.60	25.8
13204	525	0.0959	4.26	30.4
13213	500	0.0954	5.34	38.0
13224	475	0.0963	6.19	43.9
13233	550	1.0106	6.44	46.2
13241	525	1.0049	7.26	51.9
13246	500	1.0018	8.59	61.2
13251	475	1.0030	10.48	74.4
13329	550	3.5981	8.80	63.1
13343	525	3.6002	10.30	73.6
13353	500	3.5468	12.39	88.2
13359	475	3.4992	13.12	93.1
13776	550	0.0125	2.05	14.7
13769	525	0.0126	2.62	18.7
13761	500	0.0128	3.39	24.1
13755	475	0.0154	4.21	29.9
13745	550	0.1019	3.49	25.1
13734	525	0.1371	4.59	32.8
13727	500	0.1028	5.27	37.5
13720	475	0.1034	6.41	45.5
13709	550	0.8001	6.11	43.8
13701	525	1.2854	8.10	57.9
13694	500	1.1883	9.29	66.2
13687	475	1.0666	11.15	79.1
13678	550	3.4206	8.47	60.7
13669	525	3.4991	10.37	74.1
13659	500	3.9451	12.13	86.4
13652	475	3.9396	13.68	97.1

Table A-11 *AlMgMn, heat treated.*

Lognr.	T_{def}.	ω	M_{max}	σ
	°C	rad/s	Nm	MPa
14059	550	0.0100	1.87	13.5
14053	525	0.0100	2.29	16.4
14046	500	0.0100	2.62	18.8
14040	475	0.0100	3.31	23.7
14031	550	0.1061	3.44	24.7
14024	525	0.1044	3.82	27.4
14018	500	0.1055	5.04	36.0
13996	550	1.0301	5.87	42.2
13990	525	1.0312	6.82	48.9
13952	500	1.0434	8.48	60.7
13946	475	1.0464	10.16	72.6
13977	525	3.3305	9.60	68.8
13962	475	3.1428	12.67	90.6
14126	550	0.0103	1.86	13.4
14121	525	0.0108	2.15	15.4
14111	500	0.0151	2.92	20.9
14105	475	0.0105	3.50	25.0
14482	550	0.1412	3.43	24.6
14483	525	0.1397	4.17	29.9
14485	500	0.1385	5.08	36.4
14486	475	0.1378	6.38	45.6
14467	550	0.9378	5.64	40.5
14468	525	0.9381	6.60	47.3
14469	500	0.9395	8.23	58.9
14470	475	0.9299	9.78	69.9
14152	550	3.4558	7.62	54.7
14147	525	3.3854	9.70	69.6
14142	500	3.4138	11.48	82.2

Table A-12 *AlMgMnZr, cast.*

Lognr.	T_{def}.	ω	M_{max}	σ
	°C	rad/s	Nm	MPa
13110	550	0.0115	2.53	18.0
13153	500	0.0115	3.57	25.3
13176	475	0.0118	4.36	30.8
13195	550	0.0980	4.00	28.5
13206	525	0.0953	5.00	35.5
13214	500	0.0963	5.75	40.7
13225	475	0.0982	7.01	49.6
13236	550	1.0156	6.76	48.1
13242	525	1.0062	8.00	56.8
13247	500	1.0070	9.54	67.6
13252	475	1.0009	11.43	80.8
13331	550	3.8763	9.80	69.7
13344	525	3.6356	11.25	79.9
13354	500	3.5594	12.24	86.7
13360	475	3.5063	13.99	98.9
13777	550	0.0126	2.71	19.3
13770	525	0.0126	3.17	22.6
13764	500	0.0128	4.07	28.9
13756	475	0.0152	4.71	33.3
13746	550	0.1017	4.15	29.5
13736	525	0.1378	5.08	36.0
13728	500	0.1031	5.99	42.4
13721	475	0.1038	7.04	49.8
13710	550	1.0268	6.88	49.0
13702	525	1.2958	8.56	60.8
13695	500	1.3188	9.96	70.6
13688	475	1.0666	11.69	82.6
13679	550	3.4212	9.32	66.3
13670	525	3.8798	11.49	81.6
13660	500	3.9690	12.99	92.0
13653	475	3.9807	14.88	105.2

Table A-13 *AlMgMnZr, heat treated.*

Lognr.	T_{def}.	ω	M_{max}	σ
	°C	rad/s	Nm	MPa
14060	550	0.0100	2.23	15.9
14055	525	0.0100	2.64	18.8
14048	500	0.0101	3.06	21.8
14042	475	0.0101	3.86	27.4
14032	550	0.1059	3.70	26.4
14026	525	0.1039	4.32	30.7
14019	500	0.1055	5.46	38.8
14012	475	0.1064	6.30	44.7
13998	550	1.0298	6.28	44.8
13992	525	1.0297	7.81	55.6
13954	500	1.0470	8.68	61.7
13948	475	1.0502	10.51	74.6
13985	550	3.1034	8.64	61.6
13979	525	3.2664	10.23	72.8
13964	475	3.3685	12.30	87.3
14127	550	0.0101	2.29	16.3
14122	525	0.0103	2.78	19.8
14112	500	0.0151	3.33	23.7
14106	475	0.0105	3.77	26.7
14190	550	0.1252	3.99	28.5
14187	525	0.1014	4.47	31.9
14183	500	0.1011	5.66	40.2
14179	475	0.1030	6.49	46.1
14173	550	1.0526	6.35	45.3
14169	525	1.0510	7.58	54.0
14164	500	1.1214	9.17	65.2
14160	475	1.0874	10.56	75.0
14153	550	3.4677	9.13	65.1
14148	525	3.3859	10.39	74.0
14143	500	3.3599	11.89	84.6
14137	475	3.7601	12.60	89.5

Table A-14 *AlMgMnZrSc, cast.*

Lognr.	$T_{def.}$	ω	M_{max}	σ
	°C	rad/s	Nm	MPa
13111	550	0.0115	2.53	18.0
13138	525	0.0115	3.00	21.3
13156	500	0.0114	3.66	25.9
13179	475	0.0119	4.36	30.8
13198	550	0.0980	3.92	27.9
13208	525	0.0969	4.86	34.5
13215	500	0.0961	5.68	40.2
13226	475	0.0967	7.07	50.0
13237	550	1.0124	6.88	48.9
13243	525	1.0075	7.96	56.5
13248	500	1.0058	9.47	67.1
13253	475	1.0013	11.31	79.9
13332	550	3.9818	9.80	69.7
13345	525	3.6502	11.25	79.8
13355	500	3.5296	12.65	89.6
13361	475	3.8331	14.49	102.4
13778	550	0.0125	2.68	19.0
13771	525	0.0126	3.30	23.4
13765	500	0.0129	3.95	28.0
13757	475	0.0152	4.86	34.3
13747	550	0.1020	4.05	28.8
13737	525	0.1378	5.25	37.2
13729	500	0.1026	5.80	41.0
13722	475	0.1036	7.54	53.2
13711	550	0.8961	6.58	46.8
13703	525	1.3211	8.61	61.1
13696	500	1.3294	10.12	71.7
13689	475	1.0641	11.95	84.4
13680	550	3.4183	9.44	67.1
13671	525	3.8661	11.28	80.0
13661	500	3.9450	13.25	93.8
13654	475	4.0040	14.26	100.8

Table A-15 *AlMgMnZrSc, heat treated.*

Lognr.	$T_{def.}$	ω	M_{max}	σ
	°C	rad/s	Nm	MPa
14128	550	0.0101	2.26	16.1
14123	525	0.0103	2.75	19.6
14113	500	0.0152	3.45	24.6
14107	475	0.0104	4.04	28.7
14191	550	0.1262	3.92	28.0
14188	525	0.1270	4.58	32.7
14184	500	0.1007	5.22	37.2
14180	475	0.1022	6.57	46.7
14174	550	1.0512	6.36	45.4
14170	525	1.0501	7.63	54.4
14165	500	1.1289	9.24	65.8
14161	475	1.0973	10.95	77.9
14154	550	3.4179	8.65	61.8
14149	525	3.3575	10.33	73.7
14144	500	3.3765	12.21	87.0
14061	550	0.0101	2.05	14.7
14056	525	0.0100	2.53	18.0
14049	500	0.0100	3.03	21.6
14043	475	0.0100	3.79	27.0
14033	550	0.1061	3.54	25.3
14027	525	0.1036	4.36	31.1
14020	500	0.1056	5.31	37.8
14013	475	0.1351	6.82	48.5
13993	525	0.9958	7.50	53.5
13955	500	1.0122	8.93	63.6
13949	475	1.0468	10.92	77.6
13986	550	3.0679	8.73	62.4
13980	525	3.2190	10.37	74.0
13965	475	3.2199	13.97	99.3

Appendix D

DISCRETE LEAST SQUARES APPROXIMATION (DLSA)[1]

If we consider a set of experimental data with k x-values, k y-values and k z-values and assuming that the data points can be approximated by a plane in the x,y,z-space the following equation is valid for the plane:

$$z = a + bx + cy \qquad \text{A-6}$$

The coefficients a, b and c are found by minimising the total least square errors given by:

$$E_s = \sum_{i=1}^{k} \left[z_i - (a + bx_i + cy_i \right]^2 \qquad \text{A-7}$$

Performing the minimisation by partial differentiation with respect to a, b and c and solving the resulting linear system by means of Gaussian elimination one obtains the following expressions for a, b and c:[1]

$$a = \frac{C - bA - cB}{k} \qquad \text{A-8}$$

$$b = \frac{(kG - AC) - c(kF - AB)}{(kD - A^2)} \qquad \text{A-9}$$

$$c = \frac{(kH - BC)(kD - A^2) - (kG - AC)(kF - AB)}{(kE - B^2)(kD - A^2) - (kF - AB)^2} \qquad \text{A-10}$$

where

$$\begin{aligned} A &= \sum_{i=1}^{k} x_i \quad B = \sum_{i=1}^{k} y_i \quad C = \sum_{i=1}^{k} z_i \quad D = \sum_{i=1}^{k} x_i^2 \\ E &= \sum_{i=1}^{k} y_i^2 \quad F = \sum_{i=1}^{k} x_i y_i \quad G = \sum_{i=1}^{k} x_i z_i \quad H = \sum_{i=1}^{k} y_i z_i \end{aligned} \qquad \text{A-11}$$

The coefficients in the constitutive equations can be determined by using the discrete least squares approximation described above. The coefficients and the variables in the constitutive equations and the corresponding coefficients and variables in the above analysis is given in Table A-16.

Table A-16 *Coefficients and variables in the constitutive equations.*

Equation	a	b	c	x	y	z
Power law	lnA	n	Q/R	$\ln\sigma$	1/T	$\ln\dot{\varepsilon}$
Exp. law	lnB	β	Q/R	σ	1/T	$\ln\dot{\varepsilon}$
Sinh law	lnC	n’	Q/R	sineh($\alpha\sigma$)	1/T	$\ln\dot{\varepsilon}$

Note that the x-variable contains the coefficient α. The coefficients in the hyperbolical sine law can not be directly determined by the DLSA method. However, the method may be used by changing the value of α and calculating the values of a, b and c until Eq. A-7 is minimised, Figure A-1. E is the total error divided by the total number of data points, i.e. $E=E_s/k$. The optimum α-values were found by fitting the E-α-data to a polynomial of third degree. The correlation factor was better than $R^2=0.99$:

$$E = d + e\alpha + f\alpha^2 + g\alpha^3 \qquad \text{A-12}$$

$$\frac{dE}{d\alpha} = 3g\alpha_{opt}^2 + 2f\alpha_{opt} + e = 0 \qquad \text{A-13}$$

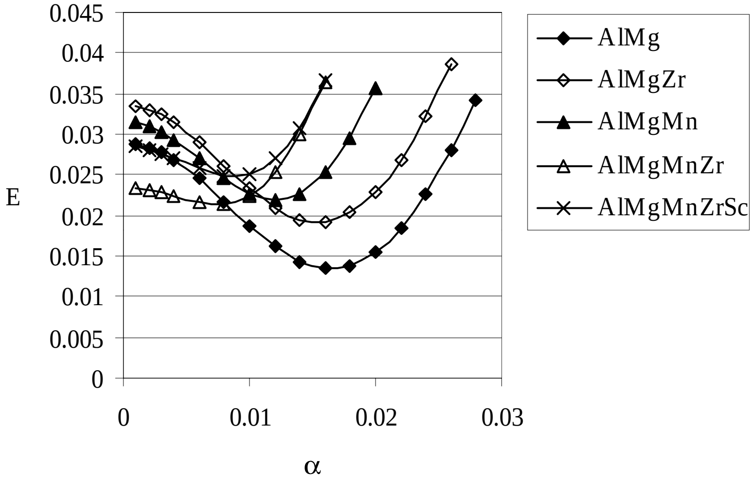

Figure A-1 *Error per data point as a function of the α-coefficient in the hyperbolical sine law for the as cast condition.*

[1] Rønning, B., Ph.D. Thesis, NTNU, Trondheim, 1998.

Appendix E

COEFFICIENTS IN THE CONSTITUTIVE EQUATIONS

The coefficients in the constitutive equations were determined by the procedures described in Appendix D. The designations after the alloy name means “c” for cast condition and “h” for heat treated condition.

Table A-17 *The power law.*

Alloy	n	ln A	Q	E_s/k
AlMg-c	3.504	6.799	141.5	0.0289
AlMgZr-c	3.686	6.415	145.0	0.0336
AlMgMn-c	4.219	4.839	151.6	0.0316
AlMgMnZr-c	4.612	3.374	154.7	0.0234
AlMgMnZrSc-c	4.604	4.154	159.6	0.0285
AlMg-h	3.439	5.924	133.6	0.0627
AlMgZr-h	3.742	4.399	133.6	0.0243
AlMgMn-h	4.072	6.571	157.1	0.0162
AlMgMnZr-h	4.423	2.222	139.9	0.0356
AlMgMnZrSc-h	4.263	5.464	157.3	0.0177

Table A-18 *The exponential law.*

Alloy	b	ln B	Q	E_s/k
AlMg-c	0.0977	14.345	136.5	0.248
AlMgZr-c	0.0959	15.676	146.2	0.246
AlMgMn-c	0.0934	16.083	151.6	0.236
AlMgMnZr-c	0.0903	16.347	154.6	0.237
AlMgMnZrSc-c	0.0913	16.893	158.8	0.237
AlMg-h	0.0955	15.948	145.4	0.267
AlMgZr-h	0.1018	13.598	134.1	0.228
AlMgMn-h	0.1019	17.510	161.1	0.299
AlMgMnZr-h	0.1006	14.321	142.3	0.219
AlMgMnZrSc-h	0.0957	15.797	150.8	0.290

Table A-19 *The hypobolical sine law.*

Alloy	α	n'	ln C	Q	E_s/k
AlMg-c	0.01694	3.109	20.935	144.0	0.0135
AlMgZr-c	0.01582	3.272	21.695	148.6	0.0192
AlMgMn-c	0.01230	3.821	23.276	154.3	0.0220
AlMgMnZr-c	0.00710	4.416	26.019	155.8	0.0214
AlMgMnZrSc-c	0.00861	4.329	25.846	161.1	0.0248
AlMg-h	0.01651	3.066	20.352	139.0	0.0486
AlMgZr-h	0.01467	3.402	20.045	135.8	0.0146
AlMgMn-h	0.00720	3.960	26.606	158.3	0.0149
AlMgMnZr-h	0.01130	4.054	21.885	141.9	0.0296
AlMgMnZrSc-h	0.00497	4.188	27.706	156.0	0.0204

Appendix F

GEOMETRY OF EXTRUSION TOOLS.

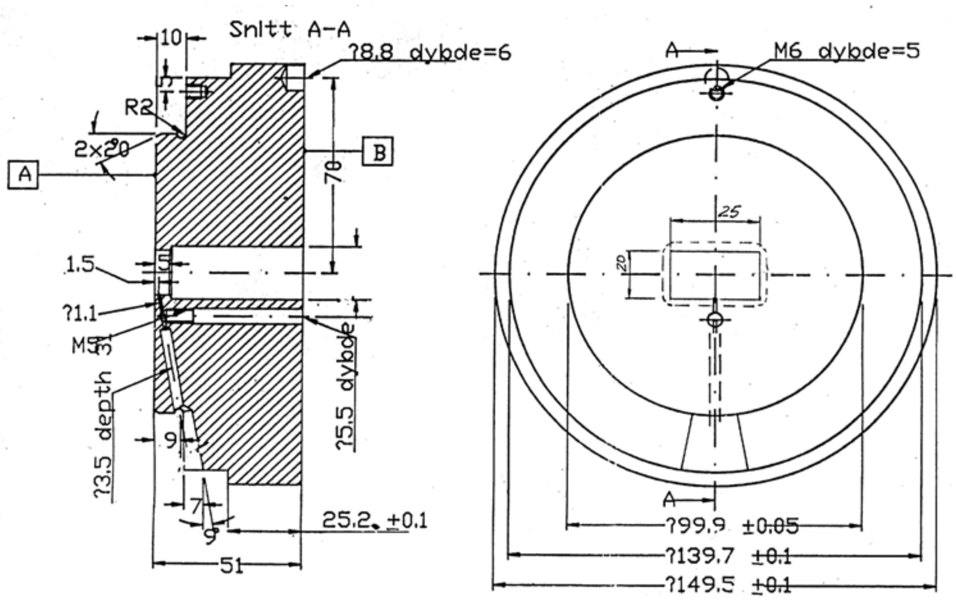

Figure A-2 *Die geometry used for the production of 20x25 mm^2 profiles.*

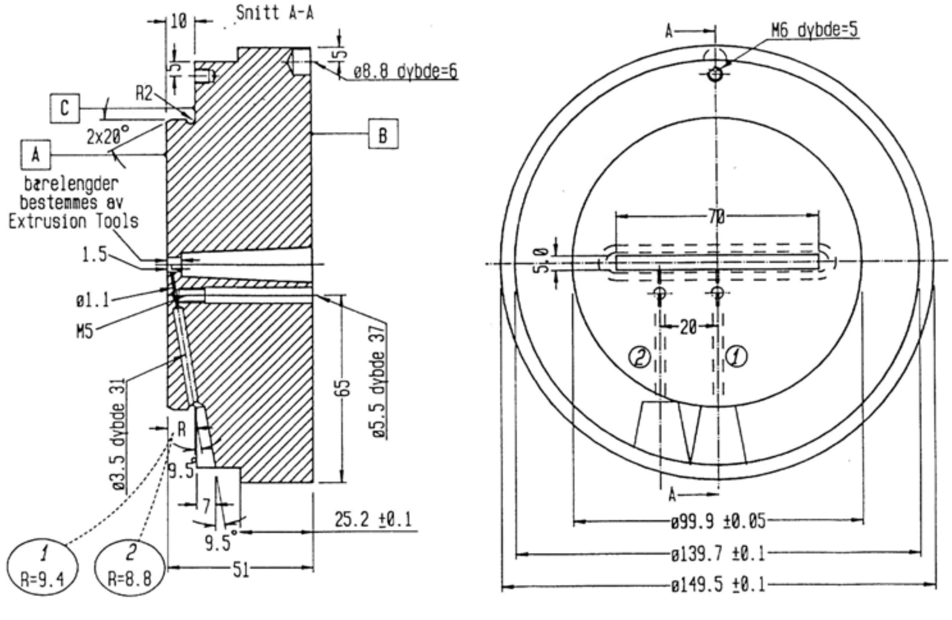

Figure A-3 *Die geometry used for the production of 5x70 mm^2 profiles.*

Appendix G
EXTRUSION DATA

Table A-20 *AlMg.*

Lognr.	Parallel nr.	Billet nr.	V_{ram}	T_{billet}	T_{cont}	T_{ram}	$T_{profile}$	F_{peak}	$F_{ss,max}$	$F_{ss,min}$	T_{peak}	$T_{ss,max}$	$T_{ss,min}$
			mm/s	°C	°C	°C	°C	kN	kN	kN	°C	°C	°C
57	1	134	0.2392	475	432	194	464	2580	2433	1800	461	459	448
62	2	135	0.3031	474	432	251	468	2603	2437	1816	462	462	451
16	1	124	1.0165	448	432	107	482	3655	2989	2138	478	481	470
27	2	126	1.0123	453	433	130	485	3571	2989	2092	480	484	474
11	1	123	1.0167	475	431	146	492	3120	2851	2069	492	491	475
21	2	125	1.02	475	428	121	490	3161	2851	2069	489	489	474
53	3	133	0.9865	476	430	130	491	3100	2759	2046	489	489	474
1	1	121	0.9042	504	433	50	496	2817	2655	2086	493	493	467
6	2	122	1.0175	498	429	181	502	2728	2575	2046	502	501	478
32	1	131	2.9894	474	430	77	513	3976	3500	2368	508	510	501
38	2	132	3.0125	470	429	223	517	3666	3402	2437	513	515	504
67	3	136	3.0241	476	433	98	513	3909	3356	2299	508	511	502

Table A-21 *AlMgZr.*

Lognr.	Parallel nr.	Billet nr.	V_{ram}	T_{billet}	T_{cont}	T_{ram}	$T_{profile}$	F_{peak}	$F_{ss,max}$	$F_{ss,min}$	T_{peak}	$T_{ss,max}$	$T_{ss,min}$
			mm/s	°C	°C	°C	°C	kN	kN	kN	°C	°C	°C
58	1	241	0.2352	475	429	214	464	2930	2621	1793	462	457	451
63	2	243	0.2918	474	428	120	463	3212	2966	1954	461	458	446
17	1	234	1.0174	451	429	173	486	3921	3287	2207	481	486	475
28	2	236	1.0161	452	429	149	490	3675	3126	2184	486	489	476
12	1	233	1.0179	477	429	160	497	3386	3126	2161	495	495	478
22	2	235	1.0147	477	430	107	494	3461	3149	2207	493	491	474
54	3	241	0.9907	474	429	126	493	3496	3126	2184	492	491	474
2	1	231	0.9067	504	434	100	502	3008	2920	2184	502	501	472
7	2	232	1.0226	500	430	124	505	3060		2188	504		476
33	1	237	3.0043	476	432	146	525	3958	3310	2322	521	525	508
39	2	238	2.9832	474	430	231	529	3733	3402	2667	525	527	505
68	3	244	3.035	474	431	109	523	4267	3776	2379	516	519	503

Table A-22 *AlMgMn.*

Lognr.	Parallel nr.	Billet nr.	V_{ram}	T_{billet}	T_{cont}	T_{ram}	$T_{profile}$	F_{peak}	$F_{ss,max}$	$F_{ss,min}$	T_{peak}	$T_{ss,max}$	$T_{ss,min}$
			mm/s	°C	°C	°C	°C	kN	kN	kN	°C	°C	°C
59	1	341	0.2282	477	432	155	463	3112	2897	1954	463	459	446
64	2	342	0.2962	477	432	129	468	3271	2920	2000	462	460	447
18	1	334	1.0249	454	432	116	493	3895	3586	2230	485	489	476
29	2	337	1.0333	451	430	220	492	3811	3103	2092	486	489	483
13	1	333	1.014	478	431	129	496	3557	3103	2161	494	495	480
23	2	336	1.0086	478	429	94	494	3580	3126	2207	493	493	477
25	3	335	1.0126	475	432	141	499	3430	3057	2184	498	497	479
3	1	331	1.0138	490	432	198	502	3213	2966	1908	502	498	482
8	2	332	1.0138	500	432	162	508	3155	2943	2138	508	507	482
34	1	338	2.998	473	429	180	529	4091	3698	2302	523	525	501
40	2	339	2.998	475	432	200	523	4244	3724	3026	515	519	499
69	3	343	3.007	477	428	116	523	3967	3586	2414	516	519	510

Table A-23 *AlMgMnZr.*

Lognr.	Parallel nr.	Billet nr.	V_{ram}	T_{billet}	T_{cont}	T_{ram}	$T_{profile}$	F_{peak}	$F_{ss,max}$	$F_{ss,min}$	T_{peak}	$T_{ss,max}$	$T_{ss,min}$
			mm/s	°C	°C	°C	°C	kN	kN	kN	°C	°C	°C
60	1	442	0.3319	477	432	42	465	3594	3333	1954	465	464	444
65	2	443	0.2664	478	431	144	473	3464	3241	2046	465	464	449
19	1	434	1.0128	446	428	109	492	4143	3750	2198	486	486	478
30	2	436	1.0145	453	434	155	498	3895	3310	2253	494	497	483
14	1	433	1.0276	470	432	136	503	3638	3287	2207	500	502	483
24	2	435	1.0231	472	432	92	498	3874	3310	2368	495	497	479
55	3	441	0.986	478	433	110	497	3721	3494	2299	492	495	479
4	1	431	1.0089	499	431	110	512	3265	3172	2299	511	512	481
9	2	432	1.0207	503	434	117	513	3305	3218	2207	512	513	484
36	1	437	3.0036	476	429	124	533	4221	3776	2224	525	530	499
41	2	438	3.003	469	429	207	529	4386	3724	3155	521	525	501
70	3	444	3.0146	474	431	119	529	4380	3672	2534	526	528	511

Table A-24 *AlMgMnZrSc.*

Lognr.	Parallel nr.	Billet nr.	V_{ram}	T_{billet}	T_{cont}	T_{ram}	$T_{profile}$	F_{peak}	$F_{ss,max}$	$F_{ss,min}$	T_{peak}	$T_{ss,max}$	$T_{ss,min}$
			mm/s	°C	°C	°C	°C	kN	kN	kN	°C	°C	°C
61	1	542	0.3127	477	430	202	467	3476	3264	2000	467	464	453
66	2	543	0.2943	477	431	150	468	3586	3356	2046	463	464	446
20	1	534	1.0203	452	432	126	495	4106	3724	2302	489	495	480
31	2	536	1.0228	451	430	190	492	4302	3879	2224	484	490	484
15	1	533	1.0146	475	428	192	499	3854	3517	1931	496	497	486
26	2	535	1.0153	475	429	113	499	3837	3540	2276	496	498	475
56	3	541	0.9832	475	432	110	500	3817	3655	2299	497	499	479
5	1	531	1.0233	494	432	45	511	3490	3425	2414	510	510	476
10	2	532	1.0219	507	429	142	516	3271		2207	516		483
37	1	537	3.0043	474	431	172	533	4527	4080	3362	523	527	498
42	2	538	3.0083	475	431	111	529	4680	4109	2586	519	525	502
71	3	544	3.0299	474	433	123	529	4542	4080	2500	523	525	505

Appendix H

HARDNESS DATA, BACK-ANNEALING OF EXTRUDED PROFILES.

Table A-25 *AlMg.*

Time	T=350°C		T=450°C		T=550°C		T=570°C		T=590°C	
(min)	HV1	St.dev	HV1	St.dev	HV1	St.dev	HV1	St.dev	HV1	St.dev
0	67.8	2.6	67.8	0.7	67.8	3.6	67.8	3.6	67.8	3.6
1					66.0	1.5	64.1	1.5	63.5	0.2
6	66.0	1.3	65.8	1.5	65.5	1.2	64.1	1.7	58.2	0.5
30	65.8	1.3	65.4	1.1	64.8	0.5	63.0	0.5	54.0	1.7
60	65.0	1.7	65.2	1.1	64.2	0.5	62.2	1.5	52.0	4.1
180	65.0	0.7	64.0	1.6	62.3	4.8	61.1	3.3	53.0	3.4
360	64.0	1.0	62.8	0.8	61.0	3.3	60.1	1.6	53.0	0.4
720	63.5	2.3			60.0	2.1				
1440			62.0	1.6	59.5	0.8	60.0	0.7		
2880	62.9	0.8	62.2	0.8	59.0	0.9				
5670	62.1	1.7			59.0	1.3				

Table A-26 *AlMgZr.*

Time	T=350°C		T=450°C		T=550°C		T=570°C		T=590°C	
(min)	HV1	St.dev	HV1	St.dev	HV1	St.dev	HV1	St.dev	HV1	St.dev
0	73.2	0.7	73.2	0.7	73.2	0.7	73.2	0.7	73.2	0.7
1					69.5	2.1	68.0	1.2	65.8	3.2
6	69.8	2.3	72.0	0.4	69.0	0.9	67.5	2.0	64.7	1.0
30	69.8	1.1	69.4	0.5	68.0	0.3	66.4	2.0	60.5	2.6
60	70.0	1.0	68.2	1.1	66.0	3.3	64.1	3.0	60.0	1.1
180	69.2	0.4	67.2	1.6	63.4	4.4	63.0	0.8	60.0	0.7
360	70.0	1.0	67.0	1.2	61.0	0.6	61.3	2.4	59.0	0.5
720	69.2	1.6			60.0	0.3				
1440			67.0	1.8	60.0	1.0	61.5	3.0		
2880	68.0	0.5	66.4	1.3	60.0	1.2				
5670	66.4	0.9			60.4	1.3				

Table A-27 *AlMgMn.*

Time	T=350°C		T=450°C		T=550°C		T=570°C		T=590°C	
(min)	HV1	St.dev	HV1	St.dev	HV1	St.dev	HV1	St.dev	HV1	St.dev
0	75.4	1.5	75.4	1.5	75.4	1.5	75.4	1.5	75.4	1.5
1					74.0	1.2	72.7	0.6	70.3	0.5
6	75.0	1.0	75.0	1.5	73.5	1.3	72.0	1.6	68.0	2.9
30	74.5	1.5	75.0	1.5	72.0	0.2	70.0	1.7	63.9	1.2
60	74.0	1.9	75.0	1.7	71.0	6.0	67.8	2.8	60.9	8.9
180	74.0	0.5	74.4	1.5	67.0	3.6	65.7	2.8	61.0	0.2
360	73.6	0.5	73.6	1.1	63.0	4.7	64.0	2.4	61.0	2.2
720	73.7	0.5			62.5	6.9				
1440			71.2	0.8	62.0	1.3	63.3	6.2		
2880	72.0	1.3	71.4	1.3	62.0	0.7				
5670	70.4	1.0			62.1	1.6				

Table A-28 *AlMgMnZr.*

Time	T=350°C		T=450°C		T=550°C		T=570°C		T=590°C	
(min)	HV1	St.dev	HV1	St.dev	HV1	St.dev	HV1	St.dev	HV1	St.dev
0	82.2	2.2	82.2	2.2	82.2	2.2	82.2	2.2	82.2	2.2
1					80.3	1.2	76.4	1.8	73.0	0.7
6	80.0	1.5	80.8	1.3	78.8	1.8	75.0	1.6	69.7	1.8
30	79.8	1.3	80.0	1.3	75.8	1.8	73.0	1.2	66.8	1.6
60	79.4	1.5	79.0	1.5	74.0	4.3	70.3	2.2	67.4	0.9
180	79.0	1.1	78.8	1.1	69.9	4.7	67.3	2.7	67.0	1.6
360	78.0	1.2	77.5	0.9	67.0	2.0	66.9	2.4	67.0	0.4
720	78.1	1.4			65.0	3.7				
1440			76.0	1.2	64.5	0.7	66.5	3.1		
2880	77.4	0.9	73.8	1.1	65.0	0.8				
5670	74.3	1.1			64.3	2.7				

Table A-29 *AlMgMnZrSc.*

Time	T=350°C		T=450°C		T=550°C		T=570°C		T=590°C	
(min)	HV1	St.dev	HV1	St.dev	HV1	St.dev	HV1	St.dev	HV1	St.dev
0	86.7	1.2	86.7	1.2	86.7	1.2	86.7	1.2	86.7	1.2
1					83.5	1.0	83.3	2.0	80.5	0.5
6	86.0	0.7	85.8	0.8	82.7	2.6	81.0	0.8	77.5	0.9
30	86.0	1.1	85.0	0.5	81.0	1.4	77.0	1.5	75.1	0.4
60	85.5	0.4	84.0	0.8	80.0	4.7	75.0	2.8	72.7	2.5
180	85.0	0.5	83.0	1.7	77.6	1.6	74.0	1.3	70.0	3.3
360	84.4	1.1	83.0	1.7	75.0	1.6	73.0	0.9	69.3	0.5
720	83.4	1.5			73.0	1.5				
1440			81.8	0.8	72.5	1.0	73.0	3.7		
2880	82.0	1.1	80.4	2.3	73.0	2.0				
5670	81.3	1.1			72.0	1.3				

Appendix I

HARDNESS DATA, BACK-ANNEALING OF EXTRUDED AND COLD ROLLED PROFILES.

Table A-30 *AlMg.*

Time	T=200°C		T=250°C		T=275°C		T=300°C		T=350°C		T=450°C		T=550°C	
(min)	HV1	St.dev.	HV1	St.dev.	HV1	St.dev.	HV1	St.dev.	HV1	St.dev.	HV1	St.dev.	HV1	St.dev.
0	122.7	2.2	122.7	2.2	122.7	2.2	122.7	2.2	122.7	2.2	122.7	2.2	122.7	2.2
1	115.2	2.8	103.9	0.1	97.0	1.7	91.8	2.0	73.6	2.8	71.4	0.9	70.6	1.9
6	107.2	2.2	98.3	0.4	90.0	1.3	83.8	2.0	69.5	1.3	72.2	1.5	70.0	1.0
30	103.4	1.5	94.7	0.7	83.8	0.8	73.5	0.4	69.4	0.3	70.0	0.7	70.6	0.9
60									69.7	1.6	68.4	1.9	69.2	1.8
180	98.4	1.9	88.5	0.1	76.2	0.8	70.4	0.8	68.0	1.1	69.0	1.2	69.0	1.0
360									68.6	0.7	69.8	0.8	69.0	0.7
1440			73.7	1.0			69.8	0.9						

Table A-31 *AlMgZr.*

Time	T=200°C		T=250°C		T=275°C		T=300°C		T=350°C		T=450°C		T=550°C	
(min)	HV1	St.dev.	HV1	St.dev.	HV1	St.dev.	HV1	St.dev.	HV1	St.dev.	HV1	St.dev.	HV1	St.dev.
0	123.4	2.1	123.4	2.1	123.4	2.1	123.4	2.1	123.4	2.1	123.4	2.1	123.4	2.1
1	118.0	1.0	107.5	1.0	103.0	1.5	97.3	0.4	76.9	3.5	77.0	1.2	75.6	0.5
6	112.2	3.7	102.2	0.3	96.4	0.9	87.1	0.1	72.7	0.1	75.0	1.0	75.2	0.8
30	106.8	1.3	98.7	0.7	88.2	2.4	74.0	1.1	74.6	1.7	75.6	1.3	74.0	1.0
60									74.4	1.4	71.8	1.1	72.4	1.3
180	103.2	2.7	92.8	0.8	75.0	2.1	74.3	0.7	73.0	1.4	76.0	1.6	71.4	0.5
360									71.6	0.6	74.0	0.7	70.8	0.4
1440			80.7	0.7			74.7	0.4						

Table A-32 *AlMgMn.*

Time	T=200°C		T=250°C		T=275°C		T=300°C		T=350°C		T=450°C		T=550°C	
(min)	HV1	St.dev.	HV1	St.dev.	HV1	St.dev.	HV1	St.dev.	HV1	St.dev.	HV1	St.dev.	HV1	St.dev.
0	135.8	2.7	135.8	2.7	135.8	2.7	135.8	2.7	135.8	2.7	135.8	2.7	135.8	2.7
1	124.6	1.5	119.2	0.8	109.4	2.1	88.7	1.8	82.2	1.7	85.0	1.9	80.8	1.3
6	121.6	1.5	114.5	1.0	84.4	0.9	81.2	1.1	81.2	0.0	83.8	1.3	78.6	0.9
30	120.0	2.1	102.7	2.1	82.2	1.9	80.3	0.4	82.3	1.0	81.8	1.5	79.4	1.5
60									81.2	0.3	81.6	0.5	77.4	1.8
180	117.6	2.5	82.7	1.3	84.0	1.2	81.0	1.7	80.2	2.3	81.8	2.2	76.6	1.7
360									81.0	1.6	78.0	1.2	76.2	1.3
1440			80.0	1.1			81.0	0.3						

Table A-33 *AlMgMnZr.*

Time	T=200°C		T=250°C		T=275°C		T=300°C		T=350°C		T=450°C		T=550°C	
(min)	HV1	St.dev.	HV1	St.dev.	HV1	St.dev.	HV1	St.dev.	HV1	St.dev.	HV1	St.dev.	HV1	St.dev.
0	136.6	3.4	136.6	3.4	136.6	3.4	136.6	3.4	136.6	3.4	136.6	3.4	136.6	3.4
1	128.2	3.3	122.4	0.8	111.8	1.8	93.2	1.7	84.8	0.6	86.6	0.9	85.4	1.1
6	123.0	4.2	118.6	0.8	84.8	0.8	82.6	1.4	84.1	1.3	86.0	1.0	83.8	0.8
30	121.8	2.2	108.9	1.6	82.6	1.3	82.6	0.6	85.3	1.0	86.4	1.8	82.4	1.1
60									83.3	0.1	82.6	1.3	79.0	1.2
180	118.4	2.1	84.5	2.7	82.0	0.7	83.5	1.6	83.2	2.0	83.0	1.0	79.6	2.1
360									84.0	2.3	81.4	0.5	78.8	1.3
1440			82.0	0.6			82.6	0.3						

Table A-34 *AlMgMnZrSc.*

Time	T=200°C		T=250°C		T=275°C		T=300°C		T=350°C		T=450°C		T=550°C	
(min)	HV1	St.dev.	HV1	St.dev.	HV1	St.dev.	HV1	St.dev.	HV1	St.dev.	HV1	St.dev.	HV1	St.dev.
0	138.4	4.6	138.4	4.6	138.4	4.6	138.4	4.6	138.4	4.6	138.4	4.6	138.4	4.6
1	133.0	4.7	123.9	1.3	120.0	10.9	113.2	1.4	96.8	1.4	94.6	0.5	90.4	0.9
6	127.6	2.6	118.1	1.8	109.0	1.4	101.1	0.1	94.1	2.4	90.8	1.5	87.6	1.3
30	126.3	2.1	116.2	3.1	103.6	1.1	98.2	0.0	95.9	3.5	91.4	1.1	85.2	0.8
60									93.3	1.0	89.4	0.9	81.4	1.7
180	121.0	3.1	112.1	1.6	100.0	2.2	97.6	1.4	92.5	0.1	90.4	1.5	80.4	0.9
360									91.8	2.0	88.6	2.1	78.8	1.8
1440			106.9	3.0			96.7	0.4						

Appendix J

WELDING PARAMETERS

Table A-35 *Welding parameters.*

Date:	1999-07-21
Base material:	AlMg-alloys
Filler material:	SAFRA 66, Ø1.2mm
Groove:	V, 60°, 1mm root face, 2 mm root gap
Welding position:	1G
Pistol angle:	10°
Contact tube distance:	13 mm
Blanket gas:	Argon Plus, 20 l/min
Welding current:	196-208 A
Welding voltage:	26.8-28 V
Feeding rate (filler wire):	13.6 m/min
Welding speed:	375 mm/min
Welding machine: - Program ID: - Adjustment:	ESAB ARISTO 500 Short puls, AlMg, Ø1.2mm -0.5V, 13.6 mm/min (feeding rate)
Treatment	Aceton, steel brush

Appendix K

TENSILE TESTING SPECIMENS.

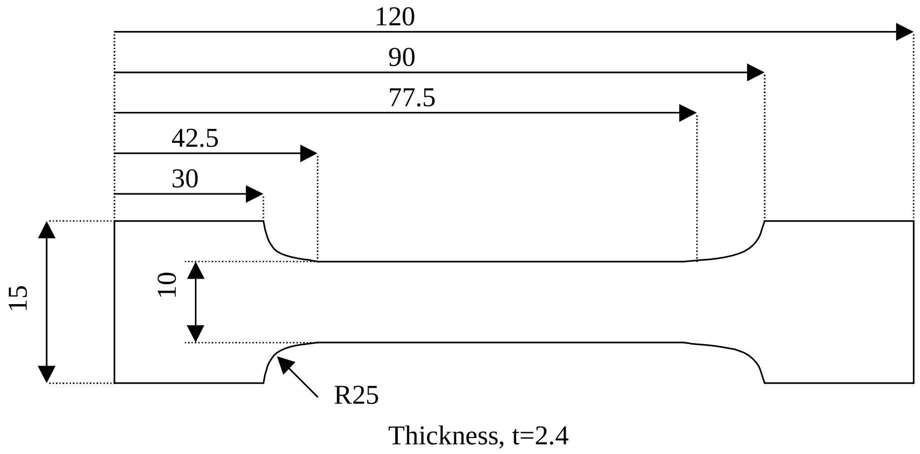

Figure A-4 *Geometry of tensile specimen used for testing of the heat treated material, extruded material and cold rolled material.*

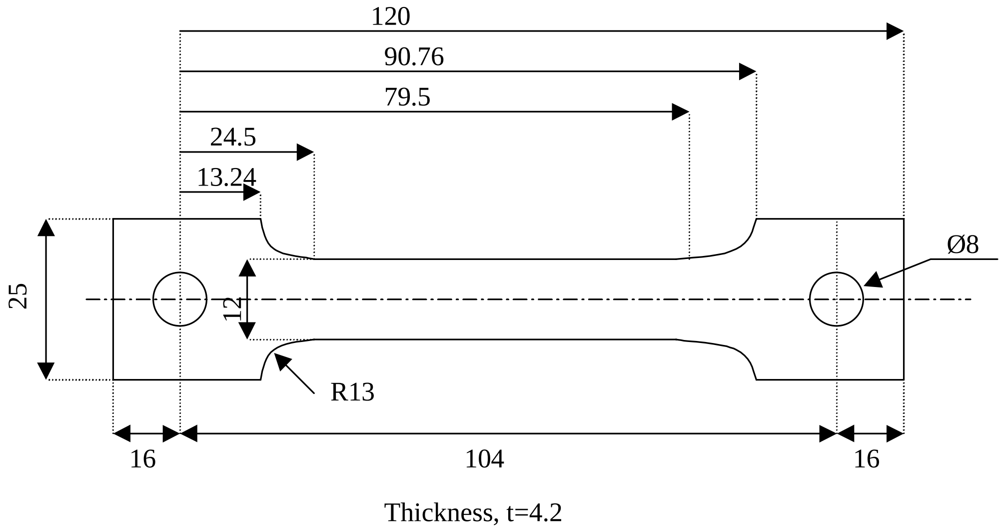

Figure A-5 *Geometry of tensile specimen used for testing of welded profiles.*

Appendix L

TENSILE TESTING DATA

Table A-36 *Heat treated material.*

Alloy	Specimen no.	Test no.	$R_{p0.2}$ (MPa)	$R_{p0.2}$ Average St.dev.	R_m (MPa)	R_m Average St.dev.	A_m (%)	A_m Average St.dev.	A_b (%)	A_b Average St.dev.	E (MPa)	Comments
AlMg	H11											
	H12	5	99.6	100.5	242.0	242.7	22.4	22.3	30.3	30.2	66614	Failure outside ext.
	H13	10	101.5	1.4	243.4	1.0	22.3	0.1	30.0	0.2	70103	
AlMgZr	H21	1	100.4		242.4		22.5		28.7		42770	-
	H22	6	103.3	103.9	238.9	242.3	19.8	21.3	24.4	27.1	71359	ok
	H23	11	107.9	3.8	245.7	3.4	21.5	1.4	28.3	2.4	60427	ok
AlMgMn	H31	2	115.7		276.5		17.8		20.1		71044	ok
	H32	7	116.5	117.0	271.6	276.2	14.6	17.4	17.2	20.0	69153	ok
	H33	12	118.8	1.6	280.6	4.5	19.9	2.7	22.6	2.7	68150	Failure outside ext.
AlMgMnZr	H41	3	125.3		250.9		7.7		9.8		60389	ok
	H42	8	125.6	124.0	256.2	263.4	9.9	11.4	12.3	14.3	72582	ok
	H43	13	121.2	2.5	283.3	17.4	16.6	4.6	20.7	5.7	68473	ok
AlMgMnZrSc	H51	4	136.8		297.6		18.8		19.6		71649	ok
	H52	9	138.4	136.9	294.4	295.7	15.6	15.8	17.1	17.4	70000	ok
	H53	14	135.4	1.5	295.2	1.7	13.0	2.9	15.5	2.1	69603	Failure outside ext.

Table A-37 *Extruded profiles.*

Alloy	Specimen no.	Test no.	$R_{p0.2}$ (MPa)	$R_{p0.2}$ Average St.dev.	R_m (MPa)	R_m Average St.dev.	A_m (%)	A_m Average St.dev.	A_b (%)	A_b Average St.dev.	E (MPa)	Comments
AlMg	E11	1	95.3		237.0		20.8		26.6		60479	Failure outside ext.
	E12	6	94.9	95.7	240.6	240.2	22.4	22.6	28.5	28.2	62166	Failure outside ext.
	E13	11	97.0	1.1	242.9	3.0	24.6	1.9	29.6	1.5	60673	Failure outside ext.
AlMgZr	E21	2	145.8		285.1		9.0		9.5		70096	Failure outside ext.
	E22	7	157.2	152.2	291.6	288.6	8.5	8.7	8.8	8.8	65315	Failure outside ext.
	E23	12	153.8	5.9	289.2	3.3	8.6	0.2	8.2	0.7	68275	Failure outside ext.
AlMgMn	E31	3	113.0		266.4		21.4		24.6		62297	ok
	E32	8	110.6	110.7	269.7	268.5	17.8	20.0	22.6	24.7	70853	Failure outside ext.
	E33	13	108.5	2.2	269.2	1.8	20.7	1.9	26.9	2.2	73410	Failure outside ext.
AlMgMnZr	E41	4	182.1		-		-		-		66367	Test aborted
	E42	9	178.4	176.4	343.7	337.9	11.1	11.4	10.3	12.1	69570	Failure outside ext.
	E43	14	168.7	6.9	332.1	8.2	11.6	0.4	13.9	2.5	69517	ok
AlMgMnZrSc	E51	5	198.4		361.9		9.9		11.3		69860	Failure outside ext.
	E52	10	200.5	199.5	358.7	361.6	11.7	11.2	13.6	12.6	71992	ok
	E53	15	199.6	1.1	364.3	2.8	11.9	1.1	12.9	1.2	73764	ok

Table A-38 *Extruded and cold rolled profiles.*

Alloy	Specimen no.	Test no.	$R_{p0.2}$ (MPa)	$R_{p0.2}$ Average St.dev.	R_m (MPa)	R_m Average St.dev.	A_m (%)	A_m Average St.dev.	A_b (%)	A_b Average St.dev.	E (MPa)	Comments
AlMg	V11	1	305.2		353.4		5.3		7.4		66544	ok
	V12	5	309.1	311.9	357.5	358.7	5.8	5.3	8.1	7.4	71918	Failure outside ext.
	V13	12	321.5	8.5	365.1	6.0	5.0	0.4	6.7	0.7	69049	ok
AlMgZr	V21	2	333.4		379.3		4.7		9.1		71144	ok
	V22	6	334.7	337.2	378.2	381.5	5.6	5.0	6.7	7.5	77719	ok
	V23	13	343.6	5.6	386.9	4.7	4.6	0.5	6.8	1.4	70192	Failure outside ext.
AlMgMn	V31	3	362.8		412.0		4.3		5.7		74867	Failure outside ext.
	V32	7	319.4	345.2	394.3	404.3	5.6	4.8	8.1	6.7	87151	ok
	V33	14	353.3	22.8	406.6	9.1	4.5	0.7	6.3	1.2	89350	Failure outside ext.
AlMgMnZr	V41											Specimen rejected
	V42	17	387.0	397.8	421.4	435.8	1.2	2.9	3.2	5.1	47900	
	V43	15	408.5	15.2	450.3	20.4	4.7	2.4	7.0	2.7	65942	ok
AlMgMnZrSc	V51	4	382.4		427.5		5.6		6.0		64450	ok
	V52	11	379.1	386.3	442.2	440.6	4.6	4.8	6.6	6.2	75125	ok
	V53	16	397.4	9.7	452.2	12.4	4.2	0.7	6.1	0.3	85314	ok

Table A-39 *Extruded and welded profiles.*

Alloy	Specimen no.	$R_{p0.2}$ (MPa)	$R_{p0.2}$ Average St.dev.	R_m (MPa)	R_m Average St.dev.	A_m (%)	A_m Average St.dev.	A_b (%)	A_b Average St.dev.
AlMg	1	107.0	106.8 1.3	256.0	256.5 1.3	21.2	21.0 0.2	25.4	25.0 0.6
	2	107.0		257.0		20.8		24.9	
	3	108.0		258.0		20.9		25.6	
	4	105.0		255.0		21.1		24.2	
AlMgZr	5	120.0	120.8 1.5	261.0	261.0 0.0	18.3	17.8 1.0	21.4	21.1 0.8
	6	119.0		261.0		16.7		20.7	
	7	122.0		261.0		17.3		20.1	
	8	122.0		261.0		18.8		22.0	
AlMgMn	9	122.0	122.5 1.0	287.0	285.0 1.6	20.5	19.0 1.3	22.8	21.4 1.0
	10	122.0		285.0		18.1		20.7	
	11	122.0		283.0		19.7		21.2	
	12	124.0		285.0		17.7		20.8	
AlMgMnZr	13	155.0	154.8 0.5	289.0	288.8 0.5	11.2	11.2 0.2	13.9	13.8 0.5
	14	154.0		289.0		11.0		13.3	
	15	155.0		289.0		11.4		13.5	
	16	155.0		288.0		11.0		14.5	
AlMgMnZrSc	17	161.0	160.8 1.0	292.0	289.5 1.9	10.1	10.0 0.4	11.7	11.9 0.3
	18	160.0		288.0		9.6		11.7	
	19	162.0		290.0		9.7		11.9	
	20	160.0		288.0		10.5		12.3	